UNIVERSITY OF OKLAHOMA

GRADUATE COLLEGE

EFFECTS OF RESTRICTIONS AND LIQUID PROPERTIES ON LIQUID LOADING IN NATURAL GAS WELLS

A DISSERTATION

SUBMITTED TO THE GRADUATE FACULTY

in partial fulfillment of the requirements for the

Degree of

DOCTOR OF PHILOSOPHY

By

Maziad Alsanea
Norman, Oklahoma
2022

EFFECTS OF RESTRICTIONS AND LIQUID PROPERTIES ON LIQUID

LOADING IN NATURAL GAS WELLS

A DISSERTATION APPROVED FOR THE
MEWBOURNE SCHOOL OF PETROLEUM AND GEOLOGICAL
ENGINEERING

BY THE COMMITTEE CONSISTING OF

Dr. Hamidreza Karami, Chair

Dr. Pejman Kazempoor

Dr. Catalin Teodoriu

Dr. Xingru Wu

Dr. Satya Putra

TABLE OF CONTENTS

LIST OF TABLES

LIST OF FIGURES

ACKNOWLEDGEMENTS

First and foremost, I must thank Allah(God) for the incredible life opportunities and the blessings that have made me the man I am today.

Whoever is not thankful to people, is not thankful to God. I would like to express my sincere gratitude to my advisor, Dr. Hamidreza Karami. I am sincerely grateful for his support, guidance, knowledge, and advice throughout my study.

I am grateful to Prof. Catalin Teodoriu, Dr. Pejman Kazempoor, Dr. Xingru Wu, and Dr. Satya Putra for serving as members of the Dissertation Committee and for offering their valuable input and constructive ideas.

This research project would not have been possible without the assistance of Jeff McCaskill's research equipment specialist at the Well Construction Technology Center (WCTC). I would like to extend my thanks to my friend Camilo Mateus-Rubiano for his support and help in the data acquisition and processing part of this study.

I would like to express my profound gratitude to Kuwait University for providing me with a scholarship to continue my graduate studies at The University of Oklahoma.

And last but not least, I would like to express my greatest love and gratitude to my father, Haithem Alsanea, my mother, Haifa Aldughaishim, and my siblings for their endless support, love and prayer. Also, I am deeply grateful to my wife, Dalal Alsaad, for

understanding, patience, prayers and continuous encouragement, which was a source of strength and a key to success. Our daily exchanges made the long distance between us short. Without my family this study would not have been possible. I ask God to bless them with good health and to keep us united in this life and hereafter. I hope this work makes all of them proud, especially my mother.

ABSTRACT

Maziad Alsanea (Doctor of Philosophy in Petroleum Engineering)

Effects of Restrictions and Liquid Properties on Liquid Loading in Natural Gas Wells

Directed by Dr. Hamidreza Karami

218 pp., Chapter 7: Conclusions and Recommendations

(458 words)

Liquid loading is one of the main challenges in the later life of a natural gas well. Several methods have been used to unload the gas wells and remedy liquid loading, with various efficiencies. The literature revealed a lack of two-phase flow experimental data under low liquid loading conditions. Furthermore, studies on the effect of restrictions used a limited number of water-air experimental data in the churn flow region. Intensive experimental tests were carried out in this study to address this gap in the literature and to better understand the effects of restrictions and liquid properties on two-phase flow and liquid loading in vertical pipes. Common available models, namely OLGA and Tulsa University Fluid Flow Project (TUFFP) unified models, provided inadequate predictions for pressure drop and liquid holdup in the churn region. Therefore, a mechanistic model was developed to better predict the pressure drop and liquid holdup in the churn region.

A total of 377 data points was collected in a state-of-the-art 0.0508-m ID vertical flow loop. Two liquids, namely, water and mineral oil were used with air as the gas phase. Tests were conducted without and with ring-shaped partial restrictions, with two IDs of 1.5 and 1.75 in. The superficial liquid and gas velocities were varied from 0.0033 to 0.02

m/s and from 1 to 27.5 m/s, respectively, to cover annular and churn flow patterns. Flow pattern, pressure drop, and liquid holdup were measured and analyzed.

The investigation revealed that for low liquid rates in vertical flow, a positive friction gradient can exist. Compared to the minimum-pressure drop technique, the positive frictional pressure technique offers considerably more reliable predictions for the onset liquid loading. The experimental results showed the differences in flow behavior of water-air and oil-air flows become more pronounced in the churn flow region, with lower holdup and pressure drop for oil-air flow, possibly due to the higher entrainment.

The tests with insert in the churn region showed a thin layer of liquid film reversing with entrained droplets travelling upward before the insert. After the insert mixing and agitation occurred generating high-amplitude liquid waves and preventing liquid fallback. The insert has a positive impact at lowering the liquid holdup and pressure drop within the churn flow region, particularly at lower liquid rates.

A 1-D mechanistic model was developed for vertical flow based on momentum and mass balances to predict the pressure drop and liquid holdup of two-phase flow by considering the effect of liquid entrainment in the gas core. In addition, a model was developed to predict the interfacial friction factor f_i, based on the calculated f_i from the experimental data. The proposed mechanistic model with the developed model for f_i showed better performance than existing models especially for low liquid rates and oil-air flow.

CHAPTER 1

Introduction

Liquid loading is a common issue for natural gas wells, especially in the later stages of their lives. When the gas velocity is high enough in a vertical well, annular or mist flow exists, where the liquids are transported to the surface and no accumulation occurs. In an annular flow pattern, the liquid is transported as a liquid film around the inner pipe wall and as dispersed droplets in the gas, both flowing continuously upward. As a natural gas well matures, the reservoir pressure decreases, leading to a decrease in gas velocity, which reduces the ability of gas to transport the liquid to the surface. The associated liquids are condensates and/or produced water. If the liquid is not removed continuously, pressure builds up in the wellbore, resulting in intermittent flow, lowering production, and eventually killing the well.

Many mechanisms have been introduced as the liquid loading initiation criteria with varying levels of significance. Most known models predict the onset of liquid loading by observing liquid droplet or film reversal. Droplet models are used widely in the oil industry due to their simplicity and acceptable results. However, experimental studies report that the onset of liquid loading is due to the liquid film reversal.

Many methods have been used to unload the gas wells and remedy liquid loading, such as tubing sizing, gas lift, wellhead compression, plunger lift, foam lift and pumping systems. A small number of studies on the effect of partial restrictions (inserts) revealed

that the inserts function as liquid lifting devices. The literature shows that there is a favorable region in churn flow, where the inserts improve the liquid lifting and delay the onset of liquid loading. If the inserts are installed outside this range, the liquid lifting efficiency will reduce. However, the study of the effect of restrictions on liquid loading is a relatively new topic.

According to Meng (1999), low liquid loading is defined as a flow condition at which the volumetric ratio of liquid to gas at standard conditions is less than 1100 $m^3/MMsm^3$ (200 STB/MMSCF). Such low ratios are prevalent in natural gas wells, where the gas rate is much higher than the liquid rate. Most experimental studies about low liquid loading correspond to horizontal or near-horizontal pipes. Only a limited number of studies analyze low liquid loading in vertical wells. The previous studies demonstrate that for a lower surface tension fluid, liquid entrainment increases with smaller droplet sizes and less droplet deposition to the film. This can potentially amplify the positive effects of adding inserts.

1.1 Objectives

The main objectives of this study are:

- Evaluate the effects of the inserts on two-phase flow in vertical tubes under the low liquid loading conditions.
- Study the effects of liquid properties on two-phase flow and liquid loading.
- Develop a model to better predict the two-phase behavior in vertical tubes, especially in the churn flow region.

1.2 Work Scope

The objective of this work is to experimentally and theoretically study the effects of restrictions and liquid properties on two-phase flow in vertical pipes. For this purpose, a state-of-the-art experimental facility was built specifically for two-phase flow testing in vertical tubulars. Experiments were conducted in a 0.0508-m (2-in.) ID vertical test section with a total length of 7.6 m. The two-phase flow tests are conducted using air as the gas and water or Iso-Par L oil as the liquid phase. To investigate the effect of inserts, three inserts were installed along the test section, with 1.85 m distance between consecutive inserts. The tests were carried out with and without inserts with two ID's of 1.5 and 1.75-in. The superficial liquid and gas velocities were varied from 0.0033 to 0.02 m/s and from 1 to 27.5 m/s, respectively, to cover annular and churn flow patterns. This study measured and analyzed flow pattern, pressure drop, and liquid holdup.

The performances of the existing models to predict pressure drop, liquid holdup, and flow pattern were evaluated against the acquired experimental data. A 1-D mechanistic model was developed for vertical flow to predict pressure drop and liquid holdup. In addition, a closure model for interfacial shear stress was developed for two-phase annular and churn flow. The experimental data were compared to the developed mechanistic model with various interfacial shear stress closures and some commercially available models.

1.3 Outline

In this dissertation, relevant studies in the literature are reviewed in Chapter 2. Chapter 3 provides details on the experimental facility design, instrumentation, test fluids, experimental procedure, data acquisition, and the test matrix. Experimental results for water-air and oil-air flow without inserts, and their respective modeling evaluations are presented in Chapter 4. In Chapter 5, Experimental results for water-air and oil-air flow with inserts are reported, and the effects of the inserts are investigated. Chapter 6 presents the modeling efforts, describing the developed mechanistic model and the interfacial friction factor closure. Lastly, the conclusions of this study and some recommendations for future studies are presented in Chapter 7.

CHAPTER 2

Literature Review

Two-phase flow commonly refers to gas and liquid flow. It occurs in various major industries such as petroleum, nuclear, chemical, space, and geothermal industries and other engineering applications. It is necessary to understand two-phase flow better due to its importance and widespread application. Extensive research began to be conducted on it from the late 1940's.

In the petroleum industry, two-phase flow occurs during the production and transportation of oil and gas from the bottom of the wellbore to the processing facility. The flow may occur at various angles classified as horizontal, inclined, or vertical. Design parameters such as pressure drop, liquid holdup, and pipe sizes are considered to optimize the production and ensure flow along all lines. In the nuclear industry, two-phase flow is mainly used for safety purposes to cool the nuclear core in emergencies; hence, studying flow behavior under extreme conditions is vital. Moreover, the space industry uses zero-gravity flow, which is a special form of two-phase flow occurring in space. In zero-gravity flow, the inclination angle concept is not applicable, and the flow is independent of the inclination angle. Non-zero gravity two-phase flow exists in power generation, energy storage, thermal management, and life support system in space-related vehicles.

The following sections involve the understanding of two-phase flow models, mainly in a vertical pipe. Additionally, liquid loading and two related aspects, namely, liquid loading initiation and the effect of liquid properties are presented. Accordingly, the most relevant studies in these areas are presented in this chapter.

2.1 Two-Phase Flow Fundamentals

Single-phase and two-phase flows can be differentiated by the existence of flow patterns in two-phase flow. Flow pattern refers to the geometric distribution of the gas and liquid phases inside the pipe when they flow simultaneously (see Figure 2-1). The main controlling parameters of flow patterns are gas and liquid flow rates, inclination angle, pipe diameter, and fluid densities. Additionally, less controlling parameters include viscosities, surface tension, pipe roughness, and local geometry change.

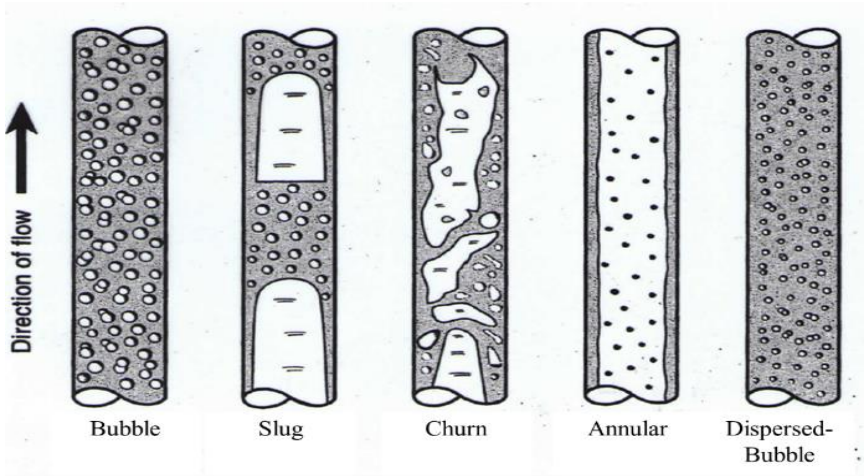

Figure 2-1: Flow patterns in a vertical pipe from (Shoham et al., 2006)

Various experimental and theoretical models centered on two-phase flow have been published, especially in the petroleum and nuclear industries. The two main modeling approaches are empirical correlations and mechanistic models. The empirical approach is to fit a correlating equation to the available experimental data, which has some limitations and shortcomings. Sometimes, it can offer illogical answers. Without dimensional analysis, it can be limited to its own range. Occasionally, it does allow the designer of the system to do the calculations in a straightforward manner without knowing what is physically happening. On the other hand, the analytical approach can be the most accurate. But the complex nature of two-phase flow renders its development impossible.

The mechanistic model, also known as the phenomenological approach, is the intermediate between the empirical and analytical approaches. The physical model is developed based on the conservation of mass, momentum, and energy and is used for prediction and design purposes. Closure relationships are used in some parts , when it is impossible to develop a physical model. The experimental measurements are performed to check the accuracy of the physical model, and it is readjusted accordingly. The model requires the prediction of flow patterns to model two-phase flow in pipes. Hence, the first step is to predict the flow pattern; then a separate model is developed, which predicts the hydrodynamics (pressure gradient and liquid holdup) and phase heat-transfer coefficient for each flow pattern.

Mechanistic modelling is considered more general and reliable than the empirical correlations for different flow conditions. This is because it includes the flow mechanism

at varying flow parameters such as pipe diameters, inclination angles, liquid and gas flow rates, and liquid and gas properties. It is called a comprehensive mechanistic model when it can predict the flow behavior for all flow patterns. If the comprehensive model predicts the flow patterns for all inclination angles, it is called a unified model.

In the following sections, a summary of well-known two-phase flow models is provided starting from early developed models. Then, the common empirical models are described. Moreover, mechanistic models are described, followed by a revision of the unified models for two-phase flow.

2.1.1 Early Models

Lockhart and Martinelli (1949) were among the first to attempt to model two-phase flow. In their correlation, the frictional pressure drop is calculated based on the separated-phases flow approach. Then, due to the complex conditions and the number of variables in two-phase flow, it was reasonable to consider the separated-phases flow model as the first attempt to correlate two-phase flow. This correlation was a result of experimental data gathered from horizontal pipes with small diameters of 0.15 to 2.5 cm (0.586–1.017 in). Four types of liquid were used, namely, benzene, kerosene, water, and various oils, with air as the gas phase. In this correlation, four types of flow mechanisms between liquid and gas were demonstrated to determine whether each phase is turbulent or viscous (laminar) flow with the other phase. Two parameters of dimensionless groups were introduced for gases and liquids. The parameters were ϕ_G and ϕ_L for gas and liquid,

respectively. They are the function of the ratio of weight rates, densities, and viscosities of each phase and pipe diameter. Parameters ϕ_L and ϕ_G were defined as the ratio of frictional pressure drop of each single phase in a two-phase flow over the frictional pressure drop when each phase flowed alone (fluid superficial pressure). Equation (2-1) presents the ratio of the parameter ϕ_G over ϕ_L:

$$\frac{\phi_G}{\phi_L} = \sqrt{\frac{-\frac{dp}{dL}\Big)_{Gas} / -\frac{dp}{dL}\Big)_{SG}}{-\frac{dp}{dL}\Big)_{Liquid} / -\frac{dp}{dL}\Big)_{SL}}} \tag{2-1}$$

The pressure drop was correlated by a newly developed parameter *X*, which equals the square root of the ratio of the pressure drop of the liquid superficial pressure to the pressure drop of the gas superficial pressure. The gas and liquid phases were assumed to have equal pressure gradients. Resultantly, Equation (2-2) shows the relation of the *X* parameter to ϕ_G and ϕ_L :

$$X = \sqrt{\frac{-\frac{dp}{dL}\Big)_{SL}}{-\frac{dp}{dL}\Big)_{SG}}} = \frac{\phi_G}{\phi_L} = \frac{b^{(m-2)/2}\left(\frac{d}{d_G}\right)^{(5-m)/2}}{a^{(n-2)/2}\left(\frac{d}{d_L}\right)^{(5-n)/2}} \tag{2-2}$$

By squaring the parameter *X* from Equation (2-2) and using Fanning friction factor, a single-phase equation was developed, as specified below:

$$X^2 = \frac{-\frac{dp}{dL}\Big)_{SL}}{-\frac{dp}{dL}\Big)_{SG}} = \frac{\frac{4C_L}{d}\left(\frac{\rho_L v_{SL} d}{\mu_L}\right)^{-n} \frac{\rho_L {v_{SL}}^2}{2}}{\frac{4C_G}{d}\left(\frac{\rho_G v_{SG} d}{\mu_G}\right)^{-m} \frac{\rho_G {v_{SG}}^2}{2}} \tag{2-3}$$

where *C*, *n*, and *m* are constants for each flow type. Moreover, a correlation based on the cross-sectional area of the pipe was formed:

$$H_L = a\left(\frac{d_L}{d}\right)^2 = 1 - b\left(\frac{d_G}{d}\right)^2 \quad (2\text{-}4)$$

where *a* and *b* are the ratios of the actual cross-sectional area of the flow of liquid and gas, respectively, to the area of a circle based on the hydraulic diameter of the phase. Equations (2-1) to (2-4) illustrate that pressure drop and liquid holdup are unique functions of parameter *X* for all four types of flow regimes, as depicted in Figure 2-2. The Lockhart and Martinelli correlation indicates a graphical relation with the parameter *X*.

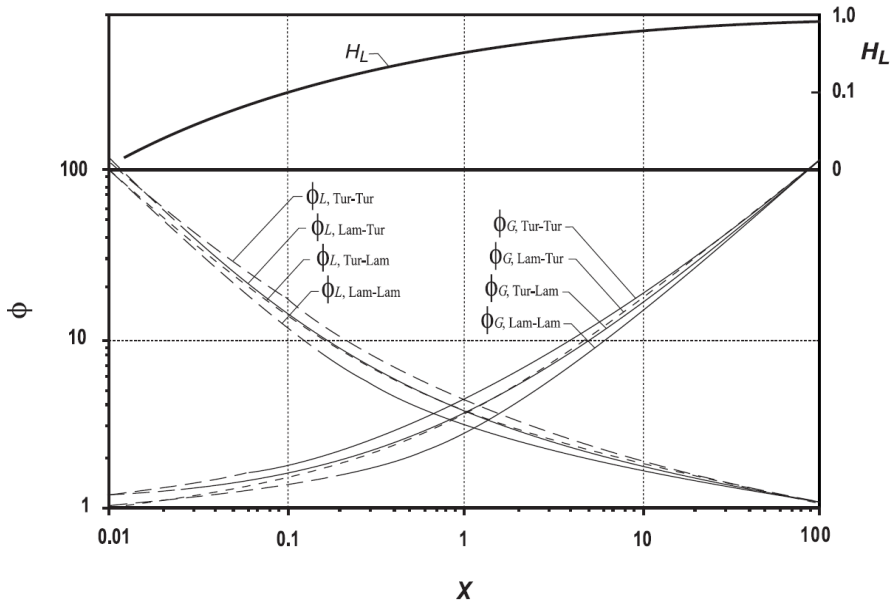

Figure 2-2: Separated model results (Lockhart and Martinelli, 1949) from (Shoham et al., 2006)

Baker (1953) experimentally studied two-phase flow for 4 to 10 in. inner diameter (ID) horizontal pipes with natural gas and oil. Their study showed that the Lockhart and Martinelli correlation is inadequate for large diameter pipes and some flow patterns. The Lockhart and Martinelli correlation was modified for each flow pattern for more accurate results.

Chisholm (1967) modified the Lockhart and Martinelli correlation by adding interfacial shear force between the two phases and developed simple and convenient equations for an engineering application for both pressure drop and liquid holdup. The equations are as follows:

$$\phi_L = 1 + \frac{C}{X} + \frac{1}{X^2} \tag{2-5}$$

$$H_L = 1 - (1 + X^{0.8})^{-0.378} \tag{2-6}$$

where C is constant for four flow types, turbulent-turbulent, laminar-turbulent, turbulent-laminar, and laminar-laminar liquid interactions, which is 20, 12, 10, and 5, respectively.

2.1.2 Empirical Correlations

Poettmann and Carpenter (1952) first attempted to study two-phase vertical flow in wells. Field data were gathered for 34 flowing and 25 continuous gas-lift wells with tubing sizes ranging from 2-3/8 to 3-1/2-in. ID. The produced flow rates and gas–liquid ratios (GLRs) were less than 500 STB/day and 1500 scf/STB, respectively. The measurements taken were surface and bottom hole pressures and flowrates; therefore, a correlation based on frictional pressure drop was developed. This correlation treated the fluid as a homogeneous single fluid with no-slip liquid holdup for mixture density, as liquid holdup was not measured in the gathered data.

Duns and Ros (1963) experimentally studied two-phase vertical flow in a laboratory facility at low pressure with a pipe diameter range of 1-1/4 to 3-1/8-in. ID. The

tests were conducted in 32 ft long pipe by using air, oil, and water as fluid components. The flow pattern map was constructed with three flow patterns, namely, bubble, slug, and mist flow patterns, as shown in Figure 2-3. The dimensionless groups were defined using superficial velocities of gas and liquid in the flow pattern map and expressed as follows:

$$N_{GV} = gas\ velocity\ number = v_{Sg}\sqrt[4]{(\rho_g/g\sigma)} \tag{2-7}$$

$$N_{LV} = liquid\ velocity\ number = v_{Sl}\sqrt[4]{(\rho_L/g\sigma)} \tag{2-8}$$

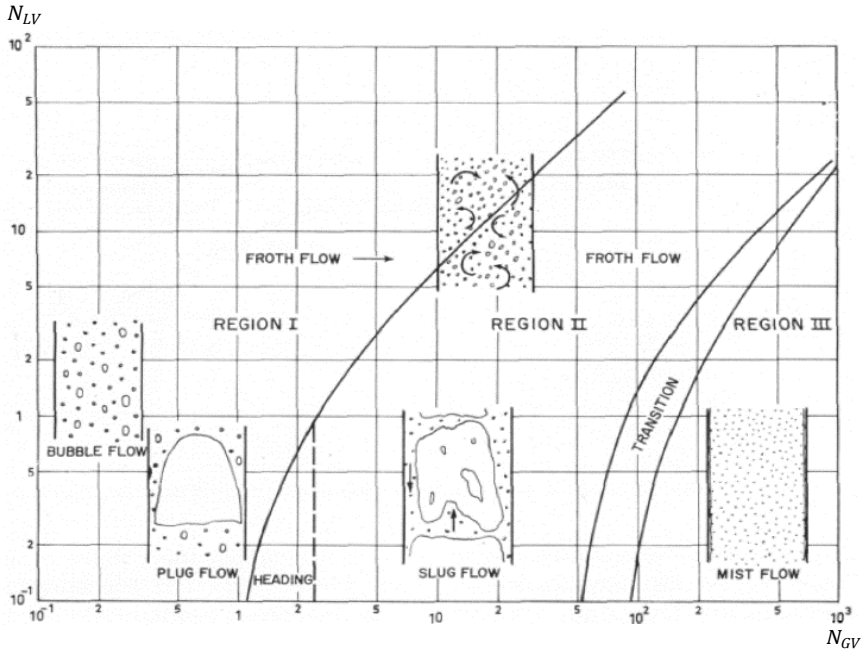

Figure 2-3: Duns and Ros flow pattern map.

Additionally, separate friction factor and liquid holdup correlations were defined for each flow pattern. The liquid holdup was calculated using the following equations:

$$v_S = \frac{v_{Sg}}{1-H_L} - \frac{v_{Sl}}{H_L} \tag{2-9}$$

$$N_S = v_S\sqrt[4]{(\rho_L/g\sigma)} \tag{2-10}$$

where the term N_S was calculated for each flow pattern using different equations. Once calculated, v_S (slip velocity) can be calculated and then substituted in Equation (2-9) to solve the liquid holdup. In region III, slip velocity was considered negligible, making the liquid holdup equal to no-slip liquid holdup, $H_L = \lambda_L$.

The correlation of Hagedorn and Brown (1965) is considered one of the most used correlations in the oil industry due to its accurate predictions and easy implementation compared to other correlations. It was developed from experimental data gathered from a vertical well with 1500 ft depth and a tubing size ranging from 1 to 2 in. ID. Various liquid and gas rates were included. The effects of liquid viscosity were studied by using oil and water in the liquid phase with various oil viscosities of 10, 35, and 110 cp.

The correlation considers the slippage between gas and liquid phases. Pressure drop was measured, but neither liquid holdup nor flow pattern were measured directly in this study. Liquid holdup was back-calculated from the pressure drop using the two-phase Moody's friction factor, which can be obtained from Reynolds number. In their first step in the model, liquid holdup was used to help calculate the viscosity term in Reynolds number. Then, the frictional pressure drop is calculated using the assumed liquid holdup. Subsequently, gravitational pressure drop is calculated using the following equation:

$$\frac{dp}{dL}\Big)_G = \frac{dp}{dL}\Big)_{measured} - \frac{dp}{dL}\Big)_{friction} - \frac{dp}{dL}\Big)_{acceleration} \quad (2\text{-}11)$$

Liquid holdup was calculated from the gravitational pressure drop term and compared to the assumed one. The procedure was continued until convergence was obtained between the assumed and calculated liquid holdup. The correlation uses the

same dimensionless numbers of Duns and Ros to correlate liquid holdup; see Equations (2-7) and (2-8).

Orkiszewski (1967) developed a correlation for bubble and slug flow patterns based on 148 measured well conditions with Hagedorn and Brown's data. The study recommended the use of the Duns and Ros method for the mist flow pattern. Furthermore, it considered the same flow patterns as Duns and Ros. In the correlation, the liquid distribution coefficient was used instead of liquid holdup. Different equations for the liquid distribution coefficient were used based on whether oil or water are the continuous liquid phase and if the mixture velocity exceeds 10 ft/sec. The Orkiszewski method is widely used because it is easy to computerize and can be applied for a wide range of well conditions. However, in some cases, the mixture velocity can be calculated as less than no-slip velocity, which is inaccurate. In addition, some discontinuities were noticed for pressure calculations at mixture velocities higher than 10 ft/sec.

The Beggs and Brill (1973) correlation was developed from experimental data gathered from a testing flow loop. The test section was 90 ft long, and two pipe diameters were used, 1 and 1-1/2-in. ID with various pipe inclinations. Different parameters were studied: 1) gas flow rate in the range of 0 to 30 Mscf/d, 2) liquid flow rate from 0 to 30 gal/min, 3) average system pressure from 35 to 95 psia, with inclination angles from -90º to +90º. Air and water were used as the fluids, and the experimental data were gathered from 584 measured tests. Although this method is applicable for vertical upward, use in vertical flow was not recommended because of pressure drop underprediction.

Three main horizontal flow patterns were defined, namely, segregated (stratified, wavy, and annular), intermittent (plug and slug), and distributed (bubble and mist). Later, this method was modified for all inclination angles based on the horizontal flow pattern. The horizontal flow pattern was used as a correlation parameter and does not correspond to the actual flow pattern for non- horizontal flow. Liquid holdup and pressure drop were calculated using different equations for each flow type. The Beggs and Brill method is considered the first method to account for all inclination angles, entirely presented in an equation form, making programming their model very simple even for small calculators.

2.1.3 Mechanistic and Unified Models

Aziz et al. (1972) proposed a mechanistic model for two-phase vertical flow. A new flow pattern map was presented for vertical flow as shown in Figure 2-4. New equations were developed for pressure drop of bubble and slug flow patterns using an empirical approach and checked with field data from 48 wells. The Duns and Ros equations were recommended for the annular flow pattern. The model predicts the flow pattern using two dimensionless groups. Based on the predicted flow pattern and mechanical energy balance equations, pressure drop and liquid holdup are calculated. The liquid holdup is calculated based on bubble rise velocity for bubble and slug flow patterns. The difference in the accuracy of this model and Orkiszewski (1967) is negligible.

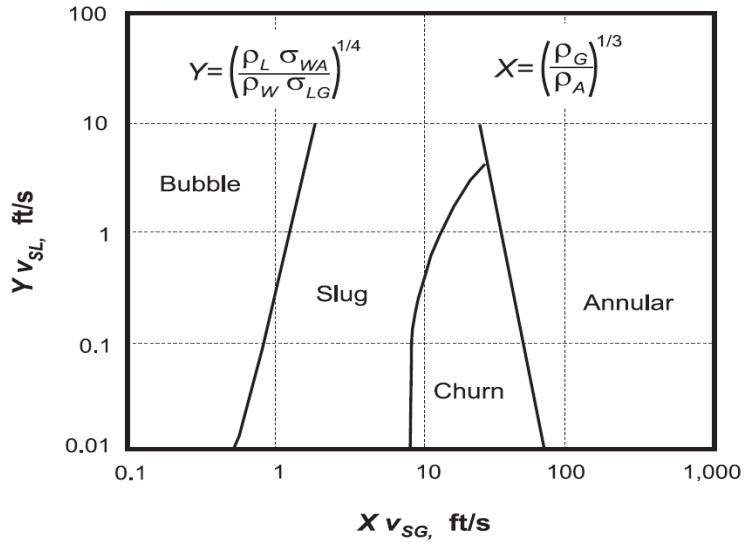

Figure 2-4: Flow pattern map of vertical flow by Aziz et al. (1972) from (Shoham *et al.*, 2006)

A mechanistic model was developed by Hasan and Kabir (1988) to predict flow pattern, pressure drop, and void fraction in vertical wells. Four flow patterns were defined and used in the model, namely, bubbly, slug, churn, and annular, each of which was modeled mechanistically. Taitel et al. (1980) model was used to predict the flow patterns. Turner et al. (1969) model was used to identify the transition from annular to churn. Steen and Wallis (1964) model was used to calculate the liquid entrainment fraction. Beggs and Brill's (1973) water-air data were used to compare with the model. The results showed that their model was superior to Beggs and Brill's model.

Ansari et al. (1994) developed a comprehensive mechanistic model for upward two-phase flow to predict flow pattern, pressure drop, and liquid holdup. Flow pattern predictions were based on Taitel et al. (1980). For bubble, slug, and annular flow patterns, Cateano (1985), Sylvester (1987), and Hewitt and Hall-Taylor (1970) were adopted for

pressure gradient and liquid holdup predictions, respectively. The developed model was evaluated against data from 1775 wells. The model's performance was compared with six empirical correlations, overperforming them with the least average error.

Zhang et al. (2003a and 2003b) developed a unified hydrodynamic model (university of Tulsa fluid flow project (TUFFP) unified model) to predict flow pattern transitions, pressure gradient, liquid holdup, and slug characteristics. The model was developed for all inclination angles of -90º to 90º from horizontal. The flow patterns were categorized into three patterns: Bubble flow including dispersed bubble and bubble flows, intermittent flow including elongated bubble, slug, and churn flows, and stratified and annular flows combined in one group. The model is based on the dynamics of slug flow. For all flow patterns, the transition boundaries are shared with the slug flow. By solving the momentum equations for slug flow, the transition from slug to annular (or stratified) flow occurs when the liquid film length is infinitely long. The slug flow calculations are used for all two-phase flow patterns instead of using a different model for each pattern. The model was validated with experimental data at different pipe diameters, inclination angles, fluid physical properties, gas-liquid flow rates, and flow patterns. The model prediction showed good agreement with the experimental data.

2.1.4 Closure Relationships

As previously mentioned, the complexity of two-phase flow makes it impossible to develop fully physical models. Therefore, closure relationships are required for

complex parts, where developing a physical model is impossible. Entrainment fraction and interfacial shear stress are two closure relationships that are crucial to this study's model development. The following sections overview these closure relationships.

2.1.4.1 Entrainment Fraction

The ratio of the mass rate of the entrained liquid droplets in the gas core to the total liquid mass rate is known as the entrainment fraction. The value of the entrainment fraction is therefore constrained to the range of 0-1. Both annular and churn flows require an understanding of the behavior of liquid entrainment. Due to the complexity of churn flow, most entrainment fraction models are developed based on annular flow. It may also be because early studies on two-phase flow did not distinguish the churn flow pattern as a distinct flow pattern. Even now, a few commercially available models classify both slug and churn flow patterns as intermittent flow pattern.

In annular and churn flow, the interface between the gas core and liquid film is primarily responsible for entrainment. The two primary types of surface disturbances are normally considered: ripples and disturbance waves. The amplitude, velocity, and lifetime of ripple waves are all low. Roll waves, also known as disturbance waves, are sporadic and can move faster than the liquid film itself. When compared to the typical liquid film thickness, their amplitude can be larger. Furthermore, as disturbance waves can travel across a large axial distance, they facilitate the movement of liquid mass in the direction of flow, as shown in Figure 2-5.

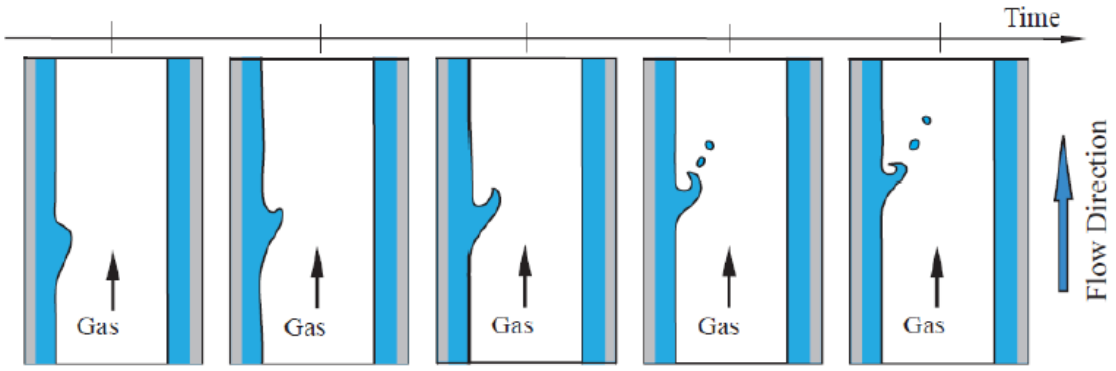

Figure 2-5:Droplet entrainment generation from disturbance waves (Thome and Cioncolini 2015)

Paleev and Filippovich (1966) method for entrainment fraction was modified by Wallis (1969). Wallis proposed the following empirical correlation by replacing the liquid viscosity, and core density with the gas viscosity and gas density. This correlation was developed using two-phase flows of silicon and water in a vertical tube with a diameter of 0.0159 m at operating pressures close to atmospheric.

$$F_E = 1 - exp\left[-0.125\left(10^4 \frac{\mu_G v_{Sg}}{\sigma_L}\sqrt{\frac{\rho_G}{\rho_L} - 1.5}\right)\right]. \quad (2\text{-}12)$$

Oliemans et al. (1986) used regression analysis to develop a correlation using the HARWELL data bank. The data bank has 728 data points for vertical flow with four distinct fluids (water-steam, water-air, genklene-air, and ethanol-air) with a pressure range of 0.1-9 MPa and a pipe ID range of 0.006 to 0.0318 m.

$$\frac{F_E}{1-F_E} = 10^{\beta_0}\rho_L{}^{\beta_1}\rho_G{}^{\beta_2}\mu_L{}^{\beta_3}\mu_G{}^{\beta_4}\sigma^{\beta_5}d^{\beta_6}v_{SL}{}^{\beta_7}v_{Sg}{}^{\beta_8}g^{\beta_9} \quad (2\text{-}13)$$

Table 2-1: Parameters of Oliemans et al. (1986) correlation

β_0	β_1	β_2	β_3	β_4	β_5	β_6	β_7	β_8	β_9
-2.52	1.08	0.18	0.27	0.28	-1.8	1.72	0.7	1.44	0.46

Ishii and Mishima (1989) developed a correlation for vertical annular flow using a modified gas Weber number and superficial liquid Reynolds number. The equations are as follows:

$$We' = \frac{\rho_G v_G^2 d_F}{\sigma}\left(\frac{\rho_L - \rho_G}{\rho_G}\right)^{\frac{1}{3}} \tag{2-14}$$

$$F_E = tanh\left[7.25\ X\ 10^{-7}(We')^{1.25} Re_{SL}^{0.25}\right] \tag{2-15}$$

Azzopardi and Wren (2004) created a simple correlation based on water-air data at pressures ranging from 0.1 to 0.3 MPa and pipe IDs varying from 0.024 to 0.05 m. They found little trend with superficial gas velocity greater than 5 m/s and no effect of pipe ID. At all superficial gas velocities, particularly those less than 5 m/s, a significant trend with superficial liquid velocities was seen. The correlation is as follows:

$$F_E = 0.47\ {v_{Sg}}^{0.16} {v_{SL}}^{0.35}, \quad for\ v_{Sg} < 5\ m/s \tag{2-16}$$

$$F_E = 0.6 {v_{SL}}^{0.35}, \quad for\ v_{Sg} > 5\ m/s \tag{2-17}$$

A correlation was created by Pan and Hanaratty (2002) based on the equilibrium of droplet atomization and deposition in vertical flow. The correlation was created using experimental data for v_{SL} between 0.012 and 1.35 m/s and v_{Sg} between 20 and 119 m/s. The following equation provides the correlation:

$$\frac{{}^{F_E}/_{F_{E,max}}}{1-{}^{F_E}/_{F_{E,max}}} = 6\ X\ 10^{-5}\left[\frac{(v_G - v_{G,cr})^2 d\sqrt{\rho_L \rho_G}}{\sigma_L}\right], \tag{2-18}$$

where the following definition is used for critical velocity at onset of entrainment $v_{G,cr}$:

$$v_{G,cr} = 40\sqrt{\frac{\sigma_L}{d\sqrt{\rho_L \rho_G}}}, \tag{2-19}$$

and the maximum entrainment is defined as in the following equation:

$$F_{E,max} = 1 - \frac{W_{F,cr}}{W_L}. \tag{2-20}$$

From the correlation by Anderussi et al. (1985), the critical liquid film flow $W_{F,cr}$ is determined as depicted by the following equation:

$$W_{F,cr} = 0.25\ \mu_L \pi d\ Re_{F,cr}, \tag{2-21}$$

where:

$$Re_{F,cr} = 7.3\ (log\omega)^3 + 44.2\ (log\omega)^2 - 263\ (log\omega) + 439, \tag{2-22}$$

and:

$$\omega = \frac{\mu_L}{\mu_G}\sqrt{\frac{\rho_G}{\rho_L}}. \tag{2-23}$$

Similar to the method used by Ishii and Mishima (1989), Sawant et al. (2008) created a correlation for the entrainment fraction based on Weber number and liquid Reynolds number. Experimental data for high flow and pressure circumstances were used to confirm the correlation. The pipe ID was 0.0094 m, the pressure range was 0.12 to 0.6 MPa, and the v_{Sg} ranged from 15 to 100 m/s. The correlation is:

$$F_E = F_{E,max}\ tanh\ (\alpha\ We_{SG}^{1.25}), \tag{2-24}$$

where

$$F_{E,max} = 1 - \frac{Re_{F,lim}}{Re_{SL}}, \tag{2-25}$$

and

$$Re_{F,lim} = 250\, ln(Re_{SL}) - 1265, \tag{2-26}$$

$$\alpha = (2.31\ X\ 10^{-4})\ {Re_{SL}}^{-0.35}\ . \tag{2-27}$$

2.1.4.2 Interfacial shear stress

The interface between the gas core and the liquid film is crucial to comprehending the behavior of annular and churn flows. As the flow pattern changes to churn, large liquid waves are observed. Interfacial shear stress models for churn flow are therefore crucial for the development of churn flow models for better predictions. Many attempts were performed to correlate the interfacial friction factor (f_i) which is the complex part of the interfacial shear stress, The interfacial shear stress is defined as:

$$\tau_I = \frac{1}{2} f_I \rho v^2, \tag{2-28}$$

where ρ and v are the density and the velocity, most studies use the gas density and velocity for interfacial shear stress calculations. The gas core density and relative velocity between the gas core and liquid film are used for this study, as demonstrated in Equation 6-32.

Wallis (1969) developed a correlation for the interfacial friction factor based on the dimensionless liquid film thickness ($\frac{\delta_L}{d}$). Considering the roughness brought on by the

film's wave structure, the interfacial shear stress rises as the film thickness increases due to larger waves. The correlation is described as follows:

$$f_i=0.005(1+300\,\frac{\delta_L}{d}) \tag{2-29}$$

Fukano and Furukawa (1998) developed a correlation to account for the effect of liquid viscosity on the dimensionless film thickness ($\frac{\delta_L}{d}$). The data was gathered in 0.026 m pipe ID with water-air and glycerol-air mixtures. The developed correlation has a power of 8, instead of 1 used by Wallis (1969). The reason given is that the power of 8 can fit the sharp increase at high ($\frac{\delta_L}{d}$). The following equation provides the correlation:

$$f_i = 0.425(12 + \frac{\eta_L}{\eta_W})^{-1.33}\left[1 + 12\,\frac{\delta_L}{d}\right]^8, \tag{2-30}$$

where η_L and η_w are the kinematic viscosities of the liquid and water.

Belt et al. (2009) presented a correlation that uses the roughness of single-phase turbulent pipe flows to predict the interfacial shear stress. They assumed that the interfacial friction factor is independent of the Reynolds number.

$$f_i = 2(1.158\,\frac{\delta_L}{d} + 3.413\,\times\,10^{-4}) \tag{2-31}$$

Bharathan and Wallis (1983) empirically studied water-air flow at atmospheric pressures and 0.025 to 0.051 m ID vertical pipe. They measured liquid holdup and pressure drop. They correlated the interfacial friction factor in churn region as follows:

$$f_i = 0.005 + 10^{\left(-0.56+\frac{9.07}{d^*}\right)}\left[\frac{d^*(1-\alpha)}{4}\right]^{\left(1.63+\frac{4.74}{d^*}\right)} \tag{2-32}$$

where:

$$d^* = d\sqrt{\frac{(\rho_L - \rho_G)g}{\sigma}} \tag{2-33}$$

Jayanti and Brauner (1994) analyzed the experimental data of Govan et al. (1991) and developed a model for churn flow. They suggested that the interfacial friction factor should be calculated as the average of Bharathan and Wallis (1983), and Wallis (1969) interfacial models for better prediction, as shown by Figure 2-6 . Bharathan and Wallis's model overestimates and Wallis's model underestimates the interfacial friction factor. The following equation shows the Jayanti and Brauner (1994) approach:

$$f_i = 0.5\ (f_{i,B} + f_{i,Wallis}) \tag{2-34}$$

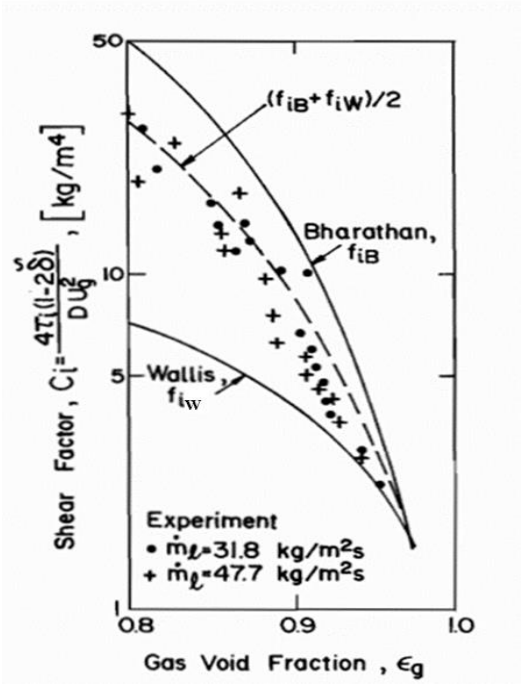

Figure 2-6: Interfacial friction factor in churn flow (Jayanti and Brauner (1994))

2.2 Liquid Loading

Liquid loading is a common issue for natural gas wells, especially in the later stages of their lives. When the gas velocity is high enough in a vertical well, annular or mist flow exists, where the liquids are transported to the surface and no accumulation occurs. In an annular flow pattern, the liquid is transported as a liquid film around the inner pipe wall and as dispersed droplets in the gas, both flowing continuously in the upward direction. As a natural gas well matures, the reservoir pressure decreases, leading to a decrease in gas velocity, which reduces the ability of gas to transport the liquid to the surface. The associated liquids are condensate and/or produced water from the aquifer or frac water. If the liquid is not removed continuously, pressure builds up in the wellbore, resulting in intermittent flow, lowering production, and eventually killing the well.

According to Lea et al. (2003), common symptoms of liquid loading in a well are as follows:

- Presence of pressure spikes in the gas measuring device.
- Erratic production and increase in the production decline rate.
- Decreased tubing pressure as casing pressure increases.
- A sharp, distinct change in pressure gradient on pressure survey.
- Annular heading.
- Cessation of liquid production.

Liquid unloading or deliquification is defined as any approach used to remove the accumulated liquid in a wellbore and increase production. Several methods are commonly

used to minimize the liquid loading in a wellbore. The main methods are velocity strings and artificial lift techniques, such as gas lift, wellhead compression, plunger lift, foam lift and pumping systems. Velocity string is a smaller tubing size used to increase the flow velocity above the velocity at which the liquid loading occurs, known as the “critical velocity.” This is a low-cost and low-maintenance method, but it increases the pressure losses and may decrease the production.

Gas lift is an artificial lift method in which additional gas is injected through valves into the tubing string, reducing the hydrostatic pressure losses. The gas injection rate is set to maintain the flow velocity in the tubing string above the critical velocity. It is a relatively low-cost method; however, it requires a gas source and surface equipment.

Wellhead compression is used to increase the tubing flow velocity by lowering the wellhead pressure. Although it increases production and decreases the abandonment pressure, bottomhole pressure cannot be lowered more. Also, this metod requires the purchase or lease of a high-cost compressor.

In plunger lift, a plunger is installed in the tubing string to lift fluids from the bottom of the wellbore to the surface intermittently. The wellbore is shut in when the plunger is at the bottom of the wellbore to allow the casing pressure to build up. The valve at the surface opens when the shut-in pressure exceeds the surface pressure, letting the plunger lift the liquid from the bottom of the wellbore to the surface. The plunger lift is a low-cost method but with intermittent production.

In foam lift, a surfactant is injected to lower the surface tension and the hydrostatic pressure by creating foam. Thereby, the critical velocity is lowered, which delays liquid loading. The surfactant can be injected continuously or intermittently by using soap sticks. This method may not require downhole modifications in the wellbore, but it requires surface equipment for continuous injection and processing to break the foam.

Pumping systems are used to unload a well when the bottomhole pressure is low and insufficient to flow naturally. A beam pump is an example, which should be used with a downhole separator or be set below the perforation to prevent the gas from entering the system and causing a gas lock. It is reliable and easy to use with no lower production rate limit. Another pump system is the progressive cavity pump (PCP), which is a downhole positive displacement pump operating to transfer the liquid to the surface. PCP has a low cost. However, it requires more maintenance, as it can be damaged by high temperatures. An electric submersible pump (ESP) is a multi-stage centrifugal pump that requires a separator to handle the gas and avoid a gas lock. Although it has a high cost, the ESP performs better than any other pump for high liquid production wells.

In the following sections, studies related to liquid loading initiation, the effects of liquid properties, and the effects of restrictions (like inserts) are presented.

2.2.1 Liquid Loading Initiation

Many studies have attempted to introduce a method for the onset of liquid loading. However, there is no agreement on liquid loading initiation criteria. One of the first

attempts to do so was by Turner et al. (1969). Two models were proposed, namely, liquid droplet removal and liquid film reversal. These models were developed and compared to the field data. The result indicated that the Turner droplet model predicted the onset of liquid loading better. The droplet removal model is one of the most common models used in the oil industry to predict liquid loading, due to its simplicity and acceptable results. In this model, the onset of liquid loading is determined by applying a force balance on a liquid droplet with a maximum diameter as shown in Figure 2-7. The droplet is assumed to be spherical and in a turbulent flow. The maximum droplet diameter is determined by using the critical Weber number, which is the ratio of inertial and surface tension forces. Hinze (1955) experimentally showed that the droplets would shatter at Weber numbers in the order of 20 to 30. The maximum droplet diameter was determined by Turner et al. (1969) using the following equation and assuming a critical Weber number of 30:

$$d_D = \frac{W_e \boldsymbol{\sigma}}{\rho_g v^2{}_g}. \qquad (2\text{-}35)$$

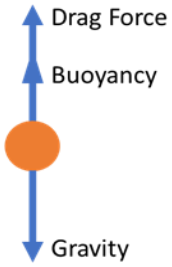

Figure 2-7 : Force balance on a liquid droplet

The minimum gas rate to avoid loading is the rate at which the drag and buoyancy forces equal the gravitational force, and its corresponding gas velocity is called the

terminal velocity. Turner et al. recommended a 20% upward adjustment in velocity to better fit the data. The resulting terminal velocity is expressed in the following equation:

$$v_{Sg,c}(m/s) = 3.72\left(\frac{\rho_L-\rho_g}{\rho_g^2}g\sigma\right)^{\frac{1}{4}}. \quad (2\text{-}36)$$

For Turner's liquid film reversal model, a characteristic velocity has to be used. The critical gas velocity is defined as the minimum gas rate required to move the film in an upward direction.

Coleman et al. (1991), compared Turner et al.'s (1969) model to low wellhead pressure field data. They demonstrated that the 20% adjustment was unnecessary and suggested to use Equation (2-37), as shown in the following:

$$v_{Sg,c}(m/s) = 3.1\left(\frac{\rho_L-\rho_g}{\rho_g^2}g\sigma\right)^{\frac{1}{4}}. \quad (2\text{-}37)$$

Li et al. (2002) modified the droplet shape to a flat shape. They stated that the deformation occurs due to the pressure difference, adjusting the droplet shape to a convex bean shape. As a result, the drag coefficient changes from 0.44 to 1, decreasing the critical gas velocity expression as specified below:

$$v_{Sg,c}(m/s) = 1.41\left(\frac{\rho_L-\rho_g}{\rho_g^2}g\sigma\right)^{\frac{1}{4}}. \quad (2\text{-}38)$$

Wang and Liu (2007) claimed that the droplets are disk shaped based on Reynold number. The drag coefficient for the proposed shape is 1.17. With this modification, the critical velocity expression is altered, as specified below:

$$v_{Sg,c}(m/s) = 1.014\left(\frac{\rho_L - \rho_g}{\rho_g^2} g\sigma\right)^{\frac{1}{4}}. \quad (2\text{-}39)$$

Belfroid et al. (2008) modified Turner et al.'s (1969) model to include the effect of inclination angle. They claimed that the deviation angle considerably impacts the critical gas velocity. Their model was validated with 20 deviated wells. It was found that the critical gas velocity is maximized at a deviation angle of approximately 40°, the equation of which is given as:

$$v_{Sg,c}(m/s) = 3.1 * Area * \sqrt{\rho_g}\left((\rho_L - \rho_g) g\sigma\right)^{\frac{1}{4}} \frac{(sin(1.7\beta))^{0.38}}{0.74}. \quad (2\text{-}40)$$

Liquid film movement in an annular flow pattern was first considered in an experimental study by Hewitt et al. (1970). In their experiments, gas flowed up in a vertical test section with liquid injected upstream. Both gas and liquid were extracted at the bottom of the test section to prevent liquid build-up. At a low gas rate, the gas flowed counter-current to the liquid film, resulting in smooth liquid extraction at the base of the pipe. When the gas rates were increased gradually, a point was reached, as shown in Figure 2-8b, where large waves were formed. At this point, liquid droplets were created from the interfacial waves, and liquid was carried above the injection point. A region was then entered when the liquid oscillated in a climbing and falling manner. This transition region is known as "flooding". On the other hand, at high gas rates with co-current upward flow, with a gradual reduction in gas rate, the liquid film close to the pipe wall started to creep down with droplets flowing upward. This transition point is defined as "film reversal", as demonstrated in Figure 2-8g.

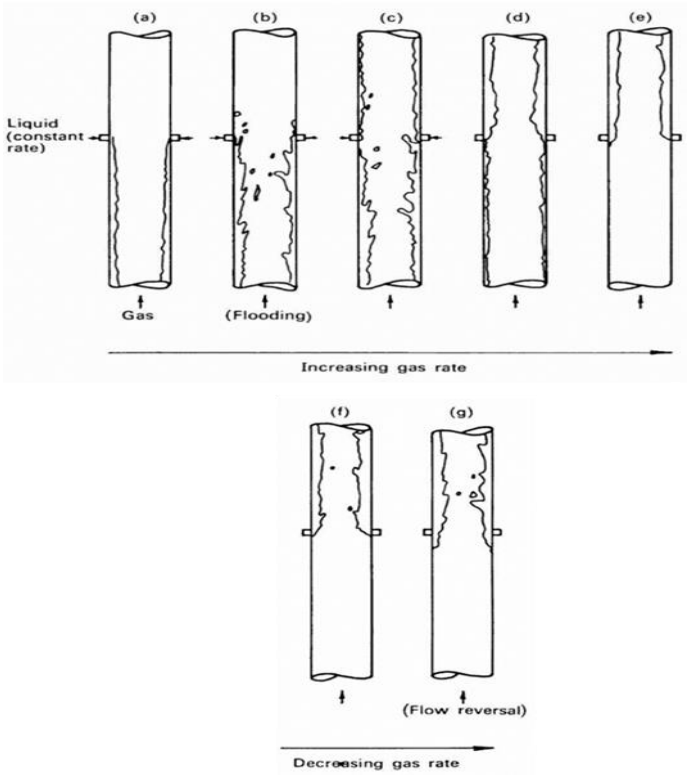

Figure 2-8: Flooding and film reversal from Hewitt et al. (1970).

Barnea (1987) developed a unified model for transition from annular to intermittent flow pattern. Two criteria were developed to determine this transition, namely, liquid film instability and liquid bridging (also known as liquid wave growth). The liquid film instability model is mainly considered for low liquid flow rates when the liquid film is too thin for complete film bridging to occur. The liquid film near the wall partially flows downward, blocking the entrance and initiating the intermittent flow pattern. Furthermore, Barnea indicated that liquid instability should correspond to the minimum interfacial shear stress at low liquid rates. At a gas rate equal to or lower than the critical gas rate, the liquid film flows downward, blocking the inlet, as shown in Figure 2-9a. In this condition, the flow is considered unstable and liquid loading will occur. The

liquid film bridging occurs when the film is sufficiently thick to provide a liquid bridge across the pipe; see Figure 2-9b. According to Barnea, the liquid film bridging begins for maximum cubic bubble packing with holdups greater than 0.24. More details on Barnea's (1987) model can be found in Chapter 6.

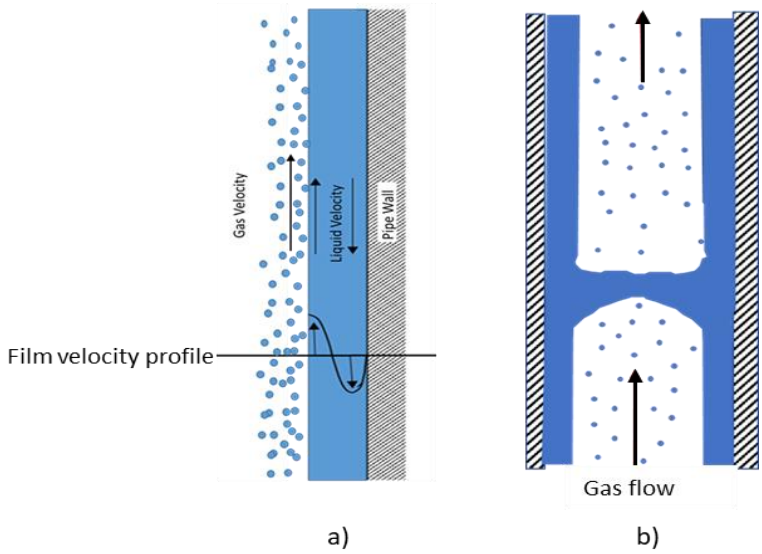

Figure 2-9: Barnea transition criteria: a) film instability, b) film bridging

An experimental study on film reversal in upward annular flow was conducted by Zabaras et al. (1986). For a given liquid rate, the wall shear stress approached zero around the gas rate that resulted in minimum pressure drop ($v_{Sg,\min}$). As the gas rate decreased ($v_{Sg} < v_{Sg,\,\min}$), the wall shear stress fluctuations amplified with a negative mean value (upward). The switching mechanism of the wall shear stress from a positive value (downward) ($v_{Sg} > v_{Sg,\min}$) to a negative value (upward) indicated the change in the film's movement direction for $v_{Sg} < v_{Sg,,\min}$ and the initiation of liquid loading. Figure 2-10 demonstrates Zabaras et al.'s wall shear stress switching mechanism.

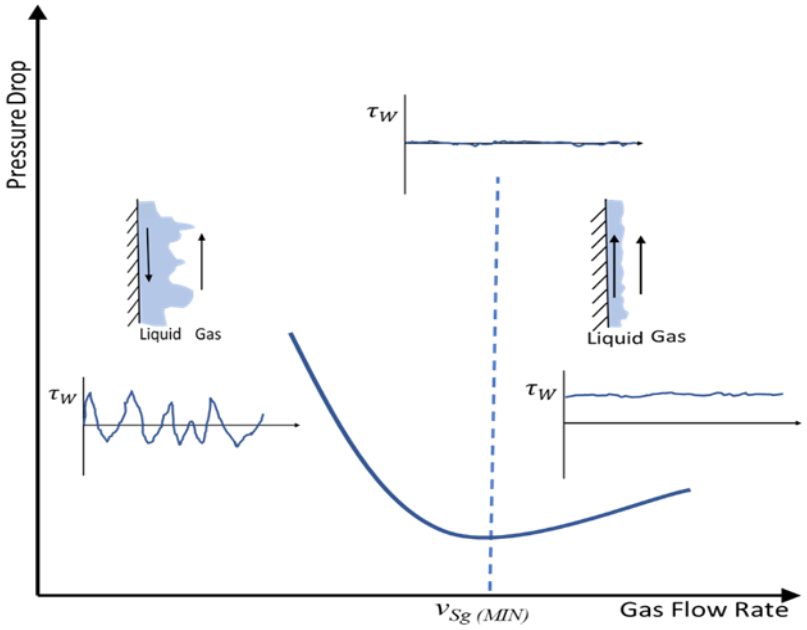

Figure 2-10 : Switching mechanism of wall shear stress as suggested by Zabaras et al. (1986)

Skopich et al. (2015) experimentally studied the effect of pipe diameter on liquid loading in vertical gas wells. A new liquid loading criterion was used to detect the onset point based on the inflection point of the liquid holdup versus v_{Sg} curve. The results indicated that the v_{Sg} at which the inflection point occurs is close to the velocity of the minimum pressure drop. They concluded that the v_{Sg} at the minimum pressure drop can be used as the onset of liquid loading.

Westende et al. (2008) experimentally investigated the transition from annular to churn flow pattern. They observed that liquid droplets always move co-current with the gas core, concluding that the mechanism behind the initiation of liquid loading is liquid film reversal, not droplet fallback. However, droplets could indirectly impact film reversal by affecting the film's thickness distribution.

2.2.2 Effects of Liquid Properties

Barnea et al. (1983) presented new data on flow pattern transition for water-air two-phase flow in horizontal and vertical small tubes of 0.004 to 0.012 m (0.16 to 0.48 in.) ID. They compared the experimental data with those of Taitel and Dukler (1976) for horizontal and Taitel et al. (1980) for vertical flow. The Taitel and Dukler's model was modified by considering the surface tension, to improve the model for stratified to non-stratified transition of horizontal flow. Taitel et al.'s model showed good agreement with the experimental data for annular-churn transition. This could be because of the use of Turner (1969), which considered the surface tension in the transition model. This emphasizes the importance of integrating liquid properties, in this case surface tension, to improve two-phase model predictions, as two-phase flow behavior is a strong dependence of liquid properties.

Alruhaimani (2015) studied the effect of viscosity on two-phase flow in a vertical 0.0508 m (2 in) ID pipe. The results showed that as the viscosity increases, the pressure drop and liquid holdup increase. In addition, he compared Barnea (1987) and TUFFP unified models with the experimental data. The results showed that the models are overpredicting the v_{Sg} of the annular-intermittent flow pattern transition.

Jepson et al. (1990) studied the effect of surface tension on annular flow behavior. An experimental study using a small pipe (0.4 in. diameter) and various fluids revealed that as the surface tension reduces, liquid entrainment increases, droplet size decreases,

and the droplets' deposition (from the gas core to the liquid film) reduces. Whalley and Jepson (1994) also studied the entrained liquid fraction, droplet size, and deposition mass transfer coefficient of droplets. They concluded that the fluid's droplet size reduces with low values of deposition mass transfer coefficient at low surface tensions, despite the high levels of entrained liquid fraction.

2.3 Effects of Restrictions (Inserts) on Liquid Lifting

The study on the effect of restrictions on liquid loading is a relatively new topic, with a limited number of studies. The first researchers to introduce a liquid lifting device or an insert as a restriction to enhance well deliquification were Yamamoto et al. (1999). They mainly focused on the development of an experimental facility. Moreover, they preliminarily investigated the performance of liquid lifting in the presence of inserts. The experiments were conducted at a 1.5-in. ID and 12.2 m (40 ft.) long facility under the unsteady state. Prior to injecting gas, the flow loop was initially filled to a liquid depth of 1-m. in this state. The gas is then injected, and the change in production over time is recorded at the outlet. The flow in this condition is not stable or consistent. Furthermore, the entrance effect was not eliminated.

Four factors that contributed to liquid lifting were studied, namely, gas flow rate, inserts' shape, deviation angle, and the exit connection type. Four gas rates were studied: 20, 25, 30, and 35 scf/min (8, 10, 12.5, and 14.5 m/s). All gas rates were below Turner et al.'s (1969) and Coleman et al.'s critical gas rates. Four different shapes of inserts were

investigated; an open disk with two diameters of 1.125 and 1.375 in., slitted disk, toothed disk, and perforated-folded-toothed disk. Two different deviation angles were used: vertical (0 º) and at 5.3º. Three exit connections were used, namely, the u-tube, dead-end tee, and sharp elbow. The results showed that sharp elbow and dead-end tee performed better, while the u-tube caused a large portion of liquid to impinge on the wall and flow back. Additionally, the inserts enhanced the liquid production, with the open disk shape having the lowest pressure drop.

A comprehensive experimental and modeling study on the effect of inserts was conducted by Putra et al. (2000). The experimental facility of Yamamoto et al. (1999) was used in this study. Water-air steady state tests were conducted, in this state the gas flow rate kept constant by adjusting the inlet pressure regulator. Limited number of tests similar to Yamamoto et al. (1999) unsteady state have been conducted as well. Different aspects of insert design were included, such as the opening and spacing of inserts, effects of gas and liquid flow rates, and performances of different types of inserts. Three different insert openings were implemented in the tests for the open disk shape (orifice), namely, 0.9, 1.125, and 1.325-in. ID. In addition, slitted disk, and open-slitted disk, which is a combination of open and slitted disks with an opening of 0.9-in. and slit diameter of 1.375-in. were tested. One to three inserts were installed and tested along the test section to study the effect of spacing and number of inserts on the liquid lifting. Four liquid rates of 50, 100, 500, and 800 ml/min (0.0007, 0.0015, 0.0075, and 0.0117 m/s) were tested with and without inserts and with various superficial gas velocities from 2 to 12.2 m/s (6.5 to 40 ft/s). The results showed that inserts improved the liquid lifting by two methods:

by generating droplets and by blocking the liquid film from falling. The tests showed a favorable region in which inserts improved the liquid lifting performance. If the inserts are installed outside of this region, they will lower the liquid lifting and cause higher pressure drops. A summary of the tested parameters in Yamamoto et al. and Putra et al. studies is shown in Table 2-2.

Table 2-2: Summary of studies related to insert effect

Study	Flow condition	Gas rates (scf/min)	Insert shape	Deviation angle
Yamamoto et al. (1999).	Unsteady state	20, 25, 30, 35 (8, 10, 12.5, and 14.5 m/s).	• Open disk (1.125-1.375-in. ID) • Slitted disk • Toothed disk • Perforated-folded-toothed disk.	0, 5.3
Putra et al. (2000).	Mostly steady state (some unsteady)	5-60 (2 to 12.2 m/s)	• Open disk (0.9,1.125,1.375-in. ID) • Slitted disk • Slitted-open disk 0.9-in. ID	0

Additionally, Putra et al. (2000) developed a mechanistic model based on Ishii and Mishima's (1984) one-dimensional model by assuming isothermal conditions,

steady-state flow, and negligible acceleration losses. The developed model was compared with other models against the experimental data and from TUFFP data bank. The results indicated that the developed model was superior and predicted better for both low and high flow rates. A comprehensive model was developed for vertical flow and three flow patterns. For annular flow, Ansari et al.'s (1994) mechanistic model was used, with a developed churn model for churn flow pattern and Chokshi et al.'s (1996) mechanistic model for slug flow. Additionally, the developed vertical flow model was modified to include the effect of the inserts by adding the Schmidt and Friedel (1993) sudden contraction-expansion model. The model can calculate the pressure drop with inserts installed.

Some limitations of Putra's study include a limited number of water-air experimental data points and the fact that the experimental tests were conducted for low v_{Sg} in the churn region, where no more than 14.5 m/s could be tested due to air compressor limitations. As a result, the annular-churn flow pattern transition was not visible or detectable. Furthermore, the pressure regulator used to control the gas flow rate was not automated, which may cause some fluctuations in v_{Sg}. These limitations were carefully considered in the current study by employing a larger compressor to cover a wider range of v_{Sg} and detect flow pattern transitions. Also, oil-air tests were included to study the effect of liquid properties on inserts. Furthermore, an automatic control valve was installed to control and maintain a constant and stable gas flow rate.

2.4 Summary

Mechanistic models are considered more accurate physical models, developed based on the conservation of mass, momentum, and energy. Closure relationships are used in complex parts, where it is impossible to develop a physical model. Some of these models for liquid-gas flow in vertical tubes were discussed in this chapter.

Many methods have been used to unload the gas wells and remedy liquid loading, such as tubing sizing, gas lift, wellhead compression, plunger lift, foam lift and pumping systems. There is no general agreement on what initiates liquid loading. Most of the studies on low liquid loading have been conducted using horizontal or near-horizontal pipes. In addition, studies on the effects of liquid properties are mostly using extremely small pipes and are not focused on liquid loading. The present study aims to bridge this gap in the literature and improve this understanding.

Moreover, the literature on the effect of inserts shows that inserts may delay loading and improve liquid lifting by generating droplets and decreasing the film thickness. The literature shows that there is a favorable region in churn flow, where the inserts improve the liquid lifting and delay the onset of liquid loading. If the inserts are installed outside this range, the liquid lifting efficiency will be reduced. Previous studies demonstrate that for a lower surface tension fluid, liquid entrainment increases with smaller droplet sizes and less droplet deposition to the film. This can potentially amplify the positive effects of adding inserts. The preceding statements justify the need to

experimentally study the effects of inserts and liquid properties on liquid loading in natural gas wells and develop a model to predict two-phase flow performance.

CHAPTER 3

Experimental Program

This chapter provides a summary of the design and planning for the experimental part of this study. Experiments investigating the effects of restrictions and liquid properties on liquid loading were conducted using a 0.0508-m (2-in.) ID (inner diameter) vertical flow loop. The experimental facility, measurement instruments, and testing fluids are described in the following sections. The standard procedure designed and followed for the tests is then outlined. Finally, the data analysis algorithm and the test matrix are presented.

3.1 Experimental Facility

A state-of-the-art experimental facility was constructed for this study at the University of Oklahoma's (OU) Well Construction Technology Center (WCTC). The facility was especially designed for two-phase flow testing in vertical tubulars. Sources of disturbance to the flow are eliminated by avoiding unwanted restrictions along the test section. The facility was built in an indoor environment to provide a controlled temperature with constant fluid properties. Moreover, the indoor environment prevents damages to the facility caused by factors such as freezing in winter and weather instability during the storm season. Therefore, it enables conducting tests all year long, allowing an increased number of gathered data points.

The facility has a 0.0508-m (2-in.) ID vertical test section, consisting of clear acrylic pipes with a total length of 7.6 m (25 ft.) The pipes are connected by straub clamps, creating three connecting joints along the test section. A specially designed tee that mixes the inlet fluids is connected to the bottom of the test section. After flowing through the test section, the fluids are sent back to the tank through a return line. This allows the gas to be vented to the atmosphere, while the liquid is recirculated. Two relief valves are installed at the inlet of the test section and after the air flow meter to keep the pressure below the allowable pressure limit of 310,000 Pa (30 psig). The liquid tank is open to the atmosphere; hence the outlet pressure is fixed at atmospheric pressure.

The two-phase flow tests are conducted using air as the gas and water or oil as the liquid phase. The liquid tank has a capacity of 380 L (100 gal.) to store the liquid. The liquid is pumped using a Masterflex L/S peristaltic pump stocked with a single channel Easy-Load® II Pump Head, providing a maximum flow rate of 2.9 L/min (0.77 gpm). Air is supplied through an Atlas Copco XAS 1600 CD6 rotary screw diesel compressor with a maximum air delivery of 2718-2328 m^3/h (1600-1370 cfm) at 800,000-1,140,000 Pa (100-150 psig). The QuadraTherm flow meter calibrated with a range of 0 to 550 kg/hr (1200 lb/hr) is used to measure the air mass flow rate. The air mass flow rate is controlled using a control valve. Each electrical equipment is connected to a DC power supply. Figure 3-1 displays a detailed schematic of the facility. This facility was built for this study, with the construction completed in April 2021. It was modified to ensure better handling of the oil, for the second phase. The ventilation Quick Closing Valve (QCV1) was connected to return the oil to the tank, as shown in red in Figure 3-1.

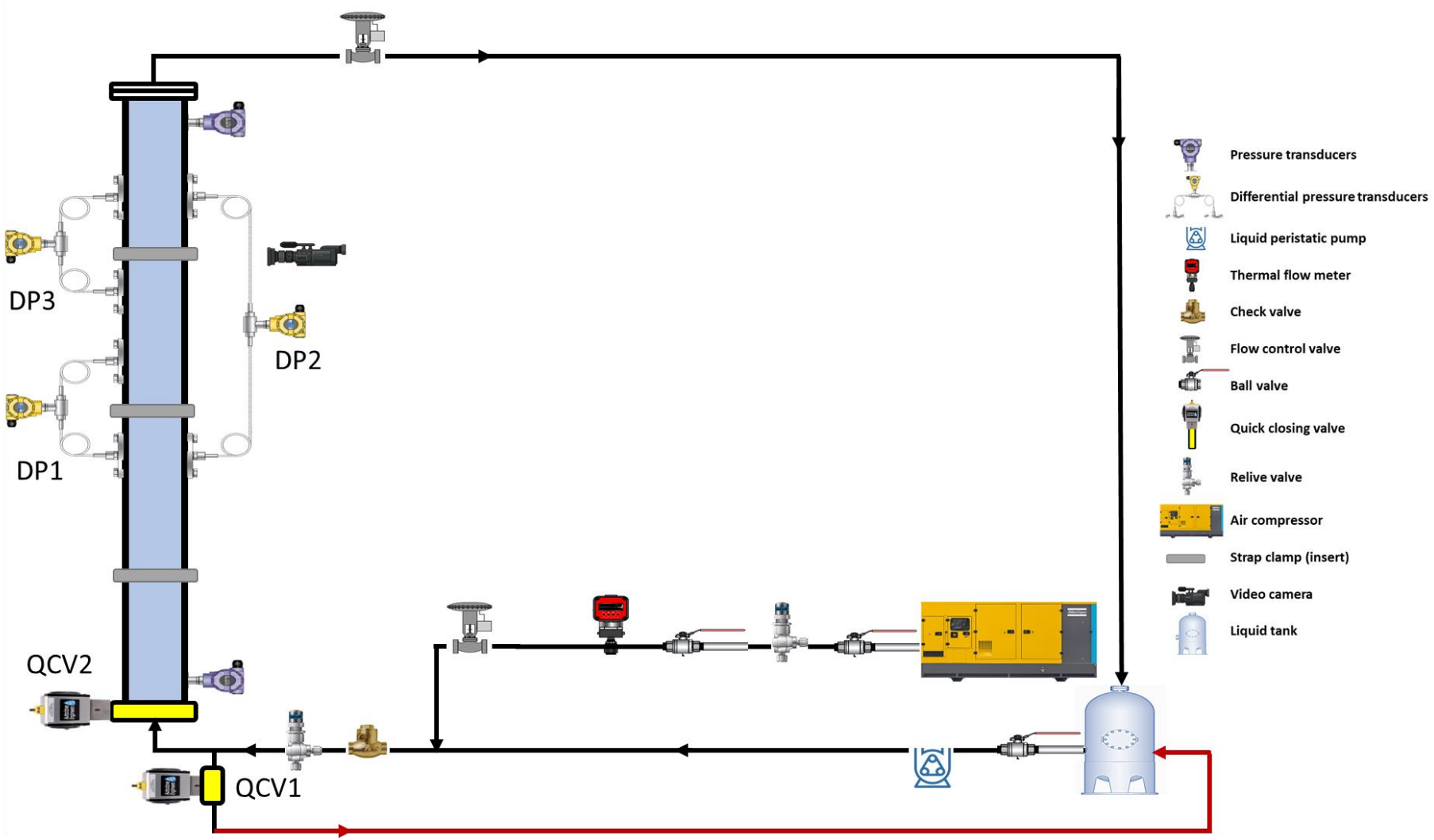

Figure 3-1: The 0.0508 m ID facility schematic diagram

3.2 Testing Instruments

The facility is equipped with the required measurement instruments. The recorded parameters include liquid and gas flow rates, pressure drop, liquid holdup, and flow pattern, all analyzed to study the effects of inserts and liquid properties on liquid loading. The instruments used to measure these parameters are described in the following sections.

3.2.1 Basic Instrumentation

The facility is equipped with three ProSense pressure transducers (PT) with ranges of 0-310,000 Pa (30 psig) placed at the inlet and outlet of the test section and at the bottom of the liquid tank. The inlet and outlet PTs provide an estimated average pressure drop across the entire test section.

Three differential pressure transducers (DP) are used to monitor the changes of pressure across the test section. The first one (DP1) is placed at the bottom, starting at 3.48-m (11.4-ft) from the bottom of the test section, to measure the pressure drop across a 0.96-m (38-in.) length, with a range of 0-40,000 Pa (0-160 in. of water). Similarly, a DP (DP3) with a range of 0-10,000 Pa (0-40 in. of water) is mounted, starting at 5.3-m (17.5-ft.) from the bottom of the test section, to measure the pressure drop across the top section. These two DP sensors provide measurements of pressure drop across the restriction inserts, placed at the second and third Straub clamps. The middle DP (DP2) is mounted at 3.48-m (11.4-ft) from the bottom of the test section, with a range of 0-50,000 Pa (0-200 in. of water). This DP measures the pressure drop of two-phase flow across a 2.82-m (9.25-ft) length of the test section.

3.2.2 Purging Differential Pressure Tap Lines

DPs are installed measure the pressure gradient of flow by looking at the pressure difference between their two ending taps. The two end's tap lines must be filled with the same fluids having constant densities. If a compressible fluid such as air enters the DP's tap lines, it can cause false readings. Considering that this is a two-phase fluid flow project, air may enter the tap lines. Hence, the water purge lines made from transparent vinyl tubing are connected to the DP tap lines. Water is injected through the purge using a water faucet prior to each test, filling the purge lines. A visual observation takes place to make sure there are no air bubbles in the lines prior to each test. The ball valve between the purge lines and water faucet is closed to keep the water pressurizing the DP and avoid forming any air bubbles. Figure 3-2 shows the purge lines schematic for water-air tests. The liquid peristaltic pump supplies oil to the purge lines during oil-air tests.

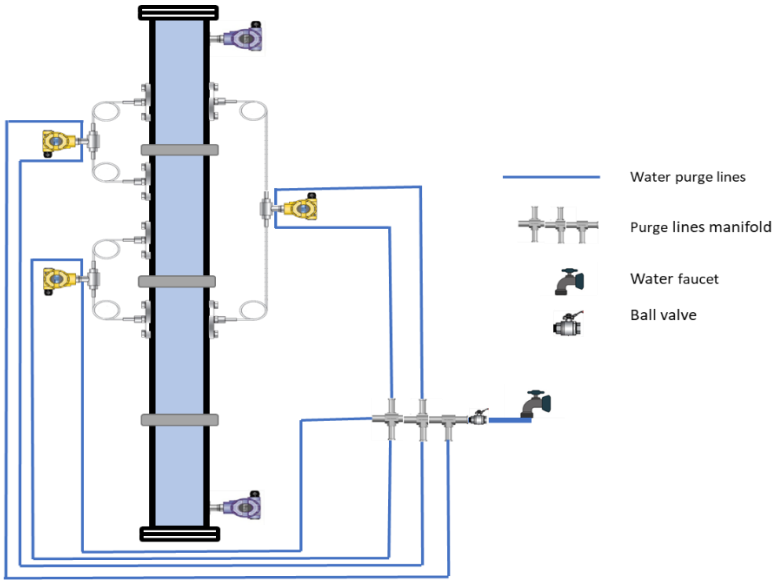

Figure 3-2: Differential pressure purge lines

3.2.3 Inserts and Straub Clamps

Partial restrictions were fabricated in form of insert rings. These rings were made from carbon fiber-reinforced nylon utilizing an advanced technology in 3-D printing. The METHOD MakerBot® printer was used to print the inserts. Three straub clamps were mounted with extra care to keep the pipes in a matching alignment by using a level. This is to avoid any unexpected disturbance to the flow. For the tests with inserts, they are installed underneath the straub clamps in the pipe connections. The clamps help to keep the inserts in place and simplify the installment or removal. These are shown in Figure 3-3. Inserts were designed using AutoCAD® 2022 software with dimensions of 1.5 and 1.75-in. ID, 0.12-in. thickness and 2.5-in. OD. The thickness of the inserts was less than the maximum allowable space between the pipes, 0.24-in., according to the straub clamp manual. The inner diameter was selected to be within the range of the common tool joints for 2-in pipes in the industry, which starts from 1.5-in. ID. The outer diameter was set at 2.5-in., to match the outer diameter of the pipe for easier installation.

a) b)

Figure 3-3: a) A 1.75-in. ID insert installed between two pipes, b) A straub clamp mounted over the insert between the two pipes.

3.2.4 Quick Closing Valves

Two quick-closing valves (QCV's) were installed in the facility. One was placed at the bottom of the test section to trap the liquid. Once trapped, the height of the liquid column in the test section was used for average liquid holdup measurement. The second QCV was used for venting the incoming fluids in the hoses after closing the first QCV and preventing any pressure buildup. Alsanea (2018) discovered that a small decrease in the pipe ID caused by a QCV was sufficient to disturb the flow, thereby causing a similar behavior as a restriction. Hence, no other QCV's were installed along the test section to avoid any disturbances to flow. The QCV's are connected to an air compressor and use pneumatic forces to fully close or open. A signal of 0 or 10 volts is sent from the data acquisition system to two relays to control the opening or closing of the QCV's. Figure 3-4 shows the QCV at the bottom of the test section The relays are shown in Figure 3-6.

Figure 3-4: Quick closing valve at the bottom of the test section

3.2.5 Visual Observations

The visual advantage of the clear acrylic pipes permits the use of cameras in any location along the test section. A GoPro camera Hero9 Black was used to record the fluid behavior and flow pattern in the test section at 5.6-m. (18.25-ft.) above the bottom. The GoPro was installed using a goose-neck clamp to record the flow.

Figure 3-5: GoPro camera on goose neck clamp

3.2.6 Data acquisition

The OMEGA multi-function I/O data acquisition (DAQ) module with 32 single-ended analog inputs and voltage range of 0-10 volts is connected to the mass flow meter, PT's and DPT's. The module reads the input signals from the sensors and sends the signals to a connected desktop computer. A user-friendly LabView program was developed, specifically for this project, to record the data from the beginning of each test into an excel sheet format. In addition, the LabView code regulates the air flow rate to match the desired set point by using a Proportional-Integral-Derivative (PID) function.

This function compares the input desired flow rate to the real flow rate measured by the flow meter. A signal is sent to the air flow control valve, to increase the opening if the desired flow rate is higher, or to decrease the opening if the desired flow rate is lower.

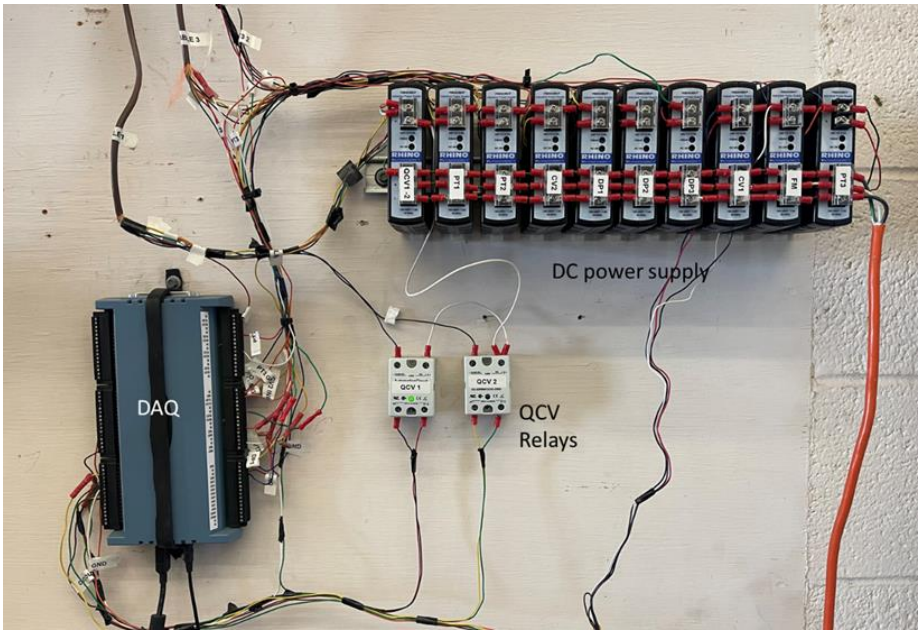

Figure 3-6: DC power supply, DAQ and the two QCV relays

3.3 Testing Fluids

The testing fluids used in this study are compressed natural air, tap water and Iso-Par L mineral oil as the gas phase, aqueous phase, and oil phase, respectively. The testing fluid properties are shown in Table 3-1.

Table 3-1 : Testing Fluid Properties at Standard Conditions

Fluid	Temperature (°C)	ρ (Kg/m3)	μ (cp)	σ (dynes/cm)
Tap Water	**15**	**1000**	**1**	**72**
Air	**15**	**1.225**	**0.0018**	**-**
Iso-Par L Oil	**15**	**760**	**1.27**	**24**

3.4 Experimental Procedure

Any experimental work needs a standard procedure to assure that the tests are conducted under consistent and equivalent conditions. The following experimental procedure was developed and followed in this study to conduct the experiments in a safe, repeatable, and accurate manner:

1. Open the purge lines valve and the liquid supply valve, let liquid flow to the DP's.
2. Check for air bubbles in the purge lines. Close the purge line valve when it is filled with liquid and there are no air bubbles. Shut off the liquid supply.
3. Open the air valve for QCV's, the main air supply valve and the two air valves located before the tee between the liquid pump and the air lines.
4. Start the air compressor by engaging the battery terminal. Check the fuel, push the start button, and load it up.
5. Connect the DC power supply cord to the AC power supply and the liquid pump cord. Open the valve at the pump.
6. Turn on the GoPro camera and make sure it is fully charged with available space in the memory card. Attach the camera to the gooseneck as shown in Figure 3-5.
7. Start the LabVIEW program, input the desired air superficial velocity. Run the program by inputting the desired liquid flow rate in the pump.
8. Record videos of the test section when pressure and mass rates are attained and stabilized. This process may take up to 45 minutes.

9. Stop the LabVIEW program and the liquid pump. The QCV at the test section automatically traps the liquid and the other QCV opens to prevent any pressure buildup. Record the liquid holdup, take a picture of it with the measured tape, and include the holdup level in the data excel file made by LabView for the same test.
10. Repeat steps 7-9 for the desired liquid and gas flow rates.
11. Shut down the liquid pump and close all the valves.
12. Vent all the air in the air lines to avoid any pressure build up that could cause damage. Afterwards, shut off the air compressor and remove the air supply hose.
13. Shut off LabVIEW, remove the power supply cord and dismount the GoPro camera.

3.5 Data Analysis

The large number of data collected in this experimental study requires an efficient and organized way to enhance the quality of the analysis and reduce errors. For this purpose, data processing must be automated. Python programming language was used to process the data obtained from pressure and differential pressure transmitters and the flow meter. The program calculates the average and uncertainty of all the measured data. See Appendix C for details on calculating the uncertainties for pressured drop, liquid holdup, and superficial gas velocity. All plots and analyses using the data and models are developed within this program. The objective of this data analysis is to reduce time, effort, and handling errors, while maintaining a high-quality and consistent data processing.

3.5.1 Air Flow Meter

Air flow meter sends an output signal of 4-20 mA corresponding to 0-550 kg/hr (0-1200 lb/hr) mass flow rate. The current output is converted to 0–10 volts using a resistor. Following this, the DAQ card sends the voltage readings to the computer, and LabView program converts the voltage to mass flow rate readings. The equation of state is used to calculate the air density by using the pressure at the bottom of the test section at a temperature of 29 ºC (85 ºF). Assuming ideal gas, the air density is calculated, as shown in Equation (3-1). Then, the air velocity is calculated using the calculated air density, as shown in Equation (3-2).

$$\rho_A = \frac{P}{R_{air}T} \tag{3-1}$$

$$v_{Sg} = \frac{\dot{m}}{\rho_A A} \tag{3-2}$$

The calculated v_{Sg} from Equation (3-2) is used to calculate the relative error compared to a set v_{Sg}. A green indicator in the LabView lights up if the error is less than 10% indicating that flow rate is stable. The stable zone should last for at least the last three minutes of the test.

The pressure data were analyzed for the last three minutes with the stable flow. Figure 3-7 displays the actual v_{Sg} fluctuations in the last three minutes for sample tests of water-air flow without inserts at $v_{SL} = 0.02$ m/s. To verify the flow stability of the tests, a variable (*t_stat*) was defined. This variable is the average value of air flow rate

divided by its standard deviation. An increase in the value of *t_stat* indicates that the test is more stable. A cut off value of 14 was used. If the value was less than 14, the test was repeated.

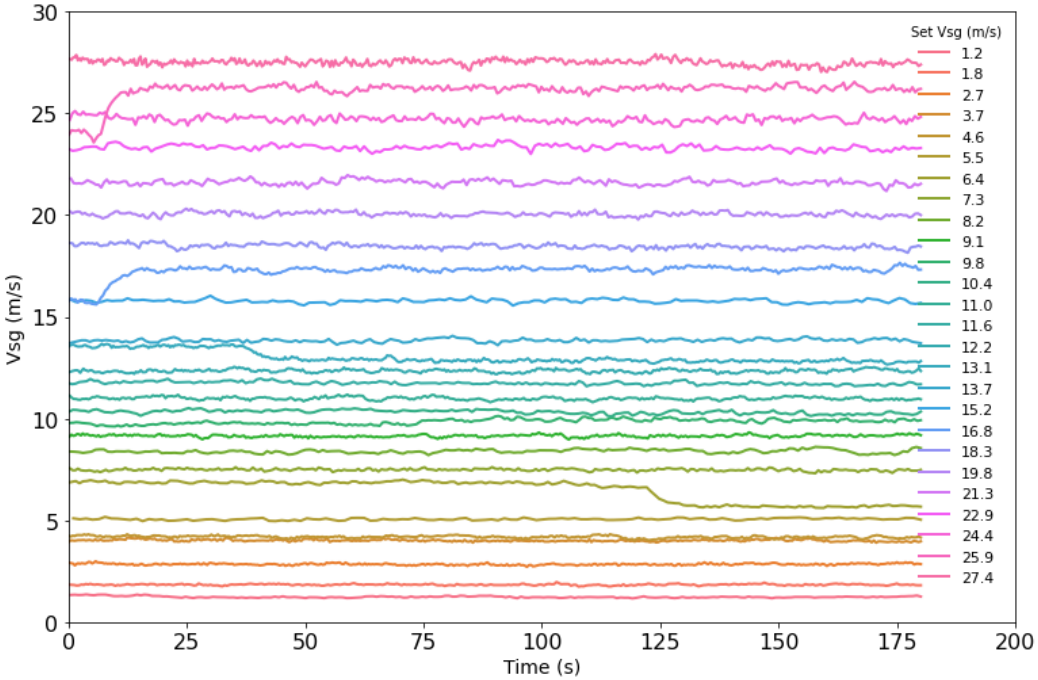

Figure 3-7: Air velocity fluctuations in the last three minutes at $v_{SL} = 0.02\ (m/s)$ for various v_{Sg} and water-air and no inserts.

Figure 3-8 shows a comparison between actual and set superficial air velocities for water-air and oil-air tests. The 10% error line is also included. This figure demonstrates that the gas flow rate is controlled well for all the conducted tests.

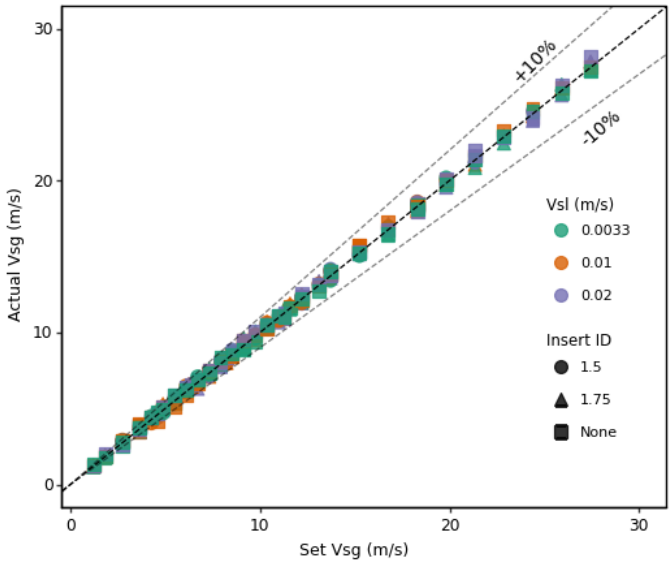

Figure 3-8: Actual air velocity vs. the set air velocity at different v_{SL} values for water-air and no inserts.

3.5.2 Pressure Drop

The three pressure transmitters each send an output signal of 0-10 *volts*, calibrated to 0-310,000 Pa (30 psig) at the DAQ system. The signal is sent to the computer and the LabView program converts the output signal to pressure readings recorded in an excel sheet. The recording is initiated at the beginning of each test. The pressure difference between the test section's top and bottom PT's is divided by the distance between them, 7.22 m (23.7 ft). It can be defined as the average pressure drop over the whole test section.

For the three DPs, resistors are used to convert the current output signals to the voltage drops. The DAQ system measures the voltage drop readings and sends them to the computer. The LabView program converts the voltage drops to pressure drop readings and records them in the excel sheet for each test. The DPs are recalibrated both in current output and lower and upper pressure range. For the bottom and top DPs, the 4-20 *mA*

current output signal is calibrated to -40 to 40 in. of water. After filling the purge lines with liquid, the DP readings are approximately -38 in. of water. Similarly, the middle DP is recalibrated, but with 4-20 *mA* current corresponding to -120 to 120 in. of water. This DP's reading is around -110 in. of water when the purge lines are filled with liquid. The LabView program considers the first value of each DP at the start of each test as zero. This is to accurately calculate the differential pressure and then convert it to adequate pressure units. If the test section and purge lines are not fully filled with liquid, the DP's read wrong values as zero. Therefore, it is crucial to fill the purge lines and remove any air bubbles from the lines.

Figure 3-9 compares the pressure drop readings by taking the pressure difference between the top and bottom PT's versus using the three DPs for all the water-air tests without inserts. The results show a good agreement between the pressure drops, thereby indicating that all methods can be used in case of no inserts. Also, this provides assurance that the flow was fully developed along the test section.

A data comparison was conducted between the results of this study and some other studies that used similar facilities and test matrices. Figure 3-10 shows the average pressure drop comparison between this study, Skopich (2012), Barreto (2016) and Alsanea (2018) for air-water at v_{SL} = 0.02 and 0.01 m/s. All the studies show closely matching results, assuring the reliability of the tests conducted at the current study. For all cases, as v_{Sg} decreases, pressure drop decreases to reach a minimum. A further decrease in v_{Sg} increases the pressure drop because of the increase in gravitational losses.

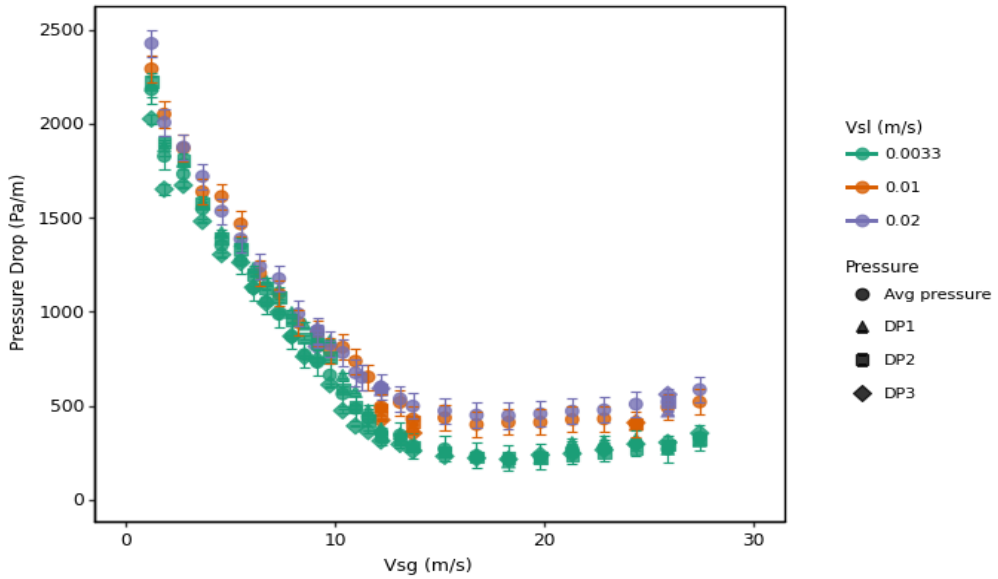

Figure 3-9: Average pressure drop and pressure drops of all DPs at various v_{SL} values

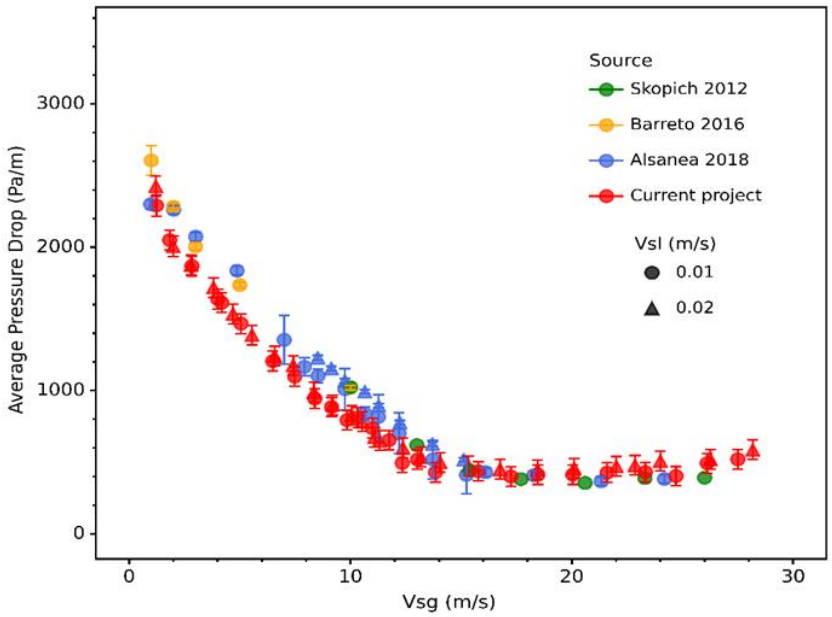

Figure 3-10: Average pressure drop comparison with other studies at various v_{SL} values for water-air and no inserts.

3.5.3 Liquid Holdup

Liquid holdup is defined as the fraction of the pipe volume occupied by liquid. In this study, the test section has a constant 0.0508-m (2-in.) ID with 7.6 m (25 ft) of total length. The following equation was used to calculate the liquid holdup (see Figure 3-11):

$$H_L = \frac{h_L}{h_{total}} \tag{3-3}$$

The liquid level (h_L) is directly measured using a measured tape. The tape is attached to the test section starting from the bottom to measure the liquid level. Figure 3-12 shows the liquid level for a test at v_{SL} =0.0033 m/s and $v_{Sg} = 9.15$ m/s.

The liquid holdup results are compared to other studies using a similar pipe diameter and superficial liquid velocity, namely, Skopich (2012), Barreto (2016) and Alsanea (2018). Figure 3-13 shows this comparison for air-water experiments at v_{SL} = 0.02 and 0.01 m/s. The results of all the studies show a good agreement, verifying the liquid holdup measurements of this study. For all cases, the liquid holdup increases sharply as the v_{Sg} decreases, due to the change in two-phase flow pattern and liquid loading in the tubing.

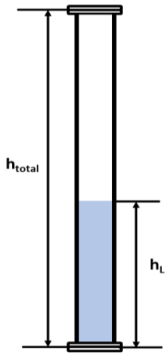

Figure 3- 11: Schematic of liquid holdup measurements

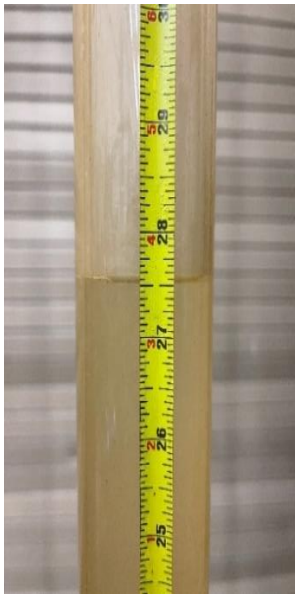

Figure 3-12: Liquid level for a test at v_{SL} =0.0033 *m/s* and v_{Sg} =9.15 m/s

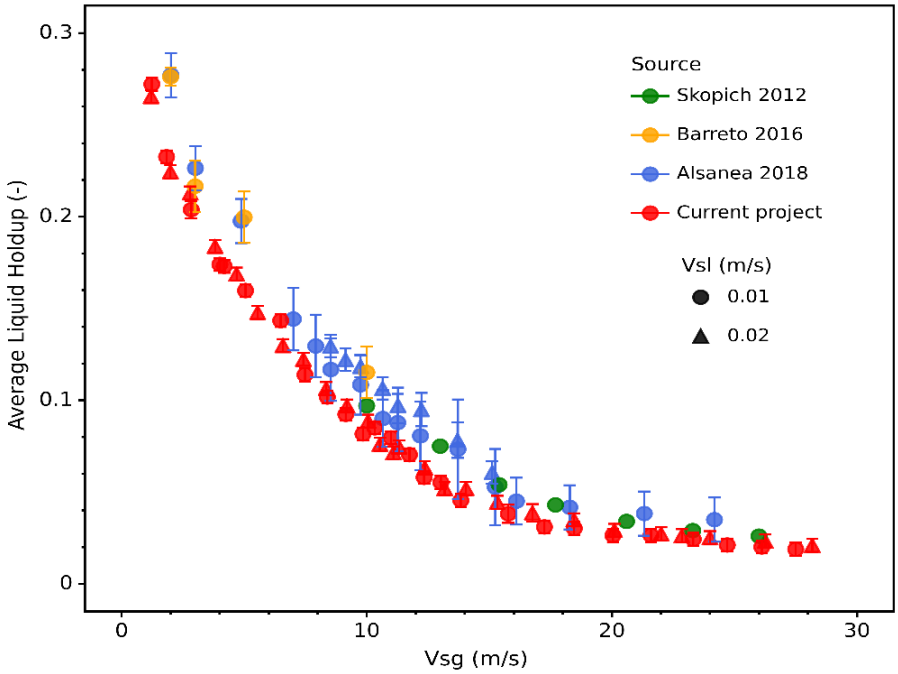

Figure 3-13: Liquid holdup comparison with other studies for water-air and no inserts at various v_{SL} values

3.6 Test Matrix

The experiments were conducted in two stages to study the effects of liquid properties on liquid lifting performance. In the first stage, water and air (WA) were used as the testing fluids. Oil and air (OA) were used as the testing fluids for the second stage. For each stage, tests were conducted with and without inserts to study the effects of inserts on liquid lifting, using two insert ID's. The size selection was based on the common tool joint diameter reductions. It was found that the diameter reduction for tool joints compared to the pipe ID is 75-95%. All the tests were conducted with three inserts along the test section, and with a spacing of 1.85 m (6.08 ft) between consecutive inserts.

Same superficial liquid velocities (v_{SL}) were used for both stages. Three velocities were tested to study the effects of liquid rate on flow behavior. These v_{SL} values were chosen to be in the instability transition according to Barnea (1987). The values were restricted by the water pump limitation and similar to the previous studies (Skopich (2012) Barreto (2016) and Alsanea (2018)) for comparison. Different v_{Sg} set values were tested, covering a wide range, starting from the annular flow pattern with pressure drops above the minimum value and finishing at the slug flow pattern. In the experimental results section, the actual average superficial gas velocity for the last three minutes of the test was shown as the v_{Sg}. As a result, it may be slightly higher or lower than the set values. The test matrix used for the experiments is shown in Table 3-2.

Table 3-2: Experimental Test Matrix

	Stage-1			**Stage-2**		
Fluids	Water-air			Air-Oil		
Inserts	-	1-1/2	1-3/4	-	1-1/2	1-3/4
v_{SL} **(m/s)** **(ft/s)**	0.0033, 0.01, 0.02 0.01, 0.033, 0.066					
v_{Sg} **(m/s)** **(ft/s)**	1, 2, 3, 4, 5.5, 6, 7, 8, 9, 10, 10.5, 11, 11.5, 12, 13, 14, 15, 17, 18, 20, 21.5, 23, 24.5, 26, 27.5 4, 6, 9, 12, 15, 18, 20, 22, 24, 26, 28, 30, 32, 34, 36, 38, 40, 43, 45, 50, 55, 60, 65, 70, 75, 80, 85, 90					

CHAPTER 4

Two-phase Flow Experiments

Two-phase flow experiments were conducted in a 0.0508-m. ID vertical pipe with superficial liquid velocities of 0.0033, 0.01, and 0.02 m/s and a range of superficial gas velocities from 30 to 1 m/s. Total pressure drop and liquid holdup were measured, and videos were recorded for visual observations of flow pattern transitions. The experimental results attained were utilized to evaluate the performance of different models, including the TUFFP unified and OLGA models. Additionally, the Barnea (1987) liquid film reversal model and the Turner et al. (1969), Coleman et al. (1991), and Li et al. (2002) liquid droplet models were evaluated. The Skopich et al. (2015) inflection point approach was also included. These models were compared to the experimental onset of liquid loading based on the visual flow pattern transition observation, minimum pressure gradient, and the positive frictional pressure gradient. The following sections present the analysis of these parameters for water-air and oil-air two-phase flows.

4.1 Onset of Liquid Loading Criteria

The superficial gas velocity at which the onset of liquid loading occurs is defined as the critical gas velocity. Experimental studies in the literature such as Hewitt et al. (1965), Zabaras et al. (1986), Skopich et al. (2015), and Westende et al. (2008) conclude

that liquid loading occurs when the liquid film starts to reverse. In most cases, liquid film reversal is detected qualitatively using visual observations by a camera. However, finding the film reversal point using visual observation is a difficult task, as the liquid film changes its direction gradually and continuously. Additionally, the liquid film movement in a pipe cannot be seen clearly even with an acrylic pipe because of the circular shape of the pipe and the entrainment of liquid droplets in the center of the pipe. Therefore, the human error in evaluating the transition of liquid film movement can be large, and each study may evaluate the liquid film reversal differently. Accordingly, the need to develop a quantitative method to detect the liquid film reversal rather than a qualitative method is justified to reduce such errors.

4.1.1 Positive Frictional Pressure Gradient.

The pressure gradient of fluid flow may be positive or negative. The pressure gradient definition is presented in the following equation:

$$\frac{dP}{dL} = \frac{P_2 - P_1}{L}, \tag{4-1}$$

where (*dP/dL*) is the pressure gradient, L is the pipe length, and -*dP* is the pressure drop. *dP/dL* is negative because the pressure is dropping with fluid flow along the pipe. As a result, a negative pressure gradient can be presented by a positive pressure drop, due to the minus sign preceding it.

A method was developed to quantitatively detect the liquid film reversal using the pressure gradient and liquid holdup experimental data. In this method, the frictional

pressure gradient $\left(\frac{dP}{dL}\right)_F$ is calculated by subtracting the gravitational pressure gradient $\left(\frac{dP}{dL}\right)_G$ from the total pressure gradient $\left(\frac{dP}{dL}\right)_T$. The gravitational and frictional pressure gradients are calculated as follows:

$$\left(\frac{dP}{dL}\right)_F = \left(\frac{dP}{dL}\right)_T - \left(\frac{dP}{dL}\right)_G. \tag{4-2}$$

$$\left(\frac{dP}{dL}\right)_G = -g(\rho_L H_L + \rho_g(1 - H_L)) \tag{4-3}$$

$$\left(\frac{dP}{dL}\right)_F = -\frac{f\rho_L v_f |v_f|}{2d} \tag{4-4}$$

This method uses the change in the sign of $\left(\frac{dP}{dL}\right)_F$ from negative to positive to identify the onset of liquid film reversal. Equation (4-4) shows that when the film velocity is downward, the sign is changed to positive. Based on the annular flow description, both liquid film and droplets must flow in an upward direction. The transition from annular to churn flow can be defined by the change in liquid film's movement direction—from upward to downward direction.

At first glance, the positive frictional pressure gradient could indicate a violation of the second law of thermodynamics, but it has already been observed in the literature. Fabre and Liné (1992) reported that the frictional pressure gradient in a vertical upward two-phase flow may be positive, as shown in the experimental studies by Koeck (1980), Souhar (1980), and Fréchou (1986). The reason of the occurrence of positive frictional pressure gradient is not explained, but it is mentioned that it does not violate the energy conservation. Spedding et al. (2000) studied two-phase and three-phase upward flow in

vertical and near-vertical 0.0127-m (0.5-in.) ID pipes. The results showed a positive frictional pressure gradient at low superficial gas and liquid velocities. Many experimental studies, including Sakharov and Mokhov (2004), Liu et al. (2005), and Akhiyarov et al. (2010) showed that the positive frictional pressure gradient occurs for two-phase vertical flow at low superficial gas and liquid velocities.

Liu (2014) used the conservation of mechanical energy for two-phase gas-liquid slug flow. He proved that even with a positive frictional pressure gradient, the energy loss due to friction is positive and the second law of thermodynamics is not violated. He claimed that there is a buoyancy-like term associated with the energy loss in vertical two-phase flow in addition to the frictional pressure gradient . By considering this buoyancy term, the second law of thermodynamics is not violated.

Alruhaimani et al. (2015) presented an experiment and modeling study to investigate the effects of oil viscosity on vertical two-phase flow in a 0.0508-m. (2-in.) ID pipe. It included several flow parameters such as flow pattern, average liquid holdup, pressure drop, and slug flow characteristics. A facility analysis was conducted to check the pressure drop and liquid holdup measurements and investigate the positive frictional pressure gradient. The analysis proved the occurrence of positive frictional pressure gradient at low superficial liquid velocities and intermittent flow pattern. In summary, the literature studies show that positive frictional pressure gradient may exist in a vertical two-phase flow in low superficial gas and liquid velocities.

4.2 Water-Air Flow

This section involves understanding the criteria for onset of liquid loading, particularly the positive frictional pressure gradient. The experimental results consist of pressure drop, frictional pressure gradient, and liquid holdup. Furthermore, a comparison of visual observations for flow pattern is presented.

4.2.1 Visual Flow Pattern Transition Observations

Figure 4-1shows the fluid behavior as the v_{SL} decreases for v_{SL} = 0.01 m/s (0.033 ft/s). Figure 4-1(a) exhibits the flow in annular region with liquid film and droplets traveling upward. Figure 4-1(b) depicts the onset of liquid loading and the transition to churn flow pattern. The onset of liquid loading occurs when the liquid film starts to reverse, and the flow is more chaotic compared to the annular flow pattern. Figure 4-1(c) shows the churn flow behavior becoming more chaotic, which may be noticed by the reversing liquid film close to the pipe wall. Figure 4-1(d) depicts the transition to slug at v_{Sg} =1 m/s. (3.2 ft/s.). The liquid slug body is clearer than in the churn region, as shown in t=0 ms and t=275 ms. In addition, the liquid film reverses and moves downward at t=600 ms and 692 ms.

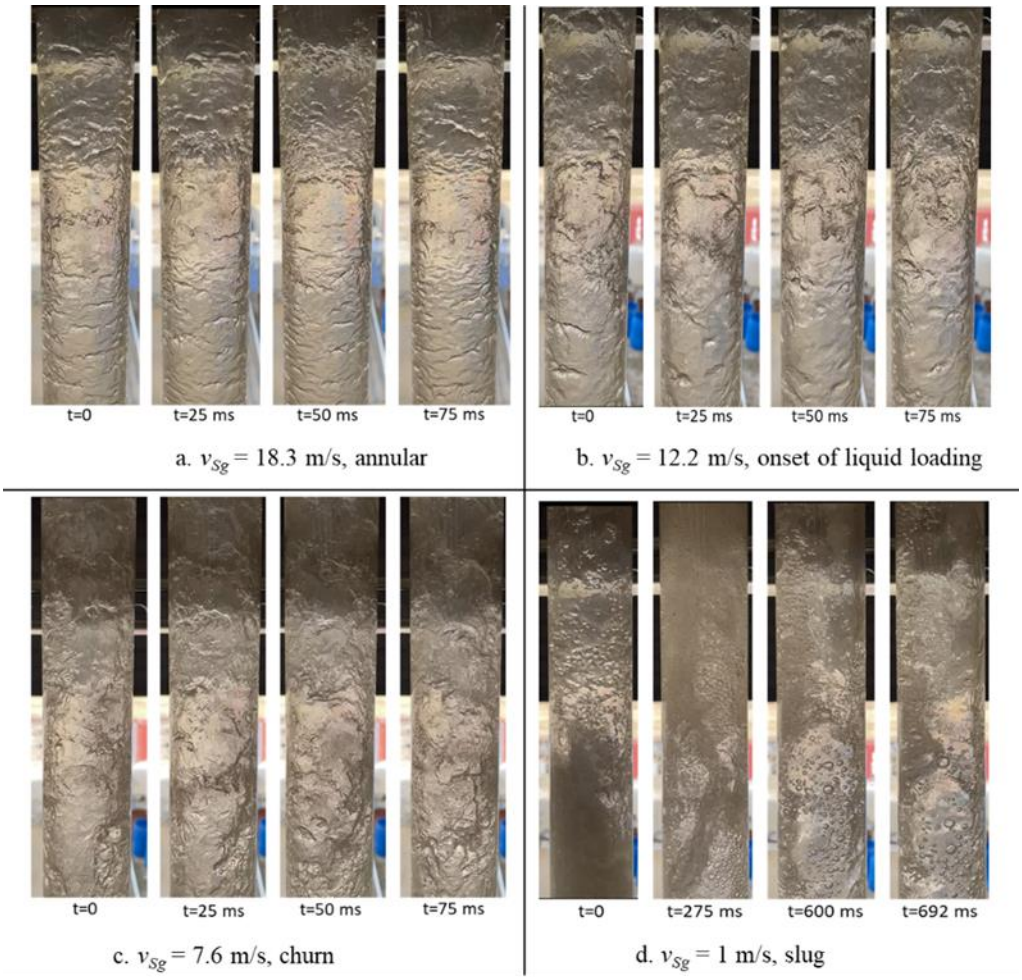

Figure 4-1: Snapshots of different flow patterns and the onset of liquid loading for $v_{SL=}$ 0.01 m/s (0.033 ft/s) and decreasing v_{Sg} values

4.2.2 Pressure Drop Results

Figure 4-2 shows the total pressure drop vs. superficial gas velocity for v_{SL} =0.0033, 0.01, and 0.02 m/s in green, orange, and purple markers, respectively. In this figure, the three flow patterns detected by visual observation, namely, annular, churn, and slug, are assigned the circular, triangular, and square shapes, respectively. The transition from annular to churn flow occurs at superficial gas velocities of 11.6, 15.4, and 13.2 m/s

for v_{SL} =0.0033, 0.01, and 0.02 m/s, respectively. The total pressure drop is a hook-shaped curve for all cases, with a minimum pressure drop ($v_{Sg,min}$) of 18.4, 17.25, and 18.44 m/s for v_{SL} =0.0033, 0.01, and 0.02 m/s, correspondingly. For a constant superficial gas velocity, the total pressure drop increases as the superficial liquid velocity increases, because of the increase in liquid holdup, increasing the gravitational pressure drop.

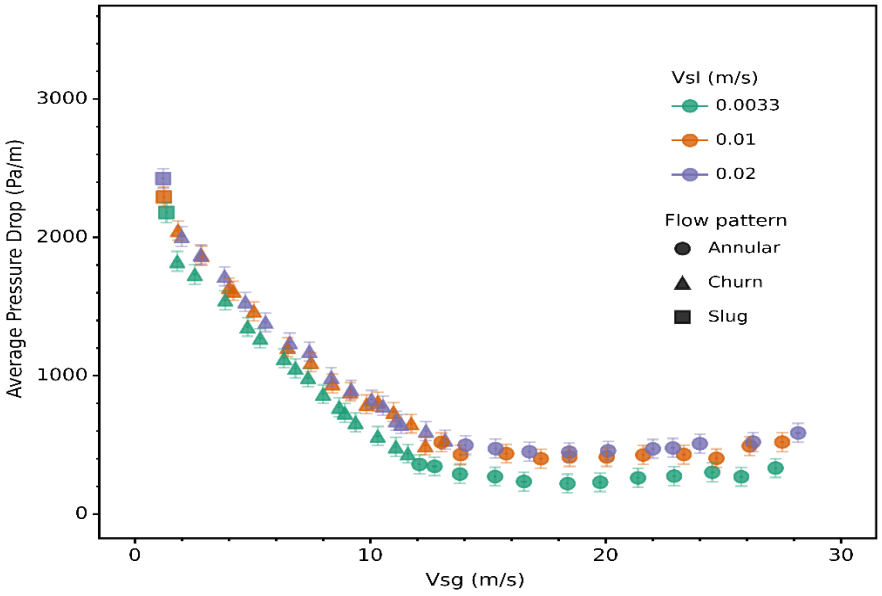

Figure 4-2: Total pressure drop vs. superficial gas velocity

Figure 4-3 shows the gravitational and frictional pressure drops vs. superficial gas velocity for water-air tests. The gravitational pressure drop $(dp/dL)_G$ is depicted with square shape markers, and frictional pressure drop $(dp/dL)_F$ is shown with diamond shape markers. The tests with v_{SL} =0.0033, 0.01, and 0.02 m/s are shown with green, orange, and purple markers, respectively. At a constant superficial liquid velocity, the frictional pressure drop increases and the gravitational pressure drop decreases by increasing the superficial gas velocity. For $v_{Sg} > v_{Sg,min}$, the frictional pressure loss becomes more

dominant. Moreover, the total pressure drop increases slightly as the superficial gas velocity increases, as shown in Figure 4-2. For $v_{Sg} < v_{Sg,min}$, the gravitational pressure loss becomes dominant. Furthermore, the total pressure drop increases significantly because of the increase in liquid holdup, resulting in liquid loading.

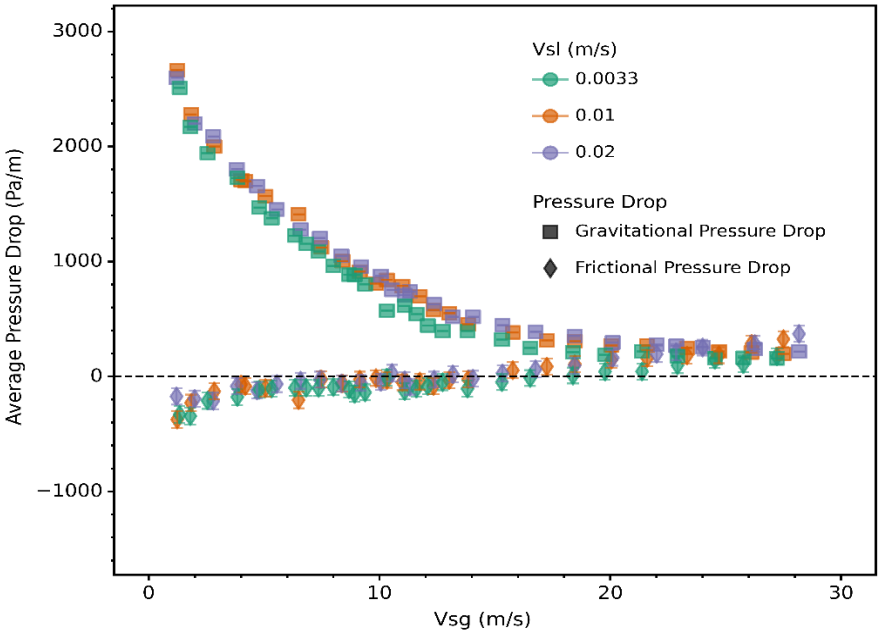

Figure 4-3:Gravitational and frictional pressure drop vs. superficial gas velocity

4.2.3 Positive Frictional Pressure Gradient.

Figure 4-4shows the frictional pressure drop vs. superficial gas velocity for v_{SL} =0.0033, 0.01, and 0.02 m/s, in green, orange, and purple markers, respectively. This figure shows that for a constant v_{SL}, the frictional pressure drop decreases as the v_{Sg} is decreased. The frictional pressure drop continues to decrease until it reaches a zero value, and then its sign changes, resulting in a positive frictional pressure gradient (negative drop). The figure shows that at v_{SL} =0.0033, 0.01, and 0.02 m/s, the frictional pressure

drop switches signs at v_{Sg} = 16.5, 13.8, and 14.1 m/s, respectively. The v_{Sg} value at which the sign switches is maximum at the lowest superficial liquid velocity of 0.0033 m/s. This could be due to the lower liquid rate making it harder to generate waves in the liquid film and tear away liquid droplets. As a result, the liquid entrainment decreases, and more of the liquid stays in the film, causing the liquid film to reverse earlier as the v_{Sg} decreases.

Magrini (2009) experimentally studied the entrainment fraction and wave characteristics in water-air two-phase flow through a vertical 0.0762-m. (3-in.) ID pipe. The result showed a decrease in the liquid film wave amplitude as the v_{SL} decreases. Also, the entrainment fraction decreases as the v_{Sg} decreases. For v_{SL} =0.01 and 0.02 m/s, the superficial gas velocities at which the switching signs occur are almost the same.

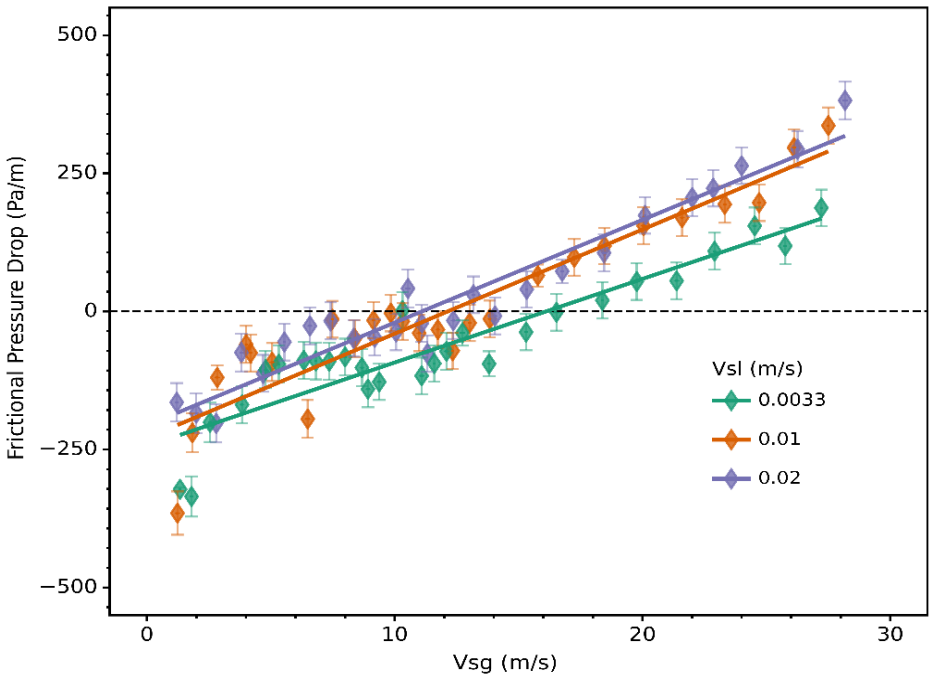

Figure 4-4: Frictional pressure drop vs. superficial gas velocity

Figure 4-5shows the frictional pressure drop vs. v_{Sg} for water-air tests in comparison to Skopich et al. (2012), Barreto et al. (2016), and Alsanea (2018) studies at 0.0508-m. (2-in.) ID and v_{SL} = 0.01 m/s. The figure shows a proof of the occurrence of positive frictional pressure gradient (negative drop) using the data of these studies.

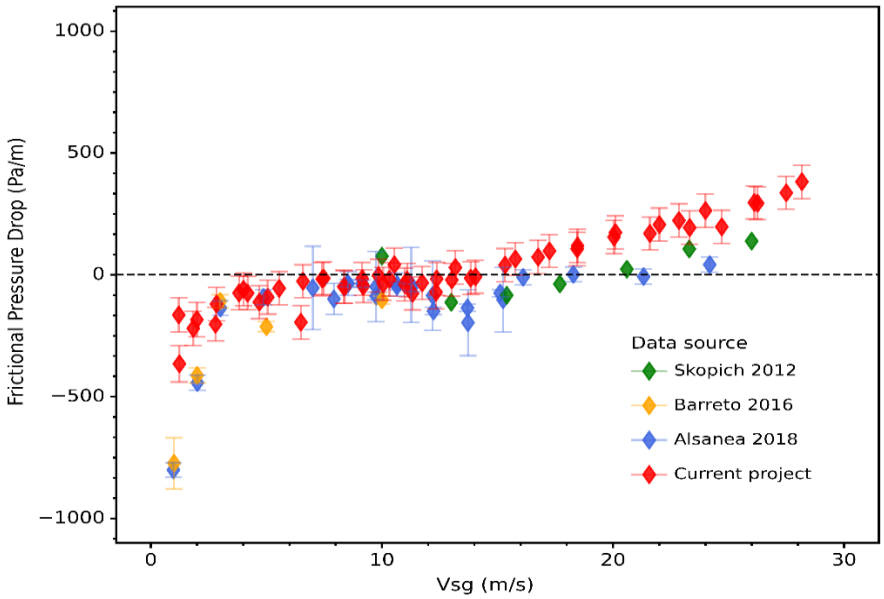

Figure 4-5: Frictional pressure drop vs. v_{Sg} for water-air tests in comparison with other experimental studies at 0.0508-m ID and v_{SL}=0.01 m/s

4.2.4 Liquid Holdup Results

Figure 4-6 shows the average liquid holdup vs. superficial gas velocity at v_{SL} =0.0033, 0.01, and 0.02 m/s, shown in green, orange, and purple markers, respectively. For a constant v_{SL}, the average liquid holdup increases as the v_{Sg} is decreased. Additionally, the liquid holdup increases as the v_{SL} is increased at a constant v_{Sg}. The increase of liquid holdup is due to the increase in volumetric flow rate of the liquid.

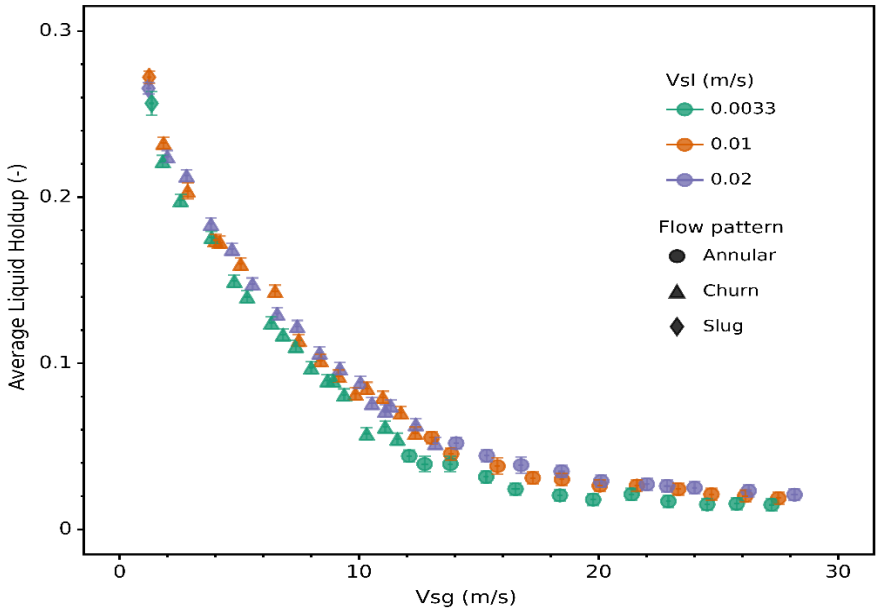

Figure 4-6: Liquid holdup vs. superficial gas velocity

4.2.5 Experimental Results Summary

Visual observations of liquid film movement using a GoPro camera were used to compare the onset of liquid loading and flow pattern transition to the positive frictional pressure gradient. For the visual observations, the change of flow pattern from annular to churn was defined as the point where the liquid film reverses in the test section and the onset of liquid loading. Figure 4-7 shows a summary of the onset of liquid loading criteria observed in water-air experiments. The positive frictional pressure gradient, minimum pressure drop, and visual observations are presented in green, purple, and yellow, correspondingly. As the v_{SL} is decreased, the transition of flow pattern is detected at a lower v_{Sg} by visual observation. The positive frictional pressure gradient occurs at superficial gas velocities higher than the visual observation transition and lower than minimum pressure drop. At higher v_{SL} values of 0.01 and 0.02 m/s, the positive frictional

pressure gradient occurs at a slightly higher v_{Sg}, but fairly close to the visually observed transitions. Overall, the results show that this approach can provide a better estimation for the onset of liquid loading than the minimum pressure drop approach.

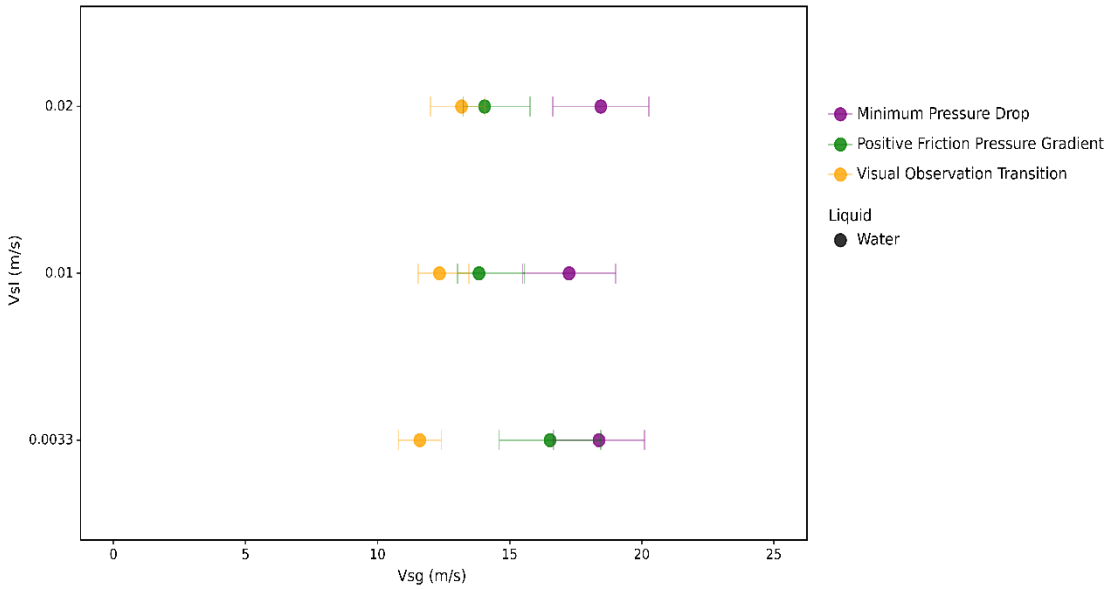

Figure 4-7: Water-air flow onset of liquid loading criteria

4.2.6 Model Evaluations

The experimental results attained in this study were utilized to evaluate the performances of different models. The Tulsa University Fluid Flow Project (TUFFP) Unified model (v2016) and OLGA (v2016.2.1) were employed for the evaluation of pressure drop, liquid holdup, and flow pattern. Both models were compared to the average value of the experimental data at the same superficial gas velocity, with the experimental data's uncertainties (see Appendix C) considered. Uncertainties in input values (fluid properties) were not considered in the models. For pressure drop and liquid holdup, the relative errors between model predictions and the experimental data are presented.

The experimental pressure drop data were compared with the TUFFP Unified and OLGA model predictions, as depicted in Figure 4-8. Overall, the Unified model overpredicts the experimental data at v_{Sg} > 14 m/s for all the superficial liquid velocities, but it underpredicts the pressure drop significantly at v_{Sg} < 14 m/s. The predictions are generally closer for v_{SL} = 0.01 and 0.02 m/s compared to v_{SL} = 0.0033 m/s. At v_{Sg} values higher than the transition to the slug flow ($v_{Sg,S}$) most of the data are overpredicted with OLGA too. At v_{Sg} values less than $v_{Sg,S}$, OLGA underpredicts the experimental data at v_{Sg} < 10 m/s. In this region, OLGA is closer to the experimental data than the Unified model.

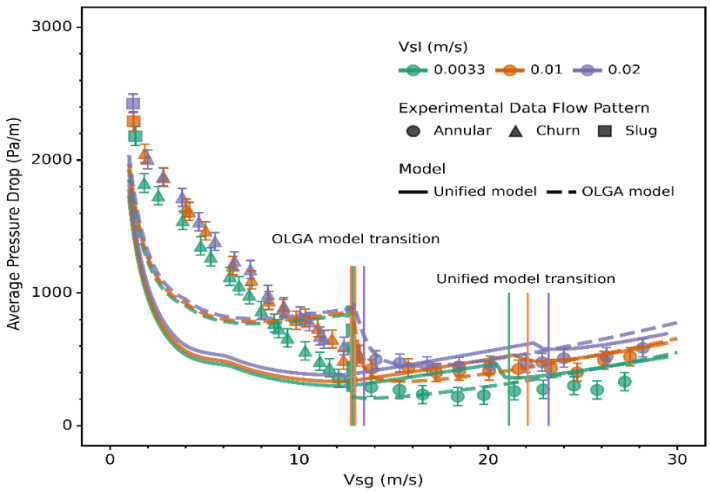

Figure 4-8: Comparison of experimental pressure drop data with OLGA and Unified model predictions at varying v_{Sg} values

Figure 4-9 displays the relative error of the pressure drop prediction vs. v_{Sg} for the Unified and OLGA models compared to the experimental data. At v_{Sg} > 14 m/s, the models have better predictions, especially for v_{SL} = 0.01 and 0.02 m/s, while slightly overpredicting the pressure drop. For v_{SL} = 0.0033 m/s and v_{Sg} > 14 m/s, unified model significantly overpredicts the pressure drop, with a maximum relative error of 90% at v_{Sg}

= 20 m/s. This can be attributed to the change of the predicted flow pattern by the model from annular to slug at that point. At v_{Sg} < 14 m/s (46 ft/s), the unified model underpredicts the pressure drop for all the superficial liquid velocities. This may be because of the lower predicted liquid holdup values compared to the experimental data.

Overall, at v_{Sg} > 20 m/s, the OLGA model overpredicts the experimental data with a lower relative error than the Unified model. OLGA underpredicts the experimental data at v_{Sg} < 20 m/s at values above the transition to slug flow ($v_{Sg,s}$). Once v_{Sg} < $v_{Sg,s}$, a sharp increase is noticed in the relative error, reaching 140%. The relative error then decreases again, and OLGA underpredicts the data at v_{Sg} < 10 m/s. For the most part, OLGA's predictions are in better agreement with the experimental data, except at around $v_{Sg,s}$. This indicates the need for the OLGA model to consider the churn flow as a separate flow pattern, instead of using the slug flow model for the churn region.

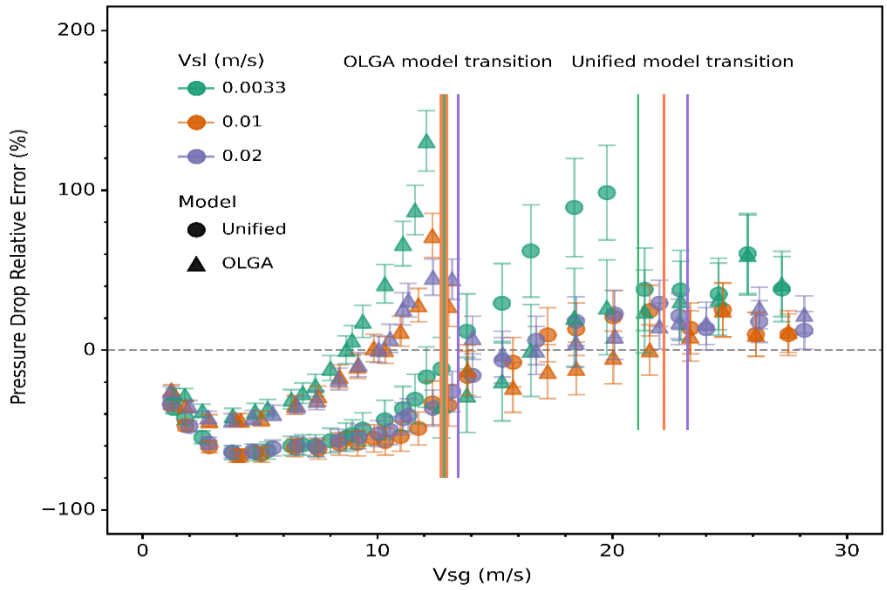

Figure 4-9: Relative error of OLGA and Unified model pressure drop predictions at varying v_{Sg} values

The experimental liquid holdup data were compared to the TUFFP Unified model data. Figure 4-10 reveals this comparison for all the v_{Sg} values tested. Overall, the Unified model overpredicts the experimental liquid holdup at v_{Sg} > 14 m/s. When close to the minimum v_{Sg}, both models have good predictions and match the experimental data. At v_{Sg}< 14 m/s, the Unified model underpredicts the liquid holdup notably for all the v_{SL} values. Contrary to the Unified model, OLGA underpredicts the experimental data at v_{Sg} > $v_{Sg,S}$ and overpredicts them at v_{Sg} < $v_{Sg,S}$.

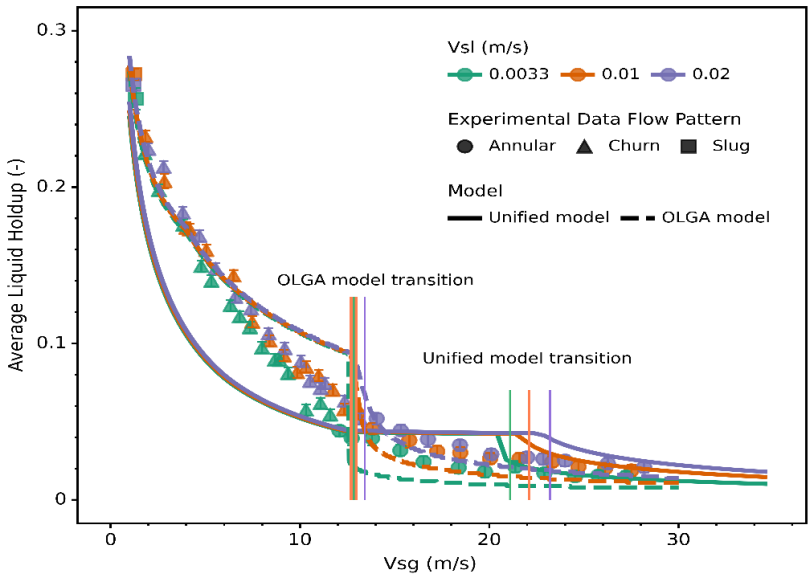

Figure 4-10: Experimental liquid holdup data vs. superficial gas velocity, compared to the Unified and OLGA models

Figure 4-11 shows the relative error of liquid holdup predictions vs. superficial gas velocity. At v_{Sg} > 14 m/s, the Unified model predictions are closer, with slight overpredictions for the liquid holdup. However, for v_{SL} = 0.0033 m/s and v_{Sg} > 14 m/s,

the Unified model highly overpredicts the holdup and reaches a maximum error of more than 100% at v_{Sg} = 20 m/s. The reason behind this increase is the change of flow pattern predicted by the model from annular to slug around that point. Churn flow has a higher liquid holdup than the annular flow pattern. At v_{Sg} < 14 m/s (46 ft/s), the unified model underpredicts the liquid holdup for all superficial liquid velocities. On the other hand, the OLGA model underpredicts the experimental data at $v_{Sg} > v_{Sg,S}$ and overpredicts it at $v_{Sg} < v_{Sg,S}$,and reaches a maximum error of more than 120%. OLGA's predictions are more accurate at very low gas rates close to the slug flow pattern (v_{Sg}<4 m/s).

Belt et al. (2011) compared the predictions of OLGA to experimental data in vertical and near vertical pipes. The result demonstrated that in churn and churn/annular flow regions, the predications were not adequate compared to the predictions in slug and annular flow patterns. This is because OLGA utilizes the same drift flux model of slug flow pattern for churn and churn/annular flow patterns. In addition, Pagan et al. (2016) compared several models including OLGA to experimental data in vertical pipes. The result showed that the model had good predictions for annular flow, while it mismatches the experimental data in churn flow region. They explained that the mismatch is due to the non-inclusion of a separate model for churn flow in the models, as slug or annular flow models are used for churn flow.

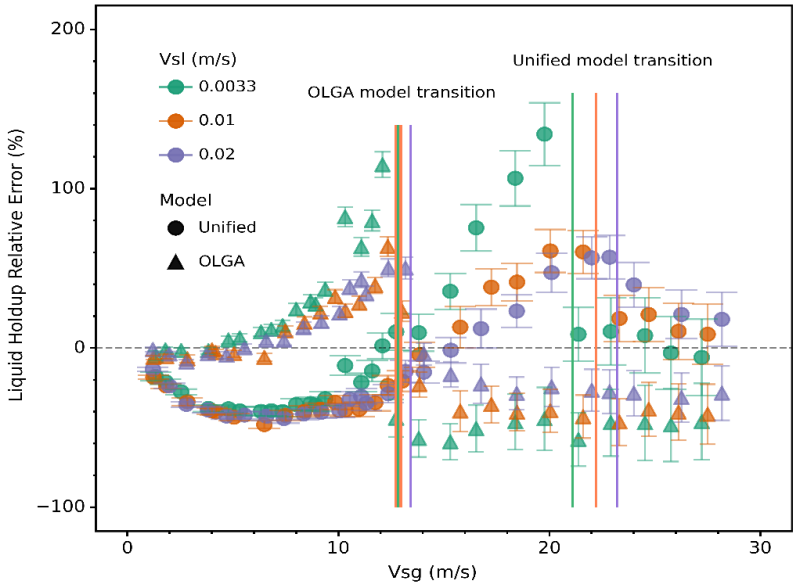

Figure 4-11: Relative error of liquid holdup model prediction vs. v_{Sg}

Several models were employed to predict the onset of liquid loading. In addition to OLGA and unified models, the liquid film reversal model (Barnea, 1987) and liquid droplet models (Coleman et al., 1991; Guo et al., 2005; Li et al., 2002; Turner et al., 1969, Wang and Liu 2007) were evaluated. The inflection point approach (Skopich et al., 2015) was also included. These models were availed in the comparison of the onset of liquid loading with the experimental values of flow pattern transition through visual observation, minimum pressure drop, and positive frictional pressure gradient.

The transition from annular to slug was defined as the onset of liquid loading for the Unified and OLGA models. For the inflection point estimation, the rate of liquid holdup change was determined using a second-degree fitted polynomial to minimize uncertainties. The second degree has a coefficient of determination (R^2) of 0.97, indicating that using a higher order polynomial is not necessary. Moreover, if a higher

order polynomial is used, the inflection points may have multiple roots, including imaginary roots.

The onset of liquid loading predictions of the aforementioned models were compared to the v_{Sg} at which the change of flow pattern was visually observed in the experiments. Table 4-1 depicts the summary of the model predictions and their relative errors compared to the visual observations. The OLGA model predicts the results more precisely than the other models for v_{SL} = 0.0033, 0.01, and 0.02 m/s with relative errors of 10.7, 4.0, and 1.7%, respectively. Surprisingly, the droplet model by Coleman et al. (1991) predicts the results with low errors of 20.7, 13.1, and 6% for v_{SL} = 0.0033, 0.01, and 0.02 m/s, respectively. This could be because low wellhead pressure data were used in Coleman et al.'s (1991) model, which is close to the conditions of this study. The Unified model, Barnea's model (1987), and inflection point method overpredict the onset of liquid loading at all superficial liquid velocities, while Li et al. (2002) and Wang and Liu's (2007) models always underpredict it. The positive frictional pressure gradient occurs at superficial gas velocities higher than the visual observation with relative errors of 42.2, 12.1, and 6.4% for v_{SL} = 0.0033, 0.01, and 0.02 m/s, respectively. Figure 4-12 shows the predictions of the liquid loading models compared to the experimental data. The liquid droplet models are independent of v_{SL} and present constant v_{Sg} values.

Table 4-1 : Onset of Liquid Loading Models' Predictions

Onset of Liquid Loading Models Prediction	v_{SL} = 0.0033 (m/s)		v_{SL} = 0.01 (m/s)		v_{SL} = 0.02 (m/s)	
	v_{Sg}, (m/s)	Relative Error (%)	v_{Sg}, (m/s)	Relative Error (%)	v_{Sg}, (m/s)	Relative Error (%)
OLGA model	12.8 (42.1 ft/s)	10.7	12.8 (42.1 ft/s)	4.0	13.4 (44.05 ft/s)	1.7
TUFFP Unified model	21.1 (69.21 ft/s)	81.9	22.1 (72.5 ft/s)	79.0	23.2 (76.1 ft/s)	75.8
Barnea (1987)	21.7 (71.2 ft/s)	87.0	23 (45.44 ft/s)	86.4	23.6 (77.4 ft/s)	78.8
Turner et al. (1969)	16.2 (53.14 ft/s)	39.5	16.2 (53.14 ft/s)	31.3	16.2 (53.14 ft/s)	22.7
Coleman et al. (1991)	14 (45.92 ft/s)	20.7	14 (45.92)	13.4	14.0 (45.92 ft/s)	6.0
Li et al. (2002)	6.3 (20.66 ft/s)	-45.7	6.3 (20.66 ft/s)	-49.0	6.3 (20.66 ft/s)	-52.3
Wang and Liu (2007)	14.9 (48.87 ft/s)	28.4	14.9 (48.87 ft/s)	20.7	14.9 (48.87 ft/s)	12.9
Guo et al. (2005)	16.7 (54.8 ft/s)	44.0	16.7 (54.8 ft/s)	35.3	16.7 (54.8 ft/s)	26.51
Inflection point	23.4 (76.75 ft/s)	102.0	23.2 (76.1 ft/s)	88.0	22.6 (74.13 ft/s)	71.2
Positive friction pressure gradient	16.5 (54.12 ft/s)	42.2	13.84 (45.4 ft/s)	12.1	14.1 (46.1 ft/s)	6.4
Minimum pressure drop	18.4 (60.35 ft/s)	58.6	17.25 (56.6 ft/s)	39.8	18.5 (60.7 ft/s)	40.1

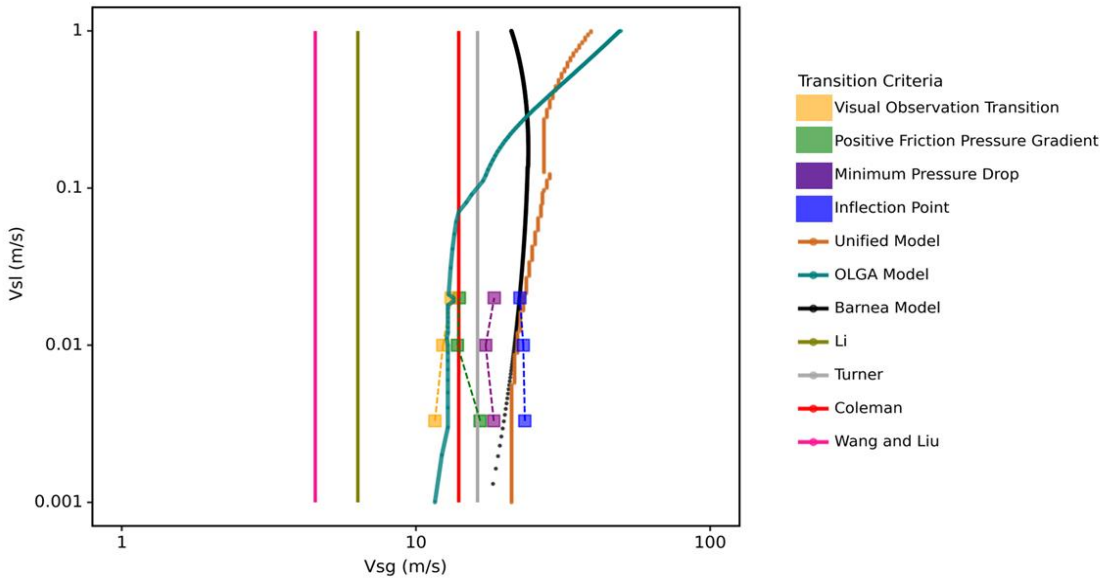

Figure 4-12: Water-Air Predictions of onset of liquid loading models compared to the experimental data

4.3 Oil-Air Flow

This section analyzes the fluid flow and onset of liquid loading for oil-air two-phase flow. A comparison of visual observations for flow pattern transitions is shown with an analysis of the pressure drop, frictional pressure gradient, and liquid holdup.

4.3.1 Visual Flow Pattern Transition Observations

Figure 4-13 shows the flow behavior as the v_{Sg} decreases for $v_{SL=}$ 0.02 m/s. Figure 4-13(a) shows the flow in the annular region, where the liquid film and droplets are continuously traveling upward. The onset of liquid loading and the change to churn flow are depicted in Figure 4-13(b). The onset of liquid loading occurs when the liquid film starts to reverse, and the flow becomes more chaotic. Figure 4-13(c) shows the churn flow behavior with larger waves when compared to that shown in Figure 4-13(b).

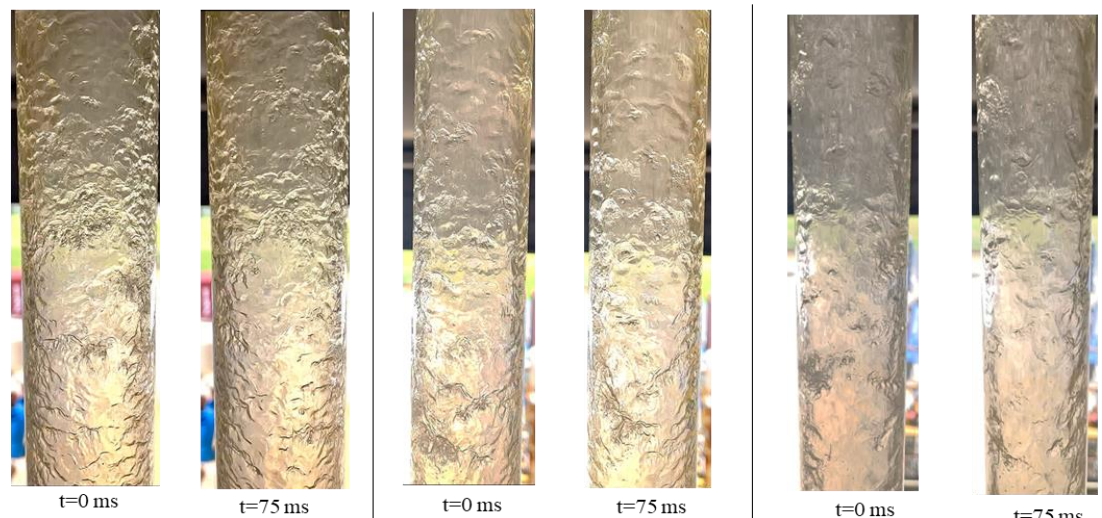

a. v_{Sg} = 15.25 m/s (50 ft/s), annular

b. v_{Sg} = 10.4 m/s (34 ft/s), onset of liquid loading

c. v_{Sg} = 6.1 m/s (20 ft/s), churn

Figure 4-13: Snapshots of flow pattern transitions for $v_{SL=}$ 0.02 m/s (0.033 ft/s) and decreasing v_{Sg} values

4.3.2 Pressure Drop Results

Figure 4-14 demonstrates the relationship between total pressure drop and v_{Sg} for v_{SL} =0.0033, 0.01, and 0.02 m/s. The pressure drop values are denoted by green, orange, and purple markers, respectively. Two flow patterns are identified by visual observation, namely, annular and churn, assigned circular and triangular marker shapes, respectively. Visual observation shows that the transition from annular to churn flow occurs at v_{Sg} values of 9.1, 9.1, and 10.4 m/s for v_{SL}=0.0033, 0.01, and 0.02 m/s, respectively. The total pressure drop curve is almost hook-shaped, with a sharp increase as v_{Sg} decreases at $v_{Sg} < v_{Sg,min}$, for all cases. The minimum pressure drop occurs at a $v_{Sg,min}$ of 6.7, 6.7, and 7.3 m/s for v_{SL}=0.0033, 0.01, and 0.02 m/s, respectively. This means that the transition to churn flow occurs at a higher v_{Sg} than the $v_{Sg,min}$ value for all cases.

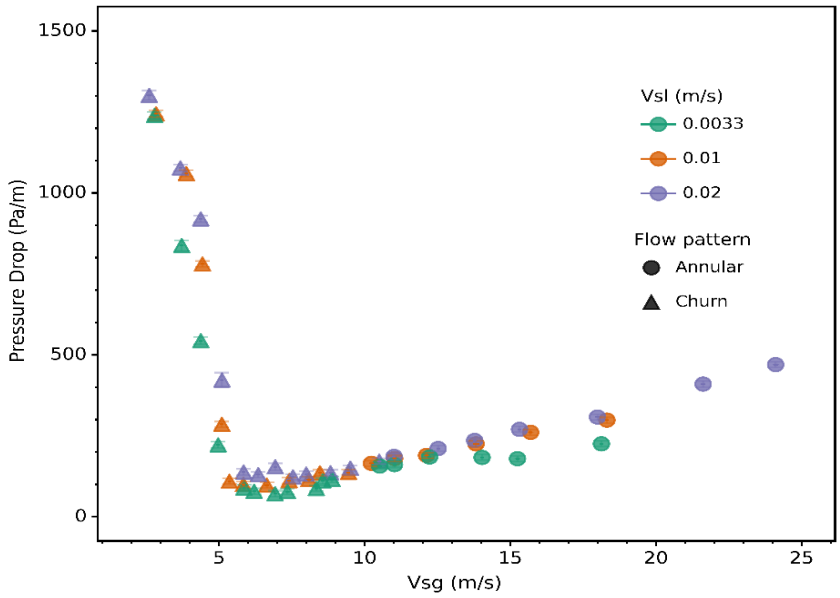

Figure 4-14: Total pressure drop vs. superficial gas velocity

Figure 4-15 illustrates the frictional and gravitational pressure drops for oil-air tests as functions of v_{Sg}. The square-shaped markers represent the gravitational pressure drop, $(dp/dL)_G$, while the diamond-shaped markers represent the frictional pressure drop, $(dp/dL)_F$. The colors used to represent v_{SL} =0.0033, 0.01, and 0.02 m/s are green, orange, and purple, respectively. At a constant v_{SL}, the frictional pressure drop increases and the gravitational pressure drop decreases by increasing v_{Sg}. When $v_{Sg} > v_{Sg,min}$, the frictional pressure loss becomes more dominant. As a result, the total pressure drop increases as the v_{Sg} increases, as shown in Figure 4-14. When $v_{Sg} < v_{Sg,min}$, the gravitational pressure loss becomes dominant, and increases sharply by decreasing v_{Sg}. This increase is because of the decrease in gas energy and generation of large liquid waves, as the gas is unable to overcome the reversed liquid film.

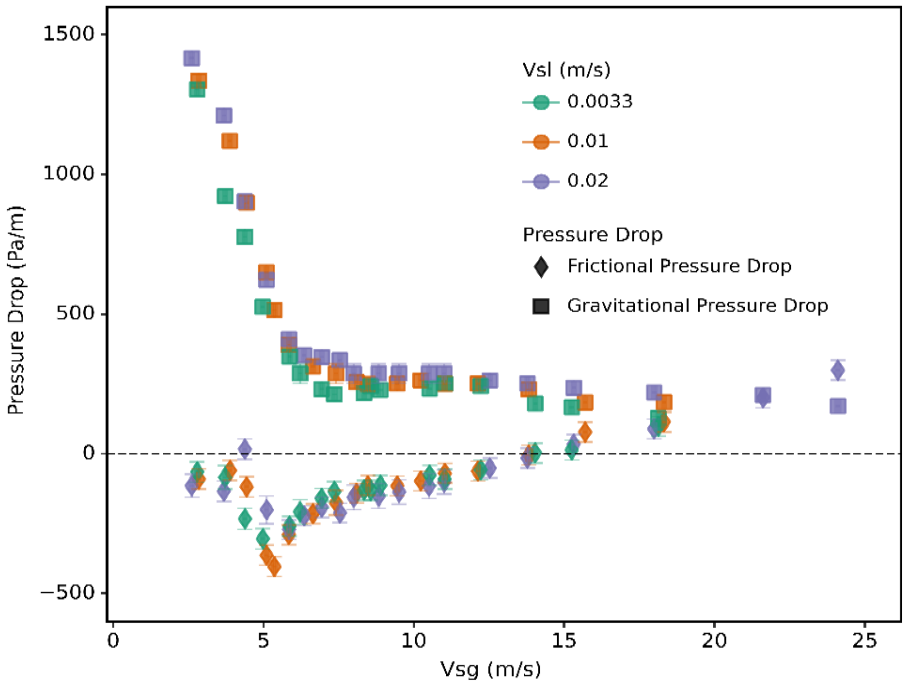

Figure 4-15: Gravitational and frictional pressure drop vs. superficial gas velocity

4.3.3 *Positive Frictional Pressure Gradient*

In this section, the positive frictional pressure gradient approach is used to analyze the experimental data of oil-air flow. Figure 4-16 shows the frictional pressure drop vs. v_{Sg} for v_{SL}=0.0033, 0.01, and 0.02 m/s, indicated using green, orange, and purple markers, respectively. The two flow patterns identified by visual observation, namely annular and churn flows, are assigned circular and triangular shapes, respectively. For a constant v_{SL}, the frictional pressure drop continues to decrease until it reaches a zero value, after which it changes to a negative drop or a positive gradient. The figure shows that at v_{SL}=0.0033, 0.01, and 0.02 m/s, the frictional pressure drop switches signs at v_{Sg} = 12.2, 13.7, and 13.7 m/s, respectively. The v_{Sg} values at which the sign switches are close for each v_{SL} and within the data uncertainty.

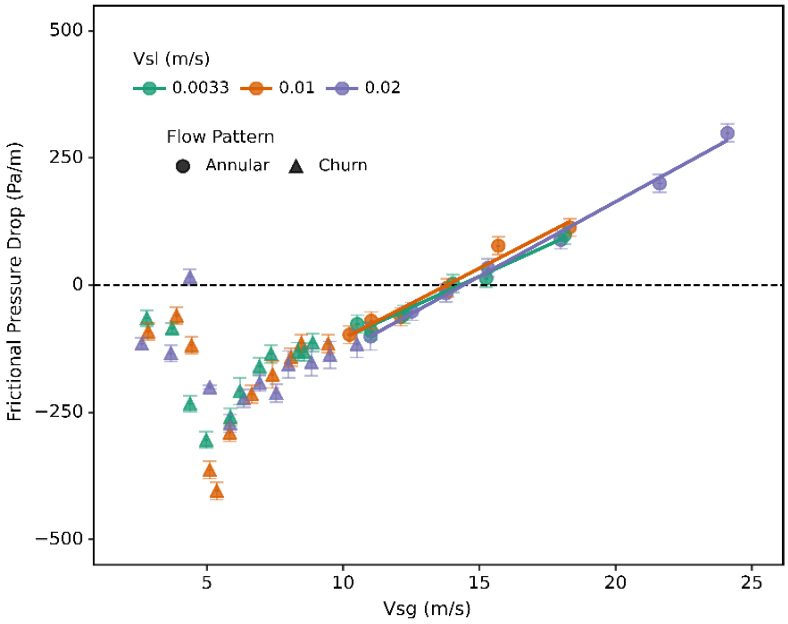

Figure 4-16: Frictional pressure drop vs. superficial gas velocity

4.3.4 Liquid Holdup Results

Figure 4-17 shows the average liquid holdup vs. v_{Sg} at v_{SL}=0.0033, 0.01, and 0.02 m/s, indicated using green, orange, and purple markers, respectively. The two flow patterns visually detected, namely annular and churn flows, are assigned circular and triangular shapes, respectively. At a constant v_{SL}, the average liquid holdup increases as the v_{Sg} is decreased. The increasing rate in holdup becomes much sharper as the flow pattern switches from annular to churn flow, due to the loading and buildup of liquids in the tubing. Additionally, the liquid holdup slightly increases as the v_{SL} is increased at a constant v_{Sg}, due to the increase in the volumetric liquid rate.

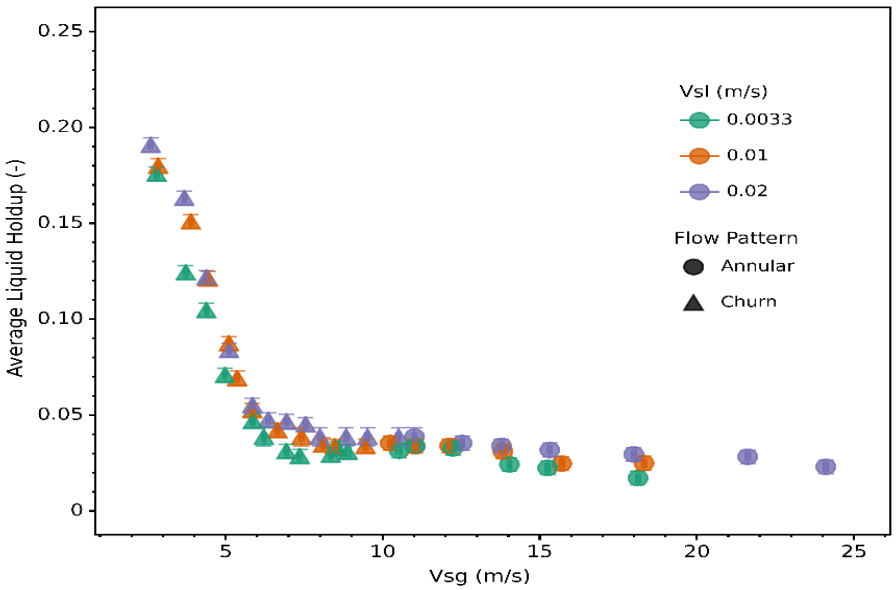

Figure 4-17: Liquid holdup vs. superficial gas velocity

4.3.5 Model Evaluations

Similar to the water-air model evaluation, the attained experimental results were applied to evaluate the performances of some commonly used models. The predictions of

the unified and OLGA models were compared to the total pressure drop, liquid holdup, and flow pattern data. In addition, the onset of liquid loading predictions of some common models were compared to the visual observations of flow pattern transition.

Figure 4-18 compares the experimental pressure drop data with the predictions of the OLGA and the TUFFP unified models. Additionally, the transitions between the annular and slug flow patterns are shown for both models. None of these two models differentiate churn and slug flows. The unified model overpredicts the experimental data at v_{Sg} > 5 m/s for all the superficial liquid velocities, but it underpredicts the pressure drop at v_{Sg} < 5 m/s. Like the unified model, OLGA underpredicts the experimental data at v_{Sg} < 5 m/s. The OLGA model also mostly overpredicts the experimental data at v_{Sg} > 5 m/s. The trends in the data seem to be better captured by the unified model while in annular flow. However, the errors of both models increase while in churn flow.

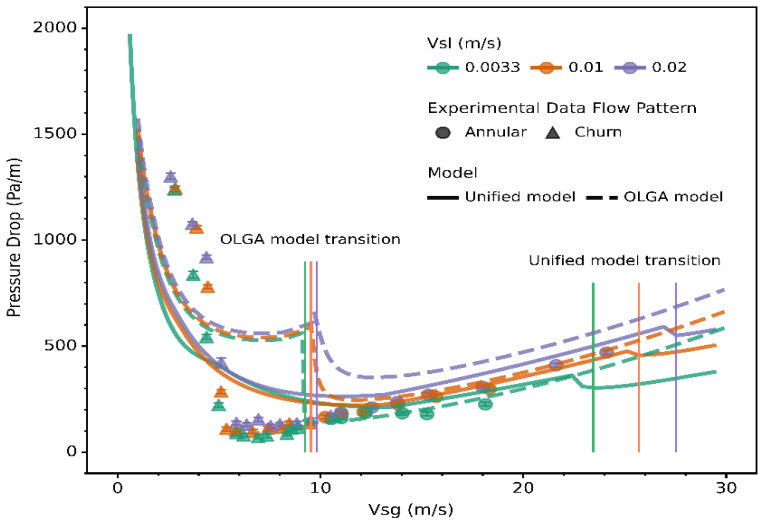

Figure 4-18:Comparison of pressure drop data with OLGA and unified model predictions at varying v_{Sg} values

Figure 4-19 displays the relative errors of the pressure drop predictions for the unified and OLGA models compared to the experimental data with respect to v_{Sg}. The figure shows an inverted V-shaped curve for both models, with most of the data being overpredicted. The maximum relative errors are observed around $v_{Sg,min}$, where OLGA's relative error exceeds 500%. This can be attributed to the change of the predicted flow regime from annular to slug flow by the OLGA model at that point. This indicates the need to consider the churn flow pattern as a separate flow regime and use churn flow models to predict the pressure drop. The errors of both models are close to zero at high gas rates, corresponding to annular flow. The errors also get close to zero at very low gas rates, when approaching the slug flow pattern.

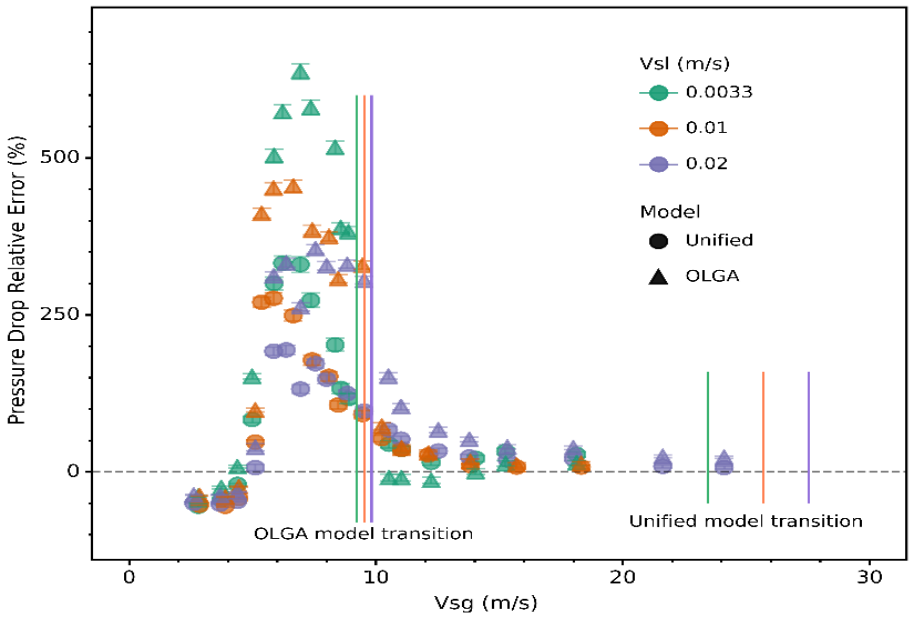

Figure 4-19: Relative error of OLGA and unified model pressure drop predictions at varying v_{Sg} values

The experimental liquid holdup data of this study were compared to the predictions of TUFFP unified and OLGA models. Figure 4-20 reveals this comparison for all the v_{Sg} values tested. Overall, the unified model overpredicts the experimental liquid holdup except at v_{Sg} < 5 m/s. Contrary to the Unified model, OLGA underpredicts the experimental data at $v_{Sg} > v_{Sg,S}$, corresponding to annular flow. At the v_{Sg} of flow pattern transition, a jump is observed in OLGA model predictions. As a result, OLGA overpredicts the holdup at $v_{Sg} < v_{Sg,S}$. When approaching the slug flow and the minimum tested v_{Sg}, both models have good predictions. But the largest errors are observed in the churn flow region, where the holdup values are overpredicted by both models.

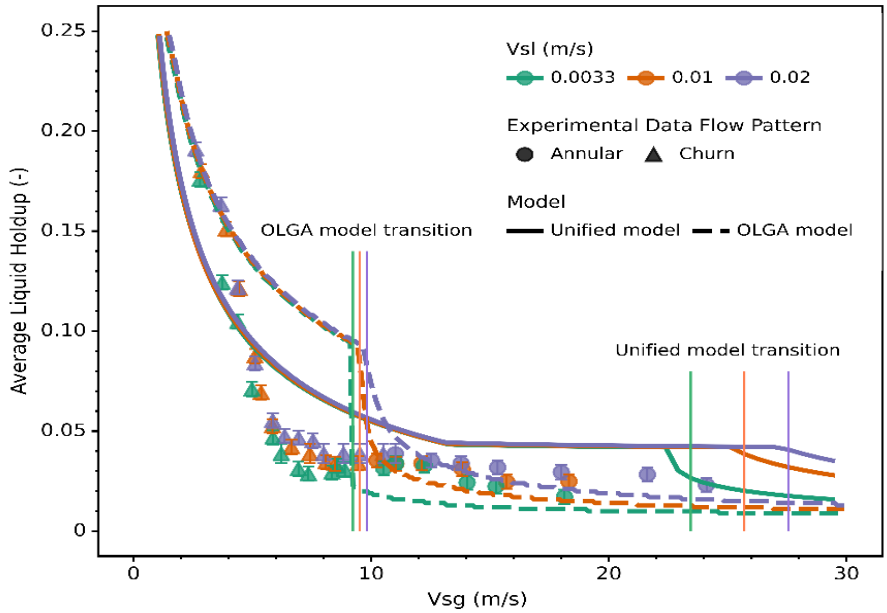

Figure 4-20: Experimental, OLGA and unified model predictions of liquid holdup data vs. superficial gas velocity

Figure 4-21 shows the relative errors of unified and OLGA model predictions for liquid holdup vs. v_{Sg}. The unified model overpredicts the liquid holdup except for the tests

with $v_{Sg} < 5$ m/s. On the other hand, the OLGA model underpredicts the experimental data at $v_{Sg} > v_{Sg,S}$ and overpredicts them at $v_{Sg} < v_{Sg,S}$. The change of predicted flow pattern by the model from annular to slug around that point could be the reason for the change of prediction. The errors of both models are maximized around the onset of liquid loading, where churn flow is expected, which is consistent with the pressure drop predictions.

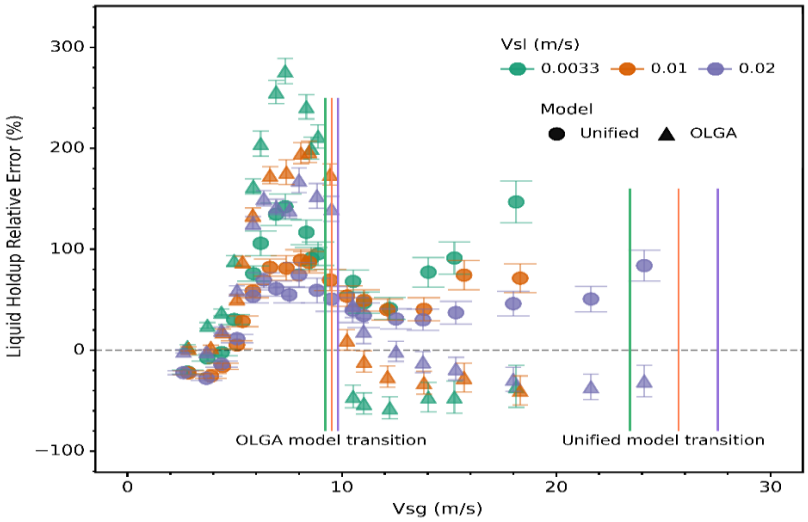

Figure 4-21: Relative errors of liquid holdup OLGA and unified model predictions vs. superficial gas velocity

4.3.6 Onset of Liquid Loading Prediction

Several models were employed to predict the onset of liquid loading. For the unified and OLGA models, the transition from annular to slug flow was defined as the onset of liquid loading. Additionally, the predictions of liquid film reversal model of Barnea (1987) and liquid droplet models of Coleman et al. (1991), Li et al. (2002), Turner et al. (1969), and Wang and Liu (2007) were used in the comparisons. The positive frictional pressure gradient, minimum pressure drop, and inflection point approach of

Skopich et al. (2012) were also included. The onset of liquid loading predictions of these models were compared to the v_{Sg} at which the change of flow pattern is visually observed in the experiments. Figure 4-22 shows the predictions of the liquid loading models compared to the experimental data. The liquid droplet models are independent of v_{SL} and predict a constant onset v_{Sg} for all the v_{SL} values.

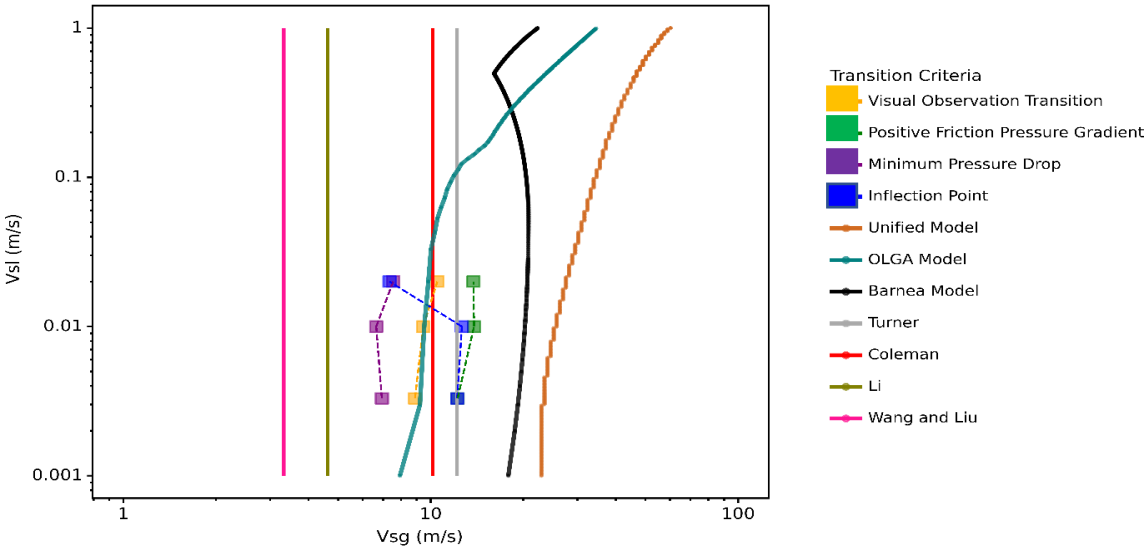

Figure 4-22: Onset of liquid loading predictions of various models compared to the oil-air experimental data

Table 4-2 summarizes the model predictions for onset of liquid loading and their relative errors compared to the visual observations. The OLGA model predicts the onset more precisely than the other models for v_{SL} = 0.0033, 0.01 and 0.02 m/s with relative errors of 3.8, 0.75, and -6.5%, respectively. The droplet model by Coleman et al. (1991) also predicts the results with low errors of 14, 7, and -3.4% for v_{SL} = 0.0033, 0.01, and 0.02 m/s, respectively. This could be because the low wellhead pressure data used in the

model by Coleman et al. (1991) are closer to the condition of this study. This is in agreement with the previously presented water-air experiments. The shift to slug flow is overpredicted by the unified, Barnea (1987), and Turner models. On the other hand, Li and Wang and Liu's models underpredict the transition. The inflection point has a close match to the minimum pressure drop and underpredicts the transition at v_{SL} = 0.02 m/s. At v_{SL} = 0.0033, and 0.01 m/s, the inflection point approach overpredicts the visually observed transition and closely matches the positive friction pressure gradient approach.

Table 4-2: Onset of liquid loading models' predictions and errors for oil-air flow

Onset of Liquid Loading Models Prediction	v_{SL} = 0.0033 m/s		v_{SL} = 0.01 m/s		v_{SL} = 0.02 m/s	
	v_{Sg} (m/s)	Relative Error (%)	v_{Sg} (m/s)	Relative Error (%)	v_{Sg} (m/s)	Relative Error (%)
OLGA model	9.225 (30.3 ft/s)	3.8	9.5 (31.2 ft/s)	0.75	9.8 (32.21 ft/s)	-6.5
TUFFP unified model	23.4 (76.9 ft/s)	164	25.7 (84.3 ft/s)	172	27.5 (90.3 ft/s)	162
Barnea (1987)	19.2 (63 ft/s)	116	20.25 (66.4 ft/s)	114	20.6 (67.6 ft/s)	96
Turner et al. (1969)	12.2 (40 ft/s)	39.5	12.2 (40 ft/s)	31	12.2 (40 ft/s)	23
Coleman et al. (1991)	10.15 (33.3 ft/s)	14	10.15 (33.3 ft/s)	7	10.15 (33.3 ft/s)	-3.4
Li et al. (2002)	4.6 (15.14 ft/s)	-48	4.6 (15.14 ft/s)	-51	4.6 (15.14 ft/s)	-56
Wang and Liu (2007)	3.3 (10.9 ft/s)	-63	3.3 (10.9 ft/s)	-65	3.3 (10.9 ft/s)	-69
Inflection point	12.2 (40 ft/s)	37	12.6 (41.3 ft/s)	34	7.4 (24.3 ft/s)	-30
Positive friction pressure gradient	12.2 (40.1 ft/s)	38	13.8 (45.4 ft/s)	46	13.8 (45.2 ft/s)	45
Minimum pressure drop	6.9 (22.7 ft/s)	-22	6.65 (21.8 ft/s)	-30	7.5 (24.75 ft/s)	-28

4.4 Effects of Liquid Properties

This section aims to demonstrate how the properties of the liquid phase affect flow behavior and the onset of liquid loading for two-phase flow. Results for water-air and oil-

air tests were compared in terms of pressure drop and liquid holdup. In addition, onset of liquid loading based on flow pattern transition using visual observation, minimum pressure gradient, and positive frictional pressure gradient were presented.

4.4.1 Pressure Drop Results

Experimental water-air and oil-air data were utilized to analyze the effects of liquid properties on the fluid flow behavior. Figure 4-23 demonstrates the total pressure drop in relation to v_{Sg} for v_{SL}=0.0033, 0.01, and 0.02 m/s, indicated using green, orange, and purple markers, respectively. The two tested liquids, oil and water, are represented using circular and triangular shapes, respectively. The water case has a noticeably higher $v_{Sg,min}$ compared to the oil case, because of the higher density of water, which expands the gravitationally dominant flow region and increases the value of $v_{Sg,min}$.

As the v_{Sg} decreases within the churn flow region, the water-air flow has a significantly higher pressure drop compared to oil-air flow. This might be because oil has a lower surface tension, which can significantly amplify the interfacial wave structure. In churn flow, the liquid is carried upward by means of large waves and droplet entrainment. As a result, this stronger wave structure for oil-air flow helps unload the liquid film and entrained droplets to a higher extent and lower the liquid holdup, and hence, the pressure drop. However, at a $v_{Sg,}$ value of around 5 m/s, the pressure drop increases sharply as the v_{Sg} is decreased for the oil case. On the other hand, the water case has a smoother trend with a more gradual increase in pressure drop. This sharp increase in pressure drop occurs

when the gravitational losses become dominant, and the entrainment fraction is insufficient to transfer the liquid to the surface.

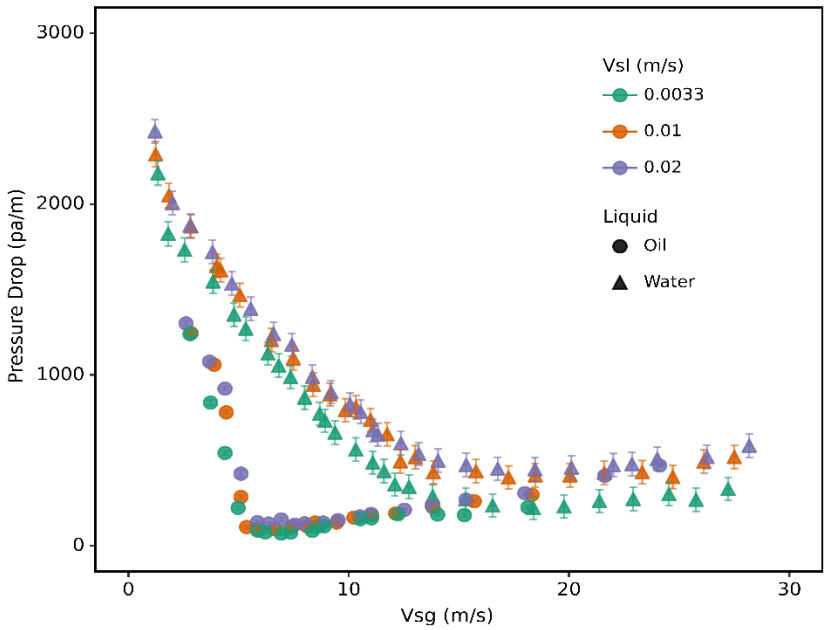

Figure 4-23: Total pressure drop comparison of oil-air and water-air flow

In order to quantify the differences between oil-air and water-air cases, a pressure drop change term was defined using the following formula:

$$\text{Pressure drop change} = \frac{\text{pressure drop of oil} - \text{pressure drop of water}}{\text{pressure drop of water}} \qquad (4\text{-}1)$$

The pressure drops of water and oil cases are determined at the same v_{Sg} values, by fitting a six-degree polynomial over the pressure drop data of water-air flow for each v_{SL}. These polynomials provide a coefficient of determination (R^2) of 99.6%. Figure 4-24 indicates that the pressure drop change is the highest (or the most negative) around the onset of liquid loading, where the oil-air flow has a significantly lower pressure drop than water-air flow. This region roughly represents a churn flow window. At $v_{Sg,} > v_{Sg,min}$, and

particularly at very high v_{Sg} values, the pressure drop change approaches zero, showing minimal liquid type effects in annular flow. Also, as the v_{Sg} decreases at $v_{Sg,} < v_{Sg,min}$, the pressure drop change approaches zero, showing similarly minimal liquid type effects in the slug flow pattern.

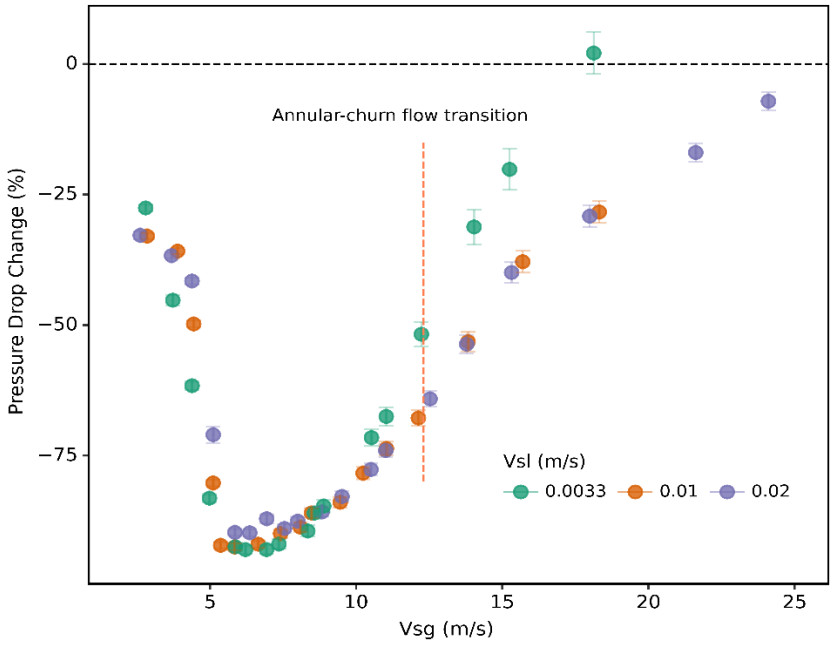

Figure 4-24: Pressure drop change of oil-air flow compared to water-air flow

4.4.2 Liquid Holdup Results

Figure 4-25 shows the liquid holdup vs. v_{Sg} for v_{SL}=0.0033, 0.01, and 0.02 m/s, indicated using green, orange, and purple markers, respectively. The tests with oil and water are represented using circular and triangular shapes, respectively. The liquid holdup changing trends are similar to that of pressure drop, seen in Figure 4-24, with a sharp increase of holdup at $v_{Sg,} < v_{Sg,min}$. The liquid holdup of oil-air flow is substantially lower than water-air flow around the onset of liquid loading, similar to what was seen for

pressure drop. As discussed earlier, this can be attributed to the lower surface tension of oil resulting in larger interfacial wave structures and droplet entrainment, which in turn helps unload the liquids from the tubing and reduces the liquid holdup.

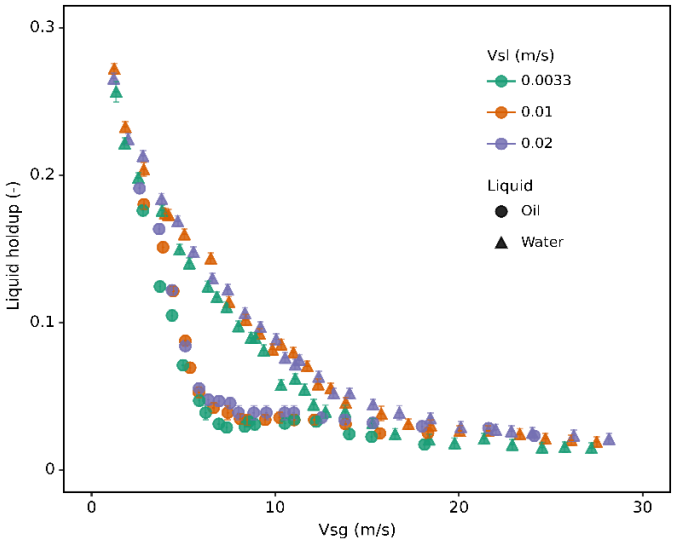

Figure 4-25: Liquid holdup comparison of oil-air and water-air flows

Figure 4-26 shows the liquid holdup change, defined to quantify the differences in the liquid holdup of oil-air flow, compared to water-air flow. This term is calculated using the following formula:

$$\text{Liquid holdup change} = \frac{\text{liquid holdup of oil} - \text{liquid holdup of water}}{\text{liquid holdup of water}} \qquad (4\text{-}2)$$

Sixth-degree ploynomials are used to fit the liquid holdup data of water-air flow for each v_{SL} and estimate the liquid holdup for the same v_{Sg} as the corresponding oil-air flow. These polynomials have a coefficient of determination (R^2) of more than 99%. A V-shaped curve is observed with the maximum liquid holdup decrease of oil-air flow

occurring around the $v_{Sg,min}$, corresponding to churn flow. This is because oil has a lower density and surface tension than water. The values of change in holdup are higher than the pressure drop change values, indicating that the liquid properties mainly affect the gravitational pressure drop. At very high v_{Sg} values, corresponding to annular flow, and very low v_{Sg} values, approaching the slug flow, the liquid holdup changes get closer to zero, showing the reduced effect of liquid phase properties on liquid holdup.

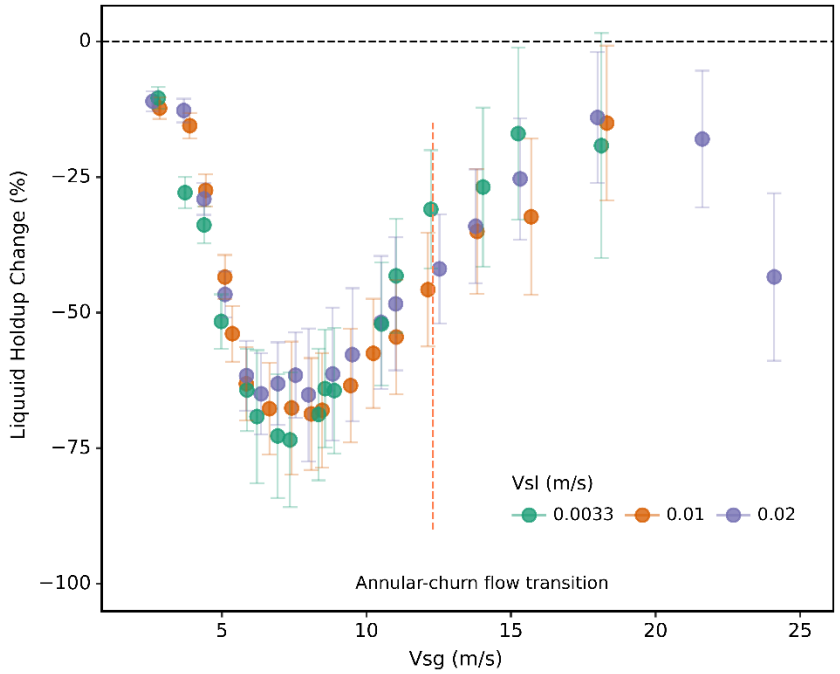

Figure 4-26: Liquid holdup change of oil-air flow compared to water-air flow

4.4.3 Experimental Results Summary

The onset of liquid loading is one of the most important parameters to predict in a gas well. Various researchers have used different techniques to identify this onset. The change in flow pattern from annular to churn can be defined as the point at which the

liquid film reverses in the test section. In this section, the visual annular-churn flow regime transition was compared to the positive frictional pressure gradient and minimum pressure drop. Figure 4-27 shows a summary of the onset of liquid loading for oil-air and water-air flow, based on positive frictional pressure gradient, minimum pressure drop, and visual observations, represented using green, purple, and yellow colors, respectively.

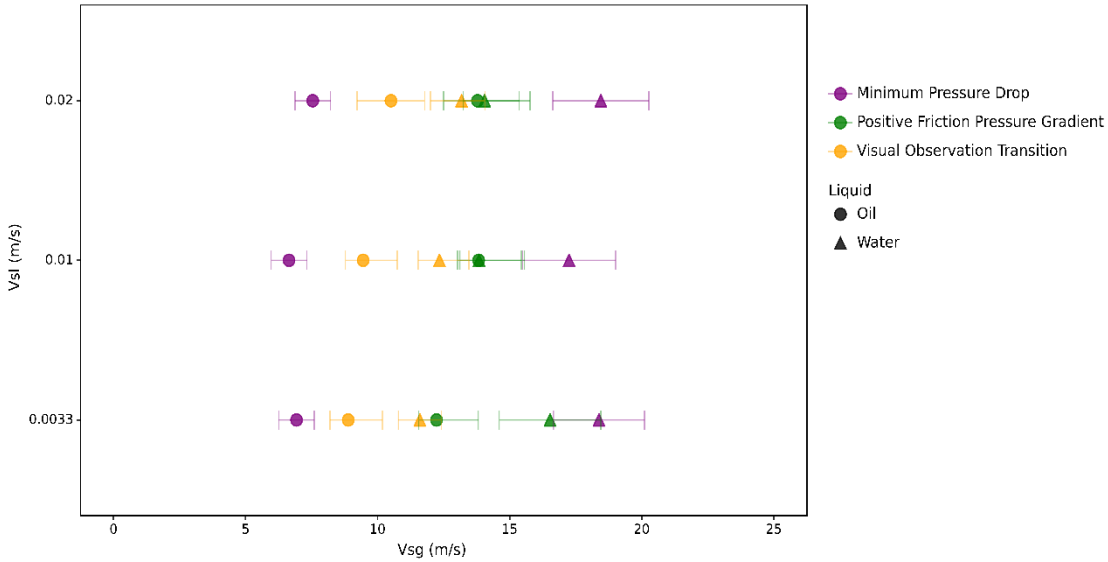

Figure 4-27:Onset of liquid loading, based on various criteria

The onset of liquid loading occurs at a lower v_{Sg} for the oil case compared to water. This is because oil has a lower density and surface tension, resulting in the improved interfacial wave structure and droplet entrainment. Moreover, the oil-air flow transition as identified through visual observation occurs at a higher v_{Sg} than the minimum pressure drop and a lower v_{Sg} than the positive frictional pressure drop. Whereas, in the water test, the visual observation transition occurs at a lower v_{Sg} than both the minimum pressure drop and positive frictional gradient approaches. The minimum pressure drop

technique is a function of balance between gravitational and frictional losses. It may occur at a different point than the onset of liquid loading depending on the liquid phase properties, as observed here. For oil-air flow, the lower oil density lowers the gravitational dominant region, and the low surface tension increases the droplet entrainment and helps transfer the liquids to the top even when the liquid film begins to reverse. This shifts the minimum pressure drop to a lower v_{Sg}. The positive friction technique provides relatively more consistent predictions, when compared to the visual observations.

CHAPTER 5

Effect of Inserts on Liquid Lifting

This chapter is an attempt to understand the effects of inserts on water-air and oil-air two-phase flow in vertical tubulars. Three pipe inserts with internal diameters of 1.5, 1.75 were tested in this study to quantify the positive and negative effects of increasing the restriction. The effects of adding restriction on the total pressure drop, its gravitational and frictional elements, and liquid holdup are analyzed in the following sections. The results can help identify the operating windows where restrictions could have a positive or a negative effect on flow dynamics.

5.1 Flow Behavior with Inserts

Firstly, we are going to visualize the multiphase flow patterns with pipe restriction. The insert is installed between the pipe sections and covered by the straub clamp, as shown in Figure 3-3. Two flow behaviors were observed before and after the insert, Figure 5-1: Flow behavior with insert along test section shows the flow behavior before and after the insert. A thin layer of liquid film is observed flowing downward before the insert, with liquid droplets traveling upward, as depicted in Figure 5-1: Flow behavior with insert along test section as the film reversal region. The liquid film is thicker at the inflow of the film reversal region, with the liquid film becoming thinner as

it approaches the insert position. This could be owing to the cumulative amount of deposited liquid droplets thickening the liquid film at the film reversal region's inflow. After the insert, a lot of mixing and agitation are observed, which generates high-amplitude liquid waves. This behavior facilitates droplet generation, as the gas in the core shears the liquid off the waves and entrains droplets, as shown in the wave growth region in Figure 5-1: Flow behavior with insert along test section.

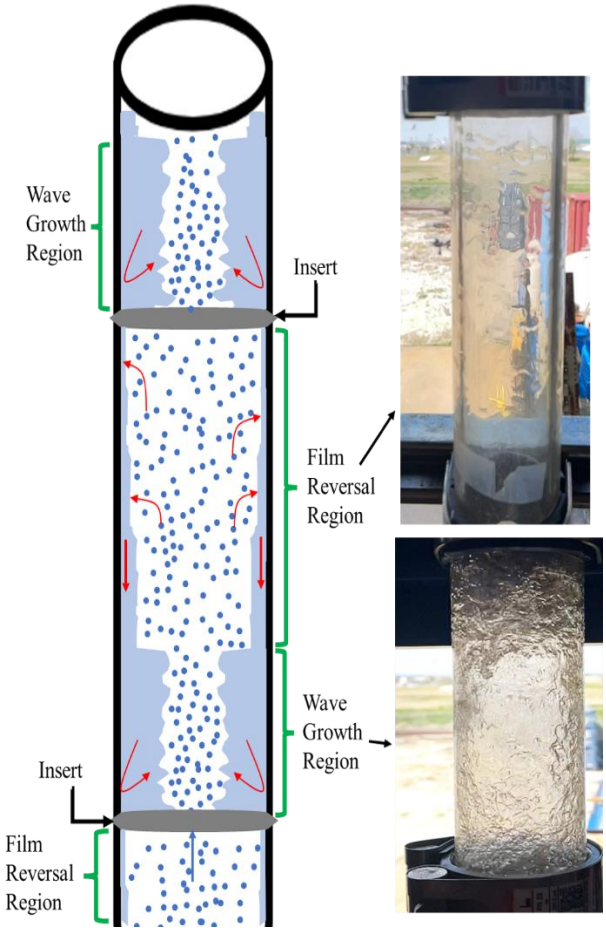

Figure 5-1: Flow behavior with insert along test section

Figure 5-2 shows snapshots of flow behavior through a 1.5-inch insert in water-air flow at v_{SL} =0.0033 m/s and v_{Sg} = 6 m/s. From these snapshots, different behaviors are observed before and after the insert, as previously described and shown in Figure 5-1. Figure 5-3 shows wave growth region after the insert size of 1.5-inch in oil-air flow at v_{SL} =0.0033 m/s and v_{Sg} = 8 m/s. Figure 5-4 illustrate the sequence of film movement in film reversal region after the insert size of 1.5-inch in oil-air flow at v_{SL} =0.0033 m/s and v_{Sg} = 8 m/s. The liquid film waves are highlighted by red circle, and it shows that the film moves in downward direction.

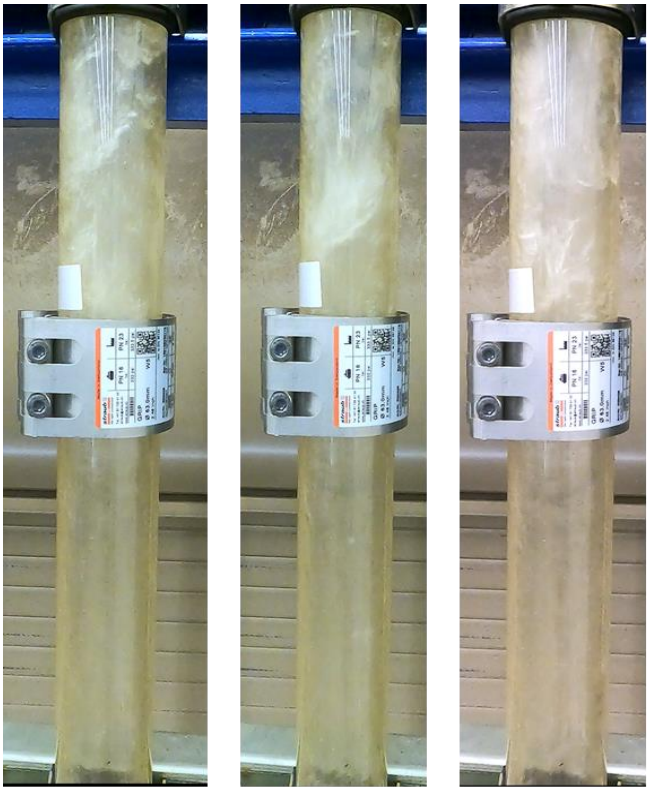

Figure 5-2: Snapshots of flow behavior around insert of 1.5-inch in water-air flow at v_{SL} =0.0033 m/s and v_{Sg} = 6 m/s

Figure 5-3: Wave growth region after the insert sixe of 1.5-inch in oil-air flow at v_{SL} =0.0033 m/s and v_{Sg} = 8 m/s

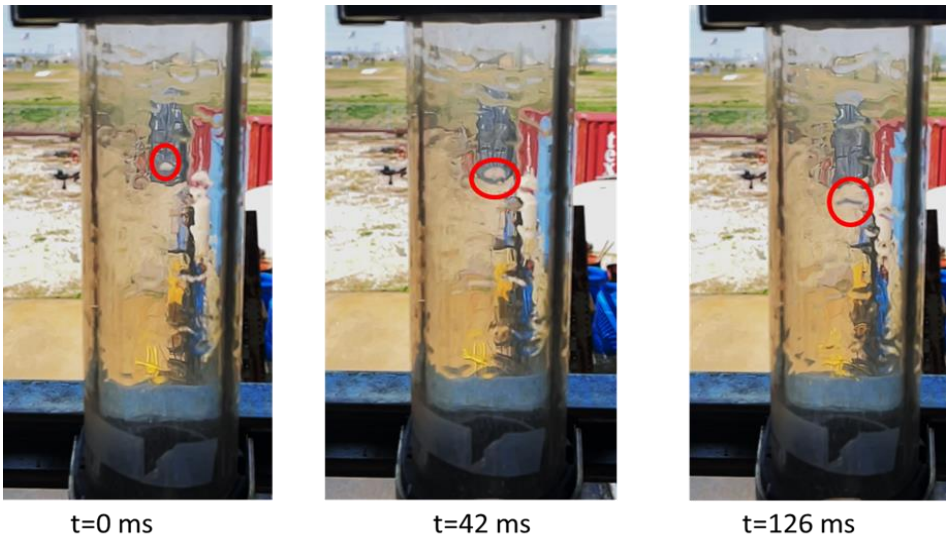

Figure 5-4: Sequence of film movement in film reversal region after the insert sixe of 1.5-inch in oil-air flow at v_{SL} =0.0033 m/s and v_{Sg} = 8 m/s

5.2 Water-air Tests

Figure 5-5 indicates the total pressure drop vs. superficial gas velocity for water-air flow at constant v_{SL} values of 0.0033, 0.01, and 0.02 m/s. The tests with insert ID's of

1.5 and 1.75 inches are shown by green and orange markers, respectively, while the tests with no inserts are presented with purple markers. In this figure, three flow patterns are identified by visual observation, namely, annular, churn and slug, assigned circular, triangular, and square marker shapes, respectively. The total pressure drop curve is hook-shaped for all cases, with an increase in pressure drop as v_{Sg} decreases at $v_{Sg} < v_{Sg,min}$. The results show that the cases with insert have significantly higher pressure drops when v_{Sg} is higher than the $v_{Sg,min}$, for all v_{SL} values. This is the friction dominated region of the flow, and the increased friction by adding the insert is the reason for such behavior. The tests with the 1.5-in. insert correspond to the highest level of restriction and produce the highest pressure drop in this region.

As the flow pattern changes to churn flow at $v_{Sg} < v_{Sg,min}$, the cases with insert have mostly lower pressure drops compared to the no-insert case. For $v_{SL} = 0.01$ m/s, shown in Figure 5-5(b), Insert ID of 1.5 inches has the highest pressure drop for $v_{Sg} > 4$ m/s. On the other hand, for $v_{Sg} < 4$ m/s, the pressure drop with 1.5-inch insert decreases below the pressure drop with no insert. Also, with insert ID of 1.75 inches, the pressure drop is mostly lower than the no-insert case in churn flow. A similar behavior is observed for $v_{SL} = 0.02$ m/s, with the insert having negative impacts at $v_{Sg} > 4$ m/s, and starting to have positive effects at $v_{Sg} < 4$ m/s.

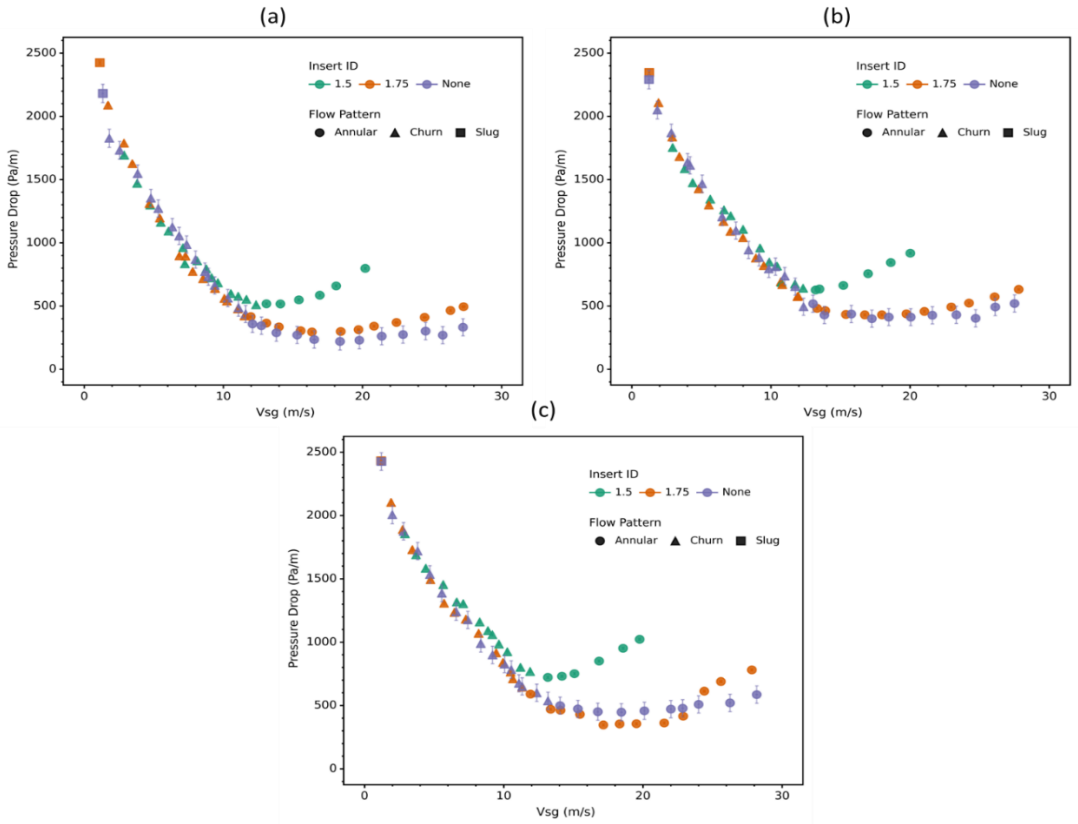

Figure 5-5: Total pressure drop vs. v_{Sg} for water-air flow and various insert cases at (a) v_{SL} = 0.0033 m/s , (b) v_{SL} = 0.01 m/s, (c) v_{SL} = 0.02 m/s

Figure 5-6 shows the gravitational and frictional pressure drops vs. v_{Sg} for various insert IDs and v_{SL} values of 0.0033, 0.01, and 0.02 m/s. Gravitational pressure drop $(dp/dL)_G$ is indicated by the square-shaped markers, while frictional pressure drop $(dp/dL)_F$ is shown by the diamond-shaped markers. Also, insert ID's of 1.5 and 1.75 inches are indicated by green and orange markers, while the no-insert case is presented by purple markers. Insert ID of 1.5 inches has noticeably higher frictional pressure drops compared to the other cases for all v_{SL} values, especially in the annular flow region. This

causes an increase in the total pressure drop, as shown in Figure 5-5. This increase is due to the decrease in insert ID, which causes higher frictional losses.

Figure 5-6(a) at v_{SL} =0.0033 m/s shows that the no-insert case has the highest gravitational pressure drop in the churn region with v_{Sg} values below 10 m/s. This indicates that the inserts have a positive impact on the liquid holdup. The lower pressure drop for the case with insert is because the inserts create large liquid waves at the liquid-gas interface. The gas flowing in the central core shears the liquid waves upward, creating more liquid droplets and carrying them within the core. Since liquid droplets have a higher velocity than the liquid film, liquid holdup and the gravitational pressure drop are reduced. At v_{SL} =0.01 m/s, no noticeable difference is found in the gravitational pressure drop for all cases. At v_{SL} =0.02 m/s, the case with an insert ID of 1.5 inches has the lowest gravitational pressure drop at the early stage of churn flow. But this insert also generates a significantly higher frictional pressure drop, which may negate the positive effect of the higher liquid droplet generation.

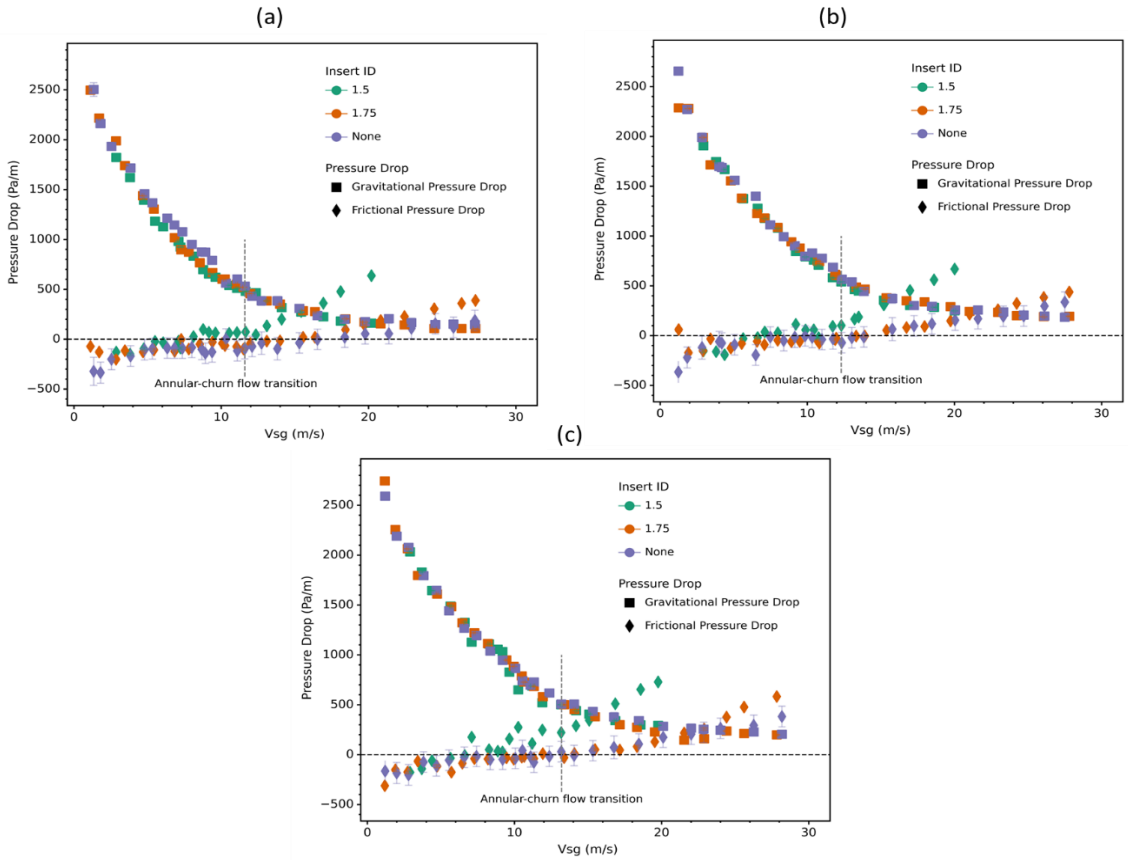

Figure 5-6: Gravitational and frictional pressure drop vs. v_{Sg} for water-air flow and various insert cases at (a) v_{SL} = 0.0033 m/s, (b) v_{SL} = 0.01 m/s, (c) v_{SL} = 0.02 m/s

To quantify the effects of adding inserts on liquid-gas flow, the differences between the tests with and without inserts may be analyzed. For this purpose, a pressure drop change term was defined using the following formula. Positive values mean a reduction in pressure drop with the insert, which is favorable.

$$\text{Pressure drop change} = \frac{\text{pressure drop of the no insert test} - \text{pressure drop of the test with insert}}{\text{pressure drop of the no insert test}} \quad (5\text{-}1)$$

The pressure drops are determined at the same v_{Sg} values, by fitting a five-degree polynomial equation over the pressure drop data of the corresponding test. These

polynomials provide a coefficient of determination (R^2) of more than 99%. Figure 5-10 shows the pressure drop change with inserts at varying v_{SL} values. The pressure drop change is mostly negative in the annular flow region, with the values decreasing as the v_{Sg} increases. The 1.5-inch insert produces the highest pressure drop (or the worst performance) in this region, due to the higher frictional pressure loss compared to the other cases. In general, the pressure drop change increases as the v_{Sg} decreases around the onset of liquid loading, where the flow pattern changes to churn flow. The highest pressure drop change occurs at v_{SL} =0.0033 m/s, especially with the 1.75-inch insert. As the v_{Sg} decreases, the pressure drop change turns negative approaching the slug flow pattern. This shows the negative insert effects in both slug and annular flow patterns. The potential positive effects of adding inserts are by delaying the liquid loading within the churn flow pattern.

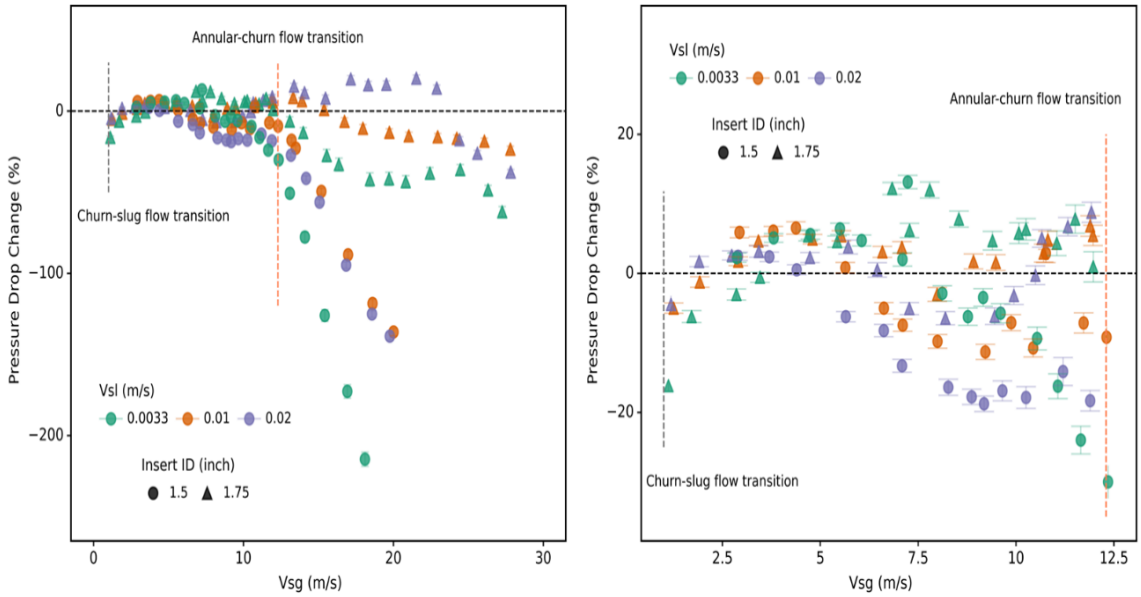

Figure 5-7: Pressure drop change vs. superficial gas velocity for water-air flow at constant v_{SL} for insert cases compared to 'no insert' case

Figure 5-11 shows the liquid holdup vs. v_{Sg} for water-air flow at v_{SL} values of 0.0033, 0.01, and 0.02 m/s. The tests with insert ID's of 1.5 and 1.75 in. are indicated using green and orange markers, respectively, and the no-insert tests are presented with purple markers. The results indicate that the cases with insert have lower liquid holdup values than the no-insert case in the churn flow region at v_{SL} =0.0033 m/s. The changes are not as noticeable for higher v_{SL} tests.

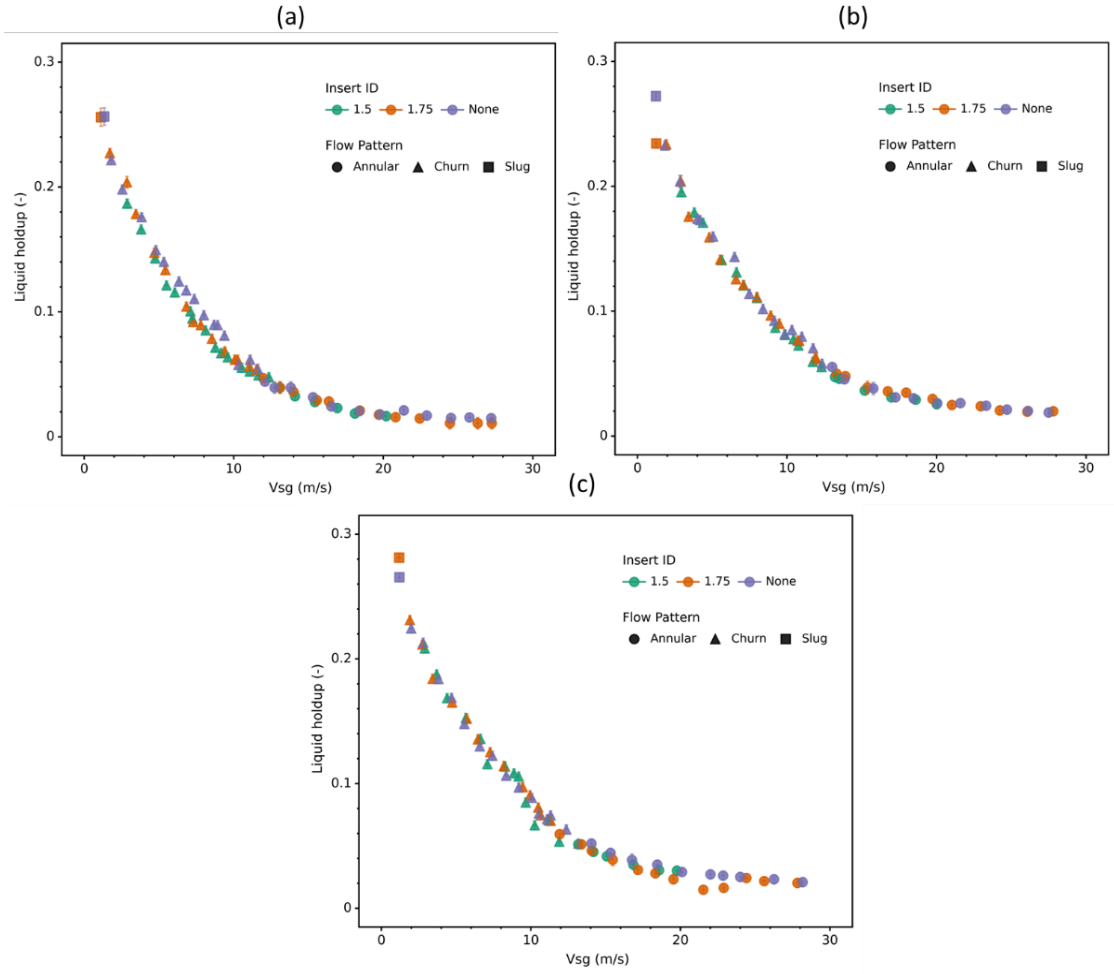

Figure 5-8: Liquid holdup vs. v_{Sg} for water-air flow with and without inserts at (a) v_{SL} = 0.0033 m/s , (b) v_{SL} = 0.01 m/s, (c) v_{SL} = 0.02 m/s

Figure 5-12 shows the liquid holdup change, a term defined to quantify the differences in the liquid holdup of the insert cases, compared to the tests with no inserts at the same v_{Sg} and v_{SL}. This term is calculated using the following formula:

$$\text{Liquid holdup change} = \frac{\text{H}_L \text{ of no insert test} - \text{H}_L \text{ of test with insert}}{\text{H}_L \text{ of no insert test}} \quad (5\text{-}2)$$

Five-degree ploynomials are used to fit the liquid holdup data of the no-insert tests at given v_{SL} values and determine the liquid holdup for the same v_{Sg} as the corresponding test with insert. These polynomials have a coefficient of determination (R^2) of more than 99%. The result shows that v_{SL} = 0.0033 m/s has the highest positive change or drop in the liquid holdup, with almost all the data in the churn region having a positive change. At v_{SL} = 0.02 m/s, most points in the churn region have a negative change or increase in the holdup. The results of v_{SL} = 0.01 m/s are close to zero in most points in the churn region, indicating a neutral impact of the insert on liquid holdup. That means that inserts are not helpful for water-air flow at v_{SL} values of 0.01 m/s or higher. The 1.5-inch insert has the highest positive change in liquid holdup at v_{SL} = 0.0033 m/s. But conversely, the 1.5-inch insert causes more frictional losses than the 1.75-inch insert, as shown in Figure 5-3. The pressure drop is a combination of gravitational and frictional losses. The 1.75-inch insert provides a lower combined pressure loss, making it more efficient, as shown in Figure 5-5

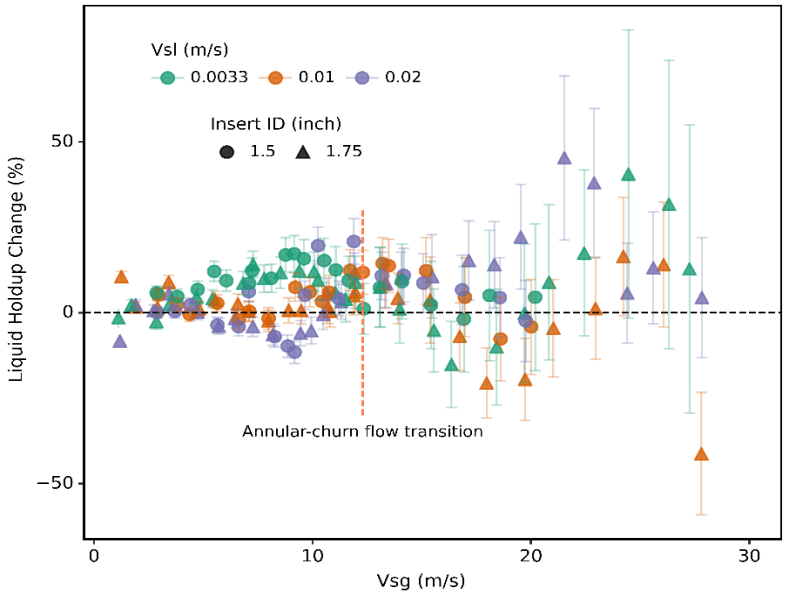

Figure 5-9: Liquid holdup change caused by inserts vs. v_{Sg} for water-air flow and various v_{SL} values

5.3 Oil-air Tests

Figure 5-13 shows the total pressure drop vs. superficial gas velocity for oil-air flow and insert diameters of 1.5 and 1.75 inches, indicated using green and orange markers, respectively. The tests with no inserts are presented in purple markers. The results are shown for v_{SL} values of 0.0033, 0.01, and 0.02 m/s. In this figure, three flow patterns are identified by visual observation, namely, annular, churn and slug, assigned circular, triangular, and square marker shapes, respectively. The total pressure drop curve is almost hook-shaped, with the pressure drop decreasing as the v_{Sg} drops down to a $v_{Sg,min}$ value. The pressure drop then increases as v_{Sg} decreases at $v_{Sg} < v_{Sg,min}$, for all cases. The results for all v_{SL} values show that the cases with insert have significantly higher pressure losses when v_{Sg} is higher than $v_{Sg,min}$. The tests with the 1.5-inch insert result in higher

pressure losses than the tests with the 1.75-inch insert in this region. This is due to the significance of increased frictional losses at high gas rates.

At $v_{Sg} < v_{Sg,min}$, as the flow pattern changes to churn and then slug flow, the cases with insert have similar or lower pressure drops compared to the no-insert cases. For v_{SL} =0.01 m/s as shown in Figure 5-13(b), the cases with insert have lower pressure drop at $v_{Sg} < 4$ m/s. However, for v_{SL} =0.02 m/s shown in Figure 5-13(c), pressure drop is lower for the tests with no inserts indicating that the insert's positive effect is mainly significant at lower liquid rates.

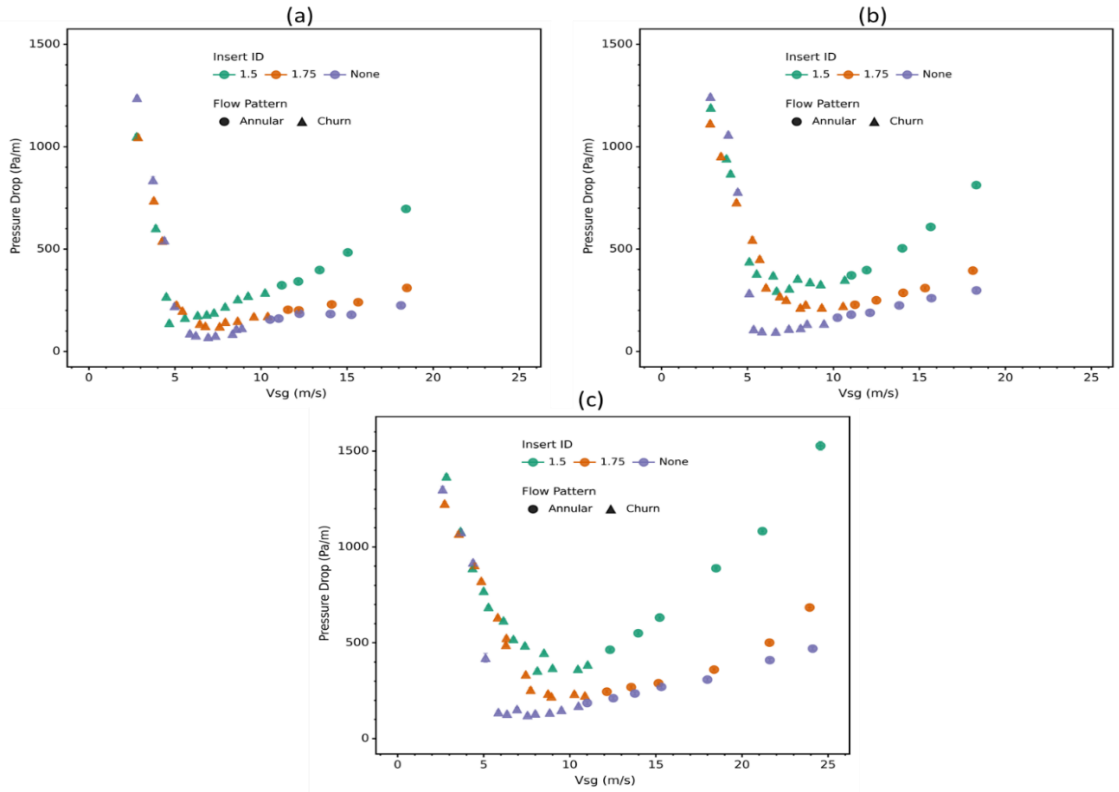

Figure 5-10: Total pressure drop vs. v_{Sg} for oil-air flow with and without inserts at (a) v_{SL} = 0.0033 m/s , (b) v_{SL} = 0.01 m/s, (c) v_{SL} = 0.02 m/s

Figure 5-14 shows the gravitational and frictional pressure drops vs. v_{Sg} for oil-air flow and various insert diameters at v_{SL} values of 0.0033, 0.01, and 0.02 m/s. Gravitational pressure drop $(dp/dL)_G$ and frictional pressure drop $(dp/dL)_F$ are indicated by the square and diamond-shaped markers, respectively. Insert diameters of 1.5 and 1.75 inches are indicated using green and orange markers, respectively, while the tests with no inserts are presented in purple markers.

For all the tested liquid rates, the insert cases have higher frictional pressure drops compared to the no-insert tests, Particularly, the insert ID of 1.5 inches has noticeably higher frictional pressure drops in the annular flow region. This is because of the decrease in the effective flow diameter and results in the increase of the total pressure drop for annular flow in insert cases, as shown in Figure 5-10. However, Figure 5-11(a) at v_{SL} =0.0033 m/s shows that the no-insert case has the highest gravitational pressure drop in the churn region, which indicates that the inserts have a positive impact on lowering gravitational losses. The lower gravitational drops with insert are because the inserts create large liquid waves from the liquid film. Then the upward-flowing gas in the core shears the liquid waves, creating more liquid droplets and trapping them in the core. This lowers the liquid holdup and lowers the gravitational pressure drop as liquid droplets travel faster than the liquid film. In Figure 5-11(b) at v_{SL} =0.01 m/s, no difference was observed in the gravitational pressure drops for all cases. In Figure 5-11(c) at v_{SL} =0.02 m/s, the cases with inserts have higher gravitational and frictional losses than the no-insert case, especially with the insert ID of 1.5-inch. This results in a sharp increase in

total pressure drop, as shown in Figure 5-10(c). Overall, it can be concluded that the insert has a positive impact at lower gas rates of churn and slug flow and at lower v_{SL} cases.

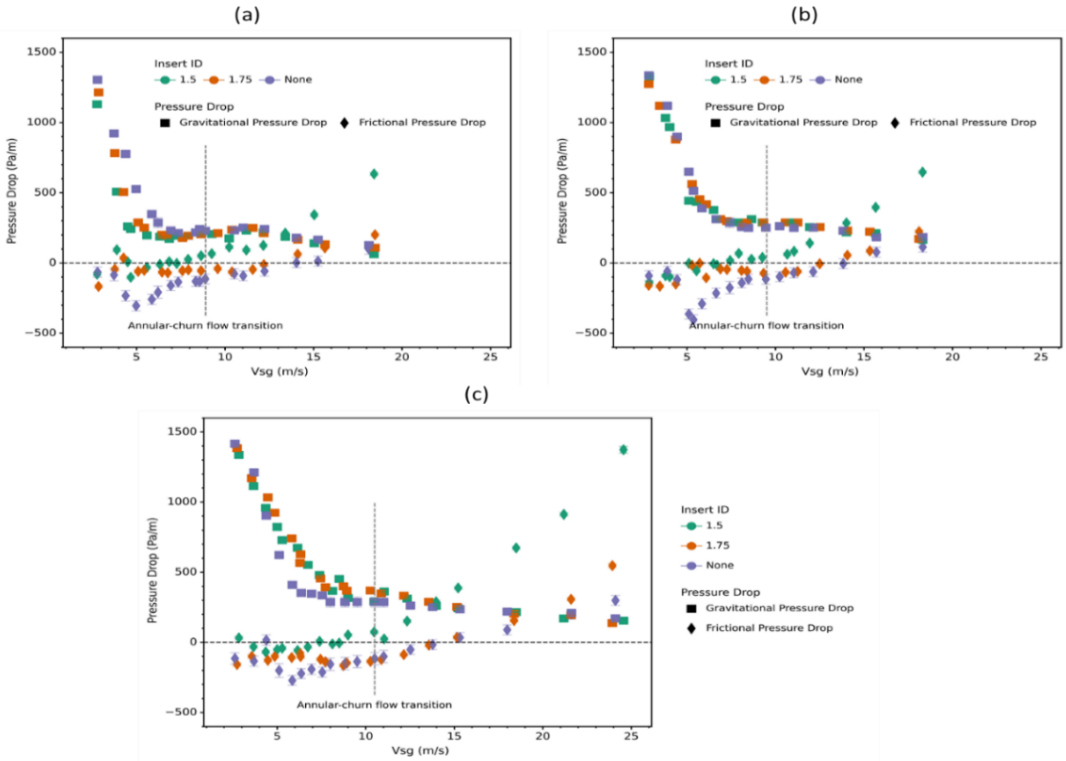

Figure 5-11: Gravitational and frictional pressure drop vs. v_{Sg} for oil-air flow with and without inserts at (a) v_{SL} = 0.0033 m/s , (b) v_{SL} = 0.01 m/s, (c) v_{SL} = 0.02 m/s

To quantify the differences between the cases with and without inserts, the previously defined pressure drop change term was applied. For this, the pressure drops were paired at the same v_{Sg} for the cases with and without inserts. Figure 5-12 shows that the pressure drop change increases in negativity as the v_{Sg} increases in the annular region. The 1.5-inch insert produces the lower (or the more negative) effect due to the higher increase of frictional pressure loss. The pressure drop change increases and approaches the positive values as the v_{Sg} decreases at $v_{Sg} < v_{Sg,min}$. The highest positive pressure drop

change occurs at v_{SL} =0.0033 m/s, particularly at v_{Sg} < 5 m/s. The insert diameter of 1.5 inches provides a more positive effect within this range, with pressure drop reductions reaching 50%.

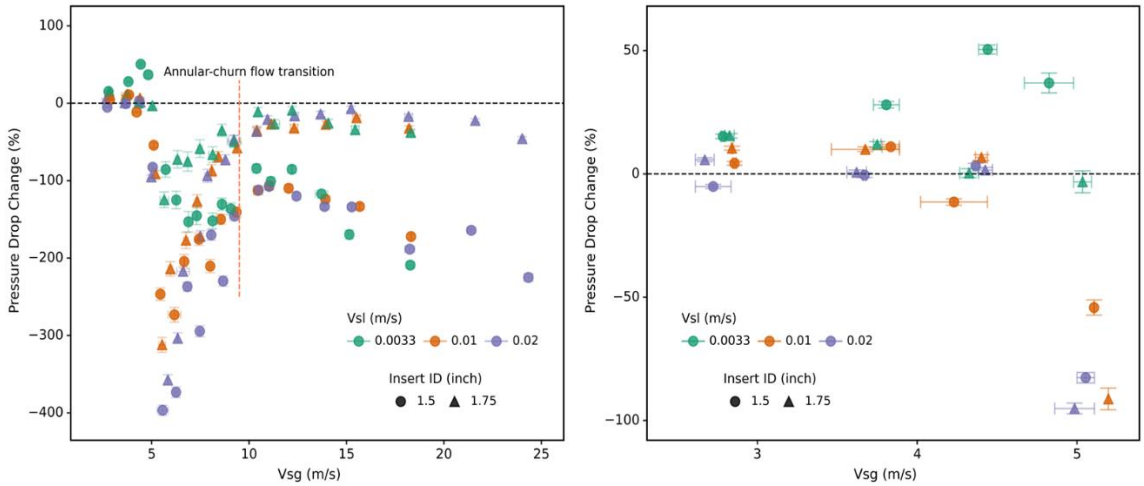

Figure 5-12: Pressure drop change vs. superficial gas velocity for oil-air flow at constant v_{SL} for insert cases compared to 'no insert' case

Figure 5-13 shows the liquid holdup with superficial gas velocity of oil-air flow with Insert diameters of 1.5 and 1.75 inches, indicated using green and orange markers, respectively, and the no-insert case presented in purple. The results are shown for v_{SL} values of 0.0033, 0.01, and 0.02 m/s. The results indicate that the cases with inserts have lower liquid holdups than the no-insert cases in the churn flow region at v_{SL} =0.0033 m/s. At v_{SL} =0.01 m/s, the cases with insert have lower liquid holdup at v_{Sg} < 4 m/s, with no noticeable changes at higher v_{Sg} values. For v_{SL} =0.02 m/s, the cases with insert have higher liquid holdups compared to the no-insert cases. This is in agreement with the previous observations that the positive insert effects are more significant at lower v_{SL} values.

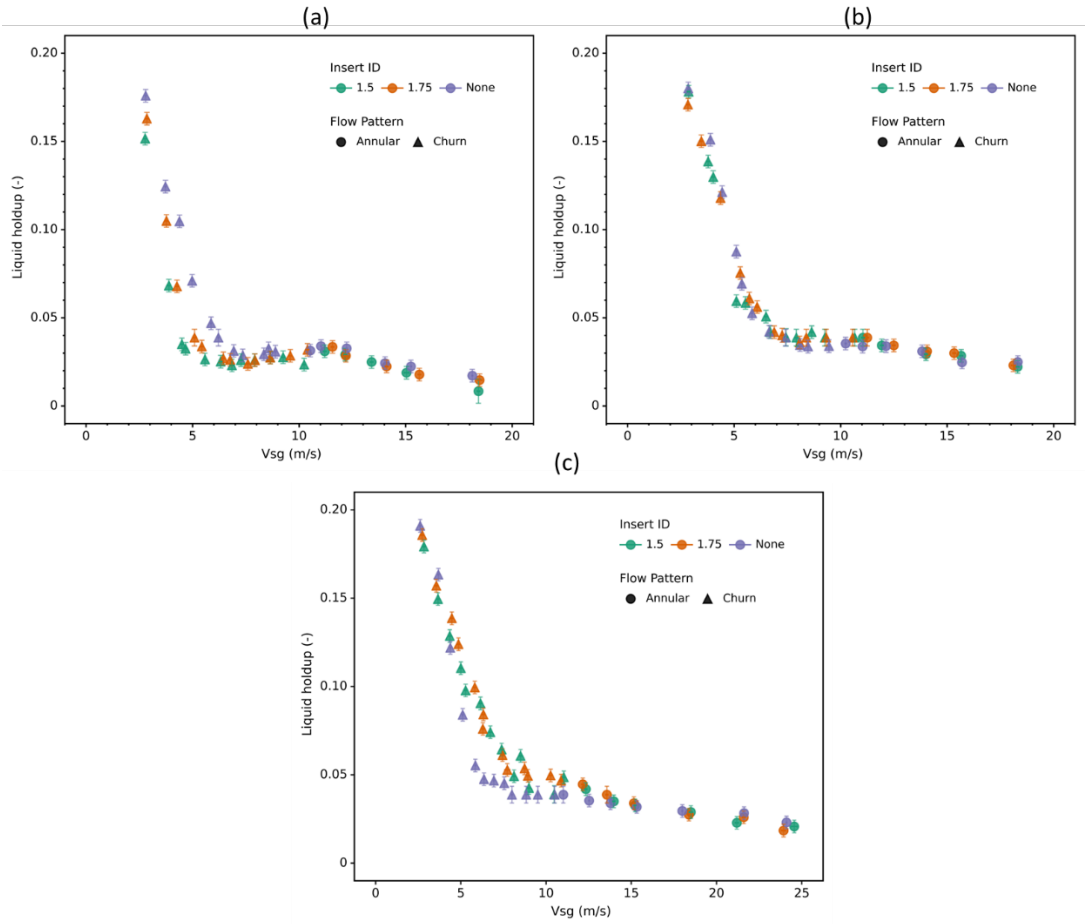

Figure 5-13: Liquid holdup vs. v_{Sg} for oil-air flow with and without inserts at (a) v_{SL} = 0.0033 m/s , (b) v_{SL} = 0.01 m/s, (c) v_{SL} = 0.02 m/s

Figure 5-14 shows the liquid holdup change of oil-air tests, defined in Equation 2 to quantify the decrease in the liquid holdup after adding the insert, compared to the no-insert case. The liquid holdups of the cases with and without inserts are determined at the same v_{Sg} values. The result shows that v_{SL} = 0.0033 m/s has the highest positive change or decrease in the liquid holdup, reaching a maximum value of 70% within the churn flow region. At v_{SL} = 0.02 m/s, mostly negative changes are observed in the holdup, even within the churn region. Only at v_{Sg} < 4 m/s, slight improvements are observed with liquid holdup

changes in the positive region. The results of v_{SL} = 0.01 m/s are close to zero in most cases, indicating that the insert has a neutral impact on the liquid holdup. This means that adding the insert has a positive effect mainly for v_{SL} values less than 0.01 m/s. The 1.5-inch insert produces a higher positive change in the liquid holdup at v_{SL} = 0.0033 m/s with a maximum value of 70%, suggesting that this insert is better at lowering the liquid holdup than the 1.75-inch insert. Conversely, the 1.5-inch insert causes more frictional loss than the 1.75-inch insert, as shown in Figure 5-11.

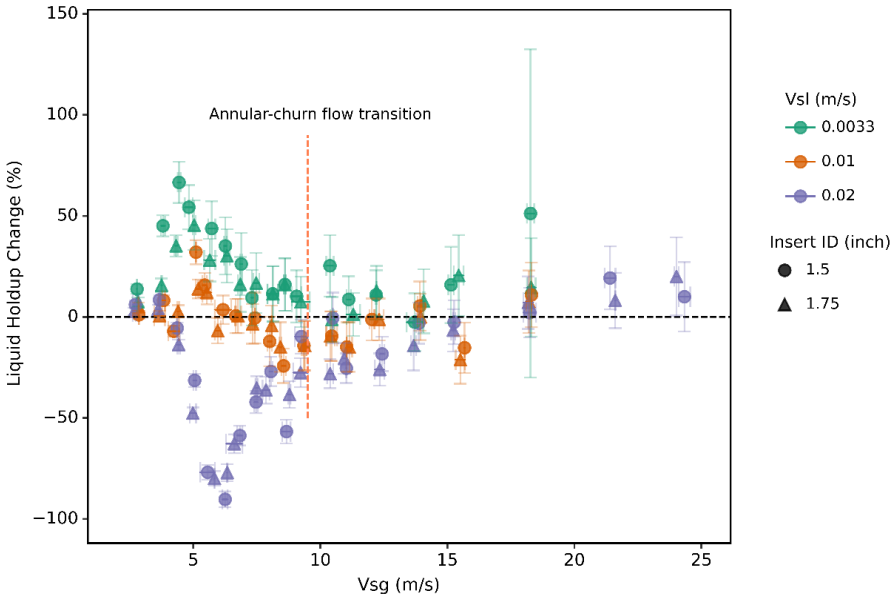

Figure 5-14: Liquid holdup change vs. superficial gas velocity for oil-air flow at constant v_{SL} for insert cases compared to 'no insert' case

5.4 Effect of Liquid Properties on Insert Performance

Figure 5-15 shows the liquid holdup change after adding the 1.5-inch or 1.75-inch inserts for water-air and oil-air flows. As observed, the inserts provide the largest reduction in the liquid holdup for oil-air flow at v_{SL} = 0.0033 m/s, with liquid holdup

reductions up to 70%. This is due to the lower density and surface tension of oil compared to water, resulting in larger interfacial wave structures, particularly after adding the inserts. These waves facilitate droplets generations as the gas in the core is sheared the liquid off the waves and entrains droplet. For both oil and water cases, the positive insert effects on the liquid holdup are diminished, as the v_{SL} increases to 0.01, and especially to 0.02 m/s. Contrary to the water case, the reduction in liquid holdup for oil-air flow is higher than the increase in frictional loss, making the insert size of 1.5-inch better at v_{SL} = 0.0033 m/s and v_{Sg} < 4 m/s, as shown in Figure 5-12.

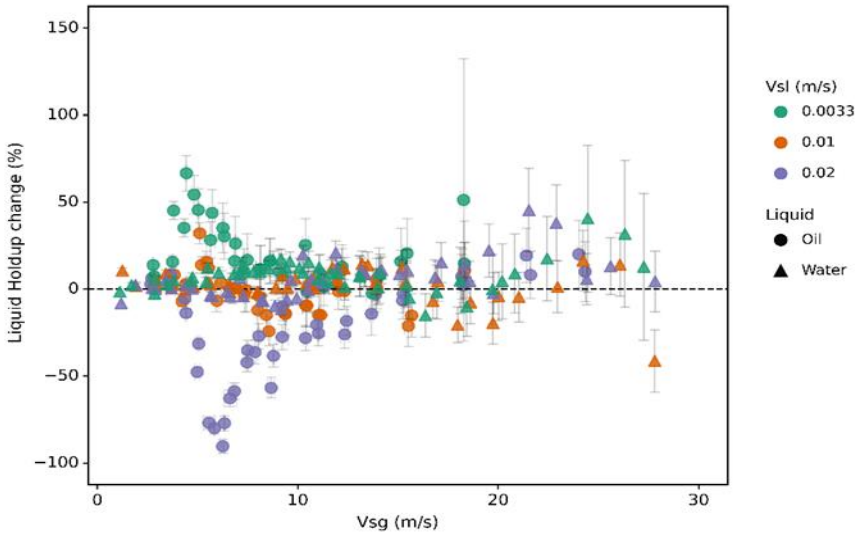

Figure 5-15: Effects of liquid properties on the liquid holdup changes vs. v_{Sg} after adding the inserts

Figure 5-16 compares the pressure drop changes for water-air and oil-air flow after adding the 1.75- and 1.5-inch inserts. The maximum positive value or decrease in pressure drop change is around 50% for oil-air tests at v_{SL} = 0.0033 m/s. The values of change in holdup are higher than the pressure drop change values. This is because the

pressure drop change term shows the combined effect of the inserts, potentially decreasing the gravitational losses, but also increasing the frictional losses. On the other hand, at v_{SL} = 0.01 and 0.02 m/s, the negative pressure drop change exceeds 400%. At higher superficial liquid velocities, the inserts cause a much higher increase in frictional pressure drop than the decrease in the gravitational pressure drop.

These results show that the inserts could enhance the liquid lifting by lowering the pressure drop and liquid holdup. However, they could also increase the pressure drop by increasing the frictional losses. Further experimental tests with some changes to the current setup's parameters, such as insert sizes, insert spacing, and the number of inserts are necessary to find the optimum setup for enhancing liquid lifting. Overall, this study shows that the positive effect of adding the inserts falls within the churn and slug flow region with low liquid rates, particularly with oil as the liquid phase.

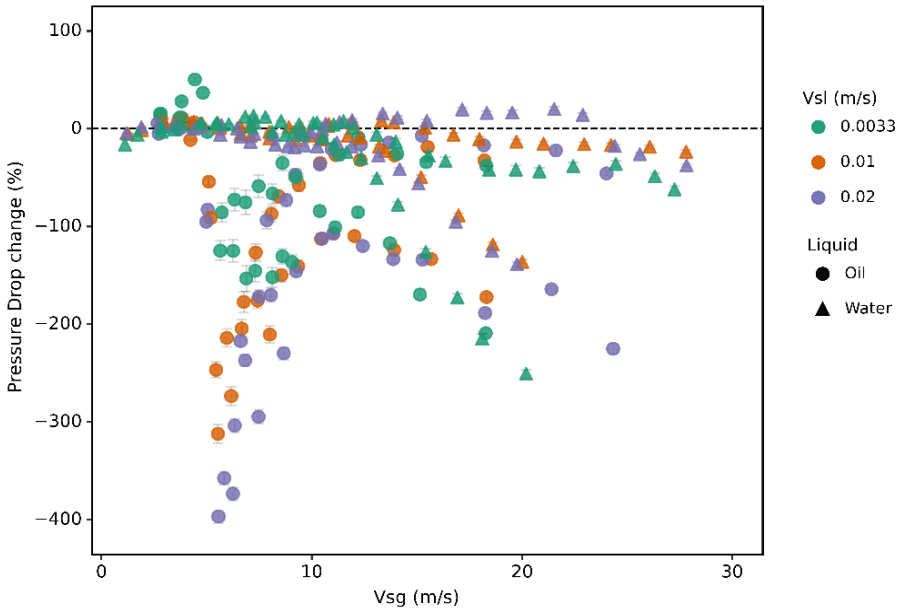

Figure 5-16: Pressure drop change vs. superficial gas velocity for water-air and oil-air for insert cases compared to 'no insert' case

CHAPTER 6

Modeling Development

This chapter describes the modeling required to predict the effects of liquid properties on two-phase flow behavior, specifically pressure drop and liquid holdup. The annular-intermittent flow transition prediction model developed by Barnea (1987) is first described. The effect of liquid entrainment in the gas core is taken into account in a new mechanistic model that is presented to predict the pressure drop and liquid holdup. Various closure relationships for interfacial shear stress and entrainment fraction are tested with the new model. The proposed model with the best closure relationships is then compared to two commercially available models, the unified and OLGA models. Finally, a new model is presented to predict the interfacial friction factor. The objective of this model is to enhance the proposed mechanistic model's prediction capabilities for pressure drop and liquid holdup.

6.1 Barnea's Model

As presented previously in Section 2.2, Barnea (1987) developed a unified model to predict the transition from annular to intermittent flow using two criteria: liquid film instability and liquid film bridging. In the physical model, given in Figure 6-1, the gas

flows in the core, and liquid flows as a liquid film around the inner pipe wall. The model uses a one-dimensional fluid flow model, with the following assumptions:

- The flow is fully developed.
- Film thickness is uniform around the pipe.
- No liquid entrainment is found in the core.
- The flow is isothermal and incompressible.

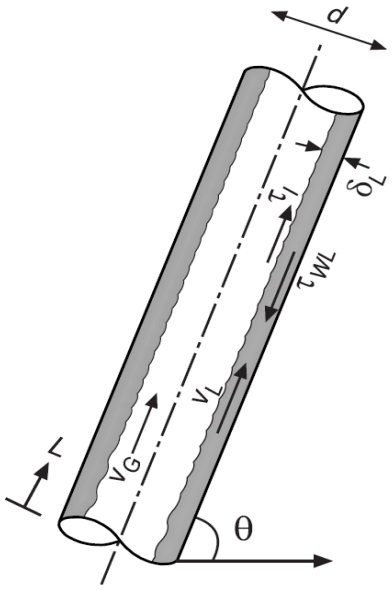

Figure 6-1: Schematic of Barnea (1987) physical model (Shoham et al., 2006)

The momentum balances for the liquid film and gas core are defined as:

$$-A_L \frac{d_P}{d_L})_L - \tau_{WL} S_L + \tau_I S_I - \rho_L A_L g \, sin\theta = 0 \quad (6\text{-}1)$$

$$-A_G \frac{d_P}{d_L})_G - \tau_I S_I - \rho_G A_G g \, sin\theta = 0 \quad (6\text{-}2)$$

Setting the momentum Equations (6-1) and (6-2) equal to eliminate the pressure gradient terms (by assuming equal pressures in the two phases) results in a combined momentum balance equation. This equation is as follows:

$$\tau_I S_I \left(\frac{1}{A_L} + \frac{1}{A_G}\right) - g(\rho_L - \rho_G) sin\theta - \tau_{WL} \frac{S_L}{A_L} = 0 \quad (6\text{-}3)$$

The geometrical relationships, shown in Figure 6-2, are defined as:

$$S_L = \pi d, \quad (6\text{-}4)$$

$$S_I = \pi(d - 2\delta_L), \quad (6\text{-}5)$$

$$A_L = \pi\delta_L(d - \delta_L), \text{ and} \quad (6\text{-}6)$$

$$A_G = \pi(d/2 - \delta_L)^2. \quad (6\text{-}7)$$

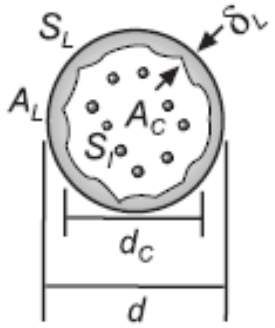

Figure 6-2: Schematic of Barnea (1987) geometrical relationship (Shoham et al., 2006)

The following equation defines the liquid wall shear stress:

$$\tau_{WL} = f_L \frac{\rho_L v_L^2}{2}, \quad (6\text{-}8)$$

The liquid friction factor (f_L) is calculated using the Blasius equation as follows:

$$f_L = C_L \left(\frac{\rho_L d u_L}{\mu_L}\right)^{-n}, \tag{6-9}$$

where the constants C_L and n are dependent on the flow type, with C_L = 0.046 and n = 0.2 for turbulent flow, and C_L = 16 and n = 1 for laminar flow.

The geometrical relationships described in Equations 6-4 to 6-7, liquid wall shear stress and dimensionless film thickness ($\widetilde{\delta_L} = \delta_L/d$) of Equation 6-3 are all combined and solved for the interfacial shear stress. This generates an equation that is a function of v_{SL}, as shown in the following:

$$\tau_I = g(\rho_L - \rho_G)\, d\, sin\theta \left(\widetilde{\delta_L} - \widetilde{\delta_L}^2\right)\left(1 - 2\widetilde{\delta_L}\right) + \frac{1}{32} C_L \rho_L \left(\frac{\rho_L d}{\mu_L}\right)^{-n} (v_{SL})^{2-n} \left[\frac{(1-2\widetilde{\delta_L})}{(\widetilde{\delta_L} - \widetilde{\delta_L}^2)^2}\right], \tag{6-10}$$

The interfacial shear stress provided by the gas-phase is given by:

$$\tau_I = \frac{1}{2} f_I \rho_G \frac{{v_{SG}}^2}{(1-2\widetilde{\delta_L})^4}. \tag{6-11}$$

Wallis's (1969) interfacial friction factor model is used as a closure relationship. It is shown in the equation below:

$$f_I = 0.005(1 + 300\widetilde{\delta_L}) \tag{6-12}$$

The liquid film instability criterion is determined by finding the loci of all the minimum points of Equation 6-10, as shown in Figure 6-3. The minimum points are obtained by differentiating equation 6-10 with respect to $\widetilde{\delta_L}$ and equating it to zero ($\frac{\partial \tau_I}{\partial \widetilde{\delta_L}} = 0$), as given below:

$$g(\rho_L - \rho_G)\, d\, sin\theta \left[\left(1 - 2\widetilde{\delta_L}\right)^2 - 2\left(\widetilde{\delta_L} - \widetilde{\delta_L}^2\right)\right] -$$

$$\frac{1}{16} C_L \rho_L \left(\frac{\rho_L d}{\mu_L}\right)^{-n} (v_{SL})^{2-n} \left[\frac{\left(\widetilde{\delta_L} - \widetilde{\delta_L}^2\right) + \left(1 - 2\widetilde{\delta_L}\right)^2}{\left(\widetilde{\delta_L} - \widetilde{\delta_L}^2\right)^3}\right] = 0 \qquad (6\text{-}13)$$

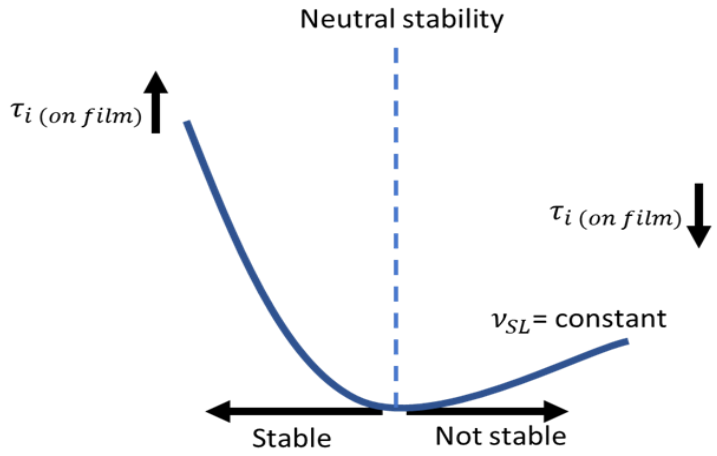

Figure 6-3: Illustration of liquid film instability occurrence at the minimum point of Equation 6-10

Figure 6-4 illustrates the solution of Barnea's (1987) model for a 0.0508-m (2-in.) ID pipe with water-air flow. Interfacial shear stress is calculated at various v_{SL} values using Equation 6-10. At each v_{SL}, different dimensionless film thicknesses are assumed to calculate the interfacial shear stress. The solid lines represent the interfacial shear stress using Equation 6-10. The supplied interfacial shear stress by gas core, as shown in Equation 6-11, is a function of v_{Sg}. It is displayed in dashed lines for each v_{Sg} value. The dimensionless film thickness can be found at the intersection of the solid and dashed lines. This value is compared to the liquid film instability and film bridging criteria. The liquid film instability initiates at the minimum point of the solid line, using Equation 6-13,

presented by the long dashed-dotted black line. The existence of liquid film bridging is defined by Barnea at H_L = 0.24, which is equivalent to $\widetilde{\delta_L}$ = 0.065, presented by a long-dashed-dotted red line. If the intersection of the solid line and the dashed lines is in zone A, the flow is stable and in an annular flow pattern. On the other hand, if the intersection is in zone B or C, the transition to intermittent flow pattern is said to occur due to liquid film instability and liquid film bridging, respectively.

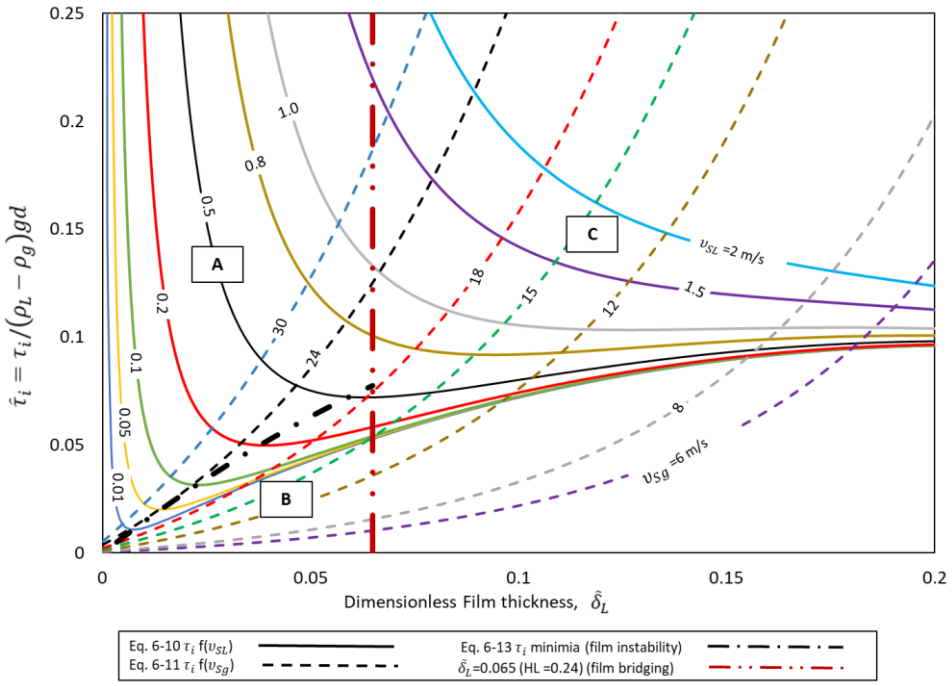

Figure 6-4: Barnea (1987) model solutions for 2-in. ID pipe with water-air

Figure 6-5 depicts the transition of flow pattern from annular to intermittent, according to Barnea (1987), using the liquid film instability and film bridging criteria. From this figure, the liquid film instability is dominant for low superficial liquid velocities, and liquid film bridging is dominant for high superficial liquid velocities.

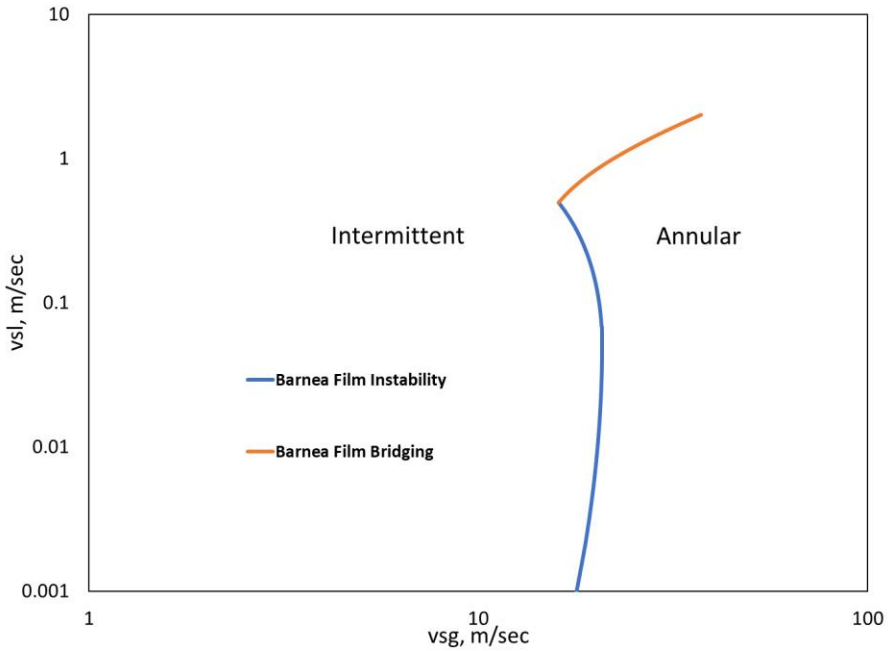

Figure 6-5: Barnea (1987) flow pattern transition

6.2 Proposed Model for Annular and Churn Flow

The Barnea (1987) model overpredicts the transition from annular to intermittent flow pattern, as shown in Chapter 4. A modified mechanistic model is provided by incorporating the influence of liquid entrainment in the core on the Barnea model. As a result, an additional closure model is required to compute the entrainment fraction.

A 1-D mechanistic model for vertical flow is suggested to predict the annular-churn transition, pressure drop, and liquid holdup in a two-phase flow. The proposed model is based on a distinct geometry and set of observable phenomena. The gas and entrained liquid in the core and the liquid film are the two fluids. This model allows for comprehensive predictions of the gas core and liquid film velocity, liquid film thickness, gas void fraction, and pressure drop for annular and churn flows at low liquid rates. Two

closure models are needed for this mechanistic, namely, interfacial shear stress and entrainment fraction. Each interfacial shear stress was tested in the proposed mechanistic model with various entrainment fraction models. Then, the best performing entrainment fraction models for each interfacial shear stress were compared in Section 6.2.1. The proposed model with the best closure relationships is then compared to two commercially available models, the unified and OLGA models in Section 6.2.2. Finally, a new model is presented to predict the interfacial friction factor. The objective of this model is to enhance the proposed mechanistic model's prediction capabilities for pressure drop and liquid holdup.

Figure 6-6a depicts the physical model's schematic while analyzing the control volume with differential axial lengths of *dL*. While the entrained liquid is flowing in the gas core at the center of the pipe, the liquid film moves along the pipe's circumference. The liquid film and the gas core are shown in Figures 6-6b and 6-6c, respectively. The pressures affecting the core and liquid film regions are depicted in the figures. Gravity, pressure, and shear forces are all present. The symbols τ_{WL} and τ_i stand for the liquid wall shear stress and the interfacial shear stress, respectively. The model's development is guided by the following assumptions:

- Fully developed flow.
- Uniform film thickness.
- Homogeneous no-slip flow between entrained liquid and gas in the core.
- Average velocity concept is used (not considering the velocity profile)
- Isothermal and incompressible flow.

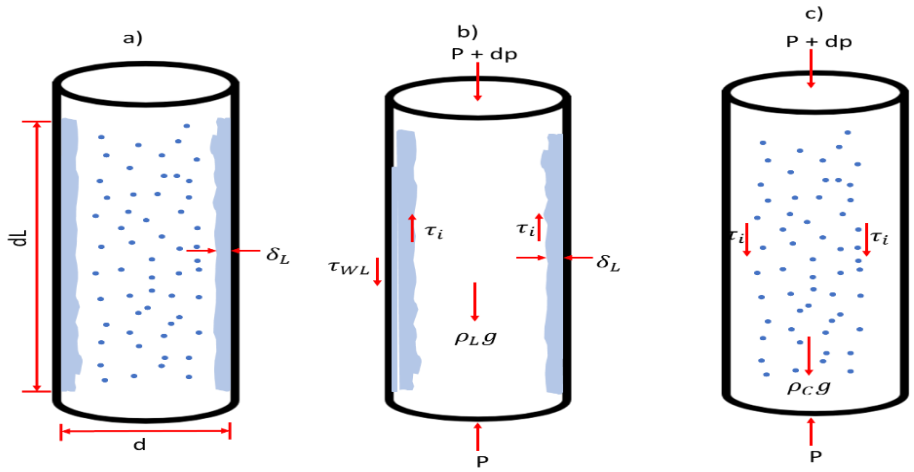

Figure 6-6: Schematic of the proposed model approach, (a) general schematic, (b) liquid film forces, (c) gas core forces

The momentum balances for the liquid film and gas core are defined as:

$$-A_F \frac{dP}{dL})_F - \tau_{WL} S_L + \tau_i S_I - \rho_L A_F g = 0 \quad (6\text{-}14)$$

$$-A_C \frac{dP}{dL})_C - \tau_i S_I - \rho_C A_C g = 0 \quad (6\text{-}15)$$

These two momentum equations are set equal to give the combined momentum balance equation, eliminating the pressure gradients (assuming they are equal) as follows:

$$\tau_i S_I \left(\frac{1}{A_F} + \frac{1}{A_C}\right) - g(\rho_L - \rho_C) - \tau_{WL} \frac{S_L}{A_F} = 0 \quad (6\text{-}16)$$

The geometrical relationships are defined as follows with a uniform film thickness:

$$A_F = \pi \delta_L (d - \delta_L)\,, \quad (6\text{-}17)$$

$$A_C = \pi (d/2 - \delta_L)^2, \quad (6\text{-}18)$$

$$S_L = \pi d, \quad (6\text{-}19)$$

$$S_I = \pi\,(d - 2\delta_L). \quad (6\text{-}20)$$

The mass balance equations are more complex than Barnea's due to the existence of liquid entrainment. The liquid film mass balance equations are expressed as follows:

$$q_F = q_L(1 - f_E) = A_p v_{SL}(1 - f_E) = v_F A_F \tag{6-21}$$

$$v_F = v_{SL} \frac{(1-f_E)\, d^2}{4\delta_L(d-\delta_L)} \tag{6-22}$$

Additionally, the mass balance equations in the gas core are specified below:

$$q_C = q_G + q_L f_E = A_p(v_{SG} + v_{SL} f_E) = A_C v_C \tag{6-23}$$

$$v_{SC} = v_{SG} + v_{SL} f_E \tag{6-24}$$

$$v_C = \frac{(v_{SG}+v_{SL}f_E)d^2}{(d-2\delta_L)^2} \tag{6-25}$$

With the assumption of homogenous no-slip flow between the gas and the entrained liquid in the core region, the core void fraction is defined as:

$$\alpha_C = \frac{v_{SG}}{v_{SG}+v_{SL}f_E} \tag{6-26}$$

The core density and viscosity are given by:

$$\rho_C = \rho_G \alpha_C + \rho_L(1 - \alpha_C) \tag{6-27}$$

$$\mu_C = \mu_G \alpha_C + \mu_L(1 - \alpha_C) \tag{6-28}$$

The total void fraction of the flow can be determined using the equation below:

$$\alpha_T = \alpha_C(1 - 2\frac{\delta_L}{d})^2 \tag{6-29}$$

The liquid film wall shear stress can be expressed as

$$\tau_{WL} = f_F \frac{\rho_L v_F^2}{2}, \tag{6-30}$$

The Reynolds number can be used based on the hydraulic diameter to calculate the film fraction factor (f_F). Using the following Blasius's equation for a smooth pipe:

$$f_F = C_F Re_F^{-n} \tag{6-31}$$

The interfacial shear stress, can be determined as follows:

$$\tau_i = f_i \frac{\rho_c (v_C - v_F)^2}{2}, \tag{6-32}$$

To calculate τ_i, the interfacial friction factor (f_i) can be calculated using a suitable interfacial shear stress model. First, various interfacial friction factor models, including Wallis (1965), Belt et al. (2009), Fukano and Furukawa (1998) , and Bharathan and Wallis (1983), were used to assess the proposed model. Also, various entrainment fraction models, such as those developed by Wallis (1969), Oliemans et al. (1986), Ishii and Mishima (1989), Azzopardi and Wren (2004), and Sawant et al. (2008), were employed and evaluated.

For low liquid rates, the Pan and Hanratty (2002) entrainment fraction model is not applicable because of the negative $F_{E,\,max}$ values, which are physically incorrect. This is a result of the calculated critical liquid film rate ($W_{F,cr}$) being higher than the total liquid rate(W_L) at low liquid rates, producing a negative value (see Equation 2-20) and 2-21). The ($W_{F,cr}$) value is a function of the parameters (ω), as shown in Equation (2-23), which ignores the impact of liquid flow rates and is only a function of the physical characteristics of gas and liquid. The effect of the disturbance waves on the entrainment fraction is disregarded, which leads to unrealistic values of ($F_{E,max}$). Also, Alsarkhi and Sarica (2011) reported negative values of ($F_{E,\,max}$) for Pan and Hanaratty (2002) model at

low liquid rates. Similarly, Sawant et al. (2008) model results in negative values of ($F_{E,max}$) for v_{SL} values less than 0.00518 and 0.00311 for oil and water, respectively.

The evaluation of the proposed model is shown in Appendix A.1 using Wallis's f_i correlation and different entrainment models. The annular-churn transition is marginally better than Barnea's, but the minimum pressure drop occurs at higher v_{Sg}, making the pressure drop and liquid holdup predictions inadequate. This causes a sharp increase in pressure drop and liquid holdup when the ($v_{Sg} < v_{Sg,min}$), resulting in sharp overpredictions in this zone. Similar behavior was observed for Belt et al. (2009), and Fukano and Furukawa (1998) f_i models with all the entrainment fraction models. These models' unreliable predictions are the results of the following limitations.

- The closure models were developed using annular flow data.
- The liquid entrainment in the gas core was neglected in the development of these interfacial shear stress models. The liquid was assumed to be fully in the film, and as a result, the calculated dimensionless film thickness ($\frac{\delta_L}{d}$) was increased. Therefore, the models underestimate the interfacial friction factor when the film thickness is reduced by liquid entrainment.
- In these models, gas density and velocity are used to calculate (f_i) (see equation 2-28). For the proposed model, gas core density (ρ_C) and the relative velocity between the gas core and liquid film ($v_C - v_f$) are used (see Equation 6-32).

The interfacial shear stress model of Bharathan and Wallis (1983) was developed based on the experimental churn flow data. Equation (2-32) demonstrates that the model

is a function of liquid holdup, pipe diameter, and fluid properties such as gas and liquid densities and surface tension. The predictions of the proposed model using the interfacial model of Bharathan and Wallis (1983) and various entrainment fraction models are displayed in Appendix A.2. Jayanti and Brauner (1994) suggested using the average of Bharathan and Wallis (1983) and Wallis (1969) for the interfacial shear stress predictions in churn flow (Equation (2-34)). A similar approach was used here to enhance the predictions of the proposed model by averaging the predictions of Bharathan and Wallis (1983) with those of Wallis (1969) (MW), Belt et al. (2009) (B), and Fukano and Furukawa (1998) (F). This method significantly enhanced the predictions of the proposed model, as shown in Appendix A.3–A.5.

6.2.1 Proposed Model Predictions with Different Closure Models

First, the performance of the proposed model was evaluated for each interfacial shear stress model in the Jayanti and Brauner (1994) method and various entrainment fraction models. In general, the Oliemans et al. (1986) entrainment fraction model predicted the experimental pressure drop and liquid holdup data better than the other entrainment fraction models (Appendix A.2-A.5). Hence, different interfacial shear stress models were combined with Oliemans's entrainment model for comparison of the water-air and oil-air flow data. Furthermore, since the performance was comparable to that of Oliemans et al. (1986), Azzopardi and Wren (2004) entrainment closure model was included in the comparison. The following sections show water-air and oil-air predictions of the proposed model using different interfacial shear stress closures.

6.2.1.1 Water-Air Proposed Model Predictions. Figure 6-7 displays the relative error of the proposed model in prediction of the water-air flow pressure drop with various closure models. In all cases, the first letters show the first letter of the interfacial shear model, and the second letters show the first letter of the applied entrainment model. For example, Bh-O shows the results of the proposed model with Bharathan's closure for f_i and Oliemens's closure for droplet entrainment. The model prediction errors are nearly zero at high v_{Sg} values with (Bh-O) closures, except at v_{SL} = 0.0033 m/s, which has higher relative errors than other models. At a constant v_{SL}, the relative errors increase for all the cases as the v_{Sg} decreases for v_{Sg} < 10 m/s, with (Bh-A) model predictions in the best agreement with the experimental data. Additionally, the results demonstrate that the error increases significantly for v_{SL} = 0.0033 m/s. This could be because most closure models were created based on data with higher v_{SL}. Both Bharathan and Azzopardi correlations were developed for churn flow with water-air flow data and pipe IDs (0.024 and 0.05 m), which are similar to the conditions of the current study. This may be the reason why the model performs best with the (Bh) and (A) closures.

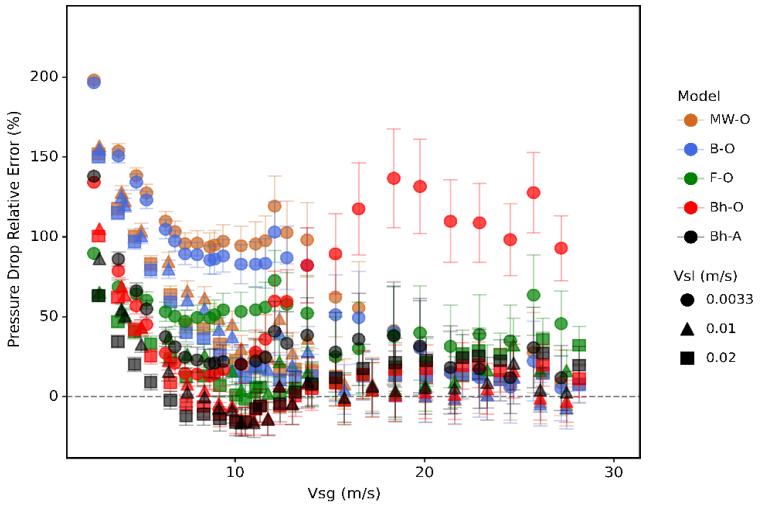

Figure 6-7: Relative error of the proposed model for water-air pressure drop at varying v_{Sg} values with different closure models.

The actual error of the proposed model in predicting water-air flow pressure drop with various closure models is shown in Figure 6-8. Similar to Figure 6-7, the actual error is nearly constant and close to zero at v_{Sg} > 10 m/s, except for the (Bh-O) case with v_{SL} = 0.0033 m/s. The actual error increases sharply as the v_{Sg} decreases at v_{Sg} <10 m/s. The results indicate that the model has the lowest actual errors with (Bh-A) closures.

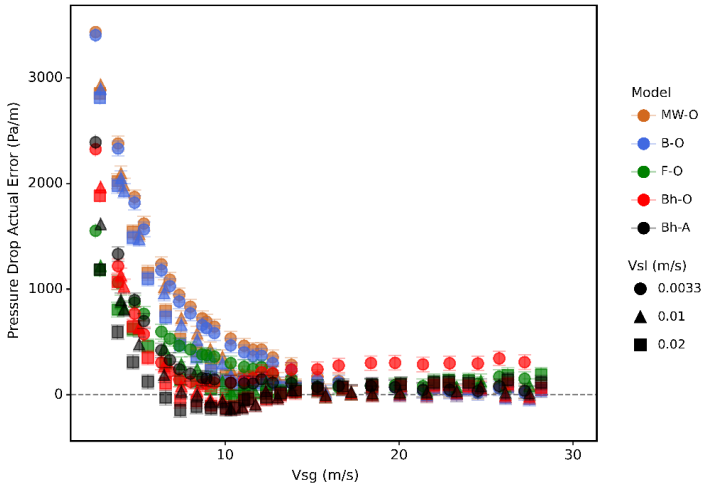

Figure 6-8: Actual error of the proposed model for water-air pressure drop at varying v_{Sg} values with different closure models.

Figure 6-9 displays the relative error of the proposed model for the water-air flow liquid holdup data with various closure models. The model predicts the liquid holdup similar to pressure drop, with most predictions slightly lower than zero at high v_{Sg} . The model prediction errors at v_{SL} = 0.0033 m/s are the highest for all closure models. Also, at v_{Sg} <10 m/s, the relative error increases as the v_{Sg} decreases. The model performs best in predicting the liquid holdup with (Bh-A) closures.

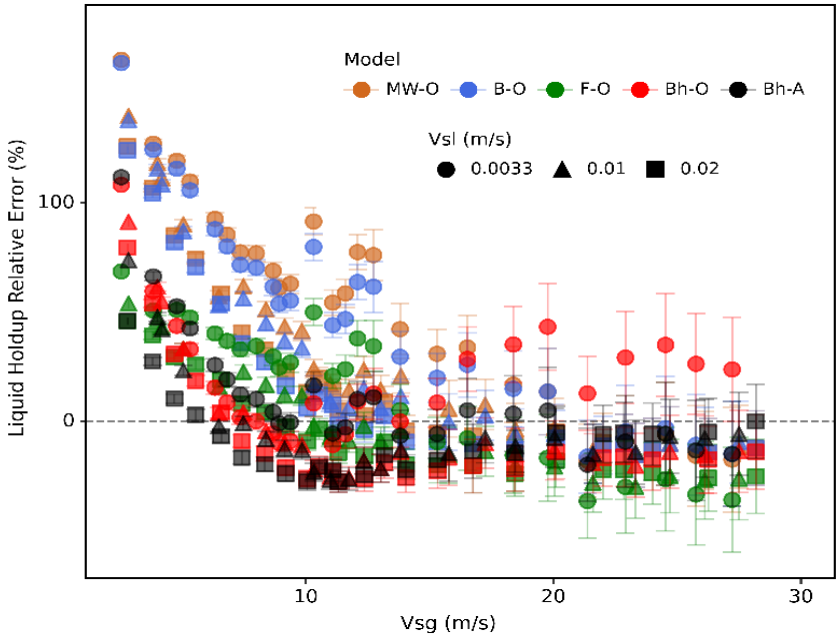

Figure 6-9: Relative error of the proposed model for water-air liquid holdup at varying v_{Sg} values with different closure models.

6.2.1.2 Oil-Air Proposed Model Predictions. Figure 6-10 displays the proposed model's relative errors in predicting the pressure drop of oil-air flow with various closure models. For all models, the figure depicts an inverted V-shaped curve, with most of the

data being overpredicted. The maximum relative errors are found around $v_{Sg,min}$ or the onset of liquid loading, where the relative errors approaches 400% using MW-O, B-O, and F-O closures. The extremely low experimental pressure drop at $v_{Sg,min}$ can be the reason for this abrupt increase in relative error, as any overprediction of pressure drop can result in high relative error. Overall, the proposed model with the Bh-A and Bh-O closure models performs better than others. In general, as the v_{SL} increases, the relative errors of the proposed model decrease.

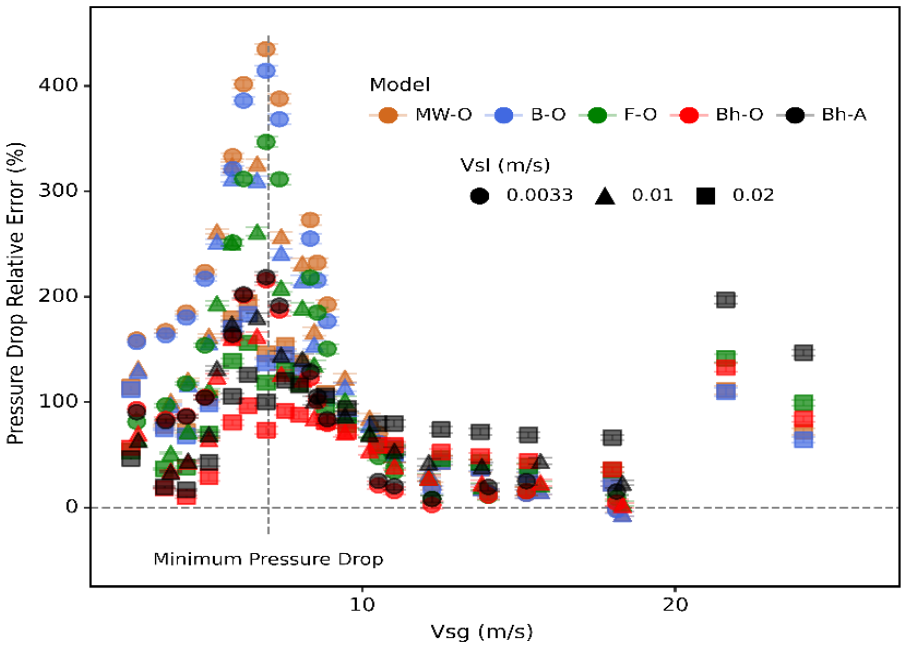

Figure 6-10: Relative error of the proposed model for oil-air pressure drop at varying v_{Sg} values with different closure models.

Figure 6-11 shows the actual error of the proposed model in predicting the pressure drop with different closure models. The actual error increases as the v_{Sg} decreases, and the model overpredicts the data with the highest actual error at v_{SL} = 0.0033

m/s. At v_{Sg} <10 m/s and v_{SL} = 0.0033 m/s, the actual error sharply increases as v_{Sg} decreases. Although $v_{Sg,min}$ is where the relative error in Figure 6-11 reaches its highest values, the actual error does not suddenly increase at this location. The results show that the suggested model has the lowest actual error with (Bh-O) closure models. Oliemans's model was developed based on data from various fluids and takes the effect of fluid properties into account, making it a better option than Azzopardi for oil-air flow.

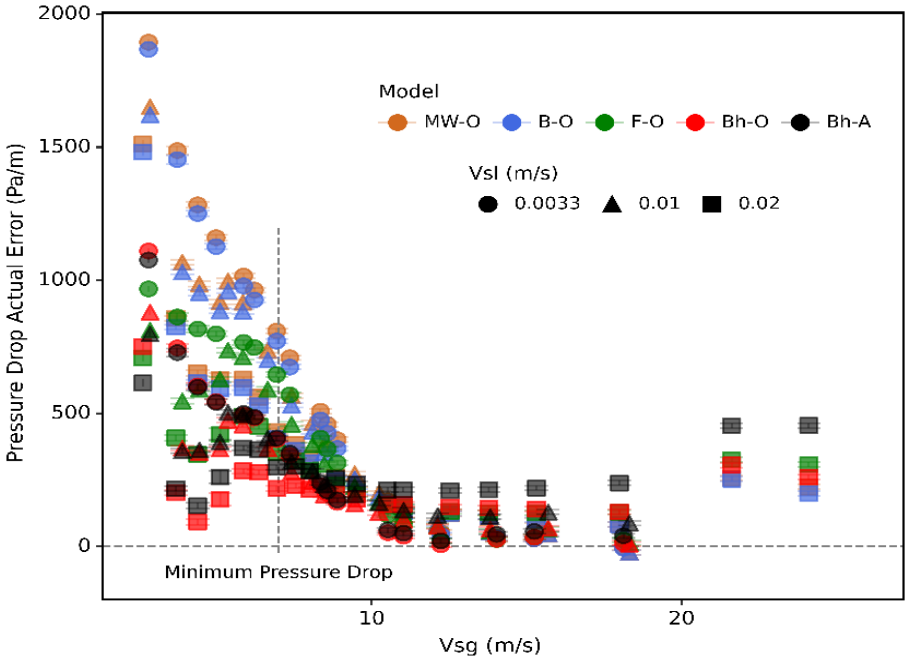

Figure 6-11: Actual error of the proposed model for oil-air pressure drop at varying v_{Sg} values with different closure relationships.

Figure 6-12 displays the relative error of the proposed model in predicting liquid holdup for oil-air flow with various closure models. Similar to the pressure drop relative error, the relative error reaches the maximum value around $v_{Sg,min,}$. At high v_{Sg}, the liquid holdup is underpredicted with negative errors that slightly increase as the v_{Sg} decreases.

At v_{Sg} <10 m/s, the relative error increases as the v_{Sg} decreases, with the maximum relative error happening at $v_{Sg,min.}$ Then, the relative error decreases as the v_{Sg} decreased at v_{Sg} < $v_{Sg,min}$. The model performs best in predicting the holdup with the (Bh-O) closure models.

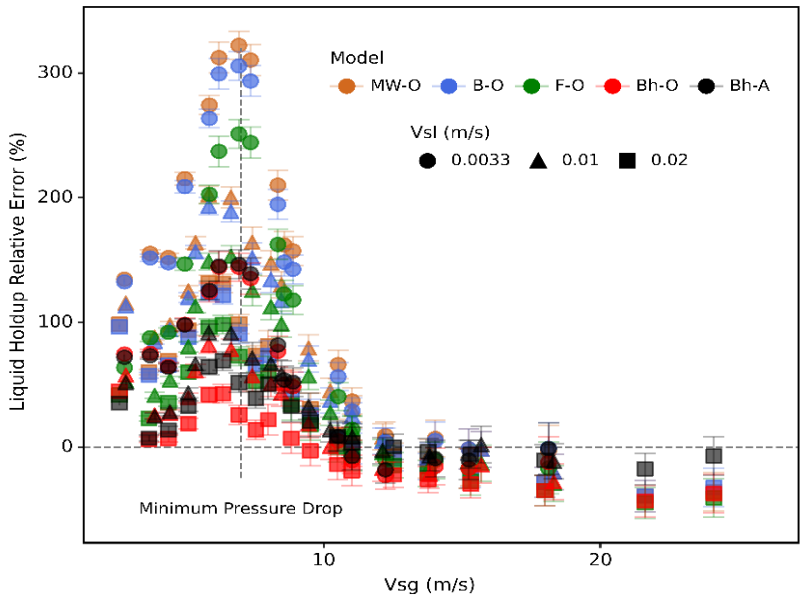

Figure 6-12: Relative error of the proposed model for oil-air liquid holdup at varying v_{Sg} values with different closure models.

6.2.1.3 Statistical Parameters. The closure models were assessed for predicting pressure drop and liquid holdup using statistical parameters. These parameters are described in detail in Appendix B. The average absolute percentage relative error, or ε_2, eliminates the masking effect of over- and under-predictions by using the absolute errors, and hence, provides a fair assessment of the models.

Figure 6-13 presents an evaluation of the proposed model in predicting the pressure drop by ε_2 with different closure relationship for water-air and oil-air flow. The result shows that (Bh-A) model has the lowest ε_2 for water-air flow. This is because (Bh)

f_i and (A) entrainment correlations were developed for churn flow using water-air data and pipe ID's (0.024 and 0.05 m) similar to the current study. On the other hand, the proposed model with (Bh-O) closures has the best performance for oil-air flow. This is because Oliemans' model was developed using various fluids and considers the effect of fluid properties. Hence, it recommended to use (Bh) interfacial shear model, with (A) entrainment model for water-air flow and (O) entrainment model for other liquids. Table 6-1 shows the statistical parameters for both pressure drop and liquid holdup predictions.

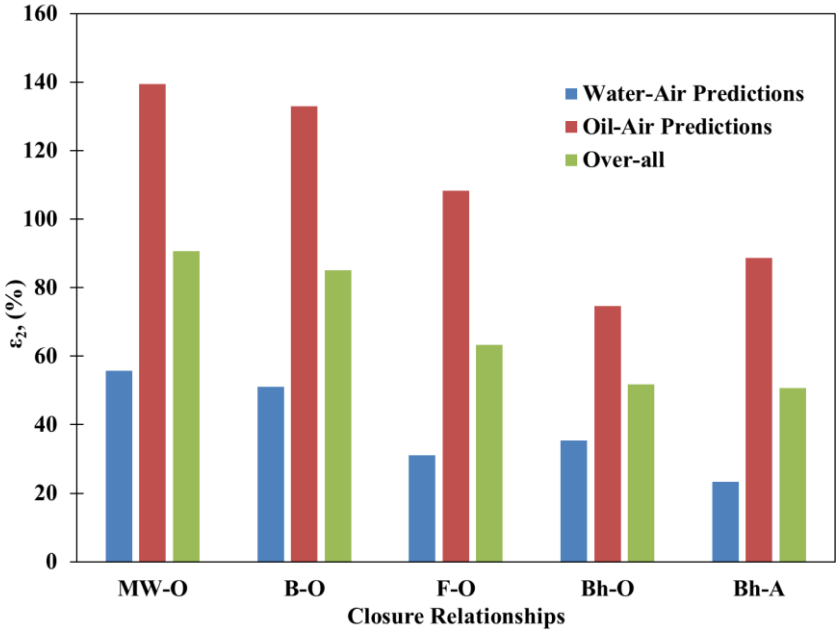

Figure 6-13: Closure models evaluation using ε_2 parameter for pressure drop

Table 6-1: Statistical Analysis of Pressure Drop and Liquid Holdup Predictions

		Pressure Drop						Liquid Holdup					
	Model	ε_1	ε_2	ε_3	ε_4	ε_5	ε_6	ε_1	ε_2	ε_3	ε_4	ε_5	ε_6
		(%)			(Pa/m)			(%)			(-)		
Water-Air Predictions	MW-O	55	**56**	49	575	577	784	37	**44**	46	0.050	0.052	0.077
	B-O	51	**51**	47	541	542	774	33	**39**	45	0.047	0.048	0.076
	F-O	31	**31**	22	273	273	331	4	**24**	28	0.016	0.022	0.033
	Bh-O	32	**35**	43	254	282	473	4	**23**	30	0.013	0.023	0.046
	Bh-A	19	**23**	26	196	231	422	0.4	**18**	26	0.010	0.020	0.041
Oil-Air Predictions	MW-O	139	**139**	111	533	534	475	92	**99**	94	0.059	0.061	0.064
	B-O	133	**133**	106	511	513	465	86	**93**	90	0.056	0.058	0.063
	F-O	108	**108**	86	372	372	268	59	**71**	75	0.036	0.039	0.038
	Bh-O	75	**75**	52	270	270	229	27	**42**	48	0.020	0.025	0.032
	Bh-A	89	**89**	54	306	306	207	38	**43**	44	0.024	0.025	0.029
Over-all	MW-O	90	**91**	90	558	559	671	60	**67**	75	0.054	0.056	0.072
	B-O	85	**85**	87	528	530	661	55	**62**	72	0.051	0.053	0.071
	F-O	63	**63**	69	314	314	309	27	**44**	59	0.024	0.029	0.036
	Bh-O	50	**52**	51	261	277	389	13	**31**	40	0.016	0.024	0.041
	Bh-A	48	**51**	53	242	262	352	16	**28**	39	0.016	0.022	0.037

6.2.2 A Comparison of the Proposed Model with Commercial Models

The performance of the proposed model was compared to the TUFFP unified and OLGA models. For this purpose, the proposed model with the best performance among the tested closure models was utilized. The proposed model with (Bh-A) and (Bh-O) closure models was used for water-air and oil-air data, respectively. The models' predictions were compared to the average value of the experimental data at the same superficial gas velocity, with the experimental data's uncertainties (see Appendix C) considered in the generation of error bars.

6.2.2.1 Comparison in Water-air Flow. Figure 6-14 compares the pressure drops predicted by the proposed model with (Bh-A) closures to that of the OLGA and unified models for water-air flow. At v_{Sg} > 7 m/s, the proposed model outperforms OLGA and unified model with most errors close to zero. The highest relative error can be seen at v_{SL} = 0.0033 m/s. The data were overpredicted by the proposed model, and the relative error

increases as the v_{Sg} decreases at v_{Sg} <7 m/s. The data are underpredicted by both unified and OLGA models, and the negative errors increase as the v_{Sg} decreased at v_{Sg} <7 m/s.

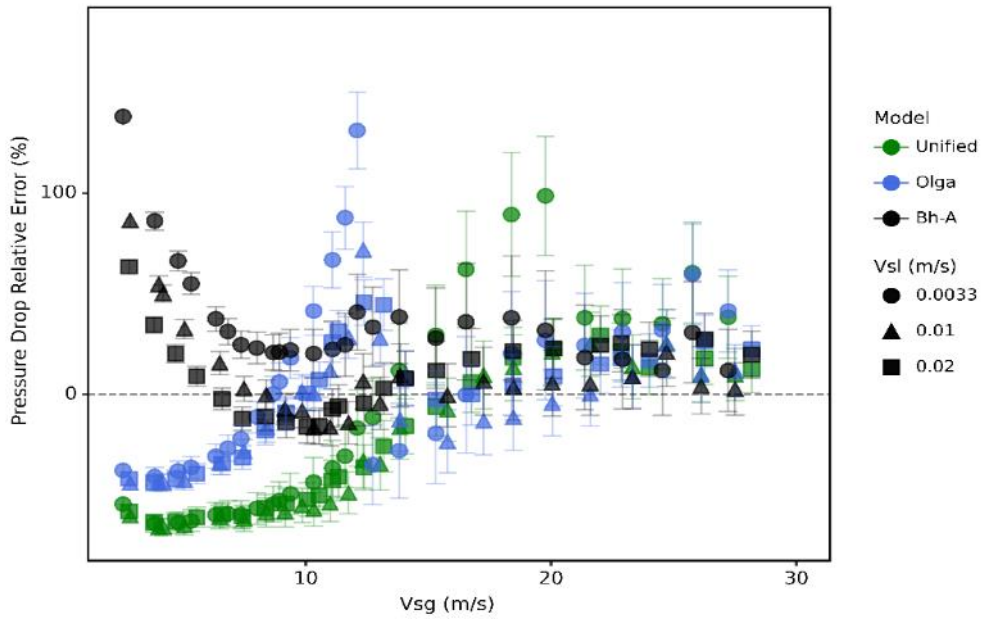

Figure 6-14: Comparison of the proposed model with OLGA and unified models in predicting pressure drop for water-air flow

Figure 6-15 compares the liquid holdups predicted by the proposed model with (Bh-A) closures to OLGA and unified models for water-air flow. The proposed model has liquid holdup prediction errors closer to zero than those of other models, with the data mostly underestimated at v_{Sg} > 7 m/s. However, at v_{Sg} < 7 m/s, the relative error increases as the v_{Sg} decreases, which could be due to approaching the transition to slug flow and the change in flow behavior. Due to their use of the slug flow model in this region, the unified and OLGA models predict more accurately at low v_{Sg}.

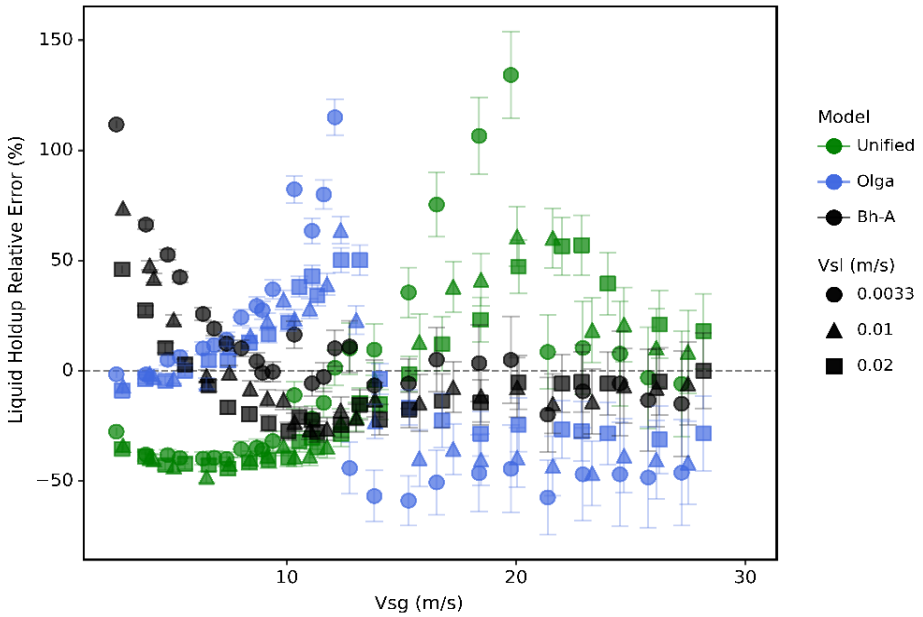

Figure 6-15: Relative errors of OLGA and unified model liquid holdup predictions compared to the proposed model for water-air flow

Figure 6-16 compares the onset of liquid loading predictions of the proposed model, unified, OLGA, and Barnea's models with experimental water-air flow data. The outcome demonstrates that OLGA predictions are superior to other models. The proposed model makes better predictions than Barnea's model, because it considers the effect of the entrainment fraction, which reduces the thickness of the liquid film and facilitates the liquid film's upward movement.

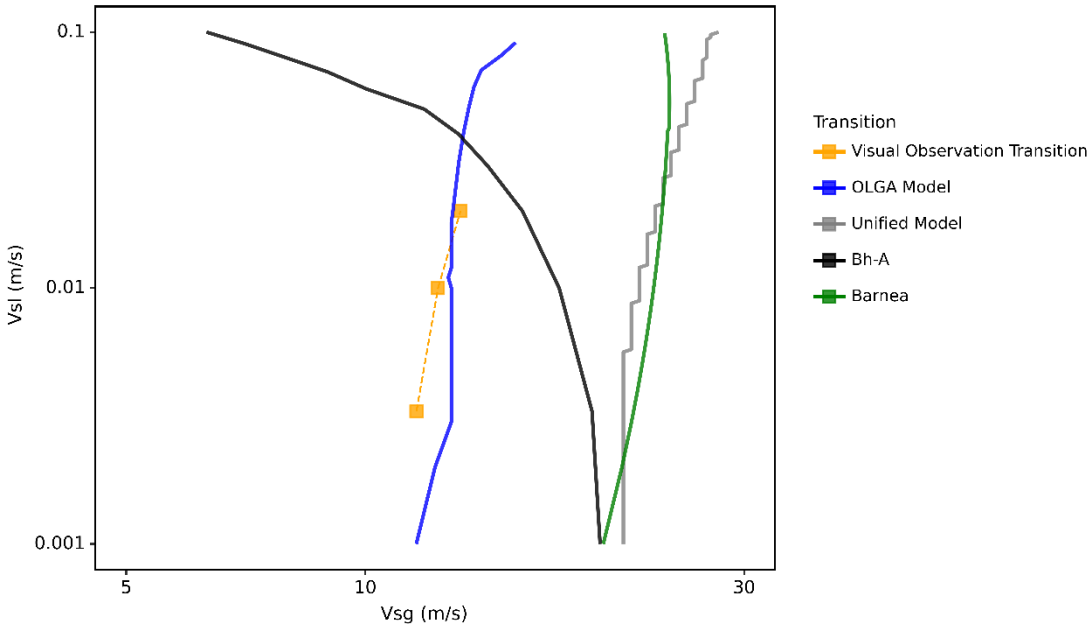

Figure 6-16: Onset of liquid loading predictions of the the unified, OLGA and Barnea's models compared to the propsed model for water-air flow

6.2.2.2 Comparison in Oil-air Flow. Figure 6-17 shows the relative errors of OLGA and unified models compared to the proposed model in predicting the pressure drops of oil-air flow. For all models, the figure depicts an inverted V-shaped curve, with most of the data being overpredicted. The highest relative errors are found close to $v_{Sg,min}$; the low experimental pressure drop values contribute to a sudden rise in relative errors. Furthermore, the low oil surface tension results in a significant increase in entrainment near the minimum pressure drop. The entrainment fraction models may under-predict the oil entrainment fraction in this region, hence over-predicting the holdup. Overall, the proposed model outperforms OLGA and unified models.

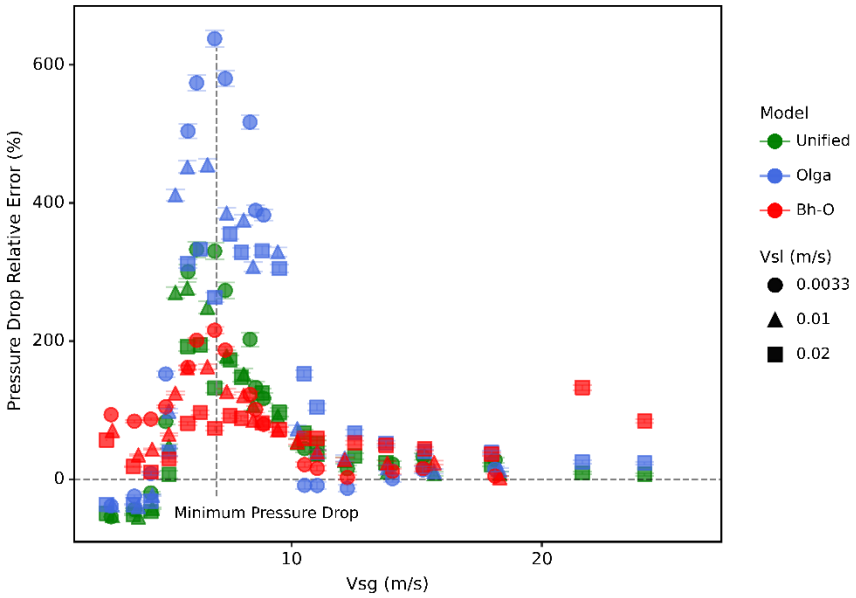

Figure 6-17: Relative errors of OLGA and unified models compared to the proposed model in predicting the pressure drop of oil-air flow

Figure 6-18 shows the relative errors of OLGA and unified models compared to the proposed model in predicting the liquid holdup of oil-air flow. Similar to pressure drop, the relative error is maximized around $v_{Sg,min}$. The proposed model underpredicts the data at high v_{Sg}. The relative error increases as the v_{Sg} decreases at v_{Sg}>10 m/s, reaching its maximum value at $v_{Sg,min}$. Overall, the proposed model with (Bh-O) closures predicts the liquid holdup better than the other models, especially around the $v_{Sg,min.}$

Figure 6-19 compares the onset of liquid loading predictions of the unified, OLGA, Barnea, and the proposed models with the experimental oil-air flow data of this study. Similar to water-air flow, OLGA outperforms the other models. The proposed model outperforms Barnea's model by considering the effect of the entrainment fraction, which thins the liquid film and makes it easier for the liquid film to travel upwards.

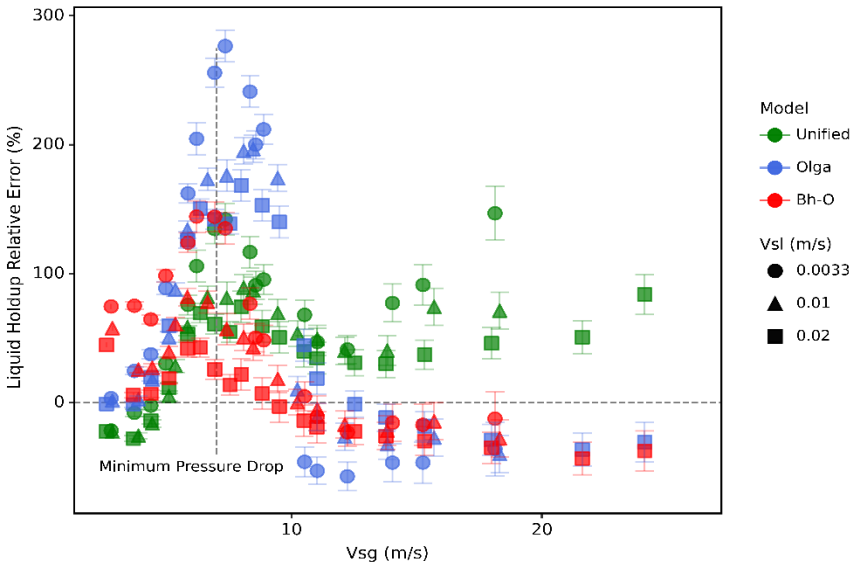

Figure 6-18: Relative error of OLGA and unified models compared to the proposed model in predicting the pressure drop of oil-air flow

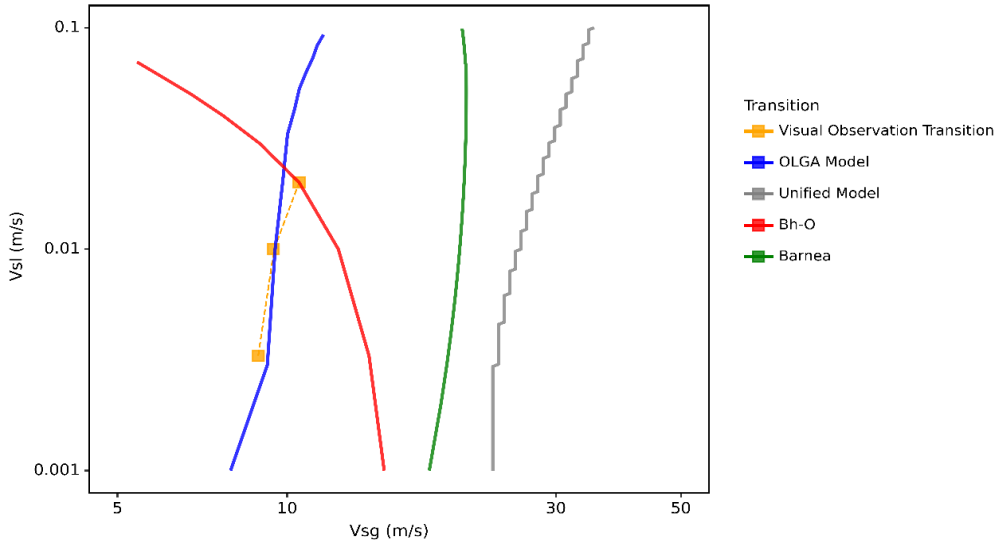

Figure 6-19: Onset of liquid loading predictions of various models compared to the oil-air experimental data

6.2.2.3 Statistical Analysis. Figure 6-20 presents the evaluation of the proposed model in predicting the pressure drop, by ε_2, compared to unified and OLGA models for

water-air and oil-air flow. The outcome demonstrates that the proposed model's predictions are superior to those of the unified and OLGA models. The lack of oil-air flow data in the literature may be the reason that all the models perform better for water-air flow compared to oil-air flow. The accuracy of the closure models, specifically the f_i and entrainment fraction correlation, could be impacted, which might affect the accuracy of the models for oil-air flow. Table 6-2 shows the statistical analysis for both pressure drop and liquid holdup.

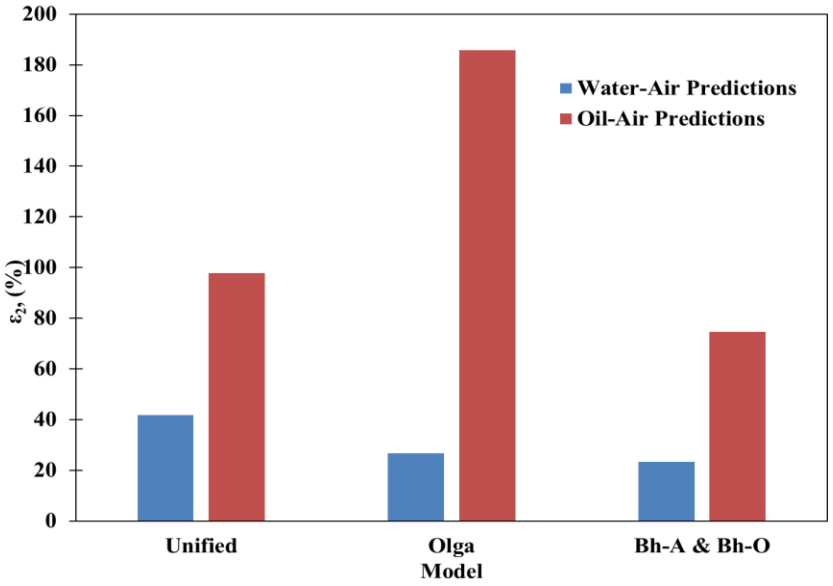

Figure 6-20: Unified, Olga, and the proposed model's evaluations using ε_2 parameter for pressure drop predictions

Table 6-2: Statistical Parameters for Pressure Drop and Liquid Holdup Predictions of the unified, OLGA and Proposed Models

		Pressure Drop						Liquid Holdup					
	Model	ε_1	ε_2	ε_3	ε_4	ε_5	ε_6	ε_1	ε_2	ε_3	ε_4	ε_5	ε_6
		(%)			(Pa/m)			(%)			(-)		
Water-Air Predictions	Unified	-21	**42**	42	-303	371	402	-7	**33**	39	-0.0205	0.0269	0.0292
	Olga	2	**27**	35	-89	219	304	-2	**30**	38	0.0049	0.0152	0.0181
	Bh-A	19	**23**	26	196	231	422	0.4	**18**	26	0.0097	0.0199	0.0408
Oil-Air Predictions	Unified	82	**98**	108	27	192	257	51	**57**	43	0.0140	0.0236	0.0220
	Olga	174	**186**	204	164	276	287	67	**88**	98	0.0299	0.0359	0.0354
	Bh-O	75	**75**	52	270	270	229	27	**42**	48	0.0204	0.0248	0.0324

6.3 Interfacial Shear Stress Model Development

The proposed mechanistic model's results with various closure models demonstrate the significance of closure models. Depending on the closure model, particularly the interfacial shear model, the result of the proposed model can significantly change. A closure model was developed for f_i to enhance the two-phase flow model's ability to predict pressure drop and liquid holdup. First, the interfacial friction factor was determined using Equation (6-32), as follows:

$$f_i = 2 * \frac{\tau_i}{\rho_c (v_C - v_F)^2} \tag{6-33}$$

where $\tau_i$can be calculated as follows, using the experimental pressure drop data:

$$\tau_i = -\frac{A_C}{S_I}\frac{d_P}{d_L})_C - \rho_C \frac{A_C}{S_I} g \tag{6-34}$$

The entrainment fraction must be used to calculate the core velocity v_C, shown in Equation $v_C = \frac{(v_{SG}+v_{SL}f_E)d^2}{(d-2\delta_L)^2}$ (6-25), and the film velocity v_F, shown in Equation $v_F = v_{SL}\frac{(1-f_E)\,d^2}{4\delta_L(d-\delta_L)}$ (6-22). At this study, the entrainment fraction models of Azzopardi and Wren (A) (2004) and Olimenas et al. (1986) were used to calculate the fi value for water-air flow and oil-air flow, respectively. Section 6.2 describes the performances of these models in detail, showing the superior performance of Azzopardi and Wren's model for water-air flow and Oliemans' model for oil-air flow.

Figure 6-21 depicts the behavior of the calculated, f_i with v_{Sg}. The figure shows that for a constant v_{SL}, as v_{Sg} decreases, f_i increases. In general, f_i is greater for water-air

flow than the oil-air flow. However, the f_i values become similar at high v_{Sg} values. This is because of the low slip velocity at high v_{Sg}, negating the influence of fluid density and dominating the frictional forces in this region. The f_i values also become similar at very low v_{Sg} values, approaching the slug flow.

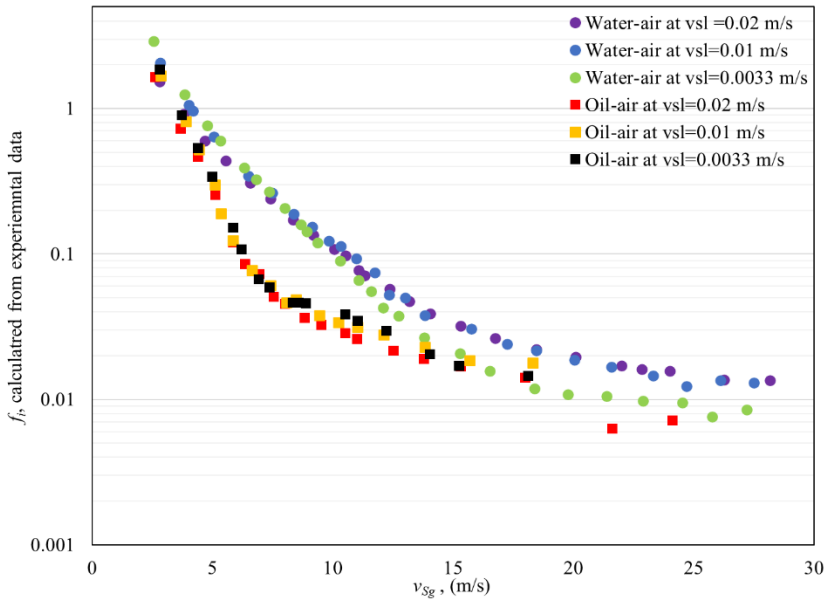

Figure 6-21: The calculated interfacial friction factor from experimental data at varying v_{Sg} values

Bharathan and Wallis (1983) introduced dimensionless parameter d^* which can be determined from the following equation:

$$d^* = d\sqrt{\frac{(\rho_L - \rho_G)g}{\sigma}} \tag{6-35}$$

Figure 6-22 shows the behavior of the back-calculated f_i value from the experimental data, at varying, $(d^* \times H_L/4)$ values. The f_i increases with the increase of $(d^* \times H_L/4)$. Also, Figure 6-21 and Figure 6-22 show that $f_i$is function of $v_{SL.}$

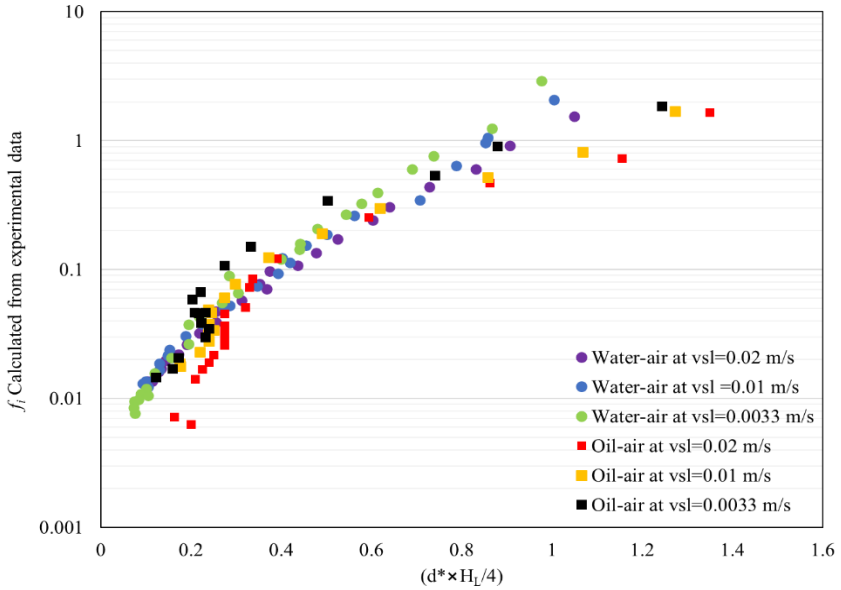

Figure 6-22: The back-calculated f_i from experimental data at varying (d^*×H$_L$/4) values

A correlation was developed to calculate f_i of annular and churn flow as a function of $(d^* \times H_L/4)$ and superficial liquid Reynolds number (Re_{SL}) based on the experimental data for water-air and oil-air flow. The coefficients of $(d^* \times H_L/4)$ and Re_{SL} were optimized to get the lowest errors, as shown in Figure 6-23. In this figure the model shows good agreement for most data points, with slight underpredictions for water-air flow at high f_i values close to the slug flow transition. The proposed f_i closure model is given as:

$$f_i = 10^{A+B*Re_{SL}} + \left(\frac{d^*(H_L)}{4}\right)^C. \quad (6\text{-}36)$$

Where d* can be calculated from Equation $d^* = d\sqrt{\frac{(\rho_L-\rho_G)g}{\sigma}}$ (6-35), and Re_{SL}, A, B, and C can be calculated as follows:

$$Re_{SL} = \frac{\rho_L v_{SL} d}{\mu_L}, \quad (6\text{-}37)$$

$$A = X_1 + X_2 d^*, \quad (6\text{-}38)$$

$$B = X_3 + X_4 d^*, \tag{6-39}$$

$$C = X_5 + X_6 d^*. \tag{6-40}$$

Coefficients X_1 to X_6 can be determined from the following table:

Table 6-3: The Proposed f_i Model Coefficients

Coefficient	Value
X_1	-0.33075
X_2	0.01896
X_3	1.029E-03
X_4	-6.052E-05
X_5	1.2305
X_6	0.03748

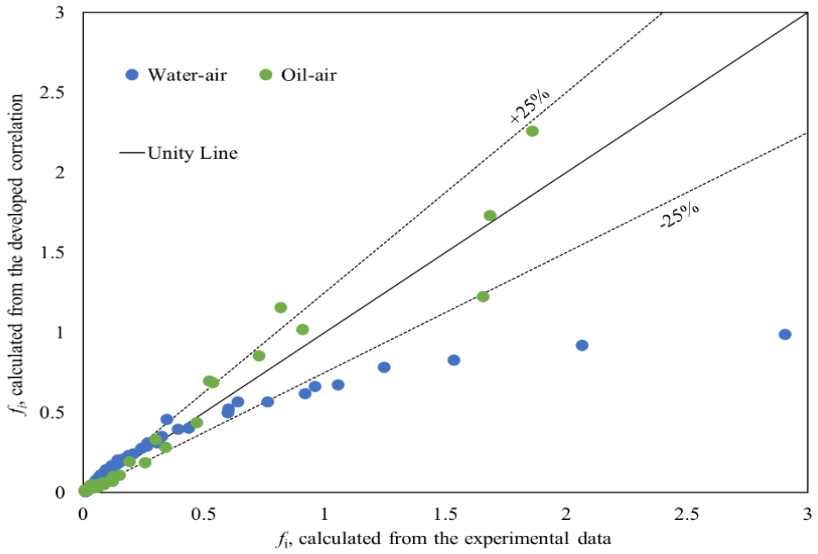

Figure 6-23: Performance of the proposed f_i correlation

6.3.1 Predictions in Water-air Flow

Figure 6-24 depicts the relative error of the proposed mechanistic model with the developed f_i closure compared to OLGA and unified models in predicting the pressure

drop (Pr-A) for water-air flow. The greatest improvement in the model predictions occurs at v_{SL} = 0.0033 m/s, where the large relative errors seen in Figure 6-14 are reduced. At v_{Sg} < 7 m/s, the relative errors of the proposed model increase as the v_{Sg} decreases, which is due to approaching the transition to slug and changing the flow behavior.

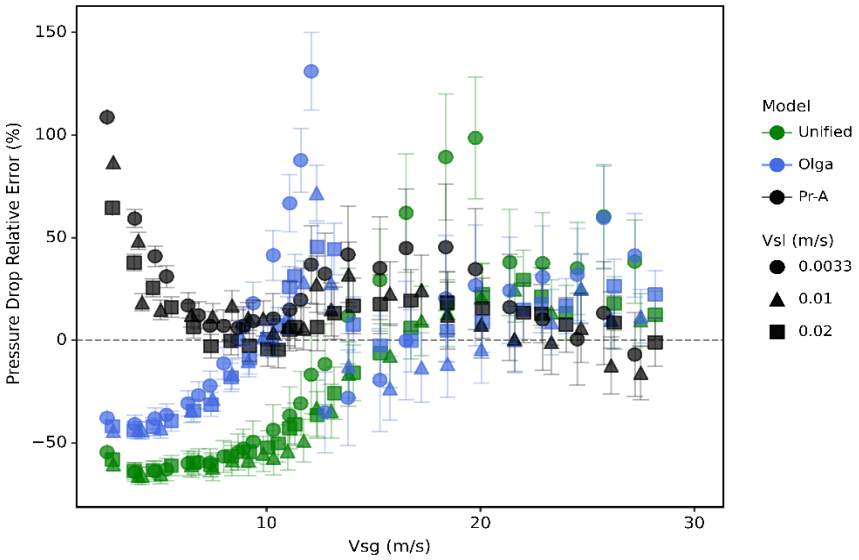

Figure 6-24: Relative errors of the proposed model with the developed f_i correlation, OLGA, and unified model for pressure drop of water-air flow

Figure 6-25 compares the relative errors of the proposed model with the developed f_i correlation, OLGA and unified model in liquid holdup prediction for water-air flow. In general, the liquid holdup predictions show lower relative errors than pressure drop predictions. However, similar behavior is observed at v_{Sg} < 7 m/s, where the relative error increases the v_{Sg} decreases by approaching the transition to slug flow.

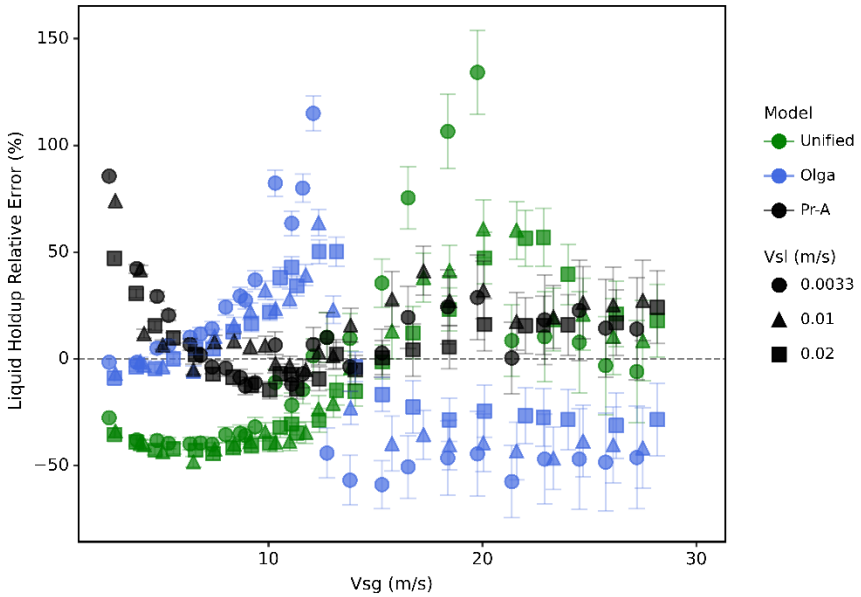

Figure 6-25: Relative errors of the proposed model with the developed f_i closure, OLGA and unified model for liquid holdup of water-air flow

6.3.2 Predictions in Oil-air Flow

Figure 6-26 depicts the relative errors of the proposed model with the developed f_i closure, OLGA and unified models for the pressure drop of oil-air flow at varying v_{Sg} values. The proposed model uses the developed f_i model and Oliemans et al. (1986) for the entrainment fraction closure model. The figure depicts an inverted V-shaped curve for all models, with most of the data being overpredicted. The highest relative errors are found near $v_{Sg,\min}$. The experimental pressure drops close to zero contribute to the sudden increase in relative errors in this region. Furthermore, the low oil surface tension result in a significant increase in droplet entrainment near the minimum pressure drop, which may not be captured by the entrainment fraction closure models. However, the proposed model does a better job in predicting the pressure drop than both OLGA and unified models in the churn flow region.

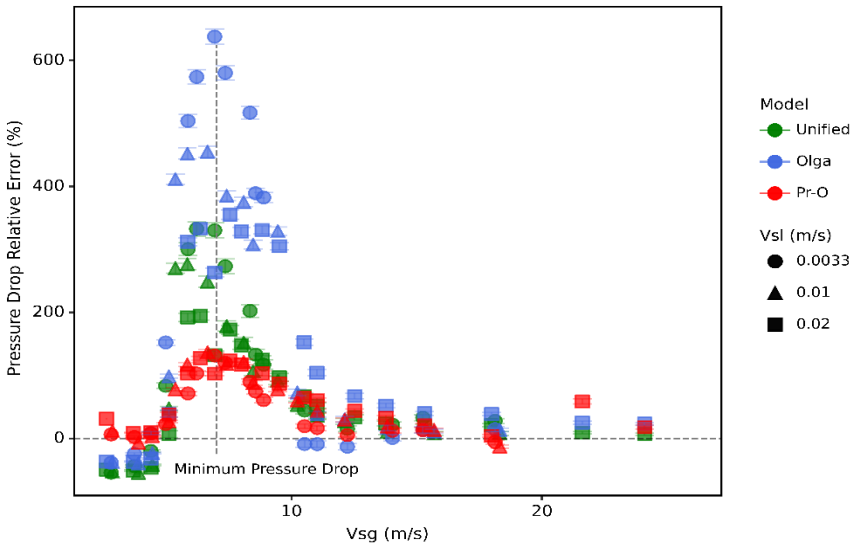

Figure 6-26: Relative errors of the proposed model with the developed f_i model, OLGA and unified model for pressure drop of oil-air flow

Figure 6-27 compares the relative errors of the proposed model with the developed f_i model, OLGA and unified model for liquid holdup of oil-air flow. Similar to pressure drop, the maximum holdup relative errors are observed around the $v_{Sg,\min}$.

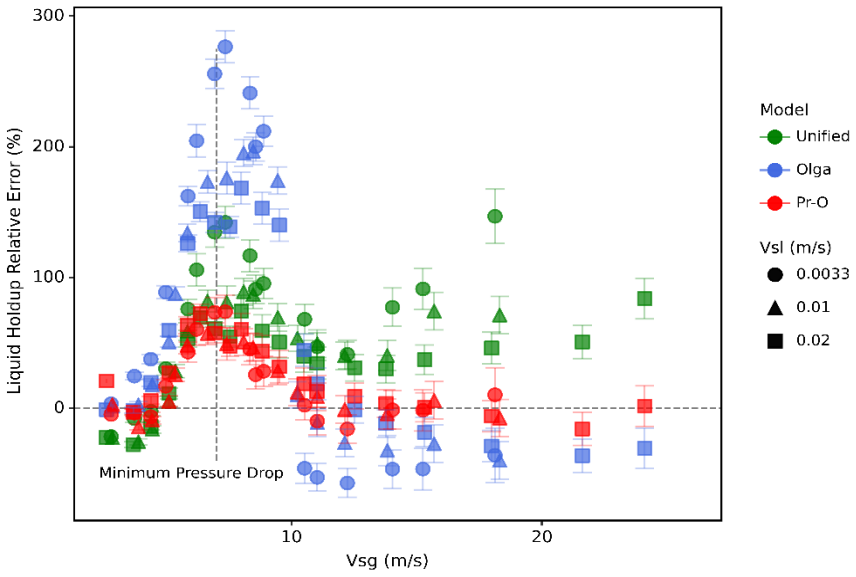

Figure 6-27: Relative errors of the proposed model with the developed f_i model, OLGA and unified model for liquid holdup of oil-air flow

6.3.3 Statistical Parameters

Figure 6-28 depicts the performance of the proposed pressure drop model with the developed f_i closure, evaluated by ε_2 for water-air and oil-air flows. The results show that the proposed model's predictions outperform the unified and OLGA models. Because of a lack of data on oil-air flow in the literature, all models perform better in water-air flow than oil-air flow. This is possibly due to more accurate closure models for water-air flow. Using the developed f_i model improves and lowers the relative errors, particularly for oil-air flow. The statistical analyses for pressure drop and liquid holdup are shown in Table 6-4. The proposed model provides the lowest ε_2 values for both liquid holdup and pressure drop predictions and for both water-air and oil-air flows.

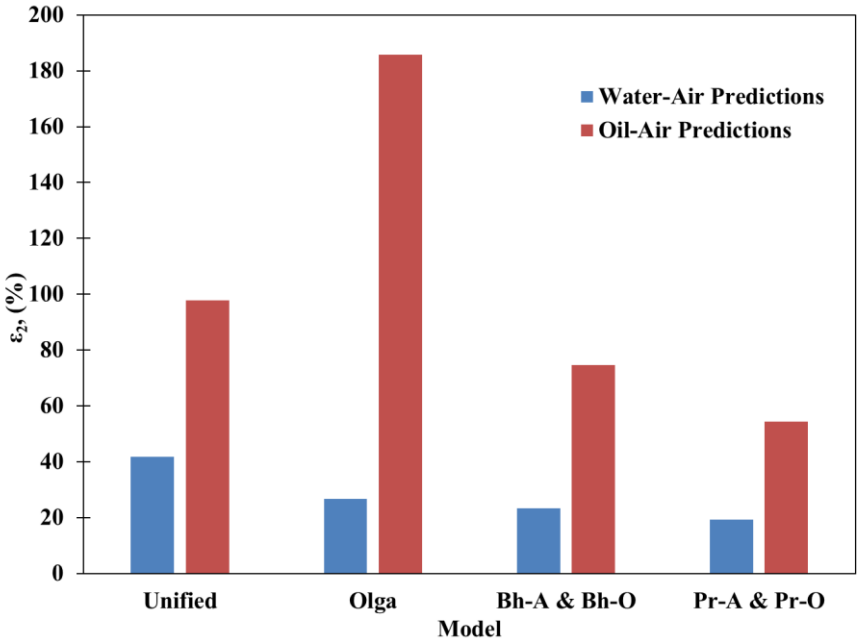

Figure 6-28: Unified, Olga, and the proposed model with the prosed f_i model's evaluation using ε_2 parameter for pressure drop

Table 6-4: Statistical analysis of pressure drop and liquid holdup predictions for the unified, OLGA and the proposed model with the developed f_i model

		Pressure Drop						Liquid Holdup					
	Model	ε_1	ε_2	ε_3	ε_4	ε_5	ε_6	ε_1	ε_2	ε_3	ε_4	ε_5	ε_6
		(%)			(Pa/m)			(%)			(-)		
Water-Air Predictions	Unified	-21	**42**	42	-303	371	402	-7	**33**	39	-0.0205	0.0269	0.0292
	Olga	2	**27**	35	-89	219	304	-2	**30**	38	0.0049	0.0152	0.0181
	Bh-A	19	**23**	26	196	231	422	0	**18**	26	0.0097	0.0199	0.0408
	Pr-A	18	**19**	21	173	181	342	11	**16**	19	0.0110	0.0147	0.0316
Oil-Air Predictions	Unified	82	**98**	108	27	192	257	51	**57**	43	0.0140	0.0236	0.0220
	Olga	174	**186**	204	164	276	287	67	**88**	98	0.0299	0.0359	0.0354
	Bh-O	75	**75**	52	270	270	229	27	**42**	48	0.0204	0.0248	0.0324
	Pr-O	53	**54**	45	150	155	115	21	**25**	26	0.0087	0.0116	0.0129

CHAPTER 7

Conclusions and Recommendations

This chapter summarizes the study's observations and results, as well as its conclusions. In addition, recommendations are made for future studies to potentially increase our understanding of liquid loading in natural gas wells and effects of inserts.

7.1 Conclusions

7.1.1 Two-phase Flow Experiments

- A quantitative method was developed to predict the onset of liquid loading using the experimental data, named the positive frictional pressure gradient. This technique provides relatively more consistent predictions of the onset of liquid loading than the minimum-pressure drop technique, which is a function of the balance between gravitational and frictional losses and may over or underestimate the onset.
- The OLGA model and Coleman’s correlation have the best performances in predicting the onset of liquid loading for the data of this study.
- Minimal differences are observed for liquid holdup and pressure drop of water-air and oil-air flow, while in the annular or slug flow patterns. However, the differences become substantial within the churn flow region or around the onset of liquid loading. In this region, oil-air flow has significantly lower pressure drops than water-air flow.

7.1.2 Effects of Restrictions on Liquid Lifting

- Two flow behaviors were observed in churn flow with partial restrictions or inserts. before the insert, a thin liquid film was observed flowing downward, with liquid droplets traveling upward. After the insert, a lot of mixing and agitation was observed, generating high-amplitude liquid waves. These waves facilitate droplet generation and prevent liquid fallback.
- As the flow pattern changes to churn and then slug flow, the cases with insert have similar or lower pressure drops compared to the no-insert cases. The insert cases have lower gravitational pressure drops in the churn region by lowering the liquid holdup. It can be concluded that the inserts have the most positive effect at lower gas rates of churn flow and at lower v_{SL} cases.
- The inserts provide the largest reduction in the liquid holdup for oil-air flow. This is due to the lower density and surface tension of oil compared to water, resulting in larger interfacial wave structures, particularly after adding the inserts. These waves facilitate droplets generation and improve entrainment.
- The values of change in holdup are higher than the pressure drop change values. This is because the pressure drop changes combine two effects of the inserts, decreasing the gravitational losses, but also increasing the frictional losses. The results show that the inserts may enhance the liquid lifting by lowering the liquid holdup, and also increase the pressure drop by increasing the frictional losses. The 1.75-inch insert provides a lower combined pressure loss than the 1.5-inch insert for water-air flow. For oil-air flow, the reduction in pressure drop is higher than the increase in frictional

loss, making the insert size of 1.5 in. better, particularly at lower v_{SL} and v_{Sg} values.*Modeling Development*

- A 1-D mechanistic model was developed, particularly for churn flow in vertical pipes, to predict the pressure drop and liquid holdup by considering the effect of liquid entrainment in the gas core. Various f_i and entrainment closure models available in the literature were tested in the proposed mechanistic model. The model with the best-performing closure models was then compared to two commercially available models, the unified and OLGA models. Finally, a model was developed to predict the f_i value based on the experimental data to enhance the proposed mechanistic model's predictions.
- The suggested model produced unsatisfactory predictions using the available f_i closures established for annular flow, with most data being sharply overpredicted in the churn zone. Jayanti and Brauner's (1994) method was used to enhance the predictions made by averaging the f_i closure of Bharathan and Wallis (1983) with the models developed for annular flow, and resulted in considerable improvements.
- The proposed model with the Bharathan's f_i closure and Azzopardi's entrainment closure predicted the data better than the other models for water-air flow. For oil-air flow, the suggested model with Bharathan's f_i closure and Oliemans's entrainment closure predicted the data better than the other closures. Oliemans' model was developed using various fluids and takes into consideration the influence of fluid properties, making it the better choice for oil-air flow.

- v_{Sg}, the proposed model and the other models sharply overpredicted the pressure drop around $v_{Sg,min}$ with high relative errors. The low oil surface tension may contribute to the significant increase in entrainment near the minimum pressure drop. The entrainment fraction models may be unable to accurately predict the significant increase in entrainment in this region. Overall, the proposed model outperformed the OLGA and unified models in terms of data prediction.The interfacial friction factor, f_i, was back-calculated from the experimental data as a function of the core and the liquid film velocities, and the core density. A correlation was developed to predict f_i , based on the data and as a function of ($d^* \times H_L/4$) and superficial liquid Reynolds number (Re_{SL}) for annular and churn flow. The proposed model with the developed f_i model predicted the experimental data better than other models, including OLGA, unified model, and the proposed model with Jayanti's f_i closure. The greatest improvement in the model predictions occurred at v_{SL} = 0.0033 m/s and for oil-air flow.

7.2 Recommendations

- The GoPro camera installation can be enhanced through automation. The current system requires a man-lift to install the camera before conducting tests. It can be replaced with an automated cable reel system that can remotely lift the camera.
- A more accurate and fast-acting control valve to control the air mass flow rate may help in reducing the time required to stabilize the tests.

- A wire mesh tomography device can be employed to monitor the phase distributions and liquid holdup, especially for the case of insert.
- Installing capacitance probes can help in estimation of the liquid film thickness and be beneficial for modeling development.
- Measuring the entrainment is a laborious task. The measuring methods might disrupt the flow and cause large uncertainties. Comparing the findings of various measuring approaches and selecting the best one may be crucial for future research.
- Repeating the tests with different fluids using a similar test matrix can help better clarify the effects of varying density and surface tension. A surfactant capable of lowering surface tension may be helpful for this.
- The results show some positive effects of the inserts. Further experiments are necessary to find the optimum setup for enhancing liquid lifting with changes to the current setup's parameters, such as insert size, spacing, and the number of inserts.
- More vertical experimental data on low liquid rates are required to validate the proposed mechanistic model and the f_i correlation.

NOMENCLATURE

Symbol	Description	Unit
A_C	Gas core area	m^2
A_F	Liquid film area	m^2
A_G	Area of gas phase	m^2
A_L	Area of liquid phase	m^2
A_p	Pipe area	m^2
d	Pipe inner diameter	m
d^*	Dimensionless coefficient	/
d_D	diameter of droplet	m
d_L	diameter of liquid phase	m
d_g	diameter of gas phase	m
$\left(\frac{dP}{dL}\right)_T$	Total pressure gradient	Pa/m
$\left(\frac{dP}{dL}\right)_G$	Gravitational pressure drop	Pa/m
$\left(\frac{dP}{dL}\right)_F$	Frictional pressure drop	Pa/m
$\left(\frac{dP}{dL}\right)_{min}$	Minimum pressure drop	Pa/m
F_E	Entrainment fraction	/
$F_{E,max}$	Maximum entrainment	/
f_F	Liquid film friction factor	/
f_i	Interfacial friction factor	/
f_L	Liquid friction factor	/
h_L	Liquid height	m
h_{total}	Total height	m
H_L	Liquid holdup	/
ID	Inside pipe diameter	m
$\dot{m}$	Air mass flow rate	Kg/s
QCV	Quick closing valve	/
q_C	Core volumetric flow rate	m^3/s
q_F	Liquid film volumetric flow rate	m^3/s
q_G	Gas volumetric flow rate	m^3/s
q_L	Liquid volumetric flow rate	m^3/s
S_I	Wetted perimeter of the core phase	m
S_L	Wetted perimeter of the liquid phase	m
t	Time	s
v_C	core velocity	m/s

v_f	Liquid film velocity	m/s
v_G	Gas velocity	m/s
v_S	slip velocity	m/s
v_{SC}	Superficial core velocity	m/s
v_{SL}	Superficial liquid velocity	m/s
v_{Sg}	Superficial gas velocity	m/s
$v_{Sg,c}$	Critical superfocoal gas velocity	m/s
$v_{Sg,S}$	Superficial gas velocity at transition to slug occurred	m/s
$v_{Sg,min}$	Superficial gas velocity at minimum pressure	m/s
R_{air}	Air gas constant	J/Kg K
We	Weber number	/
We'	Modified Weber number	/
α_C	Core void fraction	/
α_T	Void fraction	/
λ	No-slip liquid holdup	/
δ_L	Liquid film thickness	m
$\frac{\delta_L}{d}$	Dimensionless liquid film thickness	/
ρ_A	Air density	Kg/m^3
ρ_C	Core density	Kg/m^3
ρ_G	Gas density	Kg/m^3
ρ_L	Liquid phase density	Kg/m^3
μ_C	Core viscosity	Pa.s
μ_G	Gas viscosity	Pa.s
μ_L	Liquid viscosity	Pa.s
τ_I	Interfacial shear stress	Pa
τ_{WL}	Wall shear stress	Pa
σ	Liquid phase surface tension	N/m
ϕ_G	Dimensionless coefficient of gas phase	/
ϕ_L	Dimensionless coefficient of liquid phase	/

REFERENCES

Akhiyarov, D.T., Zhang, H.-Q., and Sarica, C., 2010, "High-Viscosity Oil-Gas Flow in Vertical Pipe," Presented at Offshore Technology Conference, Houston, TX, May3-6.

Alruhaimani, F. (2015). Experimental Analysis and Theoretical Modeling of High Liquid Viscosity Two-Phase Upward Vertical Pipe Flow. (Doctoral dissertation, The University of Tulsa).

Al-Ruhaimani, E. Pereyra, C. Sarica, E. Al-Safran, S. Chung, C. Torres,A study on the effect of high liquid viscosity on slug flow characteristics in upward vertical flow, Journal of Petroleum Science and Engineering, Volume 161,2018,Pages 128-146,ISSN 0920-4105,

Alsanea, M. (2018).Effect of Water Cut on Onset of Liquid Loading and Foam Lift Performance in Horizontal Well (MS Thesis, The University of Tulsa, Tulsa, Oklahoma).

Al-Sarkhi, A. and Sarica, C., 2011. Comment on "Correlation of entrainment for annular flow in horizontal pipes", by Pan, L., Hanratty, TJ, Int. J. Multiphase flow, 28 (3),(2002), pp. 385–408. International Journal of Multiphase Flow, 37(5), pp.535-536.

Andreussi, P., Asali, J.C., and Hanratty, T.J. 1985. Initiation of roll waves in gas-liquid flows. AIChE J. 31 (1): 119–126. http://dx.doi.org/10.1002/aic.690310114

Ansari, A. M., Sylvester, N. D., Shoham, O., & Brill, J. P. (1990, January 1). A Comprehensive Mechanistic Model for Upward Two-Phase Flow in Wellbores. Society of Petroleum Engineers. doi:10.2118/20630-MS

Aziz, K., Govier, G.W., and Fogarasi, M. 1972. Pressure Drop in Wells Producing Oil and Gas. J. Cdn. Pet. Tech. (7–9): 38–48.

Azzopardi, B.J. and Wren, E., 2004. What is entrainment in vertical two-phase churn flow?. International journal of multiphase flow, 30(1), pp.89-103.

Bharathan, D., and Wallis, G.B. 1983. Air-water counter-current annular flow. Int.J. Multiphase Flow, 9 (4): 349-366

Baker, Ovid. "Design of Pipelines for the Simultaneous Flow of Oil and Gas." Paper presented at the Fall Meeting of the Petroleum Branch of AIME, Dallas, Texas, October 1953. doi:https://doi.org/10.2118/323-G

Barnea, D., 1987. "A Unified Model for Predicting Flow Pattern Transitions for the Whole Range of Pipe Inclinations", Int. J. Multiphase Flow, 13 (1), pp. 1-12.

Barreto, C. 2016. Effect of Foamer Delivery Location on Horizontal Wells Deliquification. (MS Thesis, The University of Tulsa, Tulsa, Oklahoma)

Beggs, D. H. and Brill, J.P. 1973. A Study of Two-Phase Flow in Inclined Pipes. JPT 25 (5): 607–617.

Belfroid, S., Schiferli, W., Alberts, G., Veeken, C. A. M., & Biezen, E. (2008, January 1). Predicting Onset and Dynamic Behaviour of Liquid Loading Gas Wells. Society of Petroleum Engineers.

Belt, R., Duret, E., Larrey, D., Djoric, B., and S. Kalali. "Comparison of Commercial Multiphase Flow Simulators with Experimental and Field Databases." Paper presented at the 15th International Conference on Multiphase Production Technology, Cannes, France, June 2011.

Belt, RJ, van 't Westende, JMC & Portela, L 2009, 'Prediction of the interfacial shear-stress in vertical annular flow', International Journal of Multiphase Flow, vol. 35, no. 7, pp. 689-697.

Chisholm, D. 1967. A theoretical basis for the Lockhart-Martinelli correlation for two-phase flow. International Journal of Heat and Mass Transfer 10 (12): 1767–1778. doi:10.1016/0017-9310(67)90047-6.

Coleman, S. B., Clay, H. B., McCurdy, D. G. and Norris, L.H. 1991. A New Look at Predicting Gas-Well Load-Up. *J Pet Technol*, 43 (3): 329-333. SPE-20280-PA.

Duns, H., Jr. and Ros, N.C.J. 1963. Vertical Flow of Gas and Liquid Mixtures in Wells. Paper presented at the Sixth World Petroleum Congress, Tokyo, Japan

Fabre, J., and Liné, A., 1992, “Modeling of Two-Phase Slug Flow,” Annual Review of Fluid Mechanics, 24 (1): 21-46.

Fukano, Tohru and Tohru Furukawa. “Prediction of the effects of liquid viscosity on interfacial shear stress and frictional pressure drop in vertical upward gas–liquid annular flow.” International Journal of Multiphase Flow 24 (1998): 587-603.

Frèchou, D., 1986, “Etude de l’èoulelement ascendant à trois fluides en conduiteverticale,” Thèse, Inst. Natl. Polyteh. De Toulouse, France.

Hagedorn, Alton R., Brown, Kermit E., The U. of Texas, Experimental Study of Pressure Gradients Occurring During Continuous Two-Phase Flow in Small-Diameter Vertical Conduits Journal of Petroleum Technology Volume 17, Number 4 Pages 475–484 Date April 1965

Hasan, A.R. and Kabir, C.S. 1988. A Study of Multiphase Flow Behavior in Vertical Wells. SPEPE 3 (2): 263–272; Trans., AIME, 285. SPE15138-PA. DOI: 10.2118/15138-PA.

Hewitt, G. F., Lacey, P. M. C. and Nicholls, B. 1965. Transition in Film Flow in a Vertical Tube. Processings of the Two Phase Flow Conference, Exeter, England

Hinze, J. O. 1955, Fundamentals of the hydrodynamic mechanism of splitting in dispersion processes. AIChE J., 1: 289-295.

Ishii, M. and Mishima, K., 1989. Droplet entrainment correlation in annular two-phase flow. International Journal of Heat and Mass Transfer,32(10), pp.1835-1846.

Jayanti, S., and Brauner, N. 1994. Churn Flow. Multiphase Science and Technology 8: 471-522.

Jepson, D. M., Azzopardi, B. J. and Whalley, P. B. (1990) The effect of physical properties on drop size in annular flow. In 9th Intl Heat Transfer Conf., Jerusalem, Vol. 6, pp. 95-100.

Karami Mirazizi, H. (2015). Low liquid loading three-phase flow and effects of MEG on flow behavior. (Doctoral dissertation, The University of Tulsa).

Koeck, C., 1980, "Etude du frottement parietal dans un ecoulement diphasique verticalascendant," These Univ. Pierre et Marie Curie, Paris.

Lea, J. F., Nickens, H. V. and Wells, M. R. 2003. Gas Well Deliquification, Gulf Professional Publishing, Burlington, ISBN 0-7506-7724-4, 2003.

Li, J., Almudairis, F., & Zhang, H. (2014, December 10). Prediction of Critical Gas Velocity of Liquid Unloading for Entire Well Deviation. International Petroleum Technology Conference.

Li, M., Li, S. L., and Sun, L. T. 2002. New View on Continuous-Removal Liquids from Gas Wells. *SPE Prod & Fac*, 17(1):42-46. SPE-75455-PA

Liu, H., Vandu, C.O., Krishna, R., 2005, "Hydrodynamics of Taylor Flow in Vertical Capillaries: Flow Regimes, Bubble Rise Velocity, Liquid Slug Length, and Pressure Drop," Industrial & Engineering Chemistry Research, 44: 4884–4897.

Liu, H., 2014, "The Phenomenon of Negative Frictional Pressure Drop in Vertical Two-Phase Flow," Int. J. Heat and Fluid Flow, 45: 72-80.

Lockhart, R. W., and R. C. Martinelli, "Proposed Correlation of Data for Isothermal Two-Phase, Two-Component Flow in Pipes," *Chem. Eng. Progr.,* 45,39-48 (1949).

Magrini, K.L. (2009). Liquid Entrainment in Annular Gas-Liquid Flow in Inclines Pipes. MS Thesis. University of Tulsa

Meng, W. 1999, Low liquid loading gas-liquid two-phase flow in near-horizontal pipes, The University of Tulsa.

Oliemans, R.V.A., Pots, B.F.M. and Trompe, N., 1986. Modelling of annular dispersed two-phase flow in vertical pipes. International journal of multiphase flow, 12(5), pp.711-732.

Orkiszewski, J. 1967. Prediction of Two-Phase Pressure Drops in Vertical Pipe. JPT 19 (6): 829–838; Trans., AIME, 240.

Pagan, E. , Williams, W. C., Kam, S. , and P. J. Waltrich. "Modeling vertical flows in churn and annular flow regimes in small- and large-diameter pipes." Paper presented at the 10th North American Conference on Multiphase Technology, Banff, Canada, June 2016.

Paleev, I.I. and Filippovich, B.S., 1966. Phenomena of liquid transfer in two-phase dispersed annular flow. International journal of heat and mass transfer, 9(10), pp.1089-1093.

Pan, L. and Hanratty, T.J., 2002. Correlation of entrainment for annular flow in vertical pipes. International Journal of Multiphase Flow, 28(3), pp.363-384.

Poettmann, F.H. and Carpenter, P.G. 1952. The Multiphase Flow of Gas, Oil, and Water Through Vertical Flow Strings With Application to the Design of Gas Lift Installations. Drill. and Prod. Prac., API, 257–317.

Putra, Satya A., and Richard L. Christiansen. "Design of Tubing Collar Inserts for Producing Gas Wells Below Their Critical Velocity." Paper presented at the SPE Annual Technical Conference and Exhibition, New Orleans, Louisiana, September 2001.

Putra, S.A.: Development of a Mechanistic Two-Fluid Churn Flow Model and Design of Tubing-Collar Inserts for Enhancing Liquid Lifting to Prevent Liquid Load-up in Gas Wells, Ph. D. Dissertation, Colorado School of Mines, Golden, CO (2000).

Sakharov V.A., and Mokhov M.A., 2004, “Hydrodynamics of Gas-Liquid Mixtures in Vertical Pipes and Lifts,” Russia: Oil and Gas, Gubkin Russian State University of Oil and Gas, Moscow, Russia.

Sawant, P., Ishii, M., and Mori, M. 2008. Droplet Entrainment Correlation in Vertical Upward Co-Current Annular Two-Phase Flow. Nucl. Eng. Des. 238 (6): 1342–1352.

Skopich, A. 2012. Experimental Study of Surfactant Effect on Liquid Loading in 2-in and 4-in Diameter Vertical Pipes (Master of Science Thesis, The University of Tulsa).

Souhar, M., 1982, “Contribution à l'etude dynamique des ecoulements diphasiques gazliquide en conduite verticale: cas des regirnes a bulles et a poches,” These Inst. Natl. Polytech, Lorraine, Nancy.

Spedding, P.L., Woods, G.S., Raghunathan, R.S., and Watterson, J.K., 1998, “Vertical Two-Phase Flow Part III: Pressure Drop,” Trans IChemE, 76 (Part A): 628–634.

Sujumnong, M., 1998, “Heat Transfer, Pressure Drop and Void Fraction in Two-Phase, Two-Component Flow in a Vertical Tube,” Ph.D. Thesis, University of Manitoba, Winnipeg, Canada.

Taitel. Y. and Dukler. A. E.. “A Model for Predicting Flow Regime Transition in Horizontal and Near Horizontal Gas Liquid Flow”, AIChE J., 22, pp. 47-55 (1976).

Taitel. Y., Barnea, D. and Dukler. A. E.. “Modeling flow Pattern Transition for Steady Upward Gas - Liquid Flow in Vertical Tubes”, AlChE J., 26 345-354 (1980).

Thome, John & Cioncolini, Andrea. (2015). Entrained Liquid Fraction in Annular Two-Phase Flow. 10.1142/9789814623216_0022.

Turner, R. G., Hubbard, M. G. and Dukler, A. E. 1969. Analysis and prediction of minimum flow rate for the continuous removal of liquids from gas wells. Journal of Petroleum Technology, 21(11), 1-475.

Wallis, G. B. 1969 One-dimensional Two-phase Flow. McGraw-Hill, New York.

Wang, Y. Z. and Liu, Q. W. 2007. A New Method to Calculate the Minimum Critical Liquid Carrying Flow Rate for Gas Wells. Petroleum Geology and Oilfield Development in Daqing, 6 (8): 82-5.

Westende, J. Van’t, Kemp, H.K., Belt, R.J. and Portela, L.M., 2007. “On the Role of Droplets in Cocurrent Annular and Churn-Annular Pipe Flow,” Int. J. Multiphase Flow, 33, pp. 595–615.

Whalley, P. B., and D. M. Jepson. "Entrainment and deposition in annular gas− liquid flow: the effect of fluid physical properties." International Heat Transfer Conference Digital Library. Begel House Inc., 1994.

Yamamoto, H., “Enhancing Liquid Lift from Low Pressure gas Reservoirs “, SPE Paper 55625 presented at SPE Rocky Mountain Regional Meeting, Gillette, Wyoming, 15-18 May 1999

Zabaras, G., Dukler, A. E. and Moalem-Maron, D., 1986. “Vertical Upward Cocurrent Gas-Liquid Annular Flow,” AIChE J., 32(5), pp. 829-843.

Zhang, H.-Q. et al.: “Unified Model for Gas-Liquid Pipe Flow via Slug Dynamics—Part 1: Model Development,” J. Energy Res. Technol. (2003a) 125, No. 4, 266.

Zhang, H.-Q. et al.: “Unified Model for Gas-Liquid Pipe Flow via Slug Dynamics—Part 2: Model Validation,” J. Energy Res. Technology. (2003b) 125, No. 4, 274.

Appendix A

Proposed Model Prediction

The following sections present comprehensive results of annular-churn transition, pressure drop, and liquid holdup of the proposed model (Chapter 6) using different models of entrainment fraction and interfacial shear stress.

A.1 Using Wallis (1969) Model Prediction

A.1.1 Water-air Results

Annular-churn transition using Wallis (1969) model for water-air is presented in the following figure

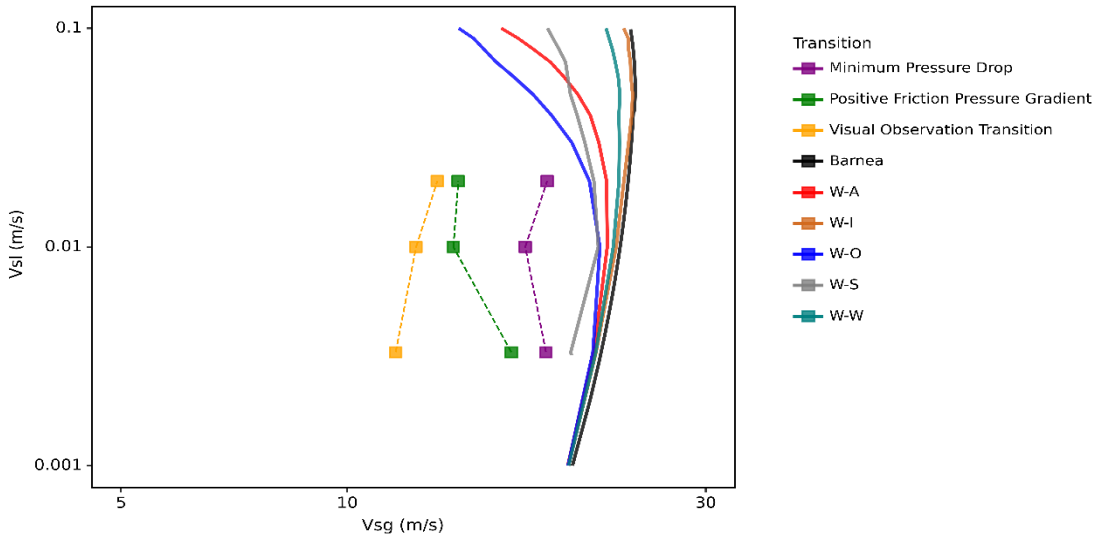

Figure A-1: Annular-churn transition using Wallis (1969) with different entrainment models in water-air flow

Pressure drop prediction using Wallis (1969) model for water-air are presented at v_{SL} = 0.0033, 0.01, and 0.02 m/s

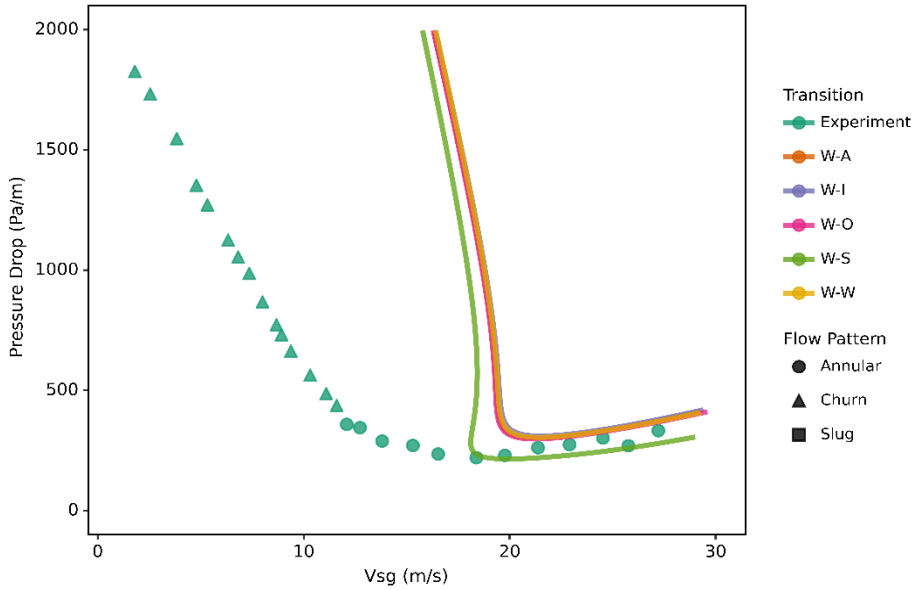

Figure A-2:Pressure drop at v_{SL} = 0.0033 m/s using Wallis (1969) with different entrainment models in water-air flow

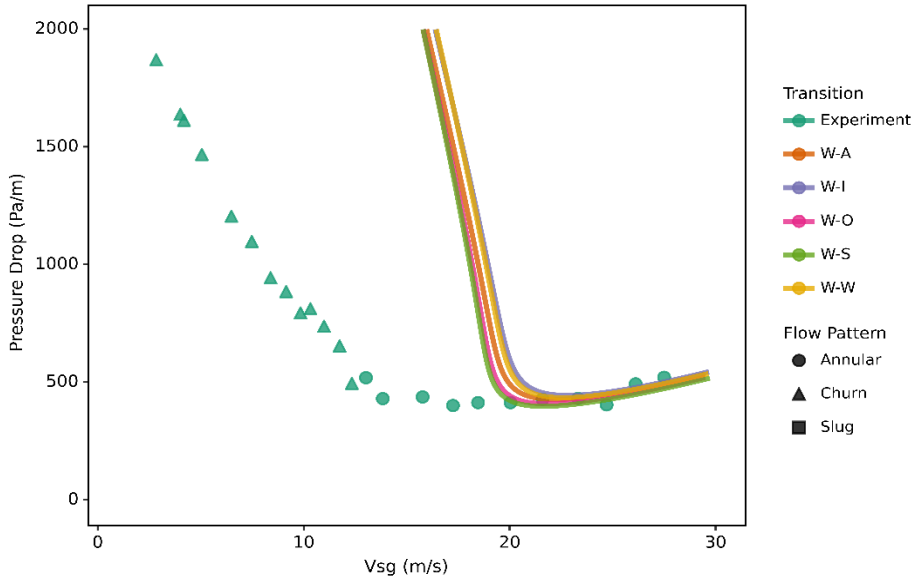

Figure A-3: Pressure drop at v_{SL} = 0.01 m/s using Wallis (1969) with different entrainment models in water-air flow

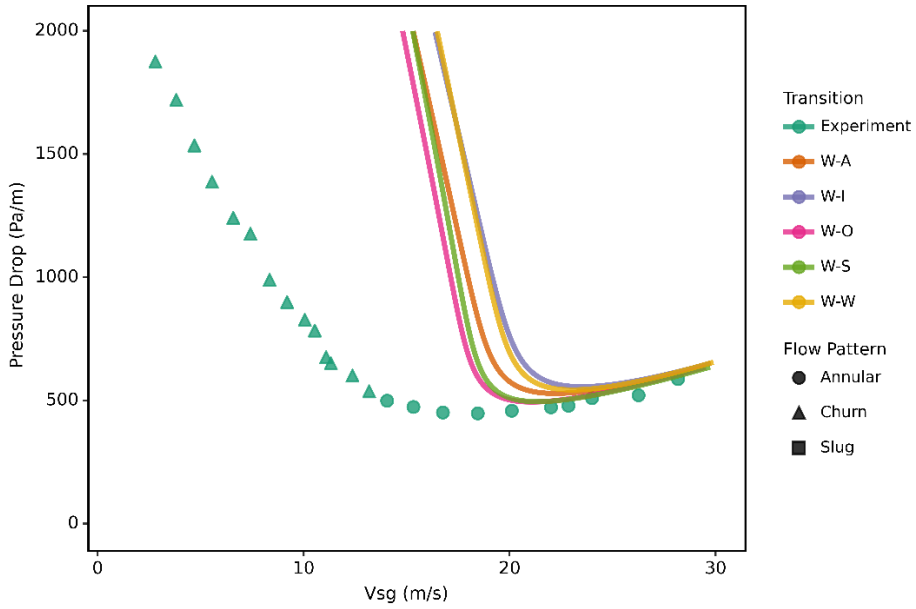

Figure A-4: Pressure drop at v_{SL} = 0.02 m/s using Wallis (1969) with different entrainment models in water-air flow

Liquid holdup prediction using Wallis (1969) model for water-air are presented at v_{SL} = 0.0033, 0.01, and 0.02 m/s

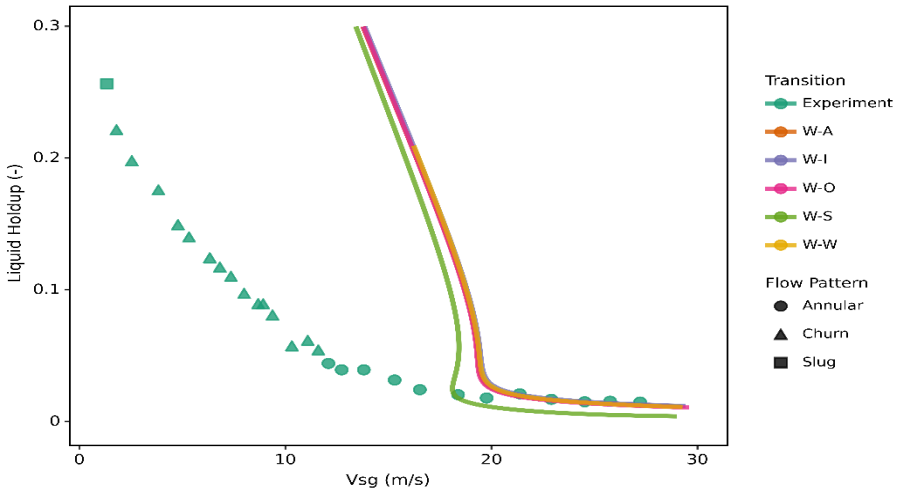

Figure A-5: Liquid holdup at v_{SL} = 0.0033 m/s using Wallis (1969) with different entrainment models in water-air flow

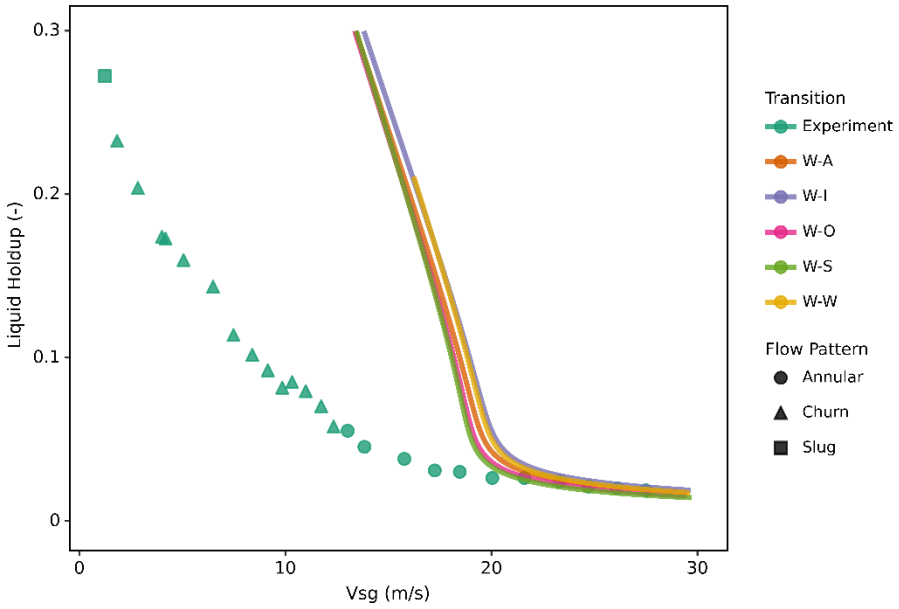

Figure A-6: Liquid holdup at v_{SL} = 0.01 m/s using Wallis (1969) with different entrainment models in water-air flow

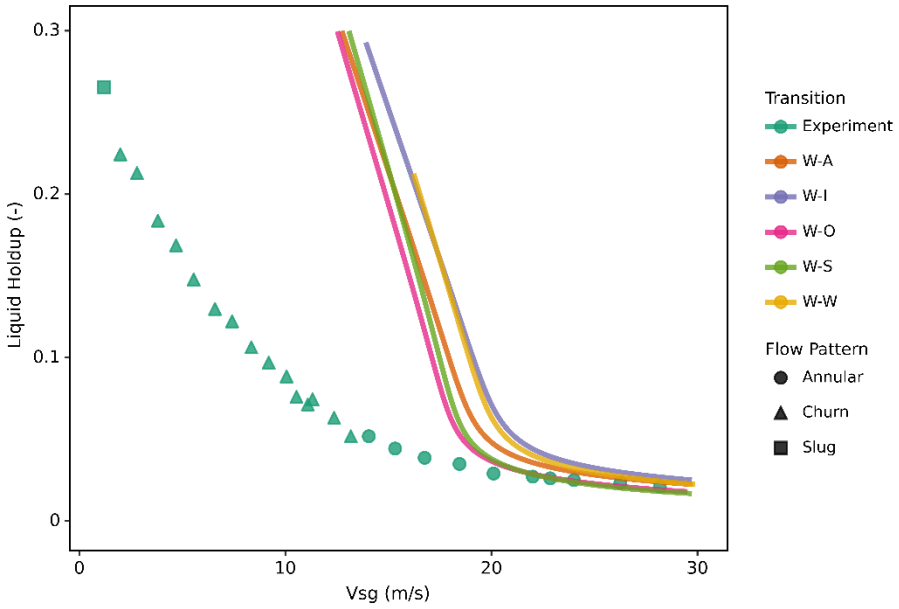

Figure A-7: Liquid holdup at v_{SL} = 0.02 m/s using Wallis (1969) with different entrainment models in water-air flow

A.1.2 Oil-air Results

The following figure shows the annular-churn transition using the Wallis (1969) model for oil-air.

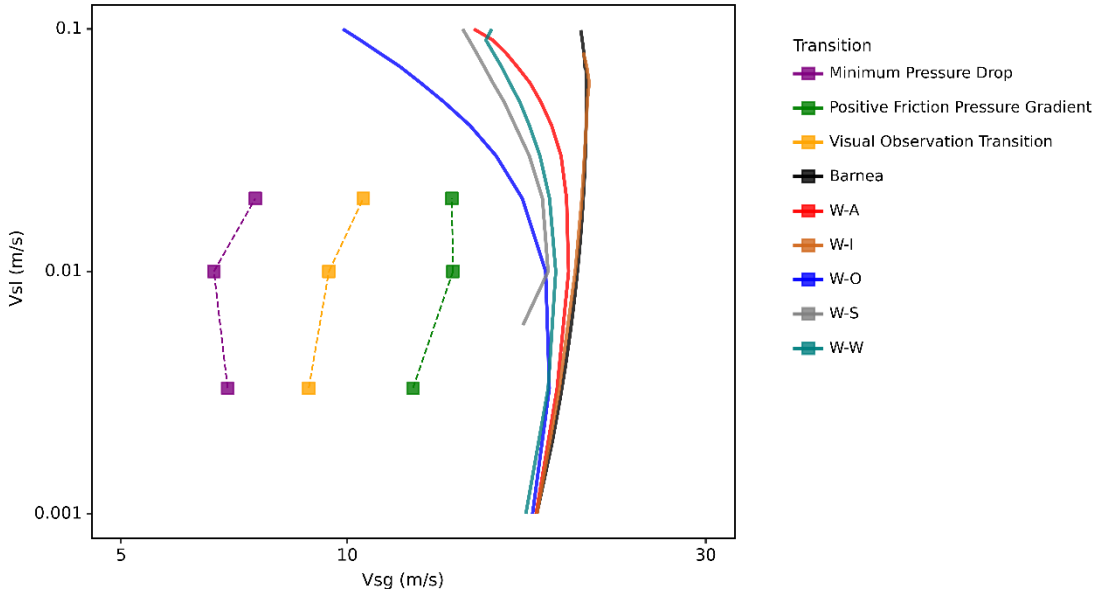

Figure A-8: Annular-churn transition using Wallis (1969) with different entrainment models in oil-air flow

Wallis (1969) model for oil-air pressure drop prediction is presented for v_{SL} = 0.0033, 0.01, and 0.02 m/s.

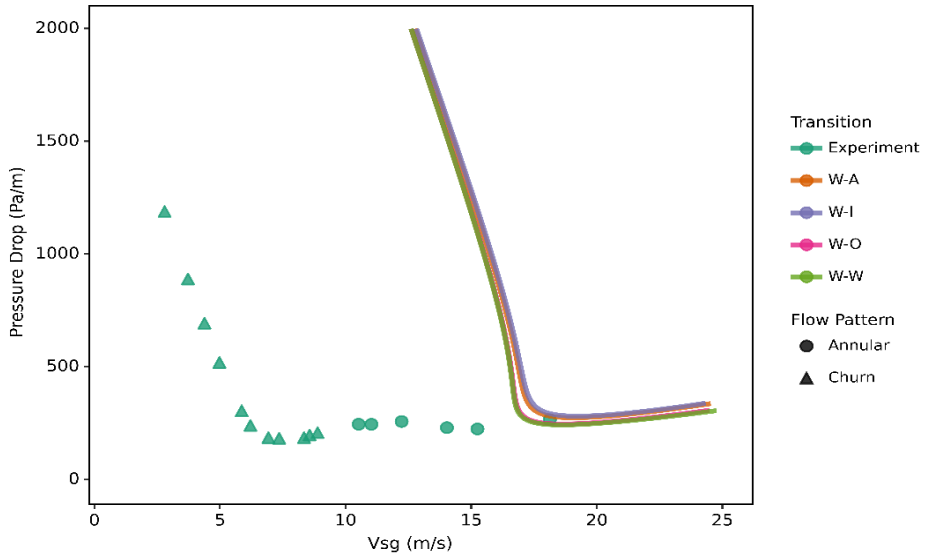

Figure A-9: Pressure drop at v_{SL} = 0.0033 m/s using Wallis (1969) with different entrainment models in oil-air flow

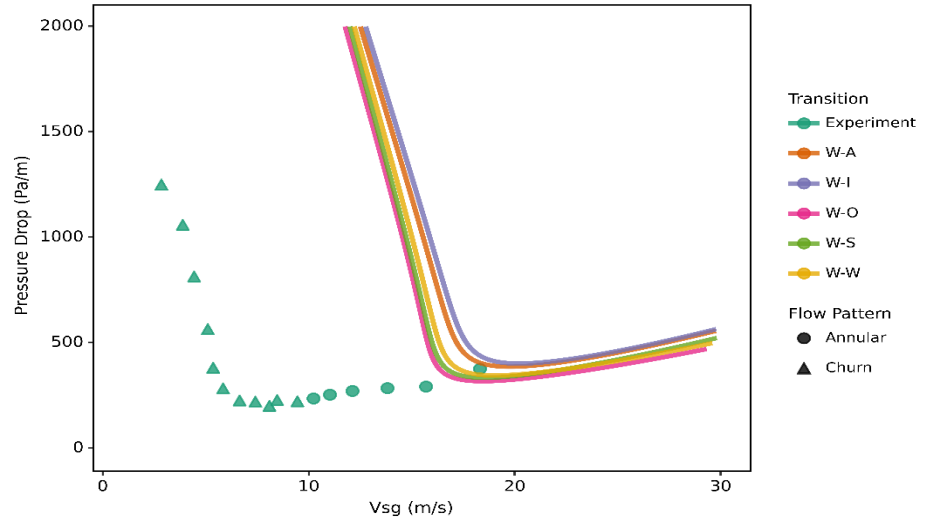

Figure A-10: Pressure drop at v_{SL} = 0.01 m/s using Wallis (1969) with different entrainment models in oil-air flow

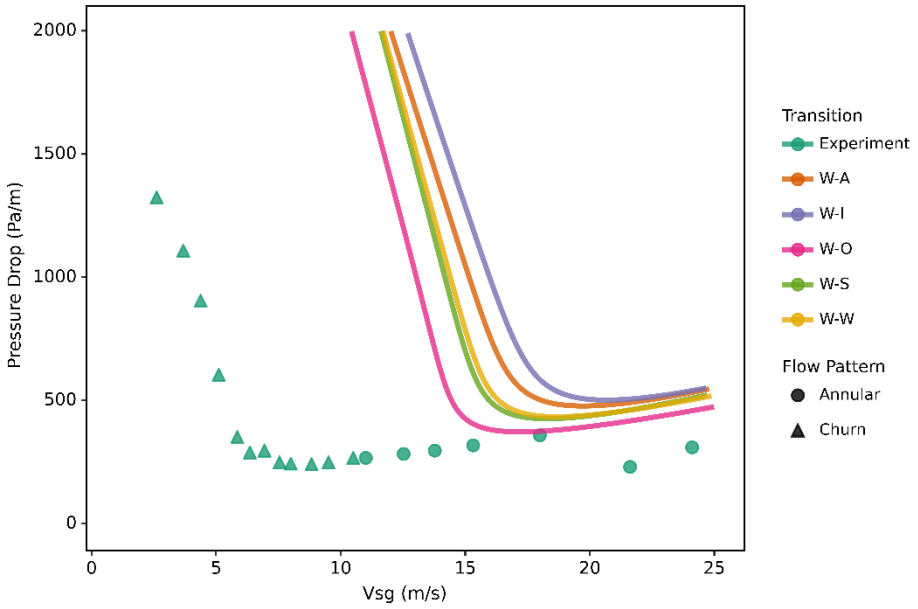

Figure A-11: Pressure drop at v_{SL} = 0.02 m/s using Wallis (1969) with different entrainment models in oil-air flow

Wallis (1969) model for oil-air liquid holdup prediction is presented at v_{SL} = 0.0033, 0.01, and 0.02 m/s.

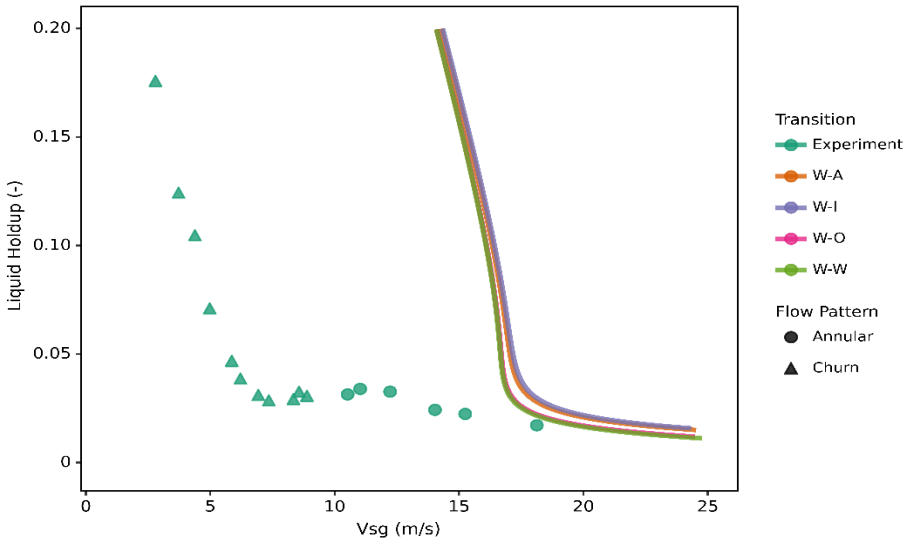

Figure A-12: Liquid holdup at v_{SL} = 0.0033 m/s using Wallis (1969) with different entrainment models in oil-air flow

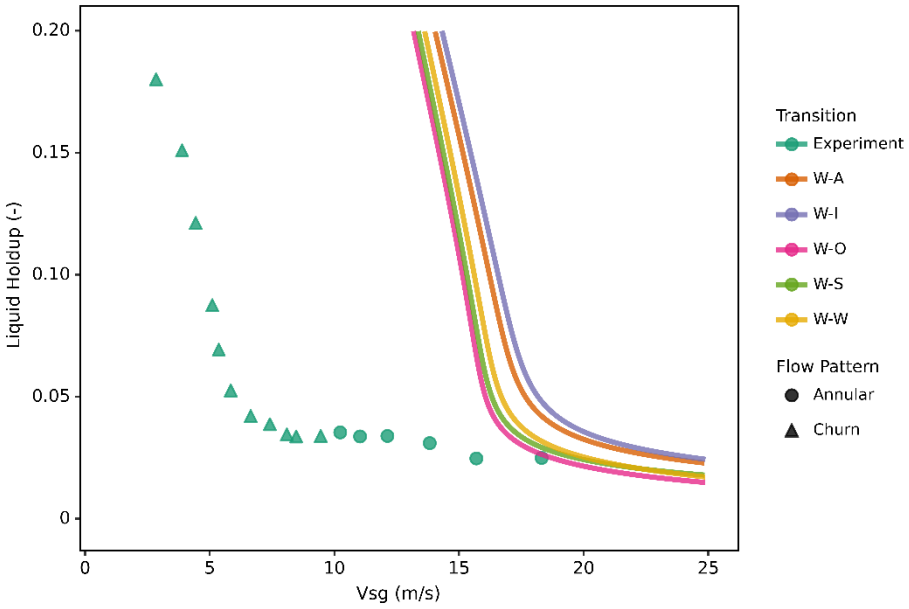

Figure A-13: Liquid holdup at v_{SL} = 0.01 m/s using Wallis (1969) with different entrainment models in oil-air flow

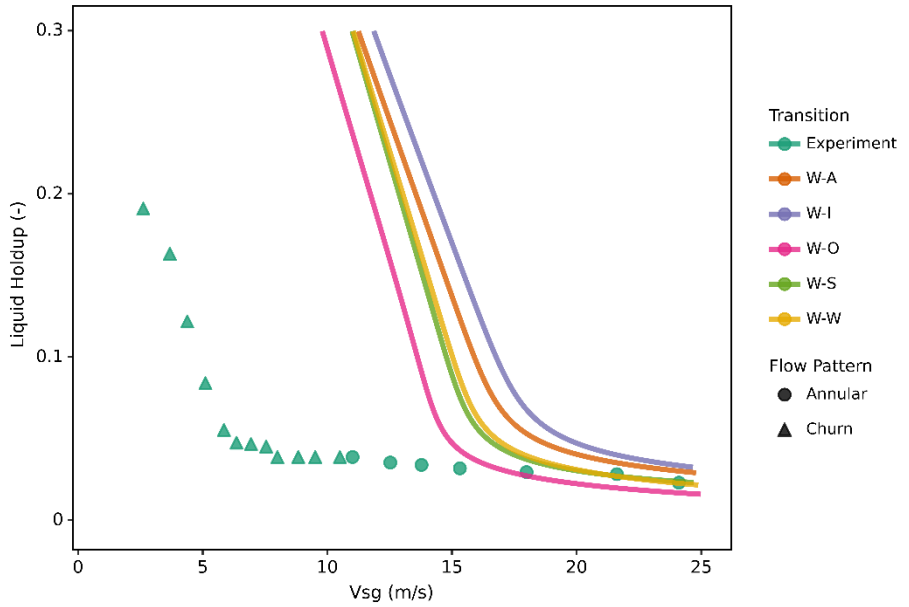

Figure A-14: Liquid holdup at v_{SL} = 0.02 m/s using Wallis (1969) with different entrainment models in oil-air flow

A.2 Using Bharathan and Wallis (1983) Model Prediction

A.2.1 Water-air results

Annular-churn transition using Bharathan and Wallis (1983) model for water-air is presented in the following figure.

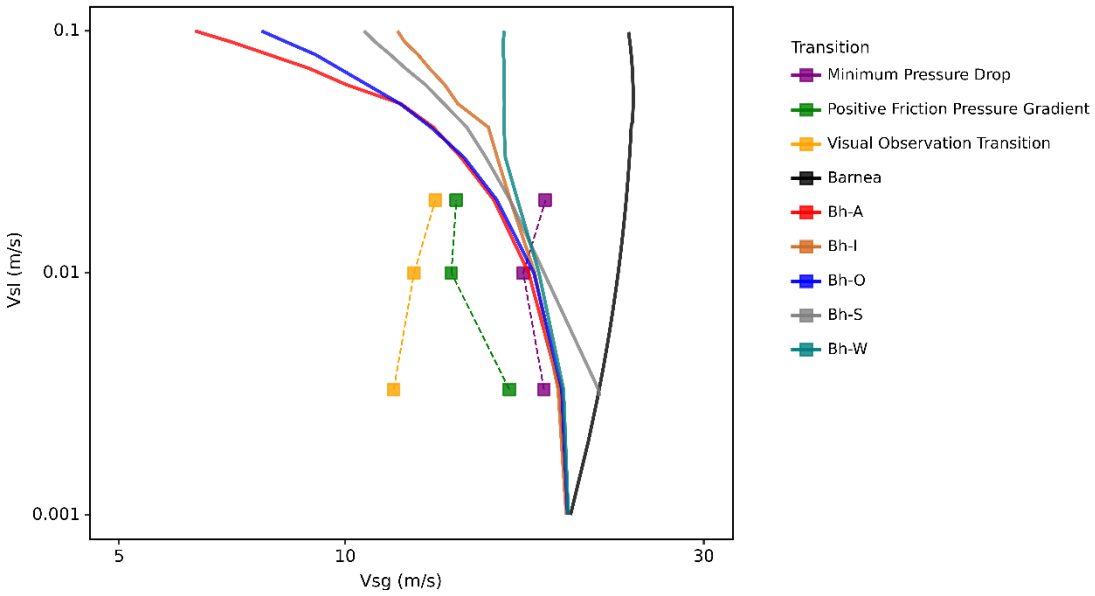

Figure A-15: Annular-churn transition using Bharathan and Wallis (1983) with different entrainment models in water-air flow

Pressure drop prediction using Bharathan and Wallis (1983) model for water-air are presented at v_{SL} = 0.0033, 0.01, and 0.02 m/s

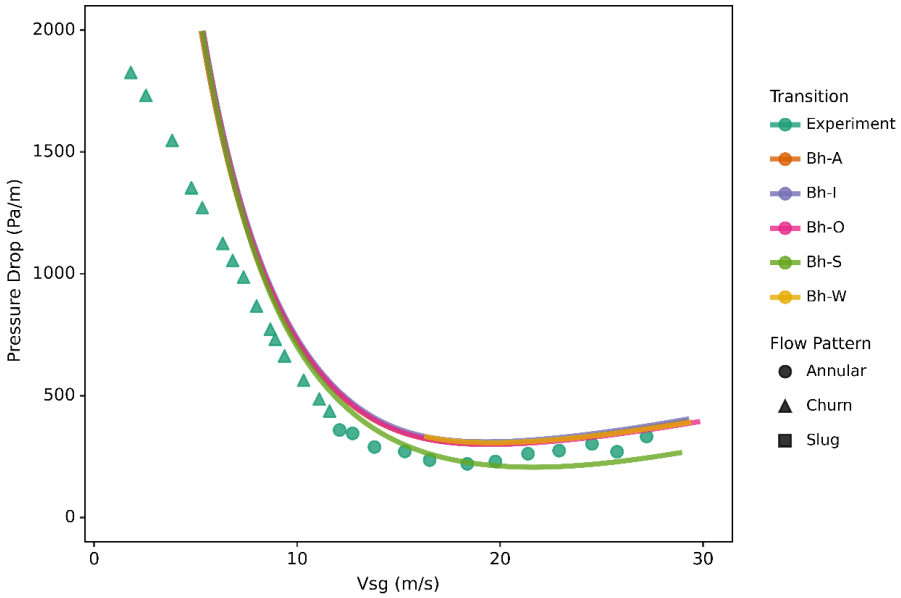

Figure A-16: Pressure drop at v_{SL} = 0.0033 m/s using Bharathan and Wallis (1983) with different entrainment models in water-air flow

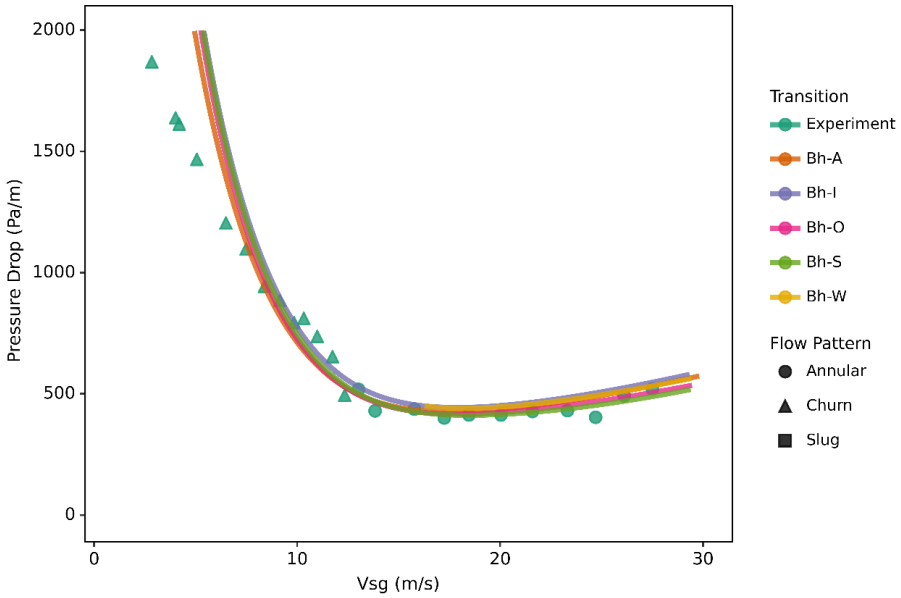

Figure A-17: Pressure drop at v_{SL} = 0.01 m/s using Bharathan and Wallis (1983) with different entrainment models in water-air flow

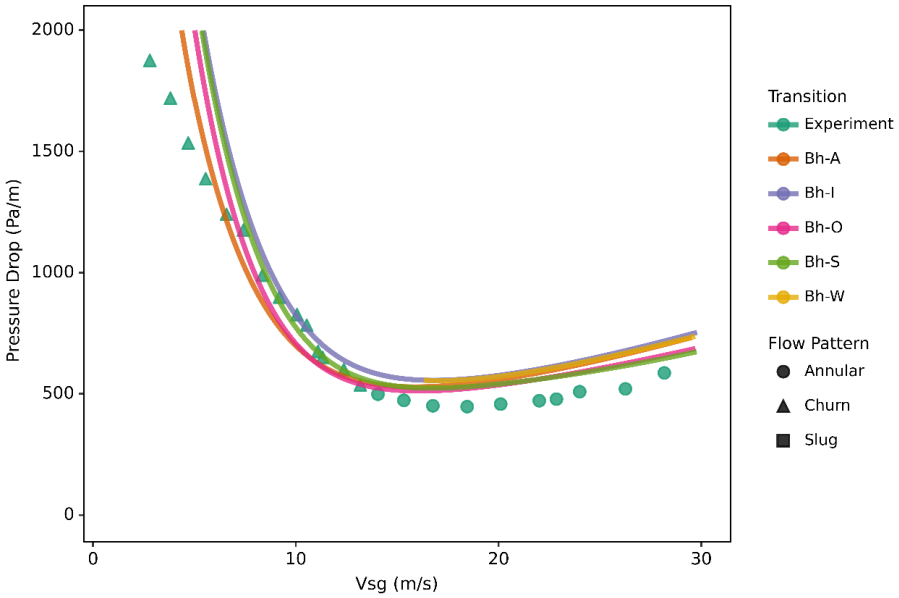

Figure A-18: Pressure drop at v_{SL} = 0.02 m/s using Bharathan and Wallis (1983) with different entrainment models in water-air flow

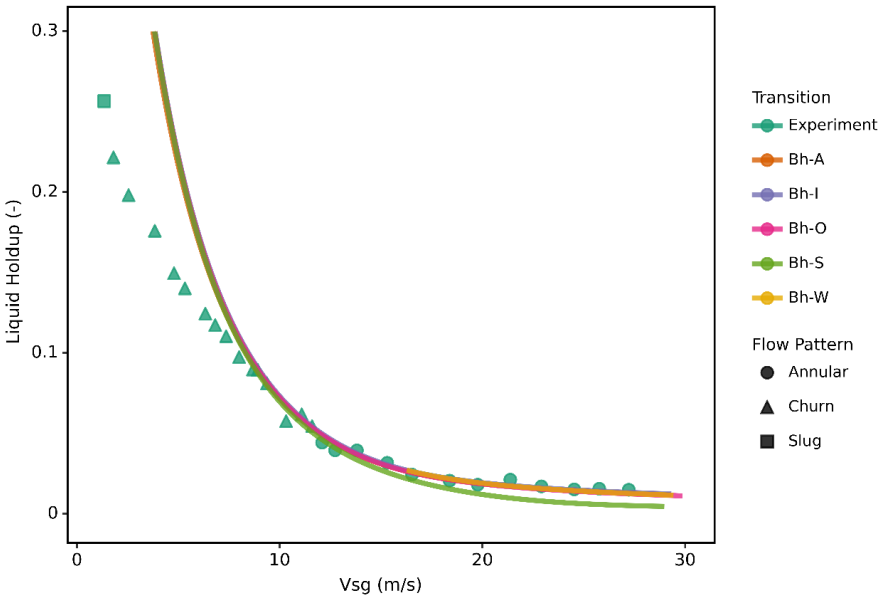

Figure A-19: Liquid holdup at v_{SL} = 0.0033 m/s using Bharathan and Wallis (1983) with different entrainment models in water-air flow

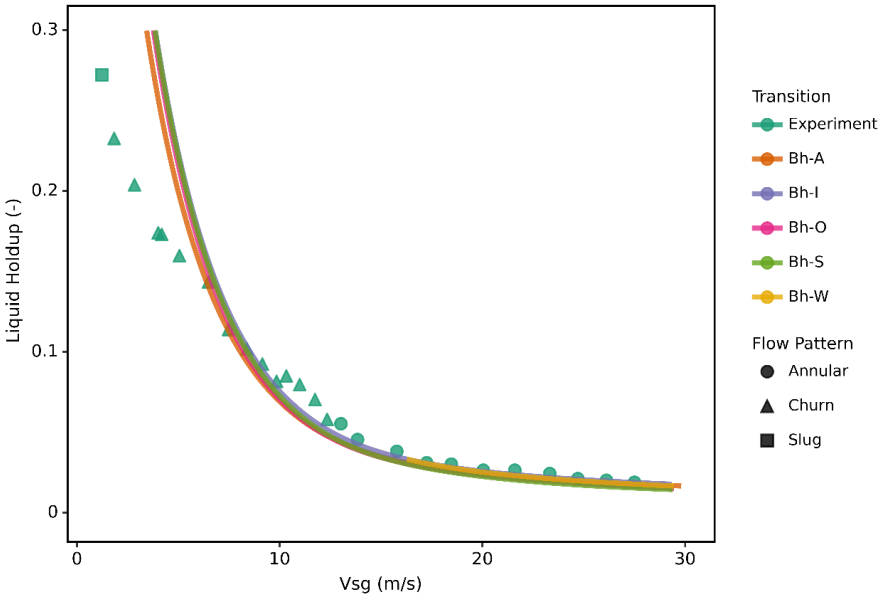

Figure A-20: Liquid holdup at v_{SL} = 0.01 m/s using Bharathan and Wallis (1983) with different entrainment models in water-air flow

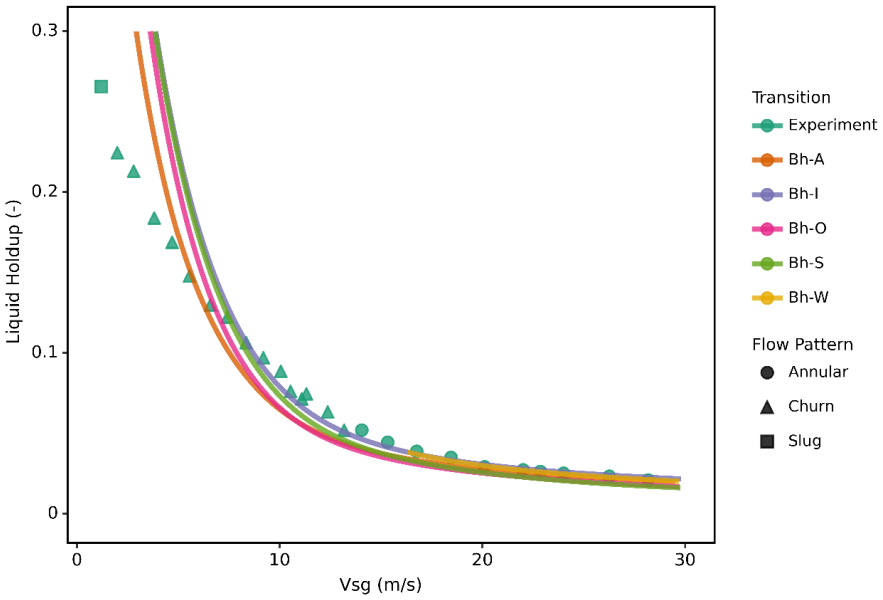

Figure A-21: Liquid holdup at v_{SL} = 0.02 m/s using Bharathan and Wallis (1983) with different entrainment models in water-air flow

A.2.2 Oil-air results

Annular-churn transition using Bharathan and Wallis (1983) model for oil-air is presented in the following figure.

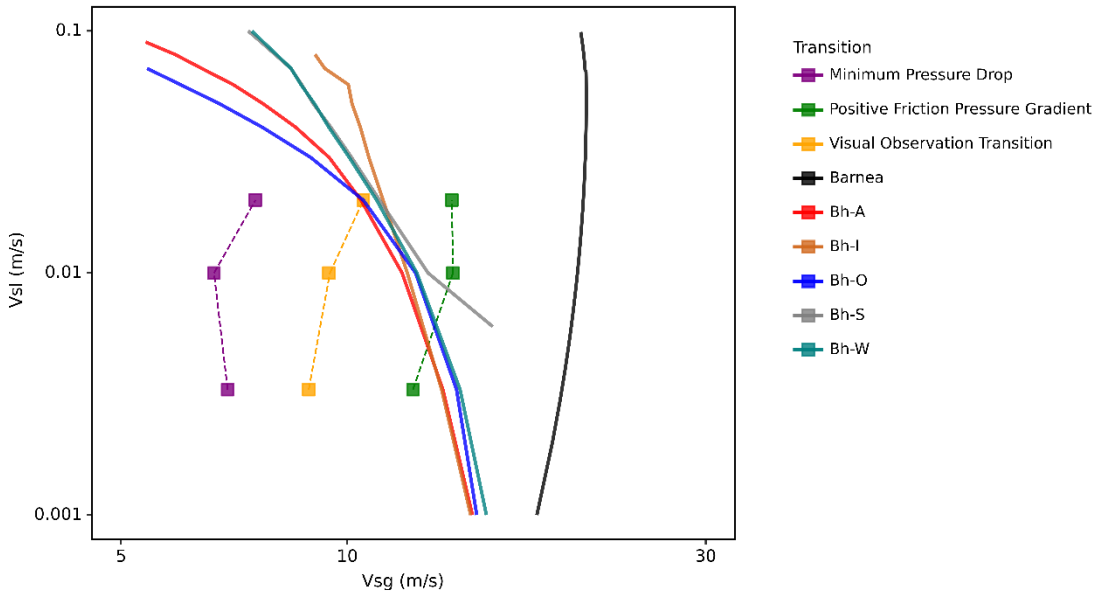

Figure A-22: Annular-churn transition using Bharathan and Wallis (1983) with different entrainment models in oil-air flow

Bharathan and Wallis (1983) model for oil-air pressure drop prediction is presented at v_{SL} = 0.0033, 0.01, and 0.02 m/s.

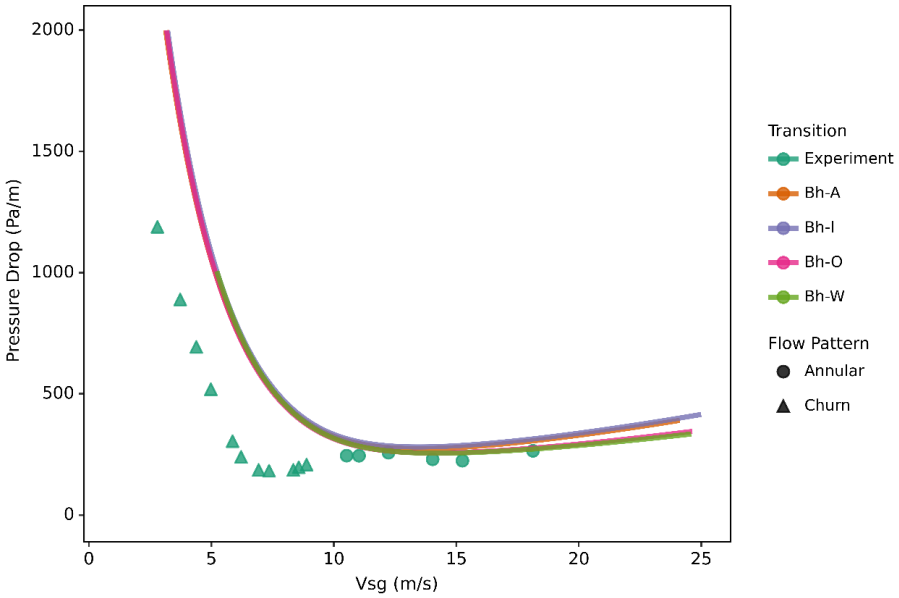

Figure A-23: Pressure drop at v_{SL} = 0.0033 m/s using Bharathan and Wallis (1983) with different entrainment models in oil-air flow.

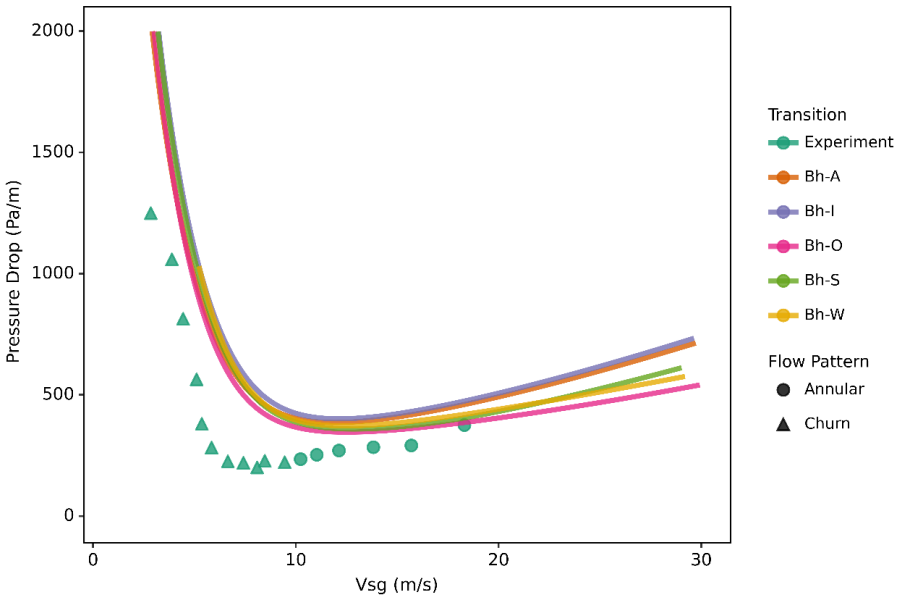

Figure A-24: Pressure drop at v_{SL} = 0.01 m/s using Bharathan and Wallis (1983) with different entrainment models in oil-air flow.

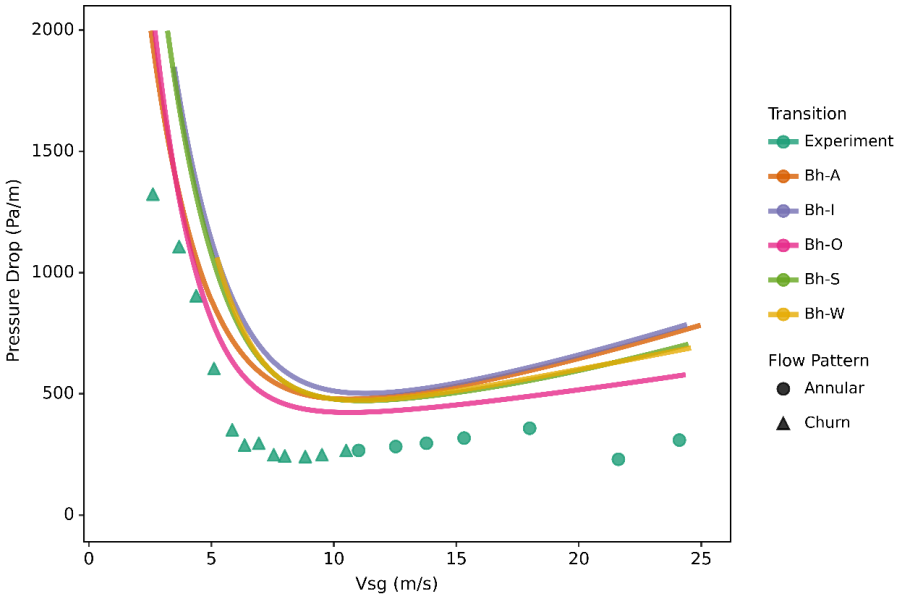

Figure A-25: Pressure drop at v_{SL} = 0.02 m/s using Bharathan and Wallis (1983) with different entrainment models in oil-air flow.

Bharathan and Wallis (1983) model for oil-air liquid holdup prediction is presented at v_{SL} = 0.0033, 0.01, and 0.02 m/s.

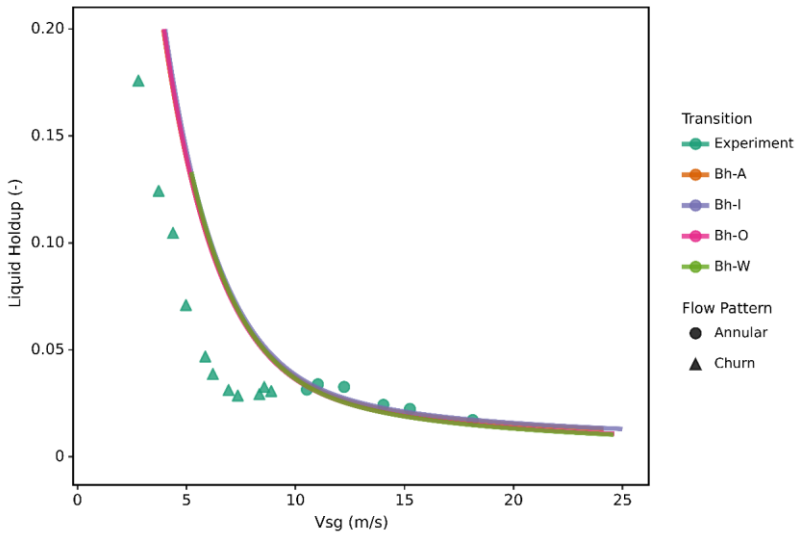

Figure A- 26: Liquid holdup at v_{SL} = 0.0033 m/s using Bharathan and Wallis (1983) with different entrainment models in oil-air flow.

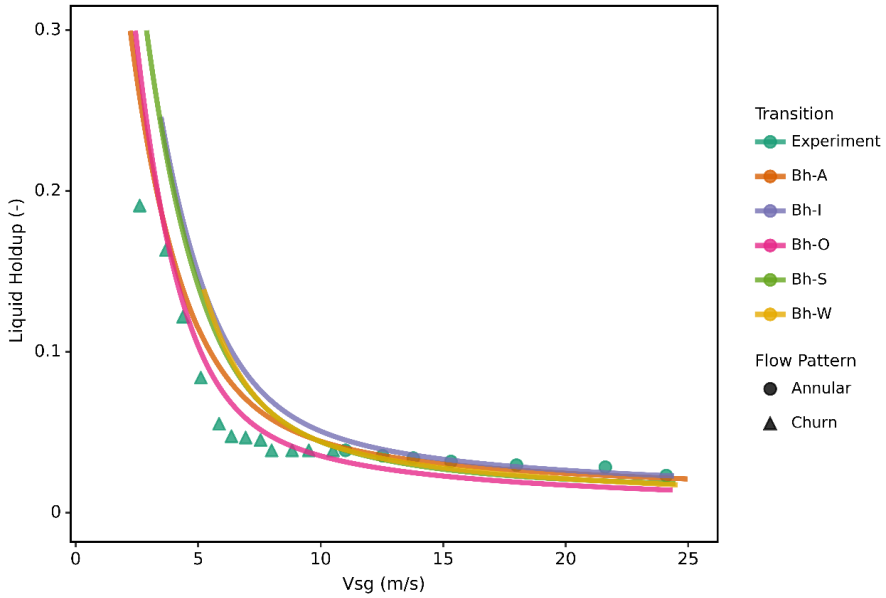

Figure A-27: Liquid holdup at v_{SL} = 0.01 m/s using Bharathan and Wallis (1983) with different entrainment models in oil-air flow.

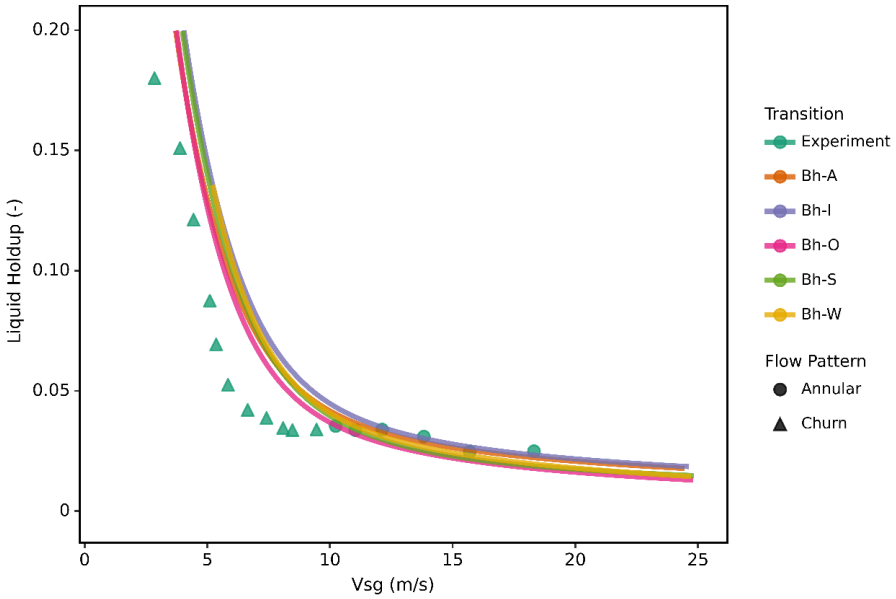

Figure A-28: Liquid holdup at v_{SL} = 0.02 m/s using Bharathan and Wallis (1983) with different entrainment models in oil-air flow.

A.3 Using Jayanti and Brauner (1994) approach with Wallis (1969)

A.3.1 Water-air Results

Annular-churn transition using Jayanti and Brauner (1994) approach with Wallis (1969) model for water-air is presented in the following figure

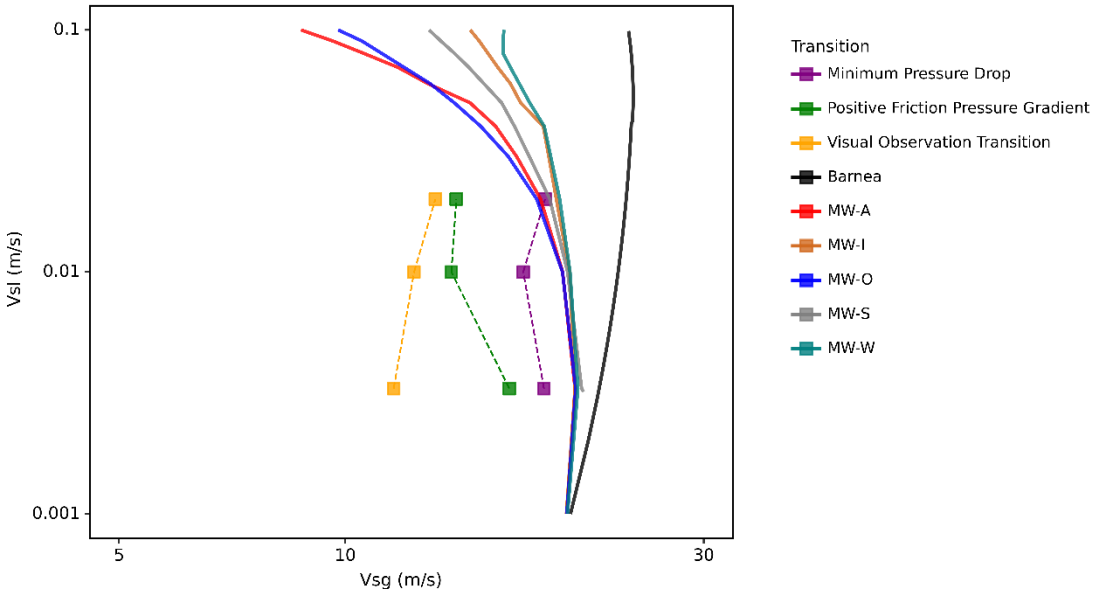

Figure A-29: Annular-churn transition using Jayanti and Brauner (1994) approach with Wallis (1969) model with different entrainment models in water-air flow

Pressure drop prediction using Jayanti and Brauner (1994) approach with Wallis (1969) model for water-air are presented at v_{SL} = 0.0033, 0.01, and 0.02 m/s

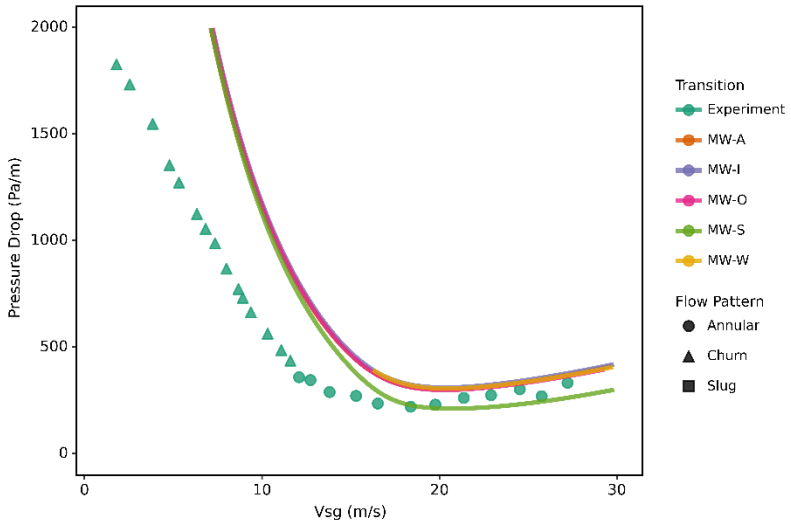

Figure A-30: Pressure drop at v_{SL} = 0.0033 m/s using Jayanti and Brauner (1994) approach with Wallis (1969) model with different entrainment models in water-air flow

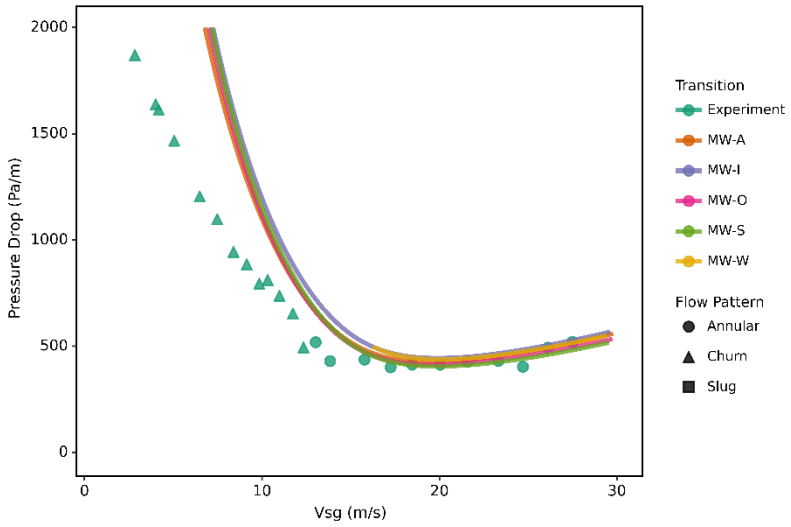

Figure A-31: Pressure drop at v_{SL} = 0.01 m/s using Jayanti and Brauner (1994) approach with Wallis (1969) model with different entrainment models in water-air flow

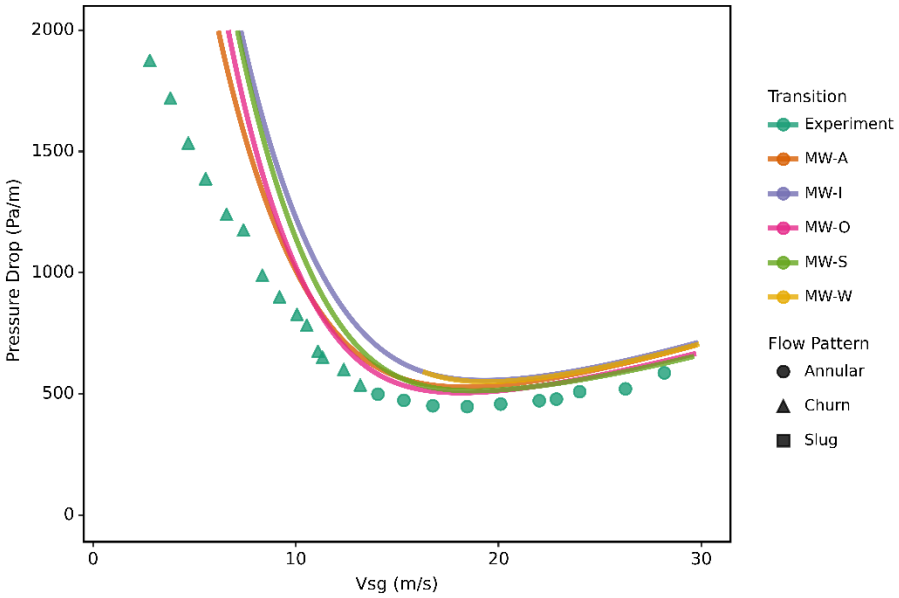

Figure A-32: Pressure drop at v_{SL} = 0.02 m/s using Jayanti and Brauner (1994) approach with Wallis (1969) model with different entrainment models in water-air flow

Liquid holdup prediction using Jayanti and Brauner (1994) approach with Wallis (1969) model for water-air are presented at v_{SL} = 0.0033, 0.01, and 0.02 m/s

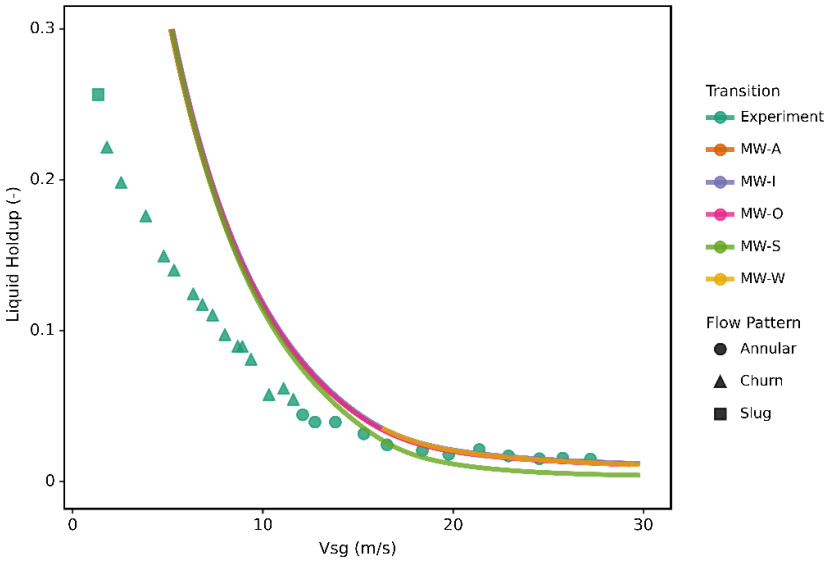

Figure A-33: Liquid holdup at v_{SL} = 0.0033 m/s using Jayanti and Brauner (1994) approach with Wallis (1969) model) with different entrainment models in water-air flow

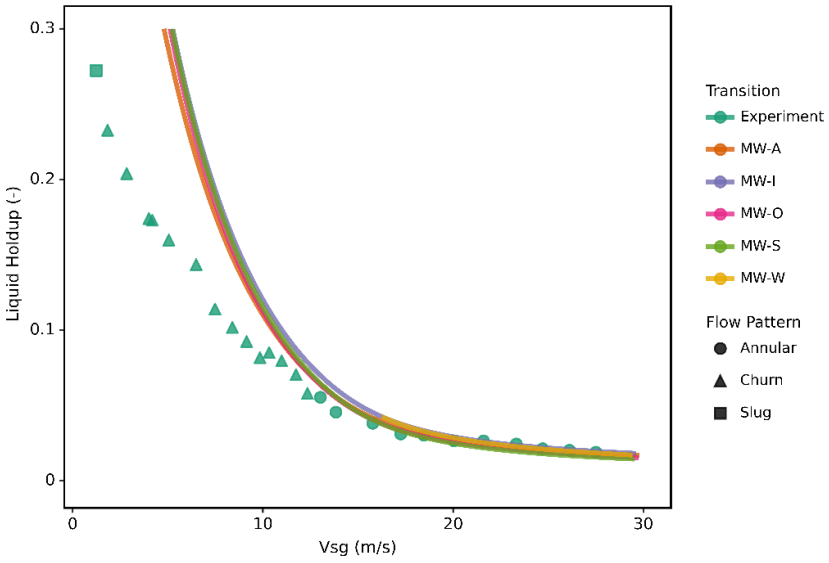

Figure A-34: Liquid holdup at v_{SL} = 0.01 m/s using Jayanti and Brauner (1994) approach with Wallis (1969) model) with different entrainment models in water-air flow

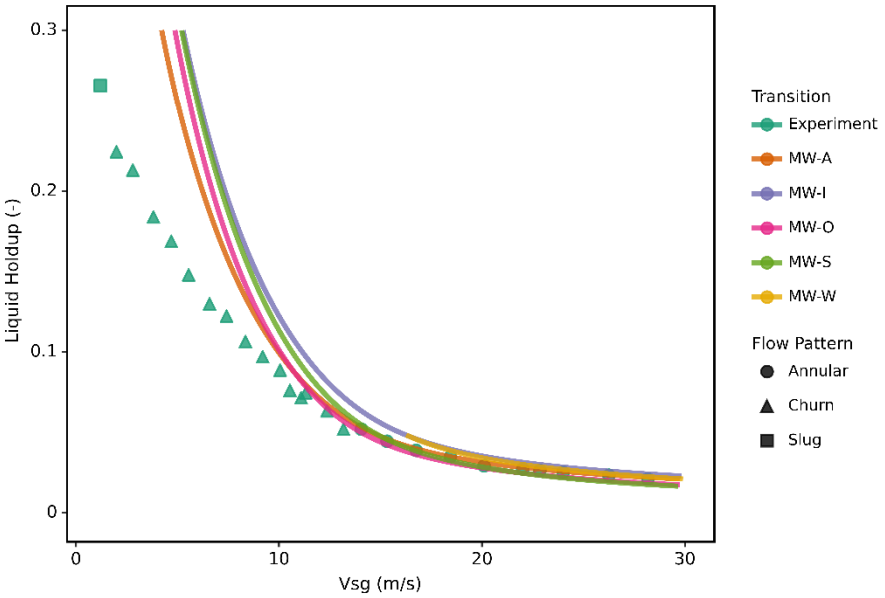

Figure A-35: Liquid holdup at v_{SL} = 0.01 m/s using Jayanti and Brauner (1994) approach with Wallis (1969) model) with different entrainment models in water-air flow

A.3.2 Oil-air Results

Annular-churn transition using Jayanti and Brauner (1994) approach with Wallis (1969) model for oil-air is presented in the following figure

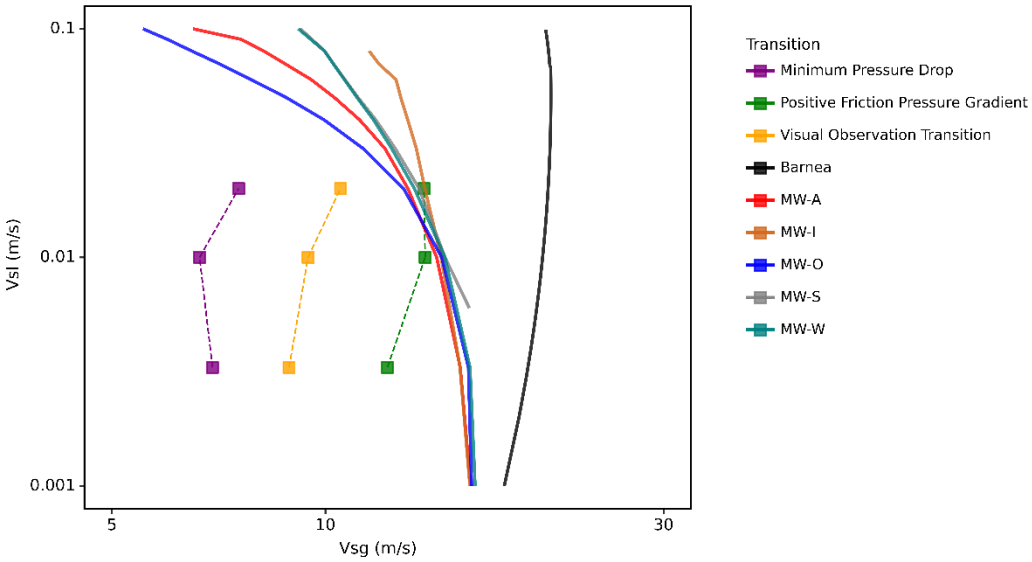

Figure A-36: Annular-churn transition using Jayanti and Brauner (1994) approach with Wallis (1969) model with different entrainment models in oil-air flow

Pressure drop prediction using Jayanti and Brauner (1994) approach with Wallis (1969) model for oil-air are presented at v_{SL} = 0.0033, 0.01, and 0.02 m/s

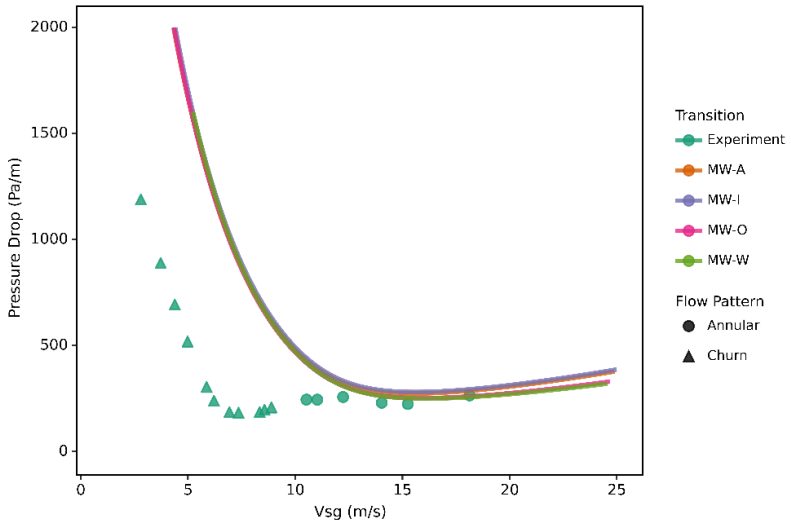

Figure A-37: Pressure drop at v_{SL} = 0.0033 m/s using Jayanti and Brauner (1994) approach with Wallis (1969) model with different entrainment models in oil-air flow

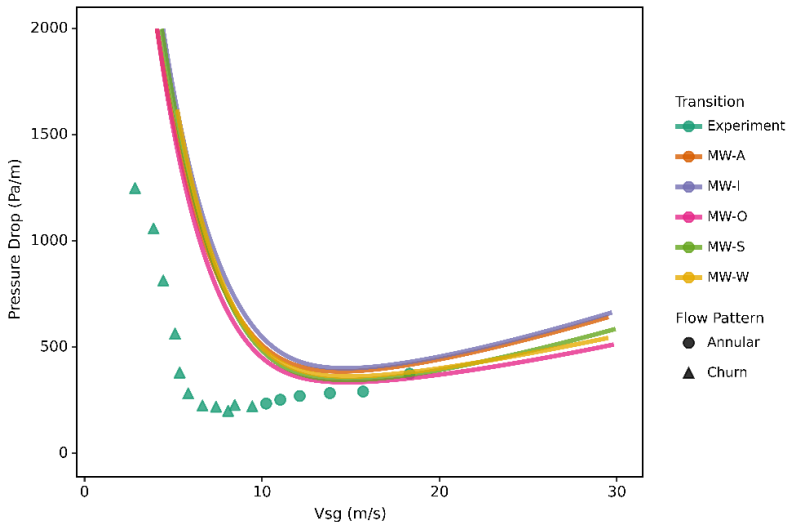

Figure A-38: Pressure drop at v_{SL} = 0.01 m/s using Jayanti and Brauner (1994) approach with Wallis (1969) model with different entrainment models in oil-air flow

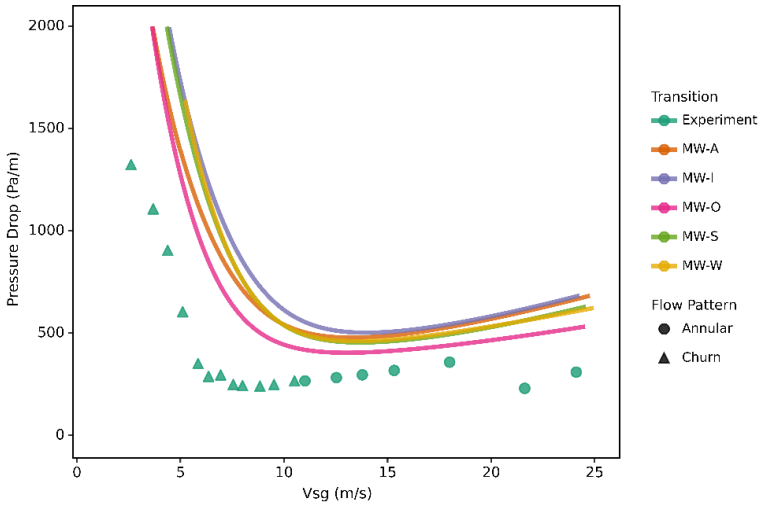

Figure A-39: Pressure drop at v_{SL} = 0.02 m/s using Jayanti and Brauner (1994) approach with Wallis (1969) model with different entrainment models in oil-air flow

Liquid holdup prediction using Jayanti and Brauner (1994) approach with Wallis (1969) model for water-air are presented at v_{SL} = 0.0033, 0.01, and 0.02 m/s

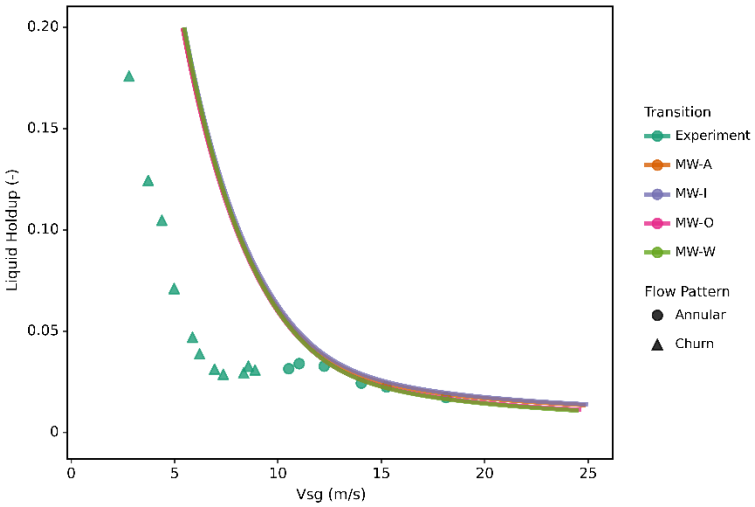

Figure A-40: Liquid holdup at v_{SL} = 0.0033 m/s using Jayanti and Brauner (1994) approach with Wallis (1969) model with different entrainment models in oil-air flow

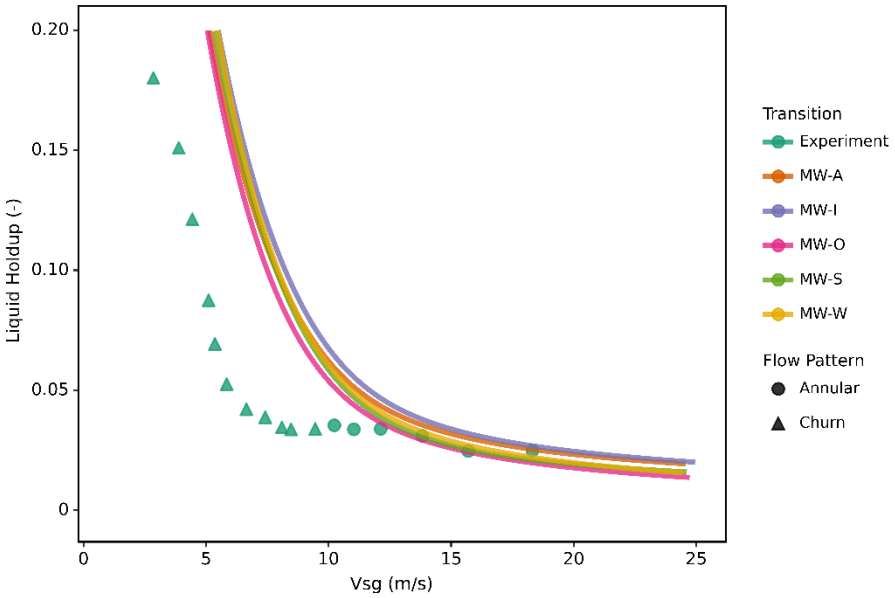

Figure A-41: Liquid holdup at v_{SL} = 0.01 m/s using Jayanti and Brauner (1994) approach with Wallis (1969) model with different entrainment models in oil-air flow

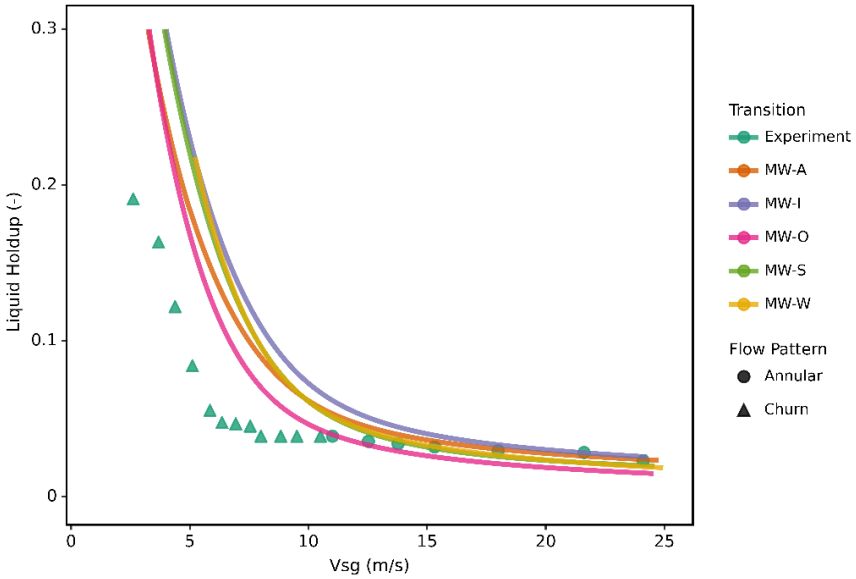

Figure A-42: Liquid holdup at v_{SL} = 0.02 m/s using Jayanti and Brauner (1994) approach with Wallis (1969) model with different entrainment models in oil-air flow

A.4 Using Jayanti and Brauner (1994) approach with Belt et al. (2009)

A.4.1 Water-air Result

Annular-churn transition using Jayanti and Brauner (1994) approach with Belt et al. (2009) model for water-air is presented in the following figure

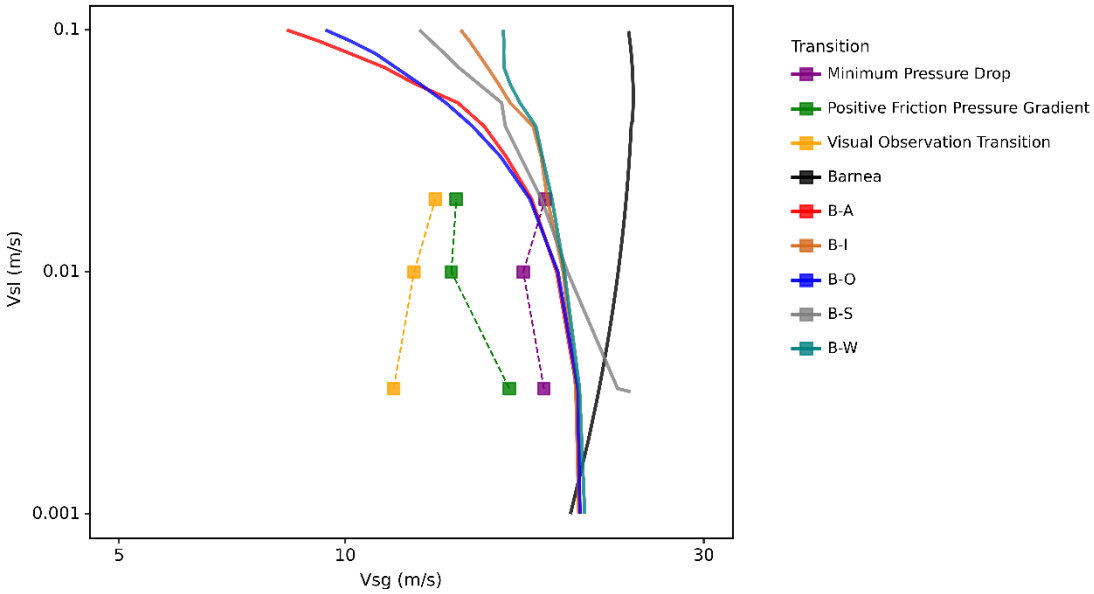

Figure A-43: Annular-churn transition using Jayanti and Brauner (1994) approach with Belt et al. (2009) model with different entrainment models in water-air flow

Pressure drop prediction using Jayanti and Brauner (1994) approach with Belt et al. (2009) model for water-air are presented at v_{SL} = 0.0033, 0.01, and 0.02 m/s

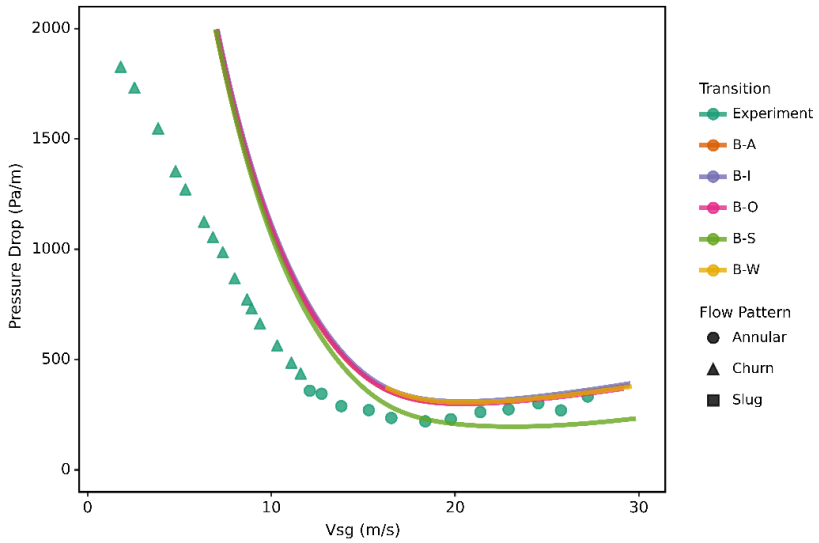

Figure A-44: Pressure drop at v_{SL} = 0.0033 m/s using Jayanti and Brauner (1994) approach with Belt et al. (2009) model with different entrainment models in water-air flow

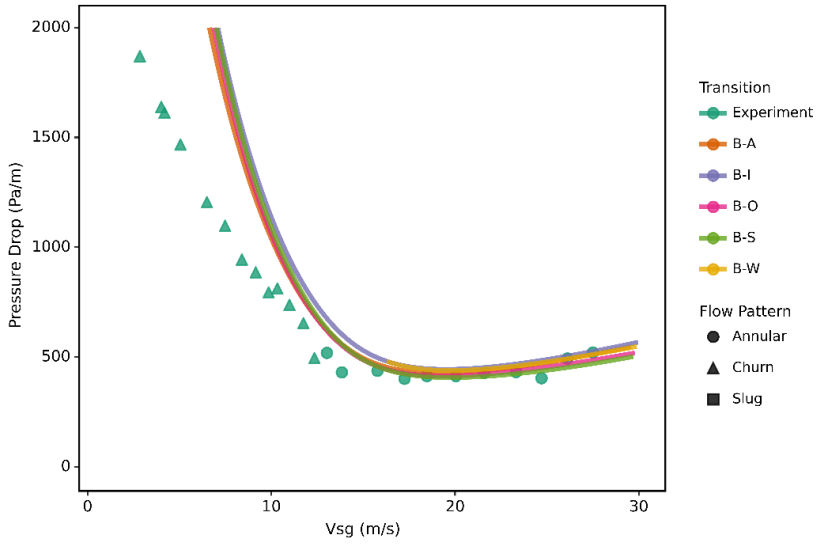

Figure A-45: Pressure drop at v_{SL} = 0.01 m/s using Jayanti and Brauner (1994) approach with Belt et al. (2009) model with different entrainment models in water-air flow

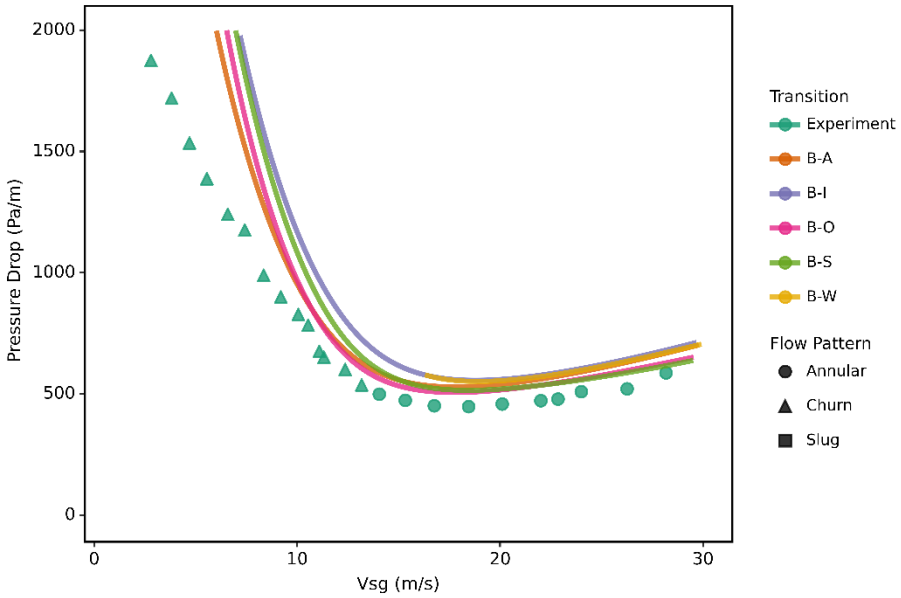

Figure A- 46: Pressure drop at v_{SL} = 0.02 m/s using Jayanti and Brauner (1994) approach with Belt et al. (2009) model with different entrainment models in water-air flow

Liquid holdup prediction using Jayanti and Brauner (1994) approach with Belt et al. (2009) model for water-air are presented at v_{SL} = 0.0033, 0.01, and 0.02 m/s

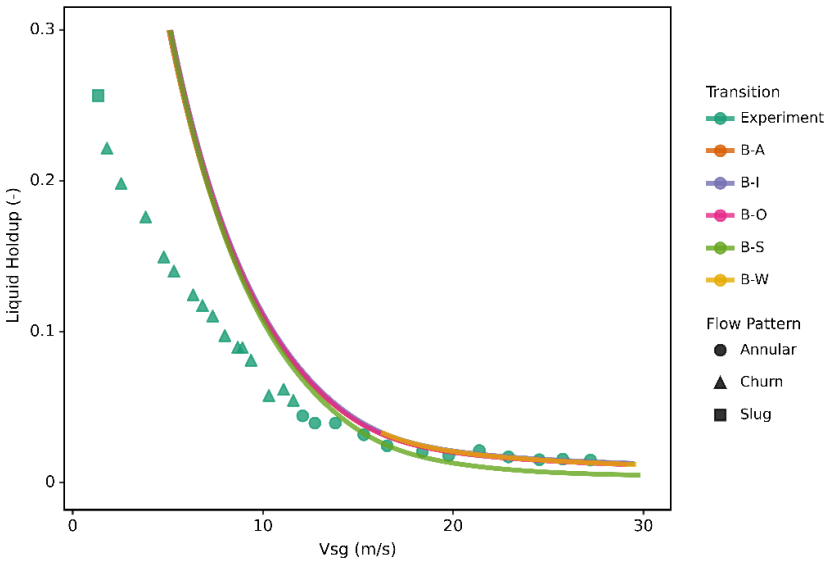

Figure A-47: Liquid holdup at v_{SL} = 0.0033 m/s using Jayanti and Brauner (1994) approach with Belt et al. (2009) model with different entrainment models in water-air flow

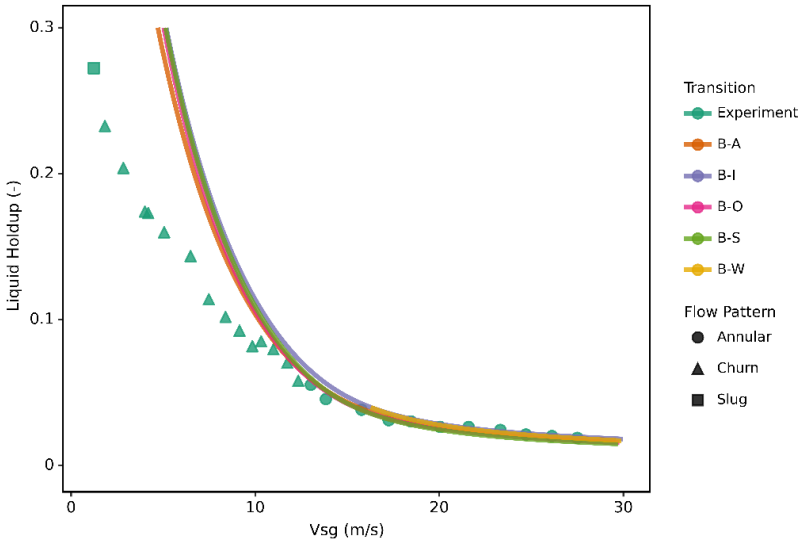

Figure A-48: Liquid holdup at v_{SL} = 0.01 m/s using Jayanti and Brauner (1994) approach with Belt et al. (2009) model with different entrainment models in water-air flow

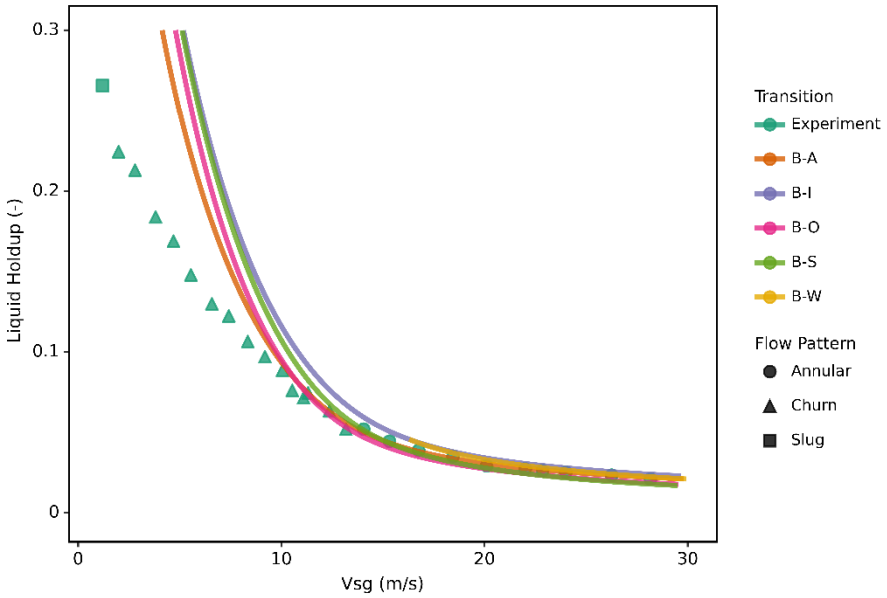

Figure A-49: Liquid holdup at v_{SL} = 0.02 m/s using Jayanti and Brauner (1994) approach with Belt et al. (2009) model with different entrainment models in water-air flow

A.4.2 Oil-air Result

Annular-churn transition using Jayanti and Brauner (1994) approach with Belt et al. (2009) model for oil-air is presented in the following figure

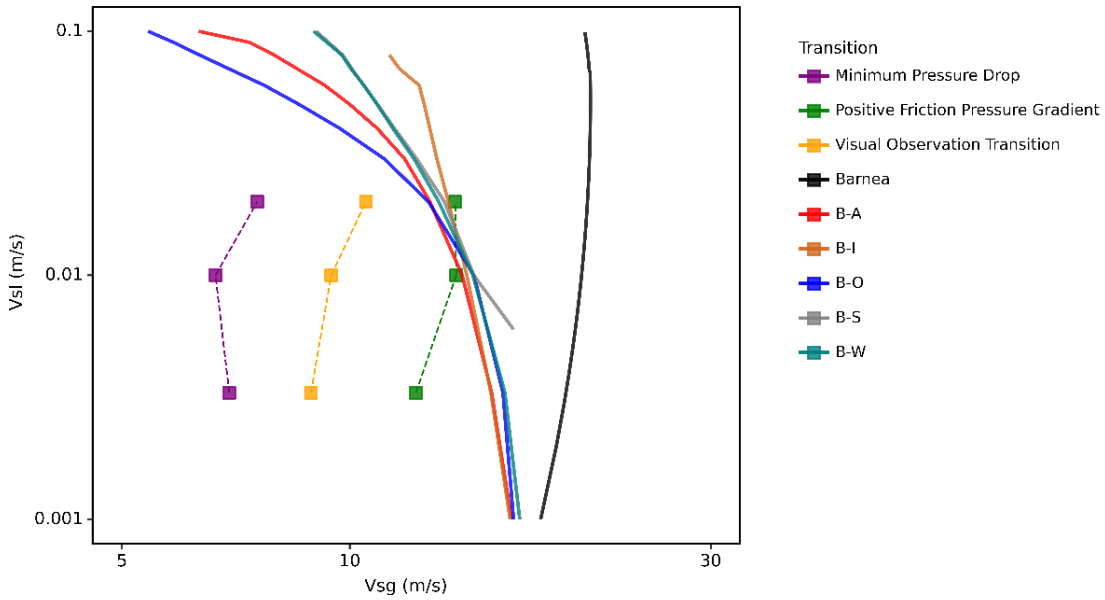

Figure A-50: Annular-churn transition using Jayanti and Brauner (1994) approach with Belt et al. (2009) model with different entrainment models in oil-air flow

Pressure drop prediction using Jayanti and Brauner (1994) approach with Belt et al. (2009) model for oil-air are presented at v_{SL} = 0.0033, 0.01, and 0.02 m/s

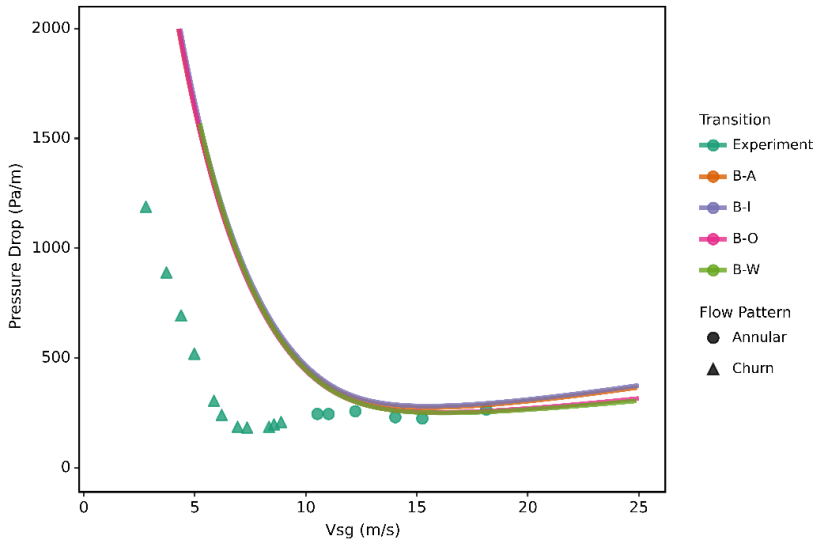

Figure A-51: Pressure drop at v_{SL} = 0.0033 m/s using Jayanti and Brauner (1994) approach with Belt et al. (2009) model with different entrainment models in oil-air flow

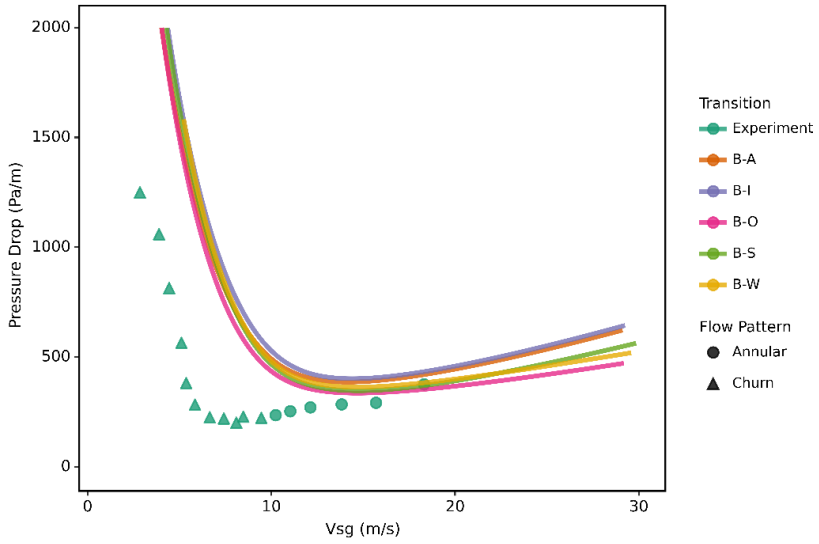

Figure A- 52: Pressure drop at v_{SL} = 0.01 m/s using Jayanti and Brauner (1994) approach with Belt et al. (2009) model with different entrainment models in oil-air flow

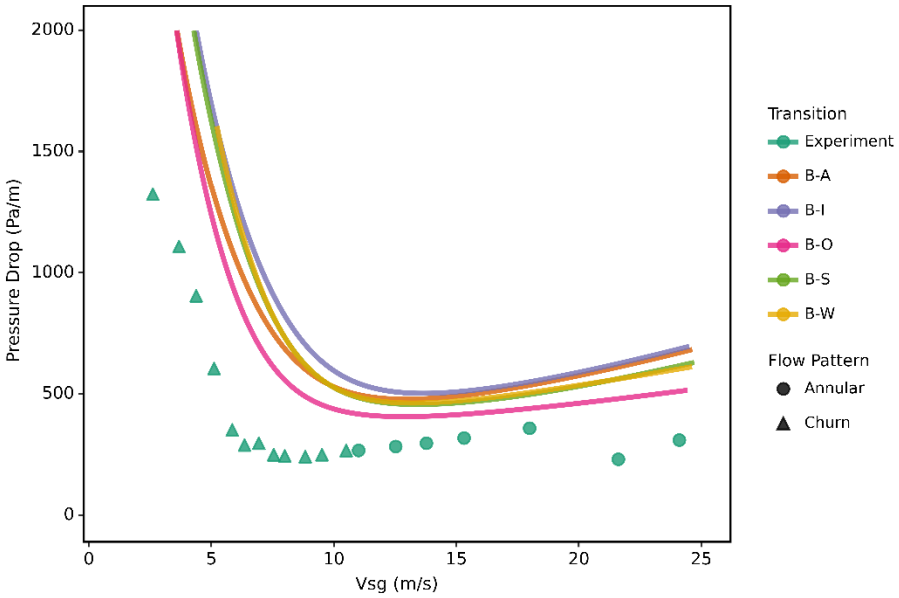

Figure A-53: Pressure drop at v_{SL} = 0.02 m/s using Jayanti and Brauner (1994) approach with Belt et al. (2009) model with different entrainment models in oil-air flow

Liquid holdup prediction using Jayanti and Brauner (1994) approach with Belt et al. (2009) model for water-air are presented at v_{SL} = 0.0033, 0.01, and 0.02 m/s

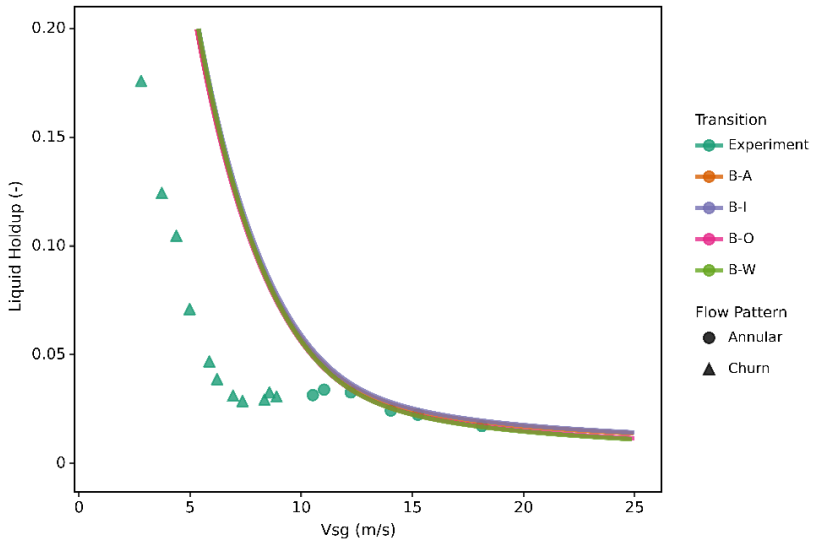

Figure A-54: Liquid holdup at v_{SL} = 0.0033 m/s using Jayanti and Brauner (1994) approach with Belt et al. (2009) model with different entrainment models in oil-air flow

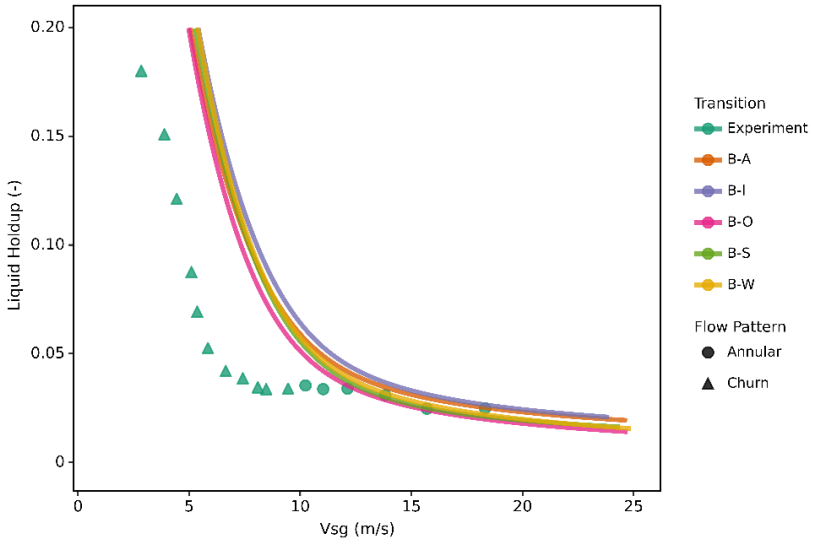

Figure A-55: Liquid holdup at v_{SL} = 0.01 m/s using Jayanti and Brauner (1994) approach with Belt et al. (2009) model with different entrainment models in oil-air flow

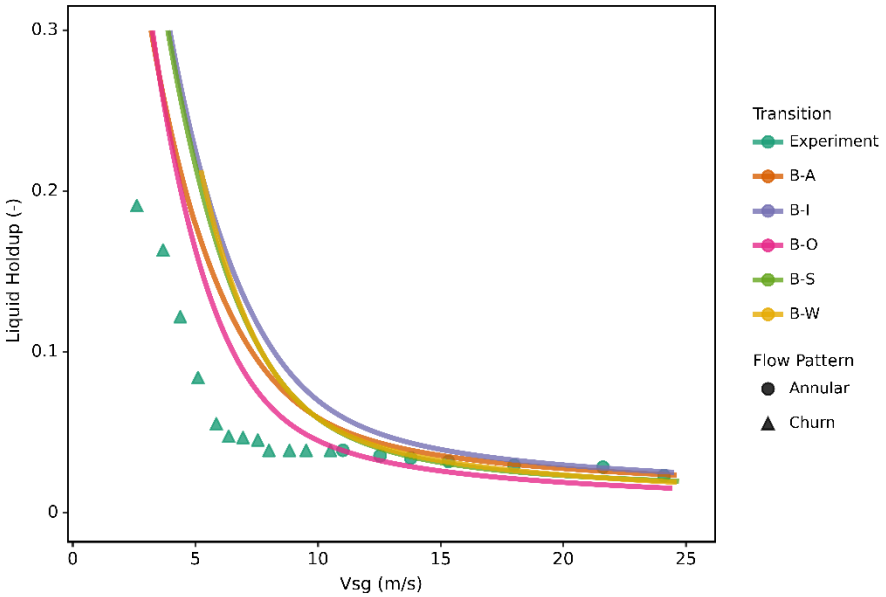

Figure A-56: Liquid holdup at v_{SL} = 0.02 m/s using Jayanti and Brauner (1994) approach with Belt et al. (2009) model with different entrainment models in oil-air flow

A.5 Using Jayanti and Brauner (1994) approach with Fukano and Furukawa (1998)

A.5.1 Water-air Result

Annular-churn transition using Jayanti and Brauner (1994) approach with Fukano and Furukawa (1998) model for water-air is presented in the following figure

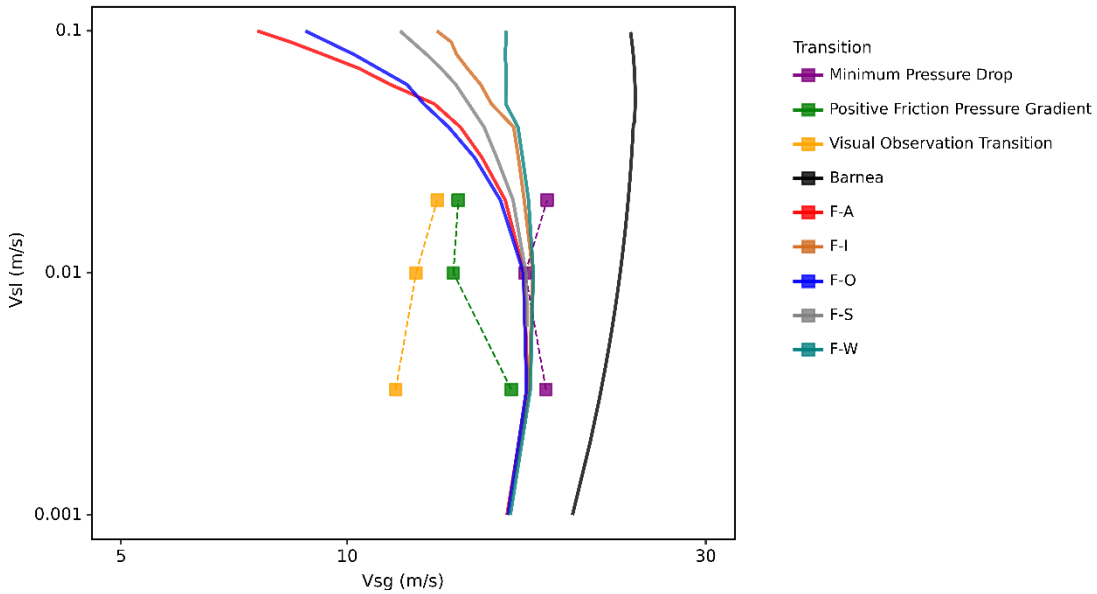

Figure A-57: Annular-churn transition using Jayanti and Brauner (1994) approach with Fukano and Furukawa (1998)l with different entrainment models in water-air flow

Pressure drop prediction using Jayanti and Brauner (1994) approach with Fukano and Furukawa (1998) model for water-air are presented at v_{SL} = 0.0033, 0.01, and 0.02 m/s.

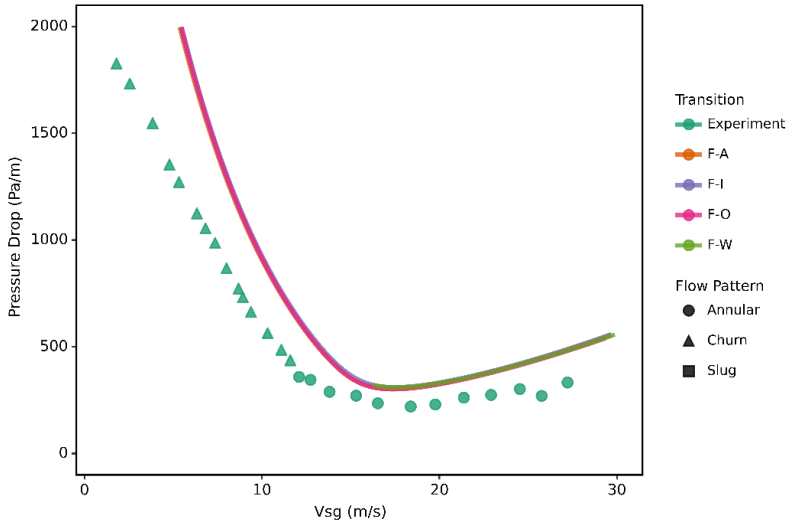

Figure A-58: Pressure drop at v_{SL} = 0.0033 m/s using Jayanti and Brauner (1994) approach with with Fukano and Furukawa (1998) model with different entrainment models in water-air flow

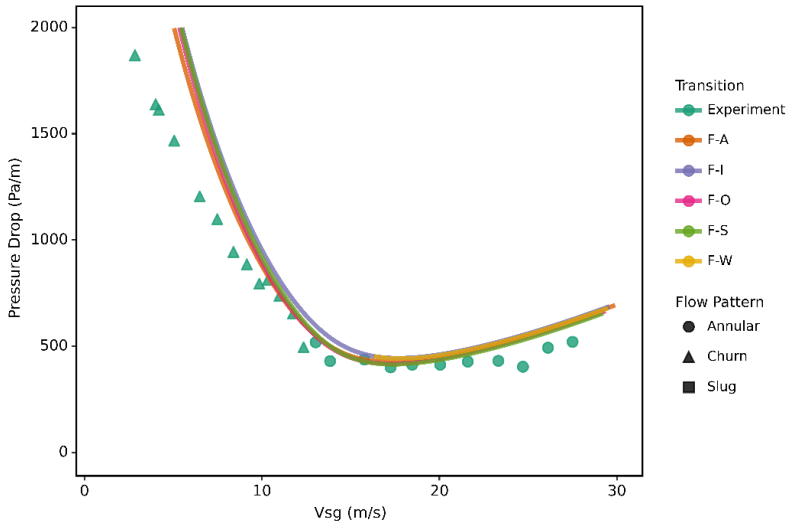

Figure A-59: Pressure drop at v_{SL} = 0.01 m/s using Jayanti and Brauner (1994) approach with with Fukano and Furukawa (1998) model with different entrainment models in water-air flow

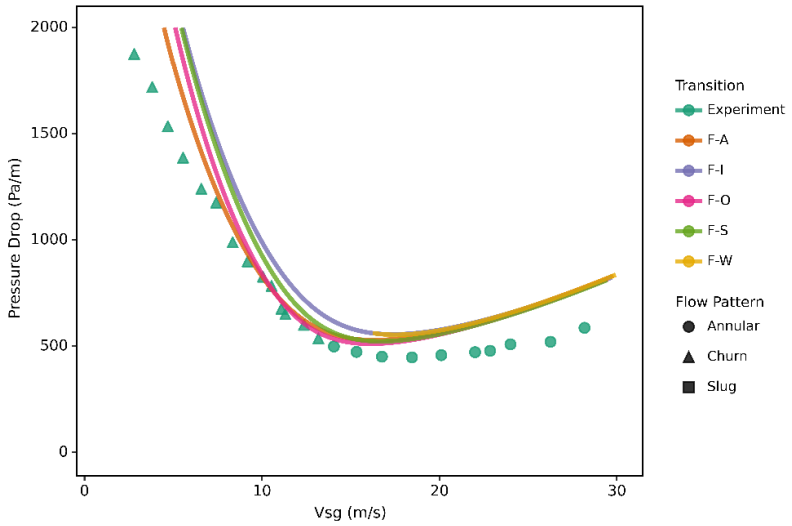

Figure A-60: Pressure drop at v_{SL} = 0.02 m/s using Jayanti and Brauner (1994) approach with with Fukano and Furukawa (1998) model with different entrainment models in water-air flow

Liquid holdup prediction using Jayanti and Brauner (1994) approach with Fukano and Furukawa (1998) model for oil-air are presented at v_{SL} = 0.0033, 0.01, and 0.02 m/s.

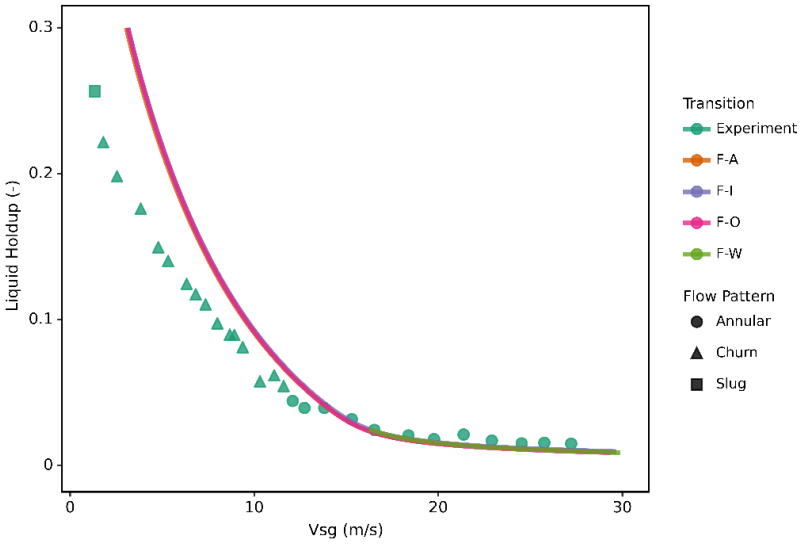

Figure A-61: Liquid holdup at v_{SL} = 0.0033 m/s using Jayanti and Brauner (1994) approach with with Fukano and Furukawa (1998) model with different entrainment models in water-air flow

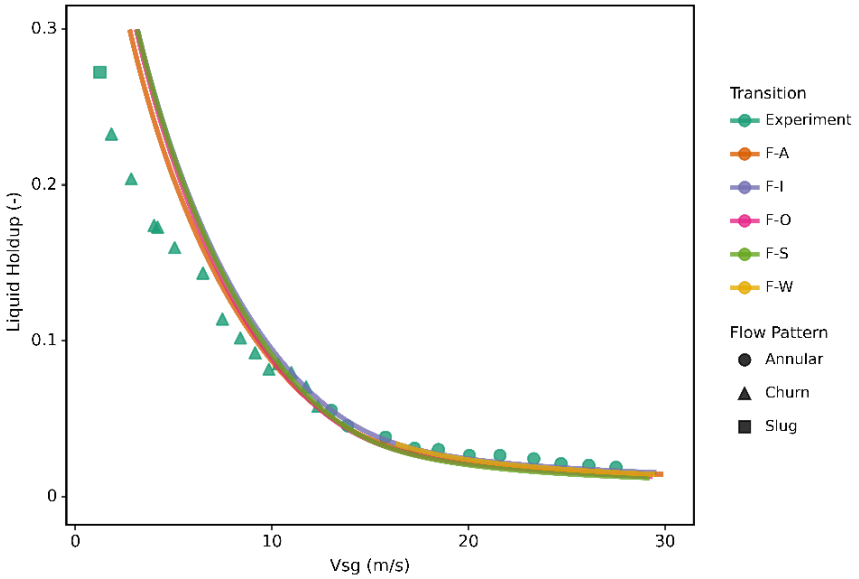

Figure A-62: Liquid holdup at v_{SL} = 0.01 m/s using Jayanti and Brauner (1994) approach with with Fukano and Furukawa (1998) model with different entrainment models in water-air flow

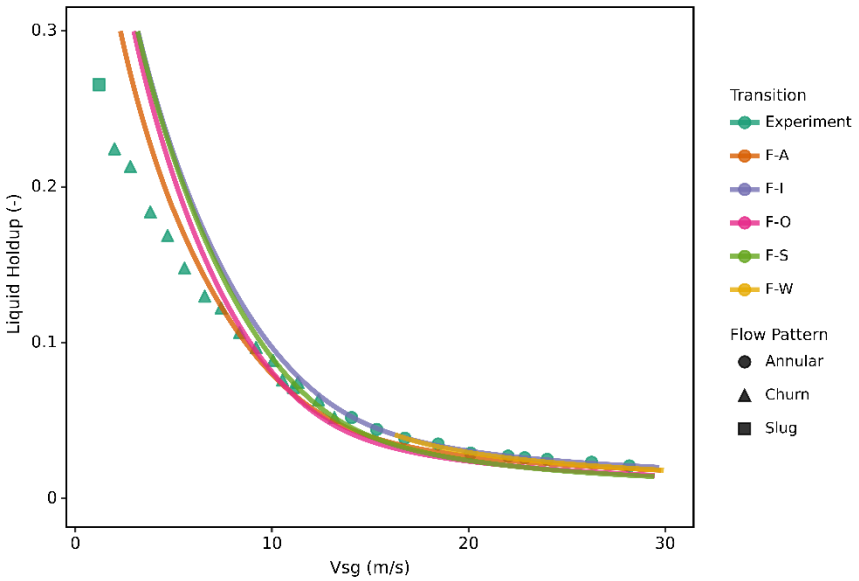

Figure A-63: Liquid holdup at v_{SL} = 0.02 m/s using Jayanti and Brauner (1994) approach with with Fukano and Furukawa (1998) model with different entrainment models in water-air flow

A.5.2 Oil-air Result

Annular-churn transition using Jayanti and Brauner (1994) approach with Fukano and Furukawa (1998) model for oil-air is presented in the following figure

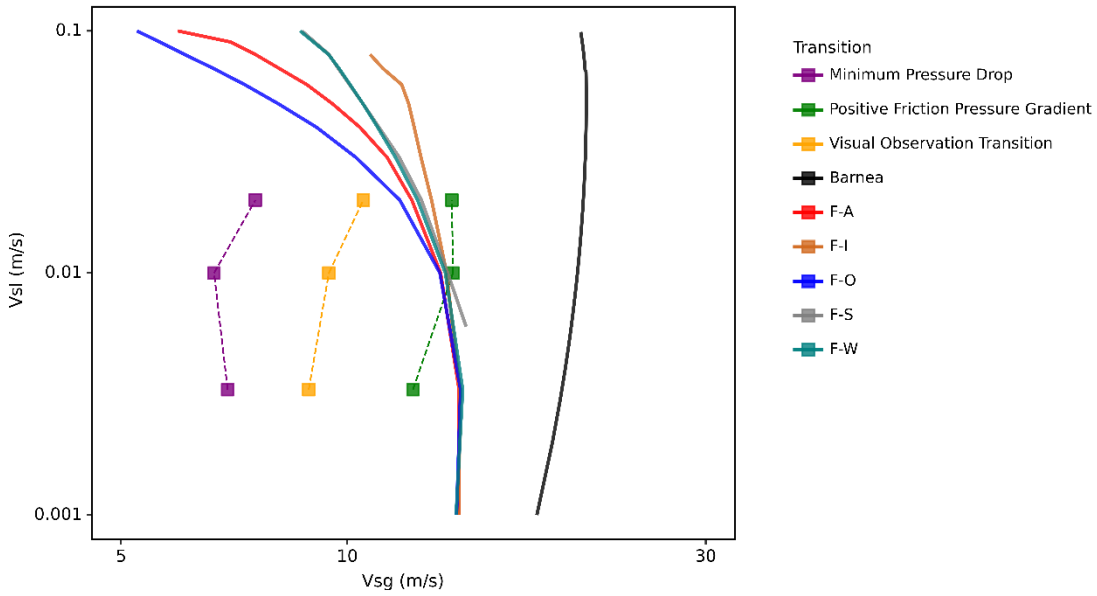

Figure A-64: Annular-churn transition using Jayanti and Brauner (1994) approach with Fukano and Furukawa (1998) with different entrainment models in oil-air flow

Pressure drop prediction using Jayanti and Brauner (1994) approach with Fukano and Furukawa (1998) model for oil-air are presented at v_{SL} = 0.0033, 0.01, and 0.02 m/s.

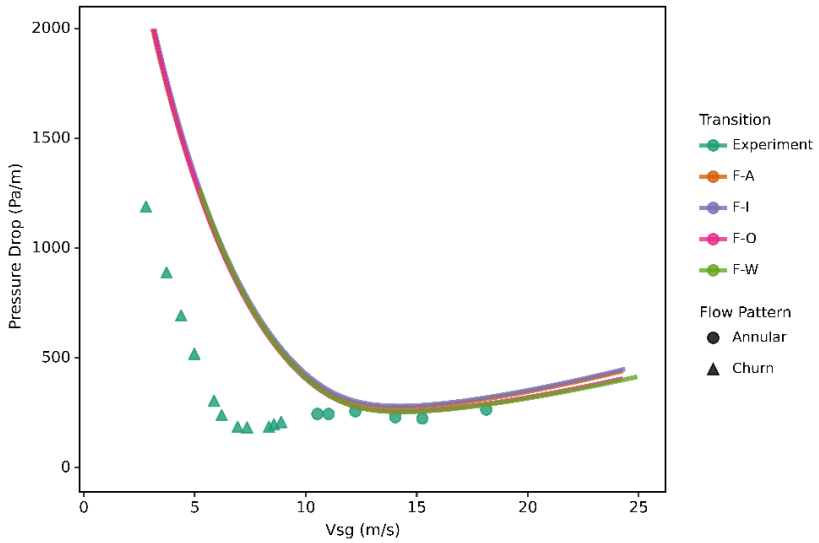

Figure A-65: Pressure drop at v_{SL} = 0.0033 m/s using Jayanti and Brauner (1994) approach with with Fukano and Furukawa (1998) model with different entrainment models in oil-air flow

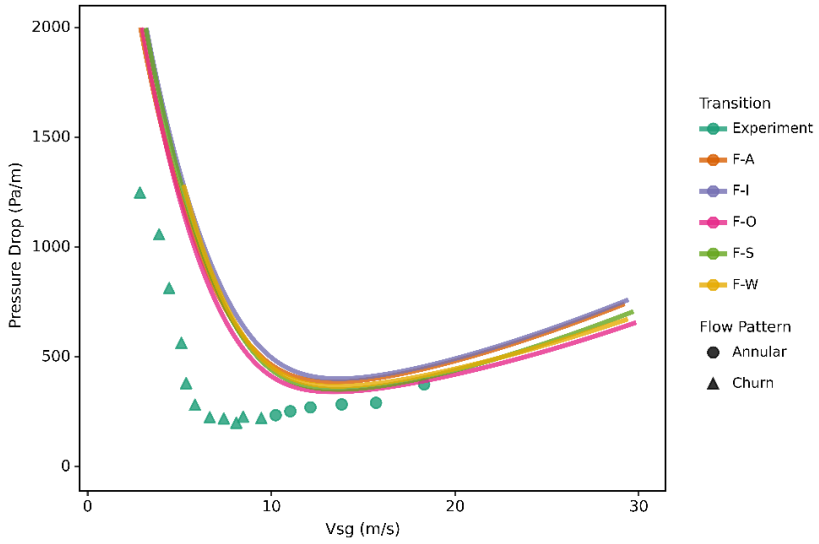

Figure A-66: Pressure drop at v_{SL} = 0.01 m/s using Jayanti and Brauner (1994) approach with with Fukano and Furukawa (1998) model with different entrainment models in oil-air flow

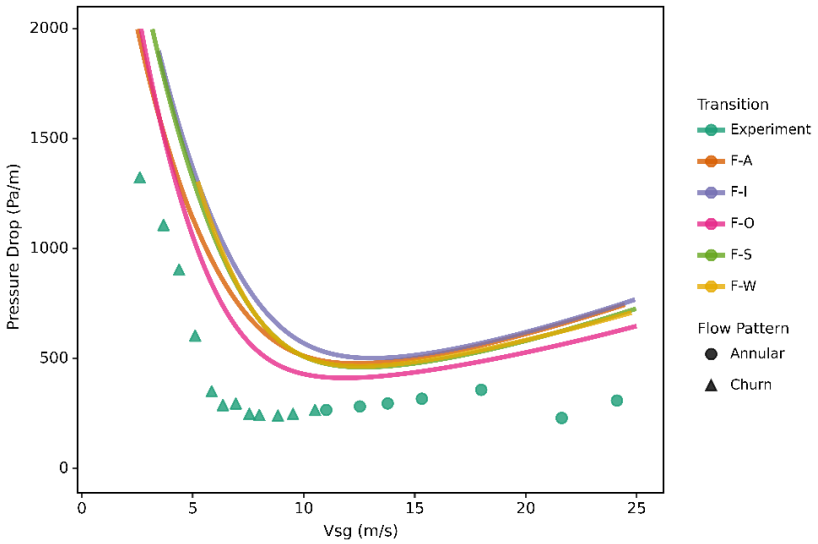

Figure A-67: Pressure drop at v_{SL} = 0.02 m/s using Jayanti and Brauner (1994) approach with with Fukano and Furukawa (1998) model with different entrainment models in oil-air flow

Liquid holdup prediction using Jayanti and Brauner (1994) approach with Fukano and Furukawa (1998) model for oil-air are presented at v_{SL} = 0.0033, 0.01, and 0.02 m/s.

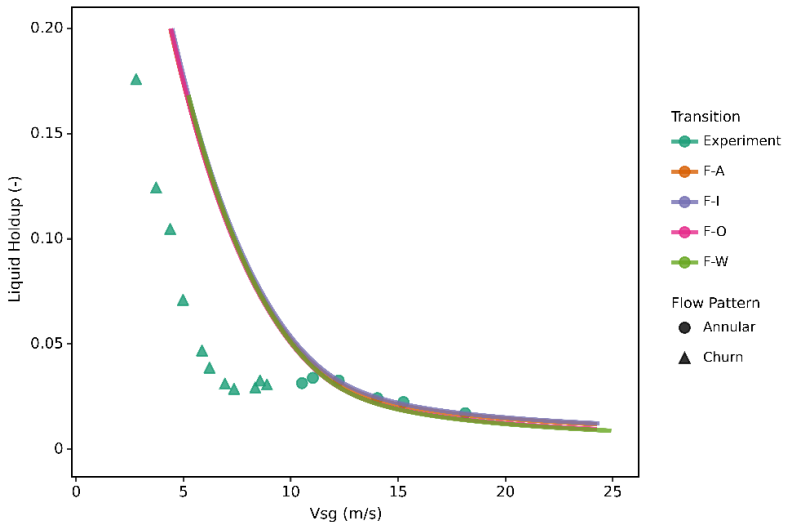

Figure A-68: Liquid holdup at v_{SL} = 0.0033 m/s using Jayanti and Brauner (1994) approach with with Fukano and Furukawa (1998) model with different entrainment models in oil-air flow

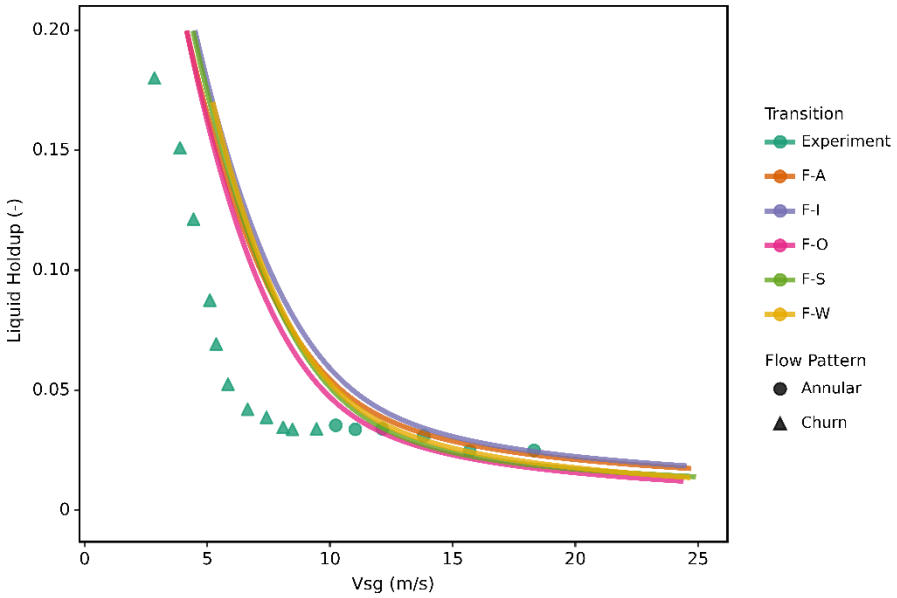

Figure A-69: Liquid holdup at v_{SL} = 0.01 m/s using Jayanti and Brauner (1994) approach with with Fukano and Furukawa (1998) model with different entrainment models in oil-air flow

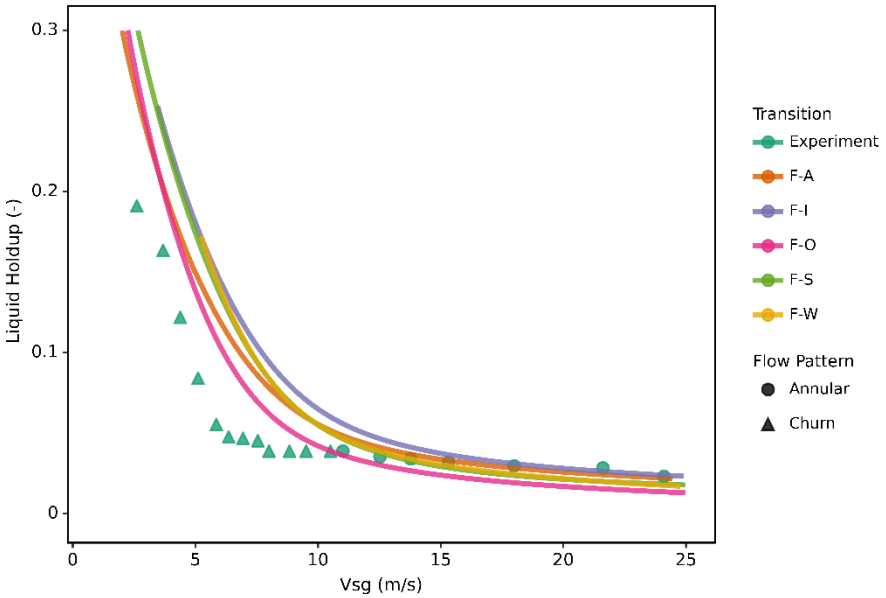

Figure A-70: Liquid holdup at v_{SL} = 0.02 m/s using Jayanti and Brauner (1994) approach with with Fukano and Furukawa (1998) model with different entrainment models in oil-air flow

Appendix B

Statistical Parameters

To assess the performance of the model for the pressure drop and liquid holdup, statistical parameters were used. Actual error (e_i) and relative error (e_{ri}) are the two types of errors used to calculate these parameters. The calculation of the actual error and relative error is done by,

$$e_i = (P_i - A_i) \quad \text{B-1}$$

$$e_{ri} = 100\ (\frac{P_i - A_i}{A_i}) \quad \text{B-2}$$

where A_i is the actual or measured value and P_i is the predicted or calculated value. The following six statistical parameters are defined based on the relative and actual errors:

a) Average relative error,

$$\varepsilon_1 = \frac{1}{N}\sum_{i=1}^{N}(e_{ri}) \quad \text{B-3}$$

b) Absolute average relative error

$$\varepsilon_2 = \frac{1}{N}\sum_{i=1}^{N}|e_{ri}| \quad \text{B-4}$$

c) Standard deviation of relative error,

$$\varepsilon_3 = \sqrt{\frac{\sum_{i=1}^{N}(e_{ri}-\varepsilon_1)^2}{N-1}} \quad \text{B-5}$$

d) Average actual error,

$$\varepsilon_4 = \frac{1}{N}\sum_{i=1}^{N}(e_i) \quad \text{B-6}$$

e) Absolute average actual error

$$\varepsilon_5 = \frac{1}{N}\sum_{i=1}^{N}|e_i| \quad \text{B-7}$$

f) Standard deviation of actual error,

$$\varepsilon_6 = \sqrt{\frac{\sum_{i=1}^{N}(e_i-\varepsilon_4)^2}{N-1}} \quad \text{B-8}$$

where *N* is the number of data point.

The average percentage relative error, ε_1 , and the average actual error, ε_4, are indicators of how closely the parameters were predicted and observed. If these average errors are positive, the parameter has been overestimated. Otherwise, they show that the parameter has been underestimated. The true performance may be hidden by individual errors, which can be either positive or negative and cancel one another. The masking effect is eliminated by the average absolute actual error, which is ε_5, and the average absolute percentage relative error, which is ε_2. They reveal the average size of the error. The relative and actual error standard deviations, which are ε_3 and ε_6 respectively, show the degree of data scattering in relation to their corresponding average errors, ε_1 and ε_4, respectively.

Appendix C

Uncertainty Analysis

Every system has an error of measurement. The error is defined as the difference between the measured value and the true value. The uncertainty is defined as the potential error which exists in all data. The purpose of this uncertainty analysis is to estimate the 95% confidence interval of the measured data, in comparison to the true data. The two types of measurement errors exist for the measurement uncertainty: systemic and random errors. Systemic id the consistent error resulting from measurement device usage, which is usually provided by the manufacturer of the device. Table C-1: Instrument Systematic Uncertainty shows the instrumentations systemic uncertainty (b_R) for measured parameters.

Table C-1: Instrument Systematic Uncertainty

Measured Parameter	Instrument	Systematic Uncertainty
Gas Flow Rate	QuadraTherm flow meter	± 0.2%
Pressure	ProSense Pressure Transducer	± 2.1 (Pa/m)
Pressure Drop	Differential Pressure Transducer	± 0.217-1.1(Pa/m)
Liquid Holdup	Measuring Tape	± 0.0036

Random errors ($S_{\bar{X}}$) are caused by uncontrollable fluctuations in variables which effect the measured parameter. Random errors cannot be controlled and can be calculated using the following equation:

$$S_X = \sqrt{\frac{\sum_{i=1}^{N}(X_i - \overline{X})^2}{N-1}}, \qquad \text{(C-1)}$$

where S_X is standard deviation of the sample, N is the number of data points, X_i is the value of the i[th] data point in the sample, and $\overline{X}$ is the sample average. The random uncertainty calculated as follows:

$$S_{\overline{X}} = \frac{S_X}{\sqrt{N}}, \qquad \text{(C-2)}$$

where $S_{\overline{X}}$ is the 68% confidence interval in $\overline{X}$. The combined random error from the effects of different sources is defined as:

$$S_{\overline{X},R} = \sqrt{\sum_{i=1}^{N}\left(S_{\overline{X},i}\right)^2}. \qquad \text{(C-3)}$$

The overall combined uncertainty (U_{95}) of the systemic and random uncertainties is calculated as follows:

$$U_{95} = \pm t_{95}\sqrt{\left(\frac{b_R}{2}\right)^2 + \left(S_{\overline{X},R}\right)^2}, \qquad \text{(C-4)}$$

where t_{95} is t-coefficient for confidence at 95%, which depends on the size of the sample and the values of b_R and $S_{\overline{X},R}$ should be at a 68% confidence. When a variable is determined from other measured data, using the Taylor's series, the uncertainty propagation is calculated as shown in the following:

$$U\left[f\left(x_1, x_2, \ldots\right)\right] = \sqrt{\left(\frac{\partial f}{\partial x_1} U\left(x_1\right)\right)^2 + \left(\frac{\partial f}{\partial x_2} U\left(x_2\right)\right)^2 + \ldots} \quad \text{(C-5)}$$

In this study, the uncertainty analysis was calculated for pressure drop, liquid holdup and superficial gas velocities.